Control of Microstructure in Porous Silicon Coatings with Closed Porosity for Functional Applications

Doctoral Thesis presented by Jaime Caballero Hernández

Institute of Material Science of Seville (CSIC-US)

Department of Inorganic Chemistry (Universtiy of Seville)

Supervisors

Prof. Dra. Asunción Fernández Camacho

Dra. Vanda Cristina Fortio Godinho

Tutor

Prof. Dr. Jose Antonio Odriozola Gordón

Seville 2016

A mi familia y amigos

Aventurarse allí donde nadie estuvo antes, allí donde nadie te sigue y te comprende. Lejos de los caminos conocidos es donde los sentimientos y las apariencias resultan más intensas.

Reinhold Messner

Table of Contents

Abbreviations..... 9

Chapter 1: Introduction: Porous Silicon Coatings. Overview..... 11

1.1. Approaches for the formation of porous silicon films..... 13

1.2. Porous silicon by magnetron sputtering: A new bottom-up methodology for porous silicon with closed porosity..... 18

1.3. Aims and layout..... 20

1.4. References..... 22

Chapter 2: Experimental Details..... 29

2.1. Materials: Targets, sputtering gases and substrates..... 30

2.2. Deposition Chamber..... 31

2.3. Deposition conditions and nomenclature of coatings..... 34

2.4. Characterization of the porous coatings..... 37

2.4.1. Microstructural characterization..... 37

2.4.2. Composition..... 40

2.4.3. Optical characterization..... 41

2.5. References..... 41

CHAPTER 3: NEW BOTTOM-UP METHODOLOGY TO PRODUCE POROUS SILICON COATINGS BY MAGNETRON..... 43

3.1. Introduction..... 43

3.2. Amorphous silicon coatings with closed porosity by magnetron sputtering..... 45

3.2.1. Preparation and characterization of the porous coatings..... 45

3.2.2. Amorphous silicon coatings with closed porosity..... 47

3.3. A structure zone diagram for closed porosity by magnetron sputtering: Influence of deposition parameters in amorphous silicon coatings..... 52

3.3.1. Deposition geometry: Oblique angle deposition..... 54

3.3.2. Particles flux towards the substrate..... 58

3.3.2.1. Sputtering gas..... 58

3.3.2.2. Helium pressure..... 62

3.3.2.3. Power supplied..... 66

3.3.2.4. Substrate bias..... 75

3.3.2.5. Deposition temperature..... 81

3.4. Post deposition processing: Stability of the porous structure..... 86

3.5. Versatility of the new methodology..... 91

3.6. Conclusions..... 94

3.7. References..... 99

CHAPTER 4: UNDERSTANDING THE FORMATION OF POROUS A-SI NANOSTRUCTURES BY COMPUTER SIMULATION..... 107

4.1. Introduction..... 107

4.2. Simulation software..... 110

4.3. Selected coatings. Experimental details for preparation and characterization..... 112

4.4. Microstructural and chemical characterization: Comparison of experimental and simulation data..... 115

4.4.1. Experimental results..... 115

4.4.2. Simulation films' growth..... 123

4.4.2.1. Angular and energy distributions..... 123

4.4.2.2. Simulation films' growth..... 127

4.4.3. Analysis of closed porosity..... 132

4.5. Conclusions..... 137

4.6. References..... 139

CHAPTER 5: DESIGN AND FABRICATION OF OPTICAL MULTILAYER DEVICES FROM A-SI COATINGS WITH CLOSED POROSITY..... 143

5.1. Introduction..... 143

5.2. Preparation of the optical devices and characterization..... 145

5.3. Design's parameters of the optical devices..... 147

5.4. Optical devices..... 151

5.4.1. Distributed Bragg reflector..... 151

5.4.2. Optical microcavity..... 162

5.5. Conclusions..... 165

5.6. References..... 167

CHAPTER 6: FINAL CONCLUSIONS..... 171

Appendices

I: Characterization techniques…… 177

II: Magnetron sputtering…… 181

III: Morphology and microstructure of thin films: Structure-zone models…….. 189

IV: STEM-EELS analysis reveals stable high-density He in nanopores of amorphous silicon coatings deposited by magnetron sputtering …… 203

V: Calculation of reflectance on multilayered structures: theory and application…… 225

Resumen en Español..... 249

Agradecimientos..... 311

Abbreviations

ADF: Annular dark field

CVD: Chemical vapor deposition

DBR: Distributed Bragg reflector

DC: Direct current

EDX: Energy dispersive X-ray

EELS: Electron energy loss spectroscopy

EFTEM: Energy filtered transmission electron microscopy

ERDA: Elastic recoil detection analysis

OAD: Oblique angle deposition

OMC: Optical microcavity

PVD: Physical vapor deposition

RBS: Rutherford backscattering spectroscopy

RF: Radio frequency

SEM: Scanning electron microscopy

STEM: Scanning transmission electron microscopy

SZM: Structure zone model

TEM: Transmission electron microscopy

XPS: X-ray photoelectron spectroscopy

XRD: X-ray diffraction

Chapter 1

Introduction: Porous Silicon Coatings. Overview

Silicon based materials are still nowadays key for the development of modern technology. The continuous advances in silicon based materials in photonic devices, microelectronics and solar energy conversion [1–4] have drawn once more the attention to porous silicon [5–7].

Porous silicon was accidentally discovered, in the of 1950s at the Bell Laboratories by the Uhlirs [8], when working on a new electrochemical method to produce silicon wafers to be used in microelectronic circuits. They observed, that silicon wafers were not uniformly dissolved when electropolished in HF solutions, but some fine holes appeared, propagating

mainly in the (100) direction of the wafers. Similar findings were reported later by other authors [9] in HF-HNO_3 solutions, and the films formed were investigated in more detail [10,11]. The first author referring to these films as porous silicon was Watanabe [12] that reported how this material could be easily converted into thick silicon oxide films.

However, it was not until the 1990s when the interest in this new material arose due to its particular structure. Lehman and Gösele [13] reported that porous silicon could exhibit increased band gap regarding silicon, and that this phenomenon could be related to quantum size effects.

At the same time Canham [14] observed strong visible photoluminescence at room temperature from p-type silicon wafers electrochemically etched in HF-based solutions. Also the electroluminescent properties of nanostructured porous silicon were reported soon after [15,16].

Under the appropriate conditions porous silicon layers can be obtained with nanometer size features (below the wavelengths of infrared and visible light). These porous silicon layers can therefore be treated as a homogeneous effective medium and its optical properties are mainly controlled by the porosity. Applications as effective silicon light-emitting diodes or devices capable of guiding, modulating and detecting light, increased the interest in porous silicon research since the 90's as it can be appreciated on figure 1.1. Porous silicon offers also a considerable technological interest as it may allow the convenient incorporation of different optical elements into silicon integrated circuits.

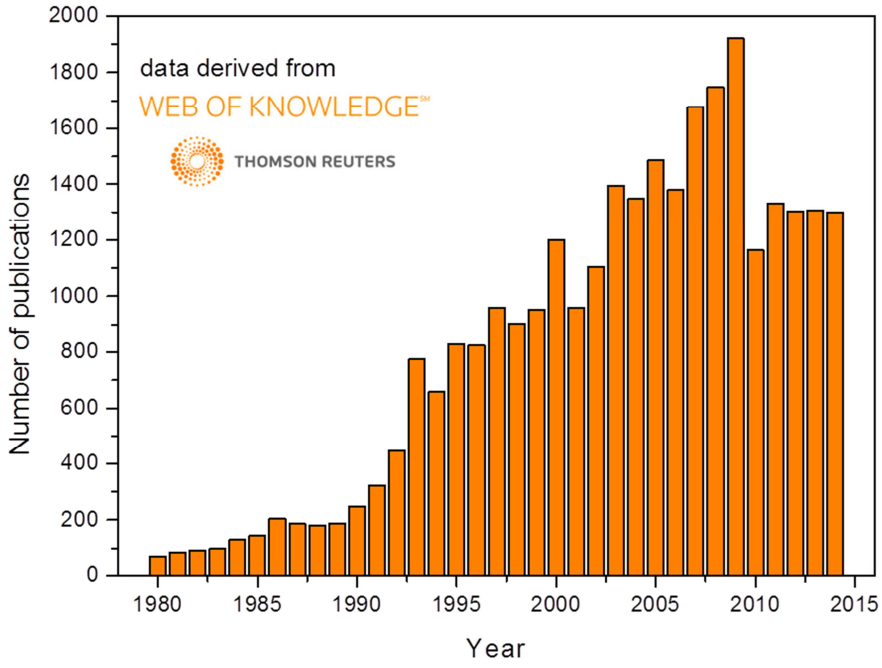

Figure 1.1: Interest in porous silicon over the last decades, number of publications per year. Data derived from WEB of KNOWLEDGE.

In this context of broad interest in this material, the work developed in this thesis is motivated by previous studies in the NanoMatMicro research group that introduced new concepts and expanded the possibilities of producing porous structures by magnetron sputtering presenting closed porosity [17–19]. These first experiments were the basis for the development of a new bottom-up methodology to produce silicon layers with a closed porosity nanostructure by magnetron sputtering [20] which will be detailed discussed in this thesis.

1.1. APPROACHES FOR THE FORMATION OF POROUS SILICON FILMS

Different approaches have been investigated for the production of porous silicon that take into consideration applications, material and process costs, chemical stability, large scale

production, etc. Mainly these processes can be classified in top-down routes starting from solid silicon (figure 1.2 (a)) or bottom-up approaches (figure 1.2 (b)) where silicon atoms or silicon based molecules act as building blocks to obtain the porous structure. Tables 1.1 and 1.2 illustrate the wide variety of routes for the fabrication of porous silicon that are available since the first results by Uhlir.

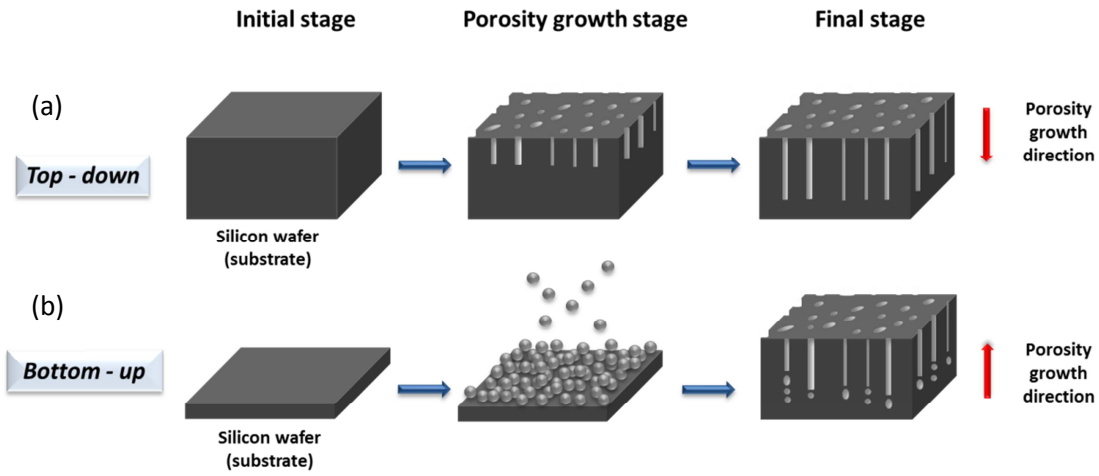

Figure 1.2: Different routes to obtain porous silicon. (a) Top – down. (b) Bottom – up.

Porous silicon has been traditionally fabricated by electrochemical etch of monocrystalline silicon in HF solutions. These top-down routes start from electronic-grade crystalline silicon under the adequate conditions to generate open porosity. In the figure 1.3 (a) it is sketched a typical anodization cell and how the porosity is formed. In figure 1.3 (b) several examples of porous silicon structures obtained by this methodology are presented as reported by Korotcenkov and Cho [21].

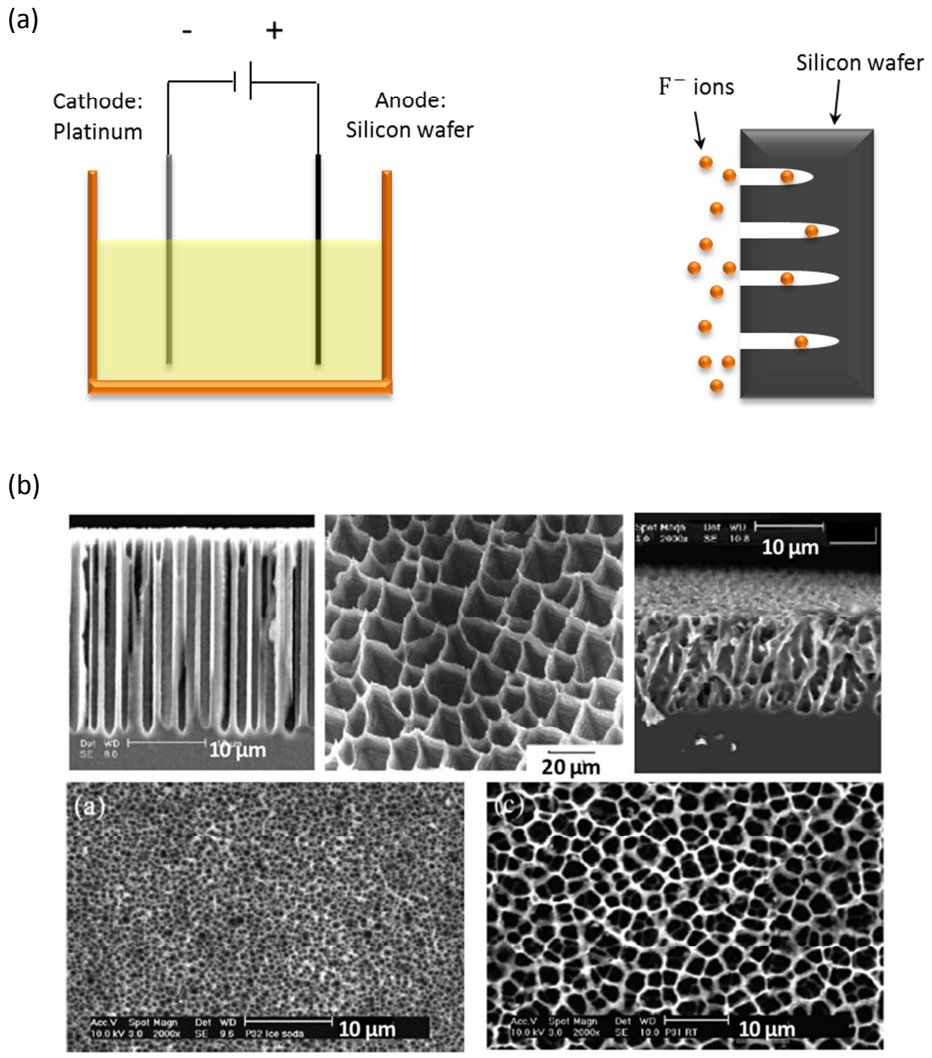

Figure 1.3: Electrochemical etching method. (a) Anodization cell and porosity formation. (b) Examples of obtained porous silicon structures [21].

However, it is known that chemically etched native porous silicon layers show ageing effects deteriorating their properties. A thermal oxidation treatment has been considered to ensure their long-term stability, however this increases the production costs. On the other hand the production of chemical etched porous silicon layers often involves the transfer of these layers to other processable or less expensive substrates [22–24] like glass.

Figure 1.4 gives an example of a transfer process of the electrochemically etched porous silicon layer to be used in solar cells technology. These procedures involve several steps and restrictions regarding substrate nature and size what is limiting an extensive use. More details about this process have been reported by Solanki et al. [22].

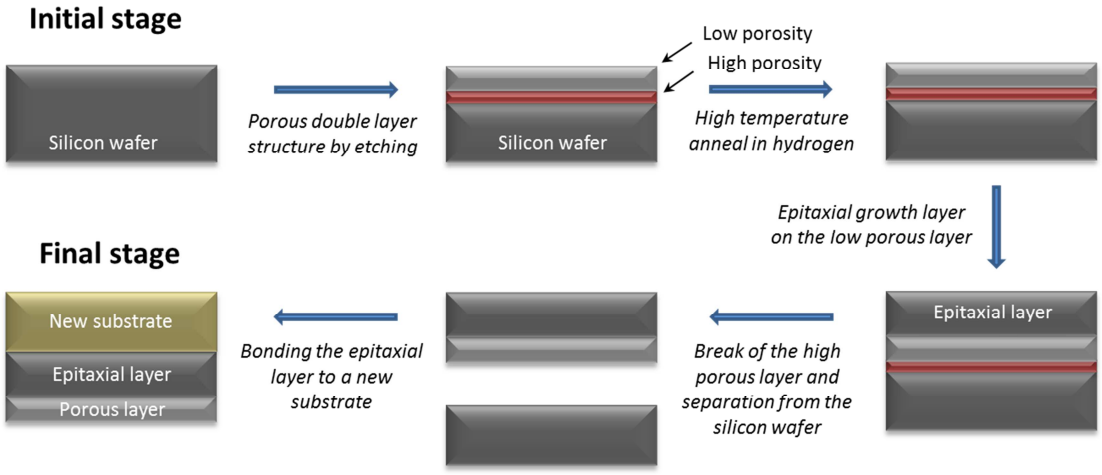

Figure 1.4: Example of a transfer process of the electrochemically etched porous silicon layer (adapted from [22].

Deposition methods were considered good bottom-up alternatives to produce porous silicon coatings in particular in cases where sensible substrates (polymeric or glass) or very thin films are required. In particular oblique angle deposition (OAD) processes allow for morphologies of highly porous columnar coatings and have been proposed as promising methods for fabricating nanoporous silicon based films with desirable optical properties [25–27].

Note that from almost all top-down techniques the porous silicon created is polycrystalline. In the case of bottom-up techniques amorphous silicon can also be obtained. A list of several bottom-up procedures, generally based on deposition methods, is summarized in table 1.2. This thesis takes into consideration these and other aspects to propose a new

bottom-up methodology to produce porous silicon coatings presenting closed porosity by magnetron sputtering.

Table 1.1: Top-down fabrication procedures for porous silicon adapted from [28].

Top-down			
Fabrication technique	**Class**	**Early paper on the technique**	**Year**
Anodization	Etching (wet)	Uhlir [8]	1956
Anodization	Etching (wet)	Canham and Groszek [29]	1992
Spark erosion	Etching (dry)	Hummel and Chang [30]	1992
Photoetching	Etching (wet)	Noguchi and Suemune [31]	1993
Hydrothermal etching	Etching (wet)	Chen et al. [32]	1996
Laser ablation	Thermal	Savin et al. [33]	1996
Metal ion-assisted chemical etching (MACE)	Etching (wet)	Dimova-Malinovska et al. [34]	1997
Galvanic etching	Etching (wet)	Ashruf et al. [35]	1999
Laser-induced plasma	Etching (dry)	Kabashin and Meunier [36]	2002
Vapour etching	Etching (wet)	Saadoun et al. [37]	2002
Magnesiothermic reduction of silica	Conversion reaction	Bao et al. [38]	2007
Femtosecond laser ablation	Thermal	Mahmood et al. [39]	2009
Micromachining and wet etching	Etching (wet)	Deng et al. [40]	2013
Platinum NP-assisted etching (PaCE)	Etching (wet)	Li et al. [41]	2013
Rochow reaction-based etching	Etching (dry)	Zhang et al. [42]	2014

Table 1.2: Bottom-up fabrication procedures for porous silicon adapted from [28].

Bottom-up			
Fabrication technique	**Class**	**Early paper on the technique**	**Year**
Plasma deposition	Deposition	Kalkan et al. [43]	2000
Glancing angle depostion	Deposition	Beydaghan [25]	2004
Melt gasification	Thermal	Nakahata and Nakajima [44]	2004
Laser-induced silane decomposition	Deposition	Voight et al. [45]	2005
Dealloying	Deposition + Etching (wet)	Fukutani et al. [46]	2005
Plasma hydrogenation	Deposition	Abdi et al. [47]	2005
Electrodeposition	Deposition	Krishnamurthy et al. [48]	2011
Magnetron sputtering	Deposition	Godinho et al. [20]	2013
Sacrificial template	Deposition	Huang et al. [49]	2013
Templated silicon tetrachloride reduction	Conversion reaction	Dai et al. [50]	2014

1.2. Porous silicon by magnetron sputtering: A new bottom-up methodology for porous silicon with closed porosity

One of the most interesting features of porous silicon is its customized refractive index.

The work developed previously to this thesis in the NanoMatMicro group shows how porous silicon oxynitride coatings with similar composition and different refractive index can be deposited by magnetron sputtering. Under the adequate conditions a microstructure of closed pores filled with deposition gas is obtained allowing to tailor the material's optical properties [18,19]. Exploratory experiments in the research group revealed that a similar microstructure could be obtained for silicon coatings when using helium as deposition gas [17,51].

Over the years, due to its chemically inert character, noble gases have been widely used in different deposition processes or to locally modify surfaces by radiation or implantation [52]. Very recently a broad interest was shown on the study of nanostructuring of thin films and surfaces obtained by low-energy He plasma treatment.

However, the first studies on the interplay of He ions irradiation with metal thin films have been mainly investigated due to its importance in nuclear technology. Helium has been reported to be insoluble in different metals, and tends to accumulate in small bubbles [53] causing radiation damage in nuclear reactors. These closed pores microstructures from high energy ion-irradiated or ion-implanted helium, generally consist in few pores situated at a certain distance from the surface.

The magnetron sputtered porous SiON [18,19] layers, and the exploratory experiments with silicon and He plasmas, showed highly porous structures with uniform porosity from the substrate to the coatings surface. Moreover, a wide range of thicknesses (from few nm to few microns) can be deposited. This methodology could be therefore a good alternative to the traditional electrochemical methods for porous silicon layer production. Magnetron sputtering is a very versatile technique that allows uniform deposition over large surfaces and over a wide variety of substrates, even sensible substrates like polymers or directly

over glass, without the need of laborious processes. It is easy to scale up being one of the most common vacuum deposition methods in industry.

Works on the introduction of He bubbles in metals by magnetron sputtering have previously been reported, mainly to re-create the conditions of the nuclear reactors and the cold plasma in contact with the reactor walls using He/Ar mixtures. However, to our knowledge no previous works have been reported on the production of closed pores silicon films and the modification of its optical properties using this methodology.

In this thesis the work is focused on the development of a new bottom-up methodology to produce silicon coatings with closed porosity. One of the main objectives is the search of the deposition conditions that can lead to the formation of controlled closed porosity microstructures in silicon coatings. From a fundamental point of view these new materials with embedded pores, filled with the deposition gas, represent a new class of nanocomposite materials presenting on demand optical properties in comparison with the matrix film. The influence of the deposition parameters on the microstructure and refractive index of the coatings will be comprehensively investigated providing new reference data. The state of the deposition gas inside the pores will be studied.

With the help of a Monte Carlo simulation model, the influence of the atomistic processes on the formation of the porous structure when helium or argon is used as process gas will be investigated.

The versatility of the deposition methodology will be demonstrated by the fabrication of single-material 1D silicon photonic structures.

1.3. Aims and layout

As described above the motivation of this thesis is the development of this new methodology, based on the magnetron sputtering technique, to produce porous silicon coatings with closed porosity. The global aim is to understand the relationship between deposition parameters, microstructure and final properties of the materials, to finally be able to fabricate devices on demand based on the new methodology. For accomplishing these general goals, in addition to this "Introduction" section as chapter 1, the thesis is divided in different parts (described in chapters 2 to 5) with their particular objectives as summarized below:

Chapter 2: ***Experimental details***

The employed materials, the deposition chamber and a description of the different characterization techniques are described in this section. The general deposition conditions and the nomenclature of coatings are also introduced in this chapter. Of special relevance here is the complete set-up of the deposition chamber with the main objective of having accessibility to a range of deposition parameters variations, adapted to the investigation of the new methodology based on the sputtering technique with He plasmas.

Chapter 3: ***New bottom-up methodology to produce porous silicon coatings by magnetron sputtering***

This chapter is a fundamental part of the thesis. It aims to control the closed porosity microstructure (size, shape and porosity distribution), as well as the amount of trapped gas from the deposition process, and the total porosity degree of the coatings. To achieve this microstructural and chemical control, an ample screening of deposition parameters was accomplished for the applied discharge power, the gas phase pressure and composition, the deposition geometry, or the substrate-bias conditions. The correlation with the microstructural and chemical analysis of the fabricated coatings finally leads in this chapter to the elaboration of empirical structure zone diagrams for the growth of sputtered amorphous silicon

films in He plasmas. It is also worth to mention here the work carried out to accomplish a full microstructural and chemical characterization of the coatings from the macroscopic measurements to the nano-scale analysis in advanced TEM facilities. These analytical tools will be also employed in all the other chapters. The correlation between microstructure and optical properties is another fundamental goal in this chapter in order to fabricate silicon coatings with tailored refractive index. The stability in time of the porous coatings structure and of the helium trapped in the closed pores is put into evidence. The effects of annealing treatments on the structure, helium state in the pores and optical properties are investigated.

Chapter 4: ***Understanding the formation of porous a-Si nanostructures by computer simulation***

In a first approach ballistic aggregation Monte Carlo (MC) simulation codes can be used to understand the influence of atomistic processes on the formation of film nanostructures during thin film deposition. The objective of this chapter was to apply available simulation methodologies to the study of the novel type of silicon coatings with occluded pores fabricated by the introduction of He as process gas. The special case of helium as process gas during magnetron sputtering deposition had not been investigated by theoretical models before. Due to the limitations of the available codes the experimental conditions for preparation of the films, to be compared with simulations, have been limited to DC magnetron sputtering deposition at oblique angles under conditions of geometric control of the nanostructure (i.e. in zone I of Thornton's structure zone model). The comparison between experiment and simulations allowed to show in this thesis that the chemical nature of the sputtering gas not only affects the sputter mechanism and the collisional processes in the gaseous/plasma phase, but also the pore formation and dynamics within the material, and thus the film microstructure.

Chapter 5: ***Design and fabrication of optical multilayer devices from porous a-Si coatings with closed porosity***

The understanding and control of the microstructure and optical properties (refractive index) of the porous silicon coatings achieved in the previous chapters opens the possibility to use these coatings for the design and fabrication of optical multilayers devices on-demand. The objective of this chapter is the fabrication of two different optical devices, a distributed Bragg refractor (DBR) and an optical microcavity (OMC), by design of the adequate multilayered structure based on a single material alternating dense and porous silicon layers. The chapter will show the good agreement between the expected and experimentally obtained optical response of the two devices. The good quality of the optical response is attributed to the good control of the fabrication with sharp interfaces in the multilayer structure. In this part of the thesis the advantages and possibilities of the new methodology are therefore emphasized.

1.4. References

1. Becker, C. *et al.* Large-area 2D periodic crystalline silicon nanodome arrays on nanoimprinted glass exhibiting photonic band structure effects. *Nanotechnology* **23,** 135302 (2012).

2. Jin, H. & Liu, G. L. Fabrication and optical characterization of light trapping silicon nanopore and nanoscrew devices. *Nanotechnology* **23,** 125202 (2012).

3. Zhang, K., Seo, J.-H., Zhou, W. & Ma, Z. Fast flexible electronics using transferrable silicon nanomembranes. *J. Phys. -Appl. Phys.* **45,** 143001 (2012).

4. Spinelli, P., Verschuuren, M. A. & Polman, A. Broadband omnidirectional antireflection coating based on subwavelength surface Mie resonators. *Nat. Commun.* **3,** 692 (2012).

5. Dubey, R. S. & Gautam, D. K. Synthesis and characterization of porous silicon layers for 1D photonic crystal application. *Optik* **122,** 494–497 (2011).

6. Abidi, D., Romdhane, S., Brunet-Bruneau, A. & Fave, J.-L. Microstructural characterization of porous silicon for use in optoelectronic devices. *Eur. Phys. J.-Appl. Phys.* **45,** 10601 (2009).

7. Ramizy, A., Hassan, Z., Omar, K., Al-Douri, Y. & Mahdi, M. A. New optical features to enhance solar cell performance based on porous silicon surfaces. *Appl. Surf. Sci.* **257,** 6112–6117 (2011).

8. Uhlir, A. Electrolytic Shaping of Germanium and Silicon. *Bell Syst. Tech. J.* **35,** 333–347 (1956).

9. Fuller, C. & Ditzenberger, J. Diffusion of Donor and Acceptor Elements in Silicon. *J. Appl. Phys.* **27,** 544–553 (1956).

10. Turner, D. Electropolishing Silicon in Hydrofluoric Acid Solutions. *J. Electrochem. Soc.* **105,** 402–408 (1958).

11. Archer, R. Stain Films on Silicon. *J. Phys. Chem. Solids* **14,** 104–110 (1960).

12. Watanabe, Y., Arita, Y., Yokoyama, T. & Igarashi, Y. Formation and Properties of Porous Silicon and Its Application. *J. Electrochem. Soc.* **122,** 1351–1355 (1975).

13. Lehmann, V. & Gosele, U. Porous Silicon Formation - a Quantum Wire Effect. *Appl. Phys. Lett.* **58,** 856–858 (1991).

14. Canham, L. T. Silicon quantum wire array fabrication by electrochemical and chemical dissolution of wafers. *Appl. Phys. Lett.* **57,** 1046–1048 (1990).

15. Halimaoui, A. *et al.* Electroluminescence in the Visible Range During Anodic-Oxidation of Porous Silicon Films. *Appl. Phys. Lett.* **59,** 304–306 (1991).

16. Koshida, N. & Koyama, H. Visible Electroluminescence from Porous Silicon. *Appl. Phys. Lett.* **60,** 347–349 (1992).

17. Fernández-Camacho, A. & Godinho, V. Procedimiento de obtención de recubrimientos mediante pulverización catódica y recubrimiento obtenible. (2009). at <Spanin. P200930085, PCT/ES 2010/070245>

18. Godinho, V., Rojas, T. C. & Fernandez, A. Magnetron sputtered a-SiOxNy thin films: A closed porous nanostructure with controlled optical and mechanical properties. *Microporous Mesoporous Mater.* **149,** 142–146 (2012).

19. Godinho, V. *et al.* SiOxNy thin films with variable refraction index: Microstructural, chemical and mechanical properties. *Appl. Surf. Sci.* **256,** 4548–4553 (2010).

20. Godinho, V. *et al.* A new bottom-up methodology to produce silicon layers with a closed porosity nanostructure and reduced refractive index. *Nanotechnology* **24,** 275604 (2013).

21. Korotcenkov, G. & Cho, B. K. Silicon Porosification: State of the Art. *Crit. Rev. Solid State Mater. Sci.* **35,** 153–260 (2010).

22. Solanki, C. S., Bilyalov, R. R., Poortmans, J., Nijs, J. & Mertens, R. Porous silicon layer transfer processes for solar cells. *Sol. Energy Mater. Sol. Cells* **83,** 101–113 (2004).

23. Bergmann, R. B. & Werner, J. H. The future of crystalline silicon films on foreign substrates. *Thin Solid Films* **403,** 162–169 (2002).

24. Van Nieuwenhuysen, K. *et al.* High-Quality Epitaxial Foils, obtained by a Layer Transfer Process, for Integration in Back-Contacted Solar Cells processed on Glass. *2012 38th Ieee Photovolt. Spec. Conf. Pvsc* 1833–1836 (2012).

25. Beydaghyan, G., Kaminska, K., Brown, T. & Robbie, K. Enhanced birefringence in vacuum evaporated silicon thin films. *Appl. Opt.* **43,** 5343–5349 (2004).

26. Poxson, D. J. *et al.* High-performance antireflection coatings utilizing nanoporous layers. *Mrs Bull.* **36,** 434–438 (2011).

27. Jang, S. J., Song, Y. M., Yeo, C. I., Park, C. Y. & Lee, Y. T. Highly tolerant a-Si distributed Bragg reflector fabricated by oblique angle deposition. *Opt. Mater. Express* **1,** 451–457 (2011).

28. Canham, L. in *Handbook of Porous Silicon* (ed. Canham, L.) 1–7 (Springer International Publishing, 2014). at <http://link.springer.com/referenceworkentry/10.1007/978-3-319-04508-5_1-1>

29. Canham, L. & Groszek, A. Characterization of Microporous Si by Flow Calorimetry - Comparison with a Hydrophobic Sio2 Molecular-Sieve. *J. Appl. Phys.* **72,** 1558–1565 (1992).

30. Hummel, R. & Chang, S. Novel Technique for Preparing Porous Silicon. *Appl. Phys. Lett.* **61,** 1965–1967 (1992).

31. Noguchi, N. & Suemune, I. Luminescent Porous Silicon Synthesized by Visible-Light Irradiation. *Appl. Phys. Lett.* **62,** 1429–1431 (1993).

32. Chen, Q. W. *et al.* Ultraviolet light emission from porous silicon hydrothermally prepared. *Phys. Lett. A* **224,** 133–136 (1996).

33. Savin, D. P., Roizin, Y. O., Demchenko, D. A., Mugenski, E. & Sokolska, I. Properties of laser ablated porous silicon. *Appl. Phys. Lett.* **69,** 3048–3050 (1996).

34. DimovaMalinovska, D., SendovaVassileva, M., Tzenov, N. & Kamenova, M. Preparation of thin porous silicon layers by stain etching. *Thin Solid Films* **297,** 9–12 (1997).

35. Ashruf, C. M. A., French, P. J., Bressers, P. & Kelly, J. J. Galvanic porous silicon formation without external contacts. *Sens. Actuators -Phys.* **74,** 118–122 (1999).

36. Kabashin, A. V. & Meunier, M. Fabrication of photoluminescent Si-based layers by air optical breakdown near the silicon surface. *Appl. Surf. Sci.* **186,** 578–582 (2002).

37. Saadoun, M. *et al.* Vapour-etching-based porous silicon: a new approach. *Thin Solid Films* **405,** 29–34 (2002).

38. Bao, Z. *et al.* Chemical reduction of three-dimensional silica micro-assemblies into microporous silicon replicas. *Nature* **446,** 172–175 (2007).

39. Mahmood, A. S., Sivakumar, M., Venkatakrishnan, K. & Tan, B. Enhancement in optical absorption of silicon fibrous nanostructure produced using femtosecond laser ablation. *Appl. Phys. Lett.* **95,** 034107 (2009).

40. Deng, T., Chen, J., Wu, C. N. & Liu, Z. W. Fabrication of Inverted-Pyramid Silicon Nanopore Arrays with Three-Step Wet Etching. *Ecs J. Solid State Sci. Technol.* **2,** P419–P422 (2013).

41. Li, X. *et al.* Fast electroless fabrication of uniform mesoporous silicon layers. *Electrochimica Acta* **94,** 57–61 (2013).

42. Zhang, Z. *et al.* Scalable Synthesis of Interconnected Porous Silicon/Carbon Composites by the Rochow Reaction as High-Performance Anodes of Lithium Ion Batteries. *Angew. Chem.-Int. Ed.* **53,** 5165–5169 (2014).

43. Kalkan, A. K., Bae, S. H., Li, H. D., Hayes, D. J. & Fonash, S. J. Nanocrystalline Si thin films with arrayed void-column network deposited by high density plasma. *J. Appl. Phys.* **88,** 555–561 (2000).

44. Nakahata, T. & Nakajima, H. Fabrication of lotus-type porous silicon by unidirectional solidification in hydrogen. *Mater. Sci. Eng. -Struct. Mater. Prop. Microstruct. Process.* **384,** 373–376 (2004).

45. Voigt, F., Bruggemann, R., Unold, T., Huisken, F. & Bauer, G. H. Porous thin films grown from size-selected silicon nanocrystals. *Mater. Sci. Eng. C-Biomim. Supramol. Syst.* **25,** 584–589 (2005).

46. Fukutani, K., Ishida, Y., Aiba, T., Miyata, H. & Den, T. Characterization of nanoporous Si thin films obtained by Al-Si phase separation. *Appl. Phys. Lett.* **87,** 253112 (2005).

47. Abdi, Y. *et al.* Light-emitting nano-porous silicon structures fabricated using a plasma hydrogenation technique. *Mater. Sci. Eng. B-Solid State Mater. Adv. Technol.* **124,** 483–487 (2005).

48. Krishnamurthy, A., Rasmussen, D. H. & Suni, I. I. Galvanic Deposition of Nanoporous Si onto 6061 Al Alloy from Aqueous HF. *J. Electrochem. Soc.* **158,** D68–D71 (2011).

49. Huang, X., Gonzalez-Rodriguez, R., Rich, R., Gryczynski, Z. & Coffer, J. L. Fabrication and size dependent properties of porous silicon nanotube arrays. *Chem. Commun.* **49,** 5760–5762 (2013).

50. Dai, F. *et al.* Bottom-up synthesis of high surface area mesoporous crystalline silicon and evaluation of its hydrogen evolution performance. *Nat. Commun.* **5,** 3605 (2014).

51. Godinho, V. Synthesis and characterization of magnetron sputtered thin films of the Ti-Al-Si-N(O) system. (2011). at <University of Seville>

52. Fleischer, E. L. & Norton, M. G. Noble gas inclusions in materials. *Heterog. Chem. Rev.* **3,** 171–201 (1996).

53. Lucas, A. Helium in Metals. *Phys. B C* **127,** 225–239 (1984).

Chapter 2

Experimental details

In this thesis a new “bottom-up” methodology for the preparation of porous silicon coatings by magnetron sputtering is explored. The coatings investigated in this work were deposited under different deposition conditions to obtain and control a closed porosity nanostructure. In this chapter the general deposition conditions employed are described, more detailed description of the chosen conditions will be introduced on the different chapters. The materials employed, the deposition chamber and a description of the different characterization techniques are here introduced.

2.1. Materials: Targets, sputtering gases and substrates

The materials used in this thesis can be divided in three groups, the target material, the sputtering gases and the substrates.

The sputtering targets used were $2''$ diameter monocrystalline silicon targets (Kurt J. Lesker company, 99.999% purity with resistivity below $1\ \Omega\ cm$). Since silicon is a semiconductor, to improve the sputtering process $0.125''$ thick targets were used.

The coatings investigated in this work were deposited using non-reactive gases: helium and/or argon. Table 2.1 presents the percentage of purity and the impurities level in ppm (parts per million) for both gases according to the specifications of the supplier. The values are given for $3.8\ m^3$ cylinder from Air Liquide Company.

Table 2.1: Specifications of sputtering gases.

Sputtering gas	Purity	Impurities		
		H_2O	O_2	C_nH_m
Helium	99.999%	$\leq 3\ ppm$	$\leq 2\ ppm$	$\leq 0.5\ ppm$
Argon	99.999%	$\leq 3\ ppm$	$\leq 2\ ppm$	$\leq 0.1\ ppm$

The versatility of magnetron sputtering technique allows to deposit over a wide variety of substrates. In this thesis different substrates were employed depending on the targeted property of the films and the technique employed for its characterization. The different substrates used in this thesis are summarized in the table 2.2.

Before deposition the substrates were cleaned following the procedure: Step I) Cleaning with acetone and drying with a cloth followed by nitrogen flow. Step II) Cleaning with distilled water and drying with nitrogen flow. Step III) Cleaning with ethanol and drying with nitrogen flow. In the case of polymeric substrates the cleaning procedure started on step II.

Table 2.2: Substrates used.

Substrate material	Supplier	Characterized property / Technique
Silicon wafer (100)	A.C.M.	Microstructure (i.e. electron microscopy), chemical composition (i.e. XPS and RBS)
Quartz	SICO Technology GmbH	Refractive index (Ellipsometry)
Carbon glass	Goodfellow	Chemical composition (i.e. Rutherford Backscattering)
Teflon	Goodfellow	Proof of concept of deposition methodology
Kapton	Goodfellow	Proof of concept of deposition methodology

2.2. DEPOSITION CHAMBER

This section is dedicated to describe the deposition chamber used to produce the coatings studied in this thesis. In the figure 2.1 a drawing of the chamber is presented in which several details about sensors and vacuum system are showed. The chamber is non-commercial and equipped with two vacuum pumps connected in series. A rotatory pump (9) to make a pre-vacuum in the chamber and a turbo molecular pump (8) to get the high vacuum (below $1 \cdot 10^{-4}\ Pa$). The pumping system is separated from the chamber by a guillotine valve (5) for controlling the outlet gas flux from the chamber; all coatings were deposited in dynamic regime. The blue arrows point the circulation of gases when go out of the chamber. The residual vacuum pressure is measured with a full range gauge (6) and the process pressure is measured with a capacitance gauge (2). With this vacuum system it is possible to reach a residual vacuum pressure of $5 \cdot 10^{-5}\ Pa$ (after baking). The deposition chamber is equipped with four ceramic resistances (16) used to pre-heat before deposition allowing to reduce as much as possible the water amount adsorbed on the chamber walls (baking).The baking temperature $(120°C)$ is controlled with the thermocouple (12).

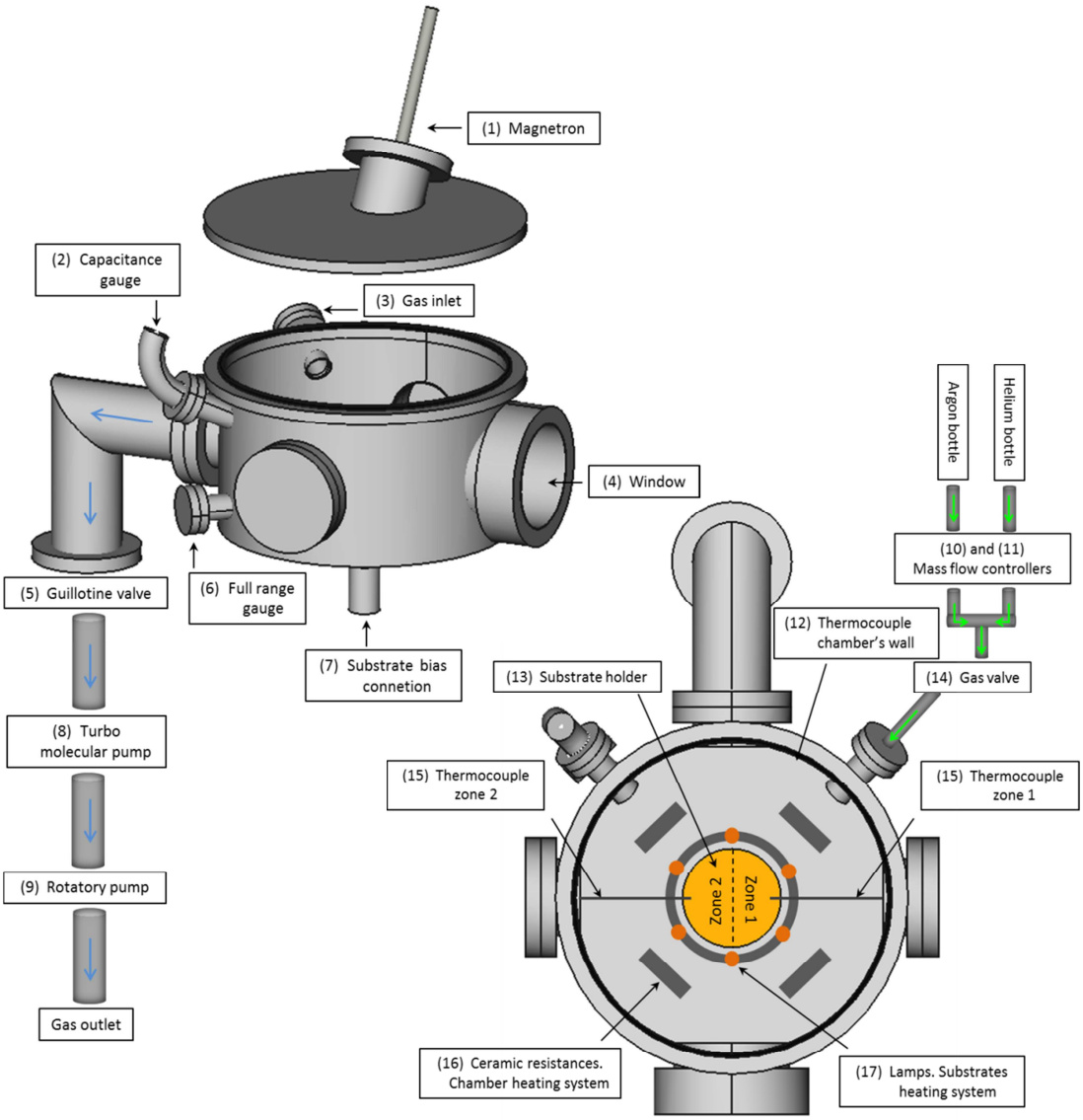

Figure 2.1: Deposition chamber with the different components.

The gases inlet (3) (argon, helium, or a mixture of both) is controlled by mass flow controllers (10) and (11) respectively, with a $100\ sccm$ maximum flux and separated from the chamber by a gas valve (14). The gas inlet in the chamber is the same for the two gases used, allowing pre-mixing when needed. The gas pressure inside the chamber (process

pressure) is controlled by balancing the gas flux and the aperture of the guillotine valve. The green arrows point the circulation of gases when introduced in the chamber.

The magnetron (1) used was a 2" ION'X Sputtering Gun from Thin Film consulting (Germany). The magnetron is tilted $30°$ with the normal to the substrate and equipped with a shutter that can be used to clean the target before deposition. The magnetron can work both in DC or RF power modes.

The substrate holder (13) is electrically insulated from the grounded chamber and is placed in the center of the deposition chamber. It has the possibility to apply a bias voltage to the substrates during growth. A system to heat the substrates (17) composed by six lamps of $50\ W$ is used to prepare the substrates before deposition and to improve the adhesion of the coatings to the substrates. The substrates temperature is controlled with two thermocouples (15), located at the extremities of the sample holder (zones 1 and 2). For deposition at higher temperatures another heating system with 3 halogen lamps of $500\ W$ was employed. Besides, the chamber is equipped with a window (4) to observe the deposition process.

The distance between the center of the target and sample holder is fixed at $5\ cm$. The relative positions of the substrates, located in two different zones on the sample holder, in respect to the magnetron are sketched in the following figure:

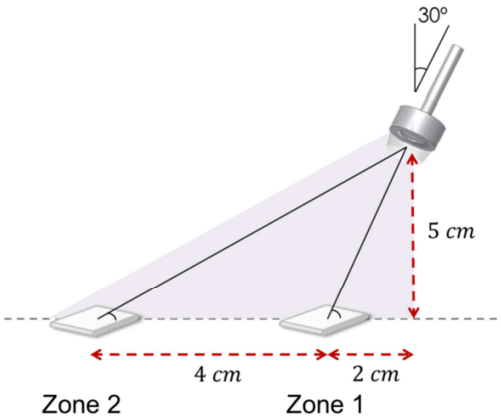

Figure 2.2: Relative position of the substrates in both zones of the sample holder with respect to the magnetron.

2.3. Deposition conditions and nomenclature of coatings

In this work different deposition conditions were investigated for the formation of closed porosity and control of properties. In this section, a simplified nomenclature that allows easy identification of the deposition conditions used is presented. On each chapter, the influence of different parameters were investigated, nevertheless the nomenclature of the samples follows a similar order.

In all cases the chamber was pumped to $1 \cdot 10^{-4}\ Pa$ before baking. Before deposition the substrates were pre-heated to $50°C$ during one hour and the target was cleaned for 15 minutes at the same deposition conditions used to deposit each coating.

Chapter 3

The nomenclature used in the coatings in the chapter 3 is:

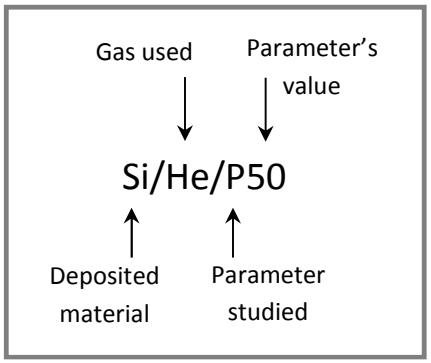

Abbreviation	Parameter studied
P	Power
pr	Gas pressure
b	Substrate bias
h	Deposition temperature

The coatings studied in this chapter are presented in the table 2.3.

Table 2.3: Deposition conditions of the coatings analyzed in the chapter 3.

Deposition parameter	Name of Coating	Gas	Incidence angle**	Mode / Power (W)	Pressure (Pa)	Substrate bias (V)	Substrate temperature $(°C)$
INCIDENCE ANGLE	Porous film (a-pSi) *	He	0°	RF 150	1.33	0	---
	Si/He		30°		4.8		
GAS	Si/He	He	30°	RF 150	4.8	0	---
	Si/Ar	Ar					
POWER	Si/He/P 50	He	30°	RF 50	4.8	0	---
	Si/He/P 150			RF 150			
	Si/He/P 300			RF 300			
GAS PRESSURE	Si/He/pr 2.7	He	30°	RF 150	2.7	0	---
	Si/He/pr 2.9				2.9		
	Si/He/pr 4.8				4.8		
	Si/He/pr 9.0				9.0		
	Si/He/pr 23.8				23.8		
	Si/He/pr 54.6				54.6		
SUBSTRATE BIAS	Si/He/b 0	He	30°	RF 150	9.0	0	---
	Si/He/b 100					−100	
	Si/He/b 200					−200	
DEPOSITION TEMPERAT.	Si/He/h As dep	He	30°	RF 150	2.7	0	---
	Si/He/h 200						200
	Si/He/h 300						300
OTHER COATINGS	Dense film (a-Si) *	Ar	0°	RF 150	1.33	0	---
	Si/Ar/bias		30°		1.5	−100	

* These coatings were grown in another deposition chamber were the geometry allows to work at normal incidence angle.

** Respect to the vertical.

The thermal stability of the coatings was investigated by post-deposition annealing treatments carried out in a furnace with helium flux, on coating deposited at $150\ W$ RF power under a helium atmosphere $p = 2.7\ Pa$ using a magnetron angle of 30°. The nomenclature used and the coatings studied are:

Table 2.4: Coatings analyzed in the thermal stability study.

Coating	Annealing temperature $(°C)$
Si/He/h As dep	No additional heating
Si/He/HT-300C	300
Si/He/HT-550C	550

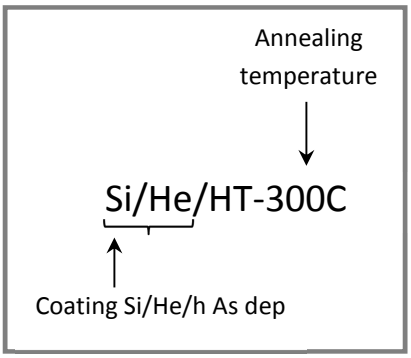

In this series of coatings the sample holder was not heated during deposition as in chapter 3. In this case a post-deposition annealing was carried out in a He flux at the indicated temperature.

Chapter 4

The nomenclature used and the coatings studied in the chapter 4 are:

Table 2.5: Coatings analyzed in the chapter 4.

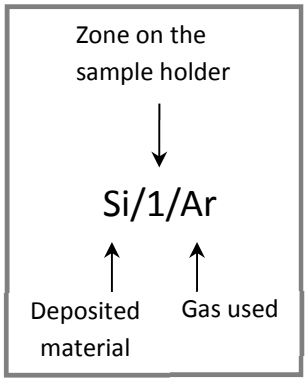

Coating	Zone on sample holder	Mode / Power (W)	Gas pressure (Pa)
Si/1/He+Ar	1	DC 150	He: 1.7 Ar: 0.8
Si/2/He+Ar	2	DC 150	He: 1.7 Ar: 0.8
Si/1/Ar	1	DC 150	1.4
Si/2/Ar	2	DC 150	1.4

Chapter 5

The coatings used to fabricate the optical devices have been described in the chapter 3. In the following table the sequence and number of coatings used in each optical device is presented.

Table 2.6: Coatings used to make the optical devices.

Optical device *	Coatings	Sequency
DBR 1	L_{n1}: Si/He/P150 H_n: Si/Ar/b100	Subst-$(H_nL_{n1})^7H_n$-air
DBR 2	L_{n2}: Si/He/b100 H_n: Si/Ar/b100	Subst-$(H_nL_{n2})^7H_n$-air
OMC	L_{n2}: Si/He/b100 H_n: Si/Ar/b100 L_c: Si/He/b100	Subst-$(H_nL_{n2})^4H_n$-L_c-$(H_nL_{n2})^4H_n$-air

* *DBR:* Distributed Bragg reflector. *OMC*: Optical microcavity.

2.4. CHARACTERIZATION OF THE POROUS COATINGS

A summary description of main characterization is described below in this section. Note that appendix I presents a complete list of all characterization techniques and equipment used during this work.

2.4.1. MICROSTRUCTURAL CHARACTERIZATION

One of the main objectives of this thesis is the search of the deposition conditions that can lead to the formation of controlled closed porosity microstructures in silicon coatings. As described in the previous section different deposition conditions were explored (power, gas nature, gas pressure, chamber geometry, substrate heating, substrate bias, etc.) for the preparation of the coatings. To screen the influence of these deposition conditions on the microstructure of the coatings, electron microscopy techniques have been widely used in this thesis.

Scanning Electron Microscopy (SEM) was carried out in a *Hitachi S4800 SEM-FEG microscope* to study the morphology and thickness of the coatings. Special attention was paid to the observation of the coatings in cross sectional views.

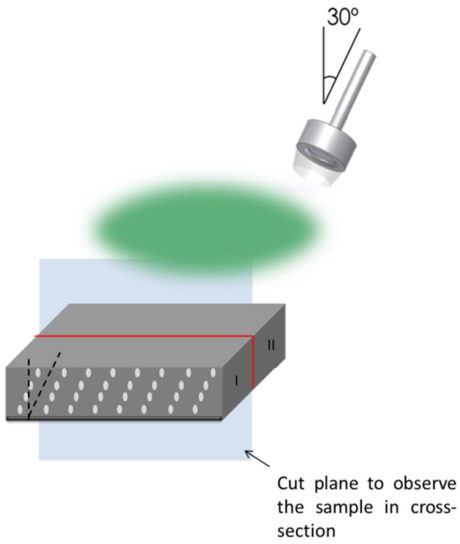

Figure 2.3: Cut direction regarding sample position for observation of the pores angle in cross sectional views.

Figure 2.3 describes how the cross section samples were cleaved from coatings grown onto silicon for observation without metallization at $1-2\ kV$.

A more detailed analysis of the coatings microstructure was performed by Transmission Electron Microscopy (TEM) using a *Philips CM200* (operated at $200\ kV$) and a *FEI Tecnai F30* (operated at $300\ kV$) microscopes (Laboratory for Nanoscopies and Spectroscopies LANE at the ICMS).

Also for TEM investigations the cross section sample preparation was necessary. The samples were first cut according to figure 2.3 and glued as indicated in figure 2.4. The conventional procedure was completed by mechanical polishing, followed by Ar^+ ion milling

to achieve electron transparency of the coatings deposited on Si substrates. Before analysis the samples were cleaned inside the TEM holder with Ar/O_2 plasma.

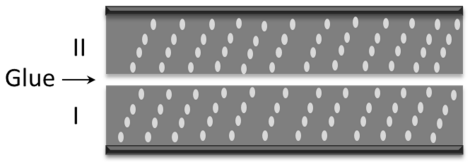

Figure 2.4: Scheme of specimen preparation for observation by TEM in coatings cross section.

Images have been mainly recorded in bright field TEM mode. Electron diffraction and high resolution TEM (HRTEM) have been used to analyze crystallization phenomena in the samples. Of special importance in this work is the pore size distribution analysis which has been evaluated from TEM micrographs using ImageJ software [1] as shown in figure 2.5. The images were processed with an image analysis software to identify the pores as well-defined dark contrast areas (see figures 2.5 (b) and (c)) which were then analyzed with the particle function of Image J software [1].

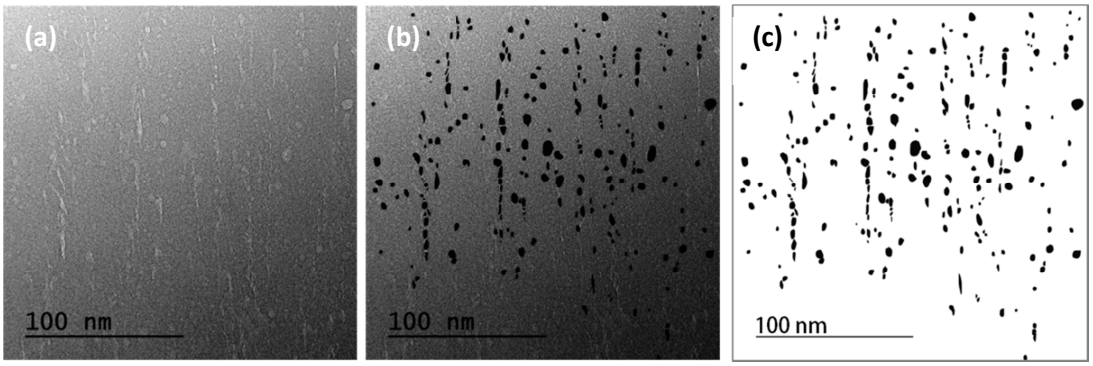

Figure 2.5: (a) As recorded TEM image. (b) Pore identification and selection on TEM image. (c) Selected and analyzed pores by Image J software.

To evaluate the crystallinity, X-ray diffraction (XRD) measurements were done using a *PANalytical X'Pert PRO diffractometer* in Bragg-Brentano $\theta - \theta$ configuration in the interval $10° - 90°$ with a step of $0.05°$ and with a time of $4\ s$ in every step. The radiation used was K_α of Cu with a wavelength of $\lambda = 1.54056$ Å.

2.4.2. Composition

The composition of the films was evaluated by Rutherford Backscattering Spectroscopy (RBS).

In this thesis two facilities were used:

- National Center of Accelerators (CNA Sevilla, Spain) using a $3\ MV$ tandem accelerator. The RBS spectra were obtained using two different energies, 1.0 and $2.3\ MeV$ for proton beam and a surface barrier detector set at $165°$. The lower energy is necessary to separate the Si signal coming from the substrate and from the film, in order to obtain the sample thickness. The higher energy is required to obtain the He content, because of the energy range where the $^4He(p,p_0)^4He$ cross section is available. To obtain the thickness and composition of the coatings, both spectra were simulated simultaneously for every coating using the SIMNRA code [2].
- PMR-LARN Laboratory (University of Namur) using a $2\ MV$ tandetrom accelerator ALTAIS. The energy used was $2.5\ MeV$. The thickness and chemical composition of the coatings were deduced by means of the Sim Target 1.0 [3] and SIMNRA 6.06 [2] codes. Non-Rutherford cross-sections were computed by SigmaCalc on the IBANDL database [4] at detection angles of $165°$ and $170°$.

The composition of the coatings in the nanoscale was evaluated inside the Tecnai F30 microscope. To get information about the composition of the individual pores at the nanoscale, the scanning mode (STEM) was used with a probe size of less than $1\ nm$. Spatially resolved electron energy loss spectra (EELS) were recorded in the low-loss range over $2048\ channels$ ($0.05\ eV/channel$), with integration time of $0.05\ s$. In this range in

addition to the plasmon peaks, the He K-edge at $22\ eV$ is accessible for quantification. Experimental details of these analyses are given in appendix IV.

2.4.3. Optical characterization

2.4.3.1. Ellipsometry measurements

The optical characterization of the coatings was performed by ellipsometry on samples deposited on quartz substrates. The measurements were executed in a *UVISEL spectroscopic ellipsometer from HORIBA Jobin Yvon* with an incidence angle of $60°$ and a wavelength range of $300 - 2100\ nm$. The data were analyzed using the Deltapsi2 software developed by HORIBA Jobin Yvon.

2.4.3.2. Reflectance measurements

The specular reflectance measurements are more particular of the presented chapter. They were performed using near-infrared spectrometer Bruker IFS-66 FTIR. Experimental spectra in the $1000 - 2500\ nm$ wavelength range were measured by a Fourier transform infrared spectrophotometer attached to a microscope and operating in reflection mode with a $4\times$ objective with 0.1 of numerical aperture (light cone angle $\pm\ 5.7°$).

2.5. References

1. Rasband W S ImageJ, U.S.N.I.o.H., Bethesda, Maryland, USA, imagej.nih.gov/ij/, 1997 – 2012.

2. Mayer, M. in *Application of Accelerators in Research and Industry, Pts 1 and 2* (eds. Duggan, J. L. & Morgan, I. L.) **475,** 541–544 (Amer Inst Physics, 1999).

3. Aeken K V. DRAFT - Design, Research And Feasibility of Thin Films at Ghent University/UGent. at <http://www.draft.ugent.be/>

4. Gurbich, A. F. Evaluated differential cross-sections for IBA. *Nucl. Instrum. Methods Phys. Res. Sect. B-Beam Interact. Mater. At.* **268,** 1703–1710 (2010).

Chapter 4

Understanding the Formation of Porous A-Silicon Nanostructures by Computer Simulation

4.1. Introduction

In chapter 3, as well as in previous papers and in the initial work with amorphous Si [1–4] it has been demonstrated that deposition parameters, and the chemical nature of the processing gas, are critical for the development of closed porous structures. Simulation tools have been introduced and used in this chapter, with the aim of getting new information on the phenomena causing the formation of the different microstructures, during grown of porous amorphous Si nanostructured coatings using different sputtering

gases. The advantage to use computer simulation is that the physical processes involved in the code are known. Therefore, by comparing experimental and simulation results it is expected to understand the phenomena determining the difference in the microstructure using different gases and conditions. Due to the limitations of the simulation software, a correct choice of the deposition parameters to deposit the coatings will be necessary for comparing experimental and simulation results.

There are few theoretical models in the literature that analyze the growth of films deposited by plasma-assisted techniques. See for instance Pelliccione and Lu [5] and references therein. Due to the amount of particles involved and the typical times required for the film growth, the use of first principles or molecular dynamics approaches is not recommended due to unaffordable computational costs. In a first approach ballistic aggregation Monte Carlo (MC) simulation codes can be used to understand the influence of atomistic processes on the formation of the film nanostructure during thin film deposition. These types of models are particularly useful in situations where geometric mechanisms govern the formation of the nanostructure, such as when the film growth takes place at low temperatures (i.e. in zone I of Thornton's structure zone model) [6–9]. Kinetic Monte Carlo codes (2D-3D) can be used for the simulation of deposition, diffusion, nucleation, and growth of films on a surface [10,11] and can explain numerous issues regarding the kinetic energy of the vapor particles and the bond structure and chemical nature of the films. Remarkably, many studies in the literature, using atomistic growth models and experiments, have analyzed the influence on the nanostructure of deposition conditions such as the angular incidence of vapor particles onto the film [12], the film temperature during growth [13] or the role of potential barriers [14]. To our knowledge, the influence of inert processing gas on the film nanostructure was not yet clear and needed for further experimental and theoretical investigations. The special case of helium as process gas during magnetron sputtering deposition had not been investigated by theoretical models. Its study in the present work can bring valuable information in the field.

It is also worth to mention here that pore formation by He ion implantation in metal surface layers has been studied thanks to its importance in nuclear technology [15,16]. Helium insolubility and mobility of atoms in the host matrix have been proposed to explain the formation of He bubbles in implanted metals [17–19]. Indeed, to re-create the conditions of reactors and cold plasma in contact with the reactor walls, He has been artificially introduced into materials using well-known plasma-assisted techniques, such as magnetron sputtering of different metals in He/Ar mixtures [20–23]. To our knowledge, no fundamental studies have been carried out in literature to discern whether mobility processes induced by embedded He affect the growth and nanostructural development of as deposited thin films. A deep microstructural and fundamental study was even not available.

At this point the aim of the present chapter is to apply available simulation methodologies, and also experience from other groups in Namur and Seville (see section 4.2), to the study of the novel type of silicon coatings with occluded pores fabricated by the introduction of He as process gas. In particular it is necessary to simulate the sputtering process on the target, the collisional processes in the gaseous/plasma phase and the film growth. In the following section 4.2 it will be first described the software available for simulation of these different processes. The description of capabilities, and the limits of applications of the theoretical programs, will define the experimental conditions for preparation of the films to be investigated. In this sense section 4.3 summarizes the deposition conditions and criteria for samples' selection based on DC magnetron sputtering deposition at oblique angles. Finally by comparison of experimental results and simulations (section 4.4), new insights are presented to understand the formation of the porous structure in nanostructured a-Si coatings when using He in the process gas.

4.2. Simulation software

To simulate the film growth and to understand the influence of atomistic processes on the formation of the film nanostructure, a ballistic aggregation Monte Carlo (MC) simulation model has been used. The well-known and widely-employed NASCAM software [10,24] has been used to analyze film growth. NASCAM (Nanoscale Modeling) is a three-dimensional kinetic Monte Carlo (kMC) code developed in the research group of Condense Matter Physic and Radiation (PMR-LARN) in the University of Namur (Belgium) [24].

The code simulates the time evolution of adatoms deposited (atoms on the substrate surface or on the film surface). The model considers that the particles are randomly thrown towards a substrate with specific energy and incident angle distribution functions. Once they land on the film surface, different mechanism and surface mobility processes are induced depending on the energy of the particles and the local bond structure [10].

NASCAM code takes into account several important parameters, as the deposition rate of the atoms deposited, the angular and energy distributions of sputtered atoms and the gas concentration, the nature of sputtered atoms and gas atoms, the kind of substrate and the deposition temperature. This last parameter is the key factor to influence the thermal events as free diffusion of the deposited atom on the substrate or the evaporation from the film among others. NASCAM code provides the simulation of final microstructure of coating and several important data as the density, roughness, gas atoms trapped in the coating among others. Some of these parameters and data need to be provided by additional software to be integrated into the NASCAM simulations. Therefore to perform simulations the followed steps have been followed:

First, the angular and energy distributions of the sputtered atoms from the target must be known. They were calculated by SRIM software [25]. SRIM takes into account the energy, the mass and the incidence angle of the ion, the mass of the atoms from the target and the surface binding energy of the target.

Second, the transport of these sputtered atoms through the sputtering gas until they reach the substrate is simulated by SIMTRA code [26]. With the information obtained by SRIM, SIMTRA calculates the angular and energy distributions of the sputtered atoms when they land on the substrate. Temperature, pressure and mass of the gas atoms are considered. Besides, the dimensions and position of the magnetron as well as the substrates position are considered. However, SIMTRA considers that the atoms are neutral particles. So the influence of the ions in the plasma is not considered. This consideration can be accepted if a correct choice of the deposition parameters is done. More details about how SIMTRA works have been reported by Van Aeken et al. [27]. The selected deposition parameters compatible with the simulation capabilities are discussed in section 4.3.

And third, with the information obtained by SIMTRA about the angular and energy distribution of the atoms landed onto the substrate, NASCAM simulates the film's growth in three dimensions.

As a summary, in the following sketch are presented the steps followed to perform the simulation of the film's growth.

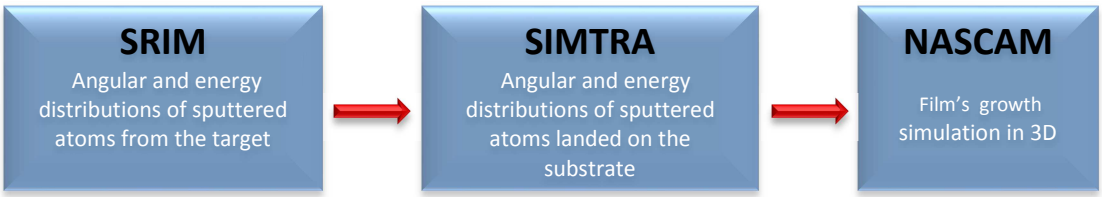

To analyze the porous structure of films simulated by NASCAM, the PORESTAT software [28] has been used. This software has been developed by the research group of Nanotechnology on Surface in the ICMSE in Sevilla (Spain). The software uses a key parameter named pore throat π_t. This quantity topologically characterizes the porous structure as follows: two voids within the material are considered connected, and thus, to belong to the same pore if a circle of diameter π_t covers a continuous path from one to the other without intercepting any material. If such a path does not exist, both voids are considered to belong to different

pores. Moreover, a void is considered occluded if it has no connectivity with the empty space above the film. In the figure 4.1 this idea is represented.

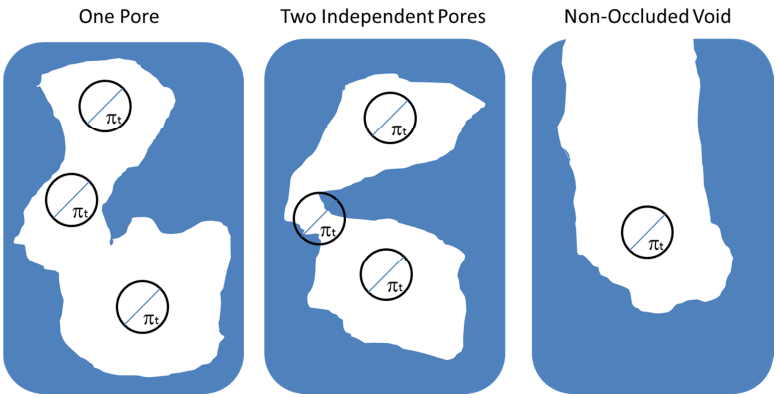

Figure 4.1: Pore throat definition.

4.3. Selected coatings. Experimental details for preparation and characterization

The correct choice of the deposition conditions makes it possible to compare the experimental results with the simulation.

The impingement of the ions in the plasma on the coating's surface during growth of thin films can modify their final microstructure. In the simulation presented herein, the ions are not considered because SIMTRA considers the sputtered particles as neutral atoms. Therefore, to reduce the effect of the ions on the microstructure, a DC power of $150\ W$ was selected in this chapter to maintain the magnetron sputtering plasma during film growth. Under these conditions the low plasma potentials during deposition, around $5\ V$, causes positive ions to impinge on the film below any surface mobility threshold [29]. This fact avoids the influence of ions. Therefore a DC discharge of low voltage was used for preparation of samples with the aim of directly compare experimental and simulation data.

To understand the effect of the sputtering gas on the microstructure and to study the formation of closed porous nanostructure, two gases have been used, helium and argon. As it has been shown, using Ar, a columnar microstructure with open porosity is formed, however, with He, a closed porosity is obtained. Therefore, coatings in pure Ar atmosphere have been deposited. However, in the case of He, it was not possible to sustain the plasma with a pure He atmosphere, so it was necessary to introduce a little amount of Ar, the minimum value to sustain the discharge, obtaining a mixture of He and Ar.

Finally, to investigate the influence of the deposition geometry on the microstructure of the coatings, for each gas atmosphere used, two different films were grown in oblique angle deposition (OAD) (magnetron head tilted $30°$ with the normal to the substrates). Both coatings are located on a plane at $5\ cm$ vertical distance from the magnetron head. As shown in the figure 4.2, one was place in the zone 1 at $2\ cm$ and the other in the zone 2 at $6\ cm$ from the vertical location of the magnetron head above the substrate holder. The coatings in different zones but in the same gas atmosphere were simultaneously grown.

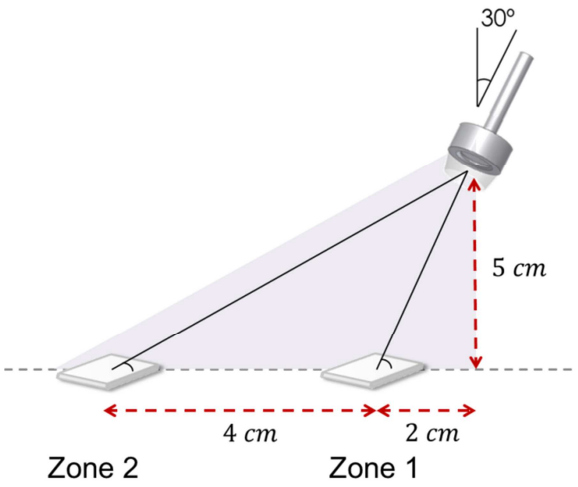

Figure 4.2: Relative position of the substrates in both zones of the sample holder with respect to the magnetron.

In the following table are presented the coatings nomenclature and the deposition conditions used. The nomenclature used in the coatings was described in the chapter 2.

Table 4.1: Deposition conditions of coatings studied.

Coating	Zone on the sample holder	Mode / power (W)	Gas pressure (Pa)	Deposition rate* (nm/s)
Si / 1 / Ar	1	DC 150	1.4	51
Si / 2 / Ar	2	DC 150	1.4	20
Si / 1 / He + Ar	1	DC 150	He: 1.7 Ar: 0.8	38
Si / 2 / He + Ar	2	DC 150	He: 1.7 Ar: 0.8	19

* Calculated from thickness values by SEM cross-sectional views.

With the deposition conditions chosen, the temperatures achieved during deposition were below $130°C$. This implies a value of the homologous temperature T_h of about $T_h = \frac{T_s}{T_m} \sim 0.2$ where T_s is the substrate temperature and T_m is the melting temperature of silicon ($1683.15\ K$). With this low deposition temperature, the film growth falls inside the zone I of Thornton's structure zone model, where thermally activated processes possess limited efficiency in comparison with geometrical effects (shadowing) [9].

The coatings were deposited on polished silicon (100) and carbon glass. The coatings deposited on silicon were used for studying the microstructure by electron microscopy while carbon glass was used only for the Rutherford backscattering spectrometry (RBS) analysis to get a better separation of the Si signal from the coating and substrate.

The microstructure of the coatings, pore size and distribution were investigated by TEM. The pore distribution was evaluated following the methodology used in previous chapters and exposed in the chapter 2. Energy filtered TEM (EFTEM) images were extracted from EFTEM spectrum-image data recorded with a $4\ eV$ slit width and $2\ eV$ energy steps using

the Tecnai F30 microscope. The cross-sectional views analysis and the thickness of coatings were measured out by scanning electron microscopy (SEM).

The composition of the films was evaluated by RBS in the accelerator ALTAIS at the PMR-LARN Laboratory (University of Namur). More details about the characterization techniques are presented in the chapter 2.

4.4. Microstructural and chemical characterization: comparison of experimental and simulation data

4.4.1. Experimental results

In this section the analysis of the coatings prepared will be presented.

By SEM cross-sectional views shown in the figure 4.3, it is difficult to observe any difference between the coatings deposited with different gas atmospheres. The main fact is the difference of thickness between the coatings in zone 1 and zone 2 in the same gas atmosphere. In the zone 1 the thickness is higher than in the zone 2 due to the shorter distance magnetron-substrate in zone 1. In the table 4.1 the reported deposition rates confirm this fact.

To analyze the microstructure in detail it is necessary to observe the coatings by cross-sectional TEM analysis. Figure 4.4 shows the micrographs at low magnification. In these pictures it is clear the geometrical effect due to the tilted position of the magnetron head respect to the substrates position, where the white contrast features correspond to the pore structure. In general, and regardless of the chemical nature of the sputtering gas, coatings show a tilted porous structure aligned along a certain preferential direction, the magnetron direction. This behavior is presented in both zones, 1 and 2. The effect can be qualitatively explained by considering only the surface shadowing effects [6,30]. In OAD, the particle flux towards the substrate is nearly unidirectional, inducing self-shadowing processes that produce tilted porous patterns and decrease the coating density [6,30].

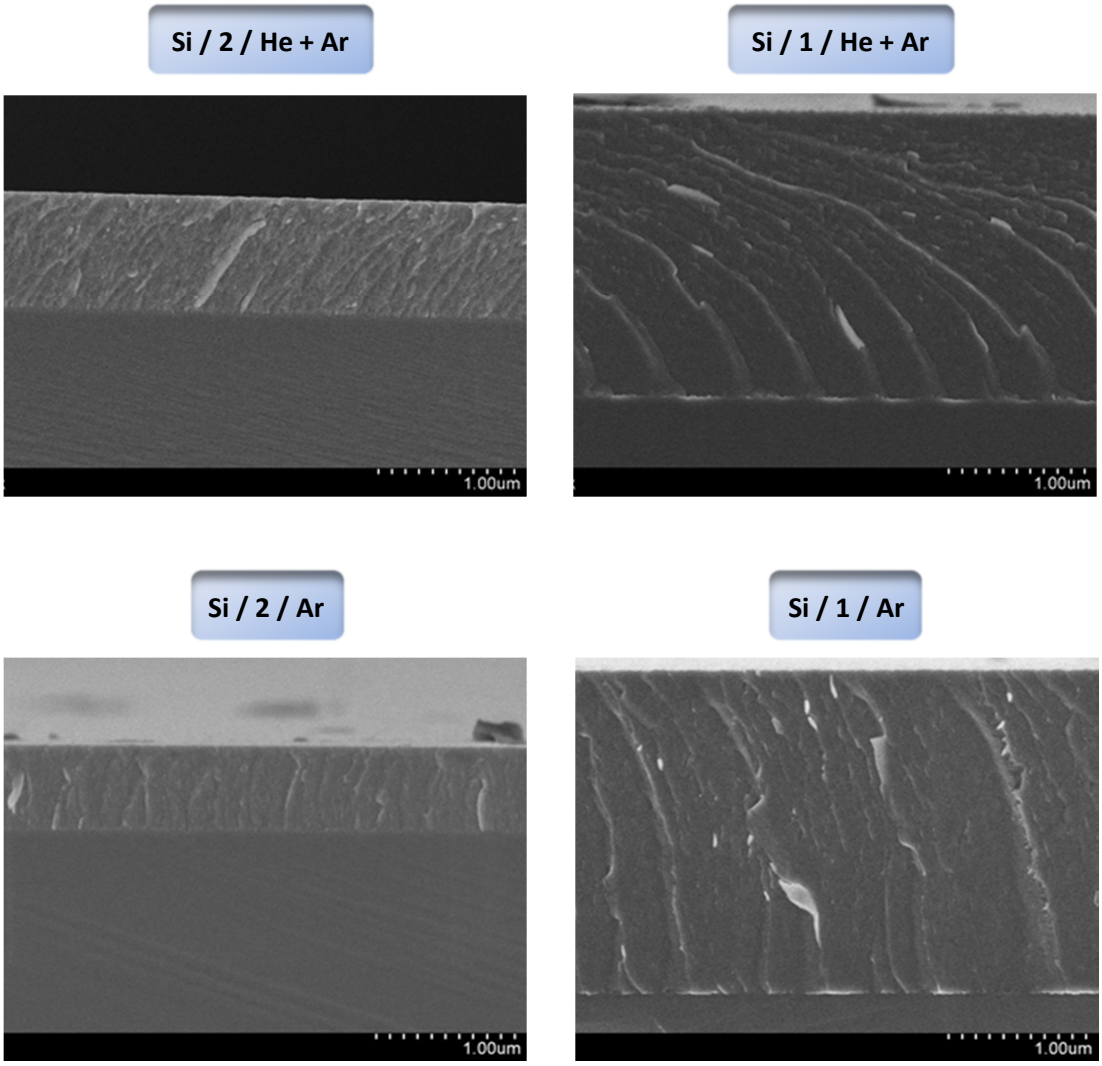

Figure 4.3: SEM cross-sectional views of investigated coatings for both zones and both gas atmospheres.

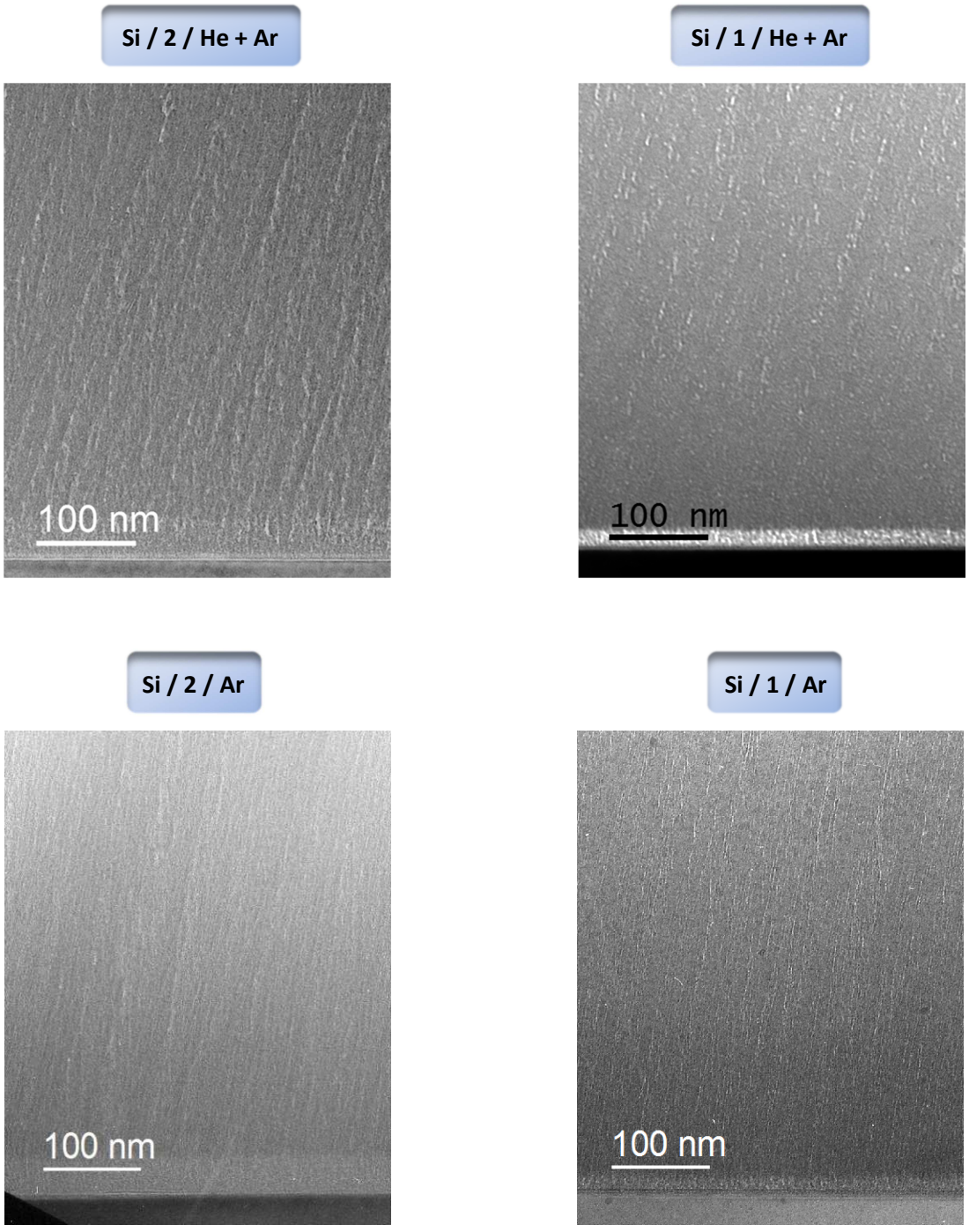

Figure 4.4: TEM cross-sectional views of investigated coatings for both zones and both gas atmospheres.

Rutherford Backscattering Spectroscopy (RBS) measurements were performed and depth profiles for Si, Ar, He, O and C clearly show the substrate, the coating and an interlayer in between. Table 4.2 presents the chemical composition of the porous coating, and in figure 4.5 the RBS elemental profiles are shown.

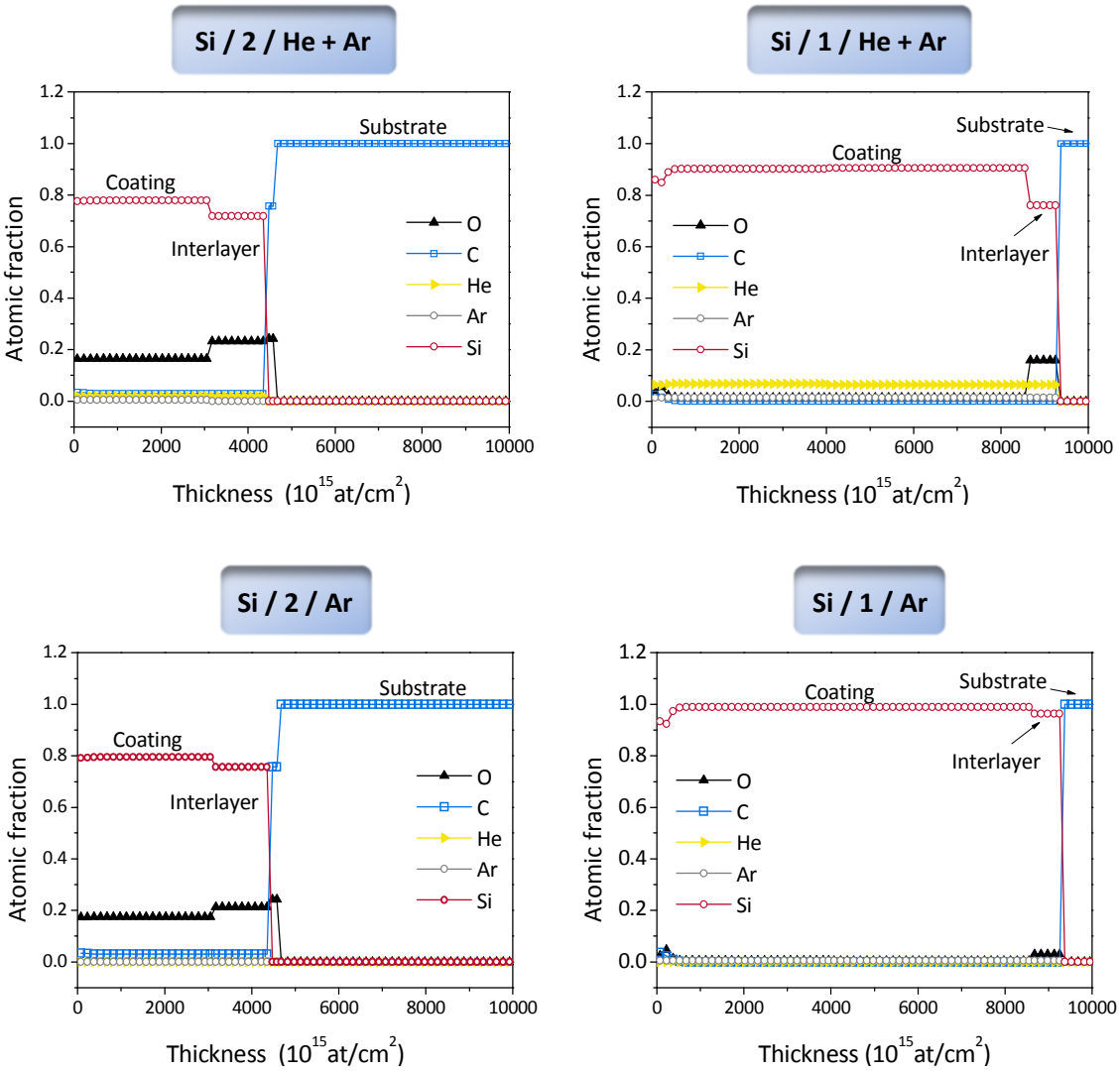

Figure 4.5: RBS elemental profiles.

Table 4.2: Composition of the coatings by RBS and ERDA analyses.

Coating	Si ($at.\%$)	He ($at.\%$)	Ar ($at.\%$)	O ($at.\%$)	Density* (at/nm^3)
Si / 1 / He + Ar	90.3	6.7	1.5	1.5	44.1
Si / 2 / He + Ar	80.4	2.0	0.6	17.0	36.2
Si / 1 / Ar	98.9	---	0.6	0.5	49.2
Si / 2 / Ar	82.0	---	0.0	18.0	39.8

* The density is related to the compact crystalline Si ($50\ at/nm^3$).

With these data, films are mainly composed by silicon with a considerable amount of oxygen in the coatings located in the Z2 regardless of the sputtering gas used. Both films were grown simultaneously in each region (Z1 and Z2), hence, exposed to the same atomic gas species during growth. Therefore, the oxygen in the coatings can only appear when the films are exposed to air. This reason proves that films grown in the more oblique incidence region, Z2, possess a larger surface area in contact with air and so seem to have a more open (non-occluded) porous structure.

An aspect that needs to be clarified is the white contrast observed in the TEM micrographs in figure 4.4 at the interface between substrate and coating. This interlayer on the silicon substrate prior to the coating also corresponds to a SiO_x composition as concluded from depth profiles in figure 4.5. This layer is most probably due to insufficient target cleaning and a native oxide layer on the silicon target. Therefore, a SiO_x layer was deposited on the substrate when the deposition started.

A good indication of the silicon oxidation produced by exposure of the coatings to air is given by EFTEM images recorded with a $4\ eV$ window at $17\ eV$ and $24\ eV$ for the four selected coatings. The plasmon losses centered at these two selected energies are characteristic of Si [31] and SiO_2 [32] respectively. The images presented in the figure 4.6 represent chemical maps of the two phases. In these images it is observed that the white contrast in the case of $17\ eV$ (related with the Si plasmon) is in the coating and in the substrate, being higher in Z1 than in Z2 regardless of the sputtering gas. As it is expected, the opposite effect happens in the case of images at $24\ eV$ (related with the SiO_2 plasmon).

The white contrast appears now clearly in the coating and at the interface and it is of lower intensity in Z1 than in Z2. So Z2 is characterized by an open porosity higher than Z1, due to more oblique deposition. In addition, it is possible to observe the white contrast in the interlayer in the case of SiO_2 plasmon confirming the results obtained by RBS.

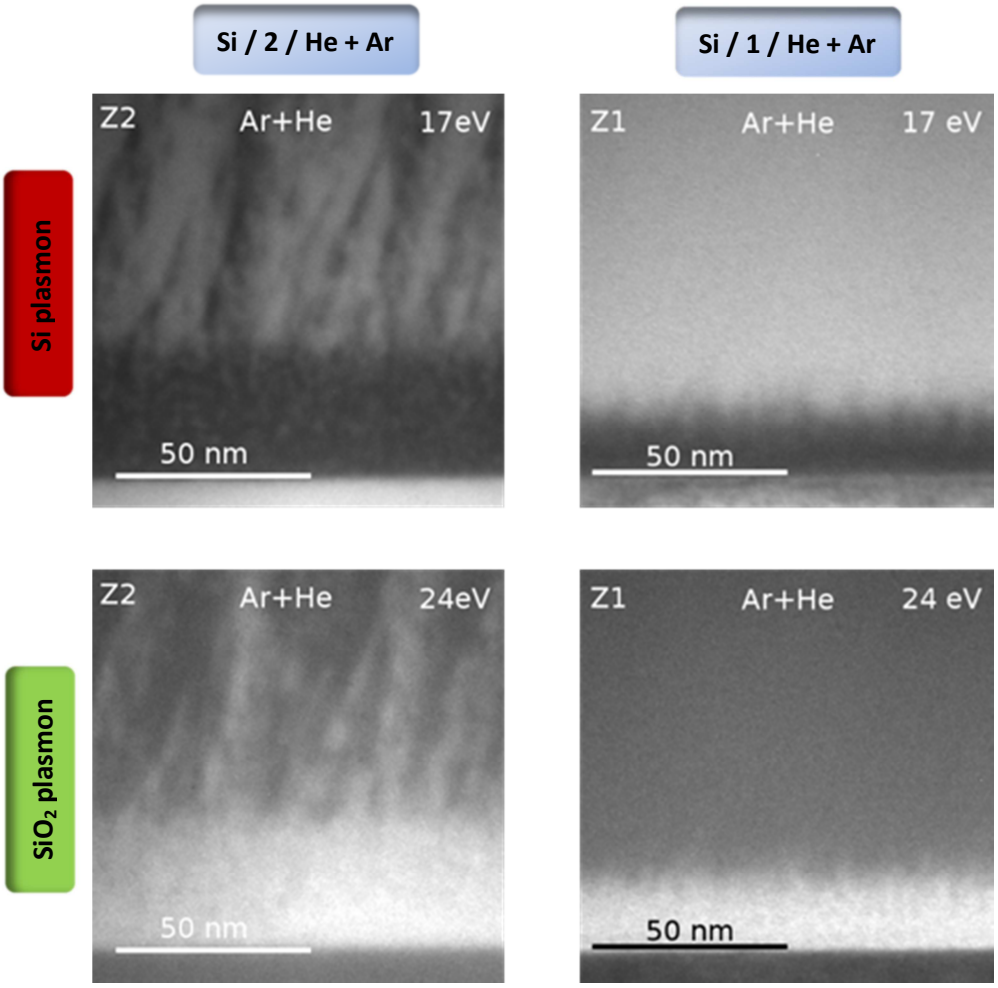

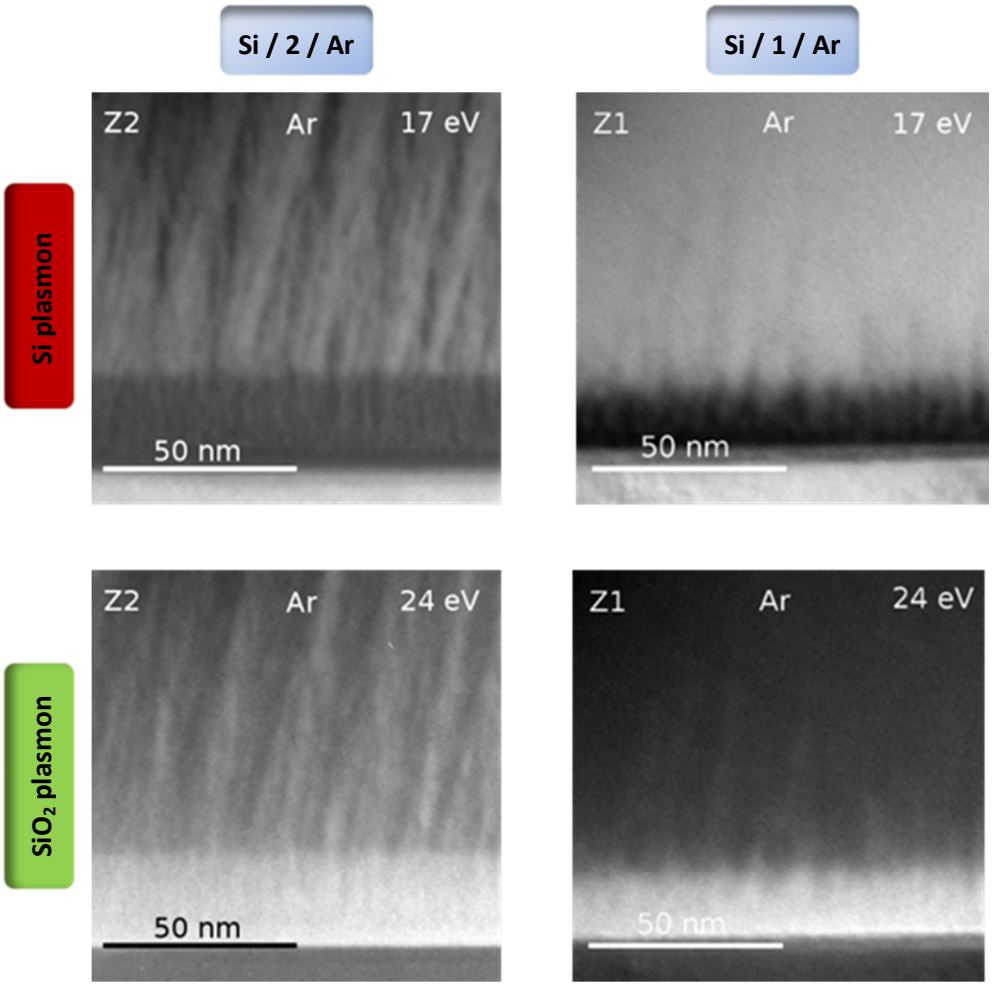

Figure 4.6: EFTEM images with a 4 eV window at 17 eV and 24 eV, representing Si and SiO_2 plasmon losses respectively.

Another interesting fact is the incorporation of sputtering gas atoms in the coatings as it is shown in the table 4.2. Under both sputtering gas atmospheres, He + Ar and Ar, the amount of gas trapped in the coating is higher in Z1 than in Z2. This could be understood as the more oblique incidence region, Z2, possesses a larger surface area, therefore, desorption mechanisms are more efficient. An opposite contribution is the film temperatures during growth in the range of $100 - 130°C$ being higher in the Z1 position what may favor gas

desorption. An important observation of the RBS results is the higher incorporation of He during film growth.

When the He + Ar mixture was used, He and Ar atoms were found in both regions with a ratio of He to Ar of about ~ 4.4 in Z1 and ~ 3.3 in Z2. These values can be explained by considering the thermal flux of Ar and He gas atoms impinging on the films during growth J_{Ar} and J_{He} respectively. These thermal fluxes are expressed by:

$$J_{Ar} = \frac{1}{4}\, n_{Ar} \sqrt{\frac{8\, k_B\, T}{\pi\, M_{Ar}}} \qquad\qquad J_{He} = \frac{1}{4}\, n_{He} \sqrt{\frac{8\, k_B\, T}{\pi\, M_{He}}} \qquad [4.1]$$

where n is the density of each gas. This value is calculated considering the gas as an ideal gas. M is the atomic mass, k_B is the Boltzmann constant and T is the gas temperature in kelvins.

The ratio between both fluxes is:

$$\frac{J_{He}}{J_{Ar}} = \frac{n_{He}}{n_{Ar}} \sqrt{\frac{M_{Ar}}{M_{He}}} \qquad [4.2]$$

And the ratio between both densities using the state equation of an ideal gas is:

$$\frac{n_{He}}{n_{Ar}} = \frac{p_{He}}{p_{Ar}} = \frac{1.7}{0.8} \qquad [4.3]$$

being p_{He} and p_{Ar} the partial pressures of He and Ar respectively. Then, the fluxes relation is:

$$\frac{J_{He}}{J_{Ar}} \sim 6.6 \qquad [4.4]$$

However, the gas ratio measured by RBS is lower. But He desorbs from the material better than Ar due to its lower mass and smaller size. This fact would explain why the gas ratio in both zones is lower than the flux ratio obtained theoretically.

So, the nanostructural features described above can be at this point qualitatively explained by considering the thermalization degree of the sputtered particles by gas-phase collisions [8], the typical shadowing effects [6] and desorption processes during film growth.

The nanostructural features related to formation of closed pores and their characterization will be discussed in section 4.4.3, both experimentally (higher TEM resolution images) and theoretically.

4.4.2. SIMULATION OF FILMS' GROWTH

To support the results exposed in the previous part (4.4.1), it is of prime interest to use a software to simulate how the atoms are deposited on a substrate. In these simulations it is taken into account only the shadowing effects but no thermal effects. The atoms deposited on the substrate can only be moved by a collision with atoms arriving from the target. However, the software does not take into account collision cascades. One atom can move on the substrate or can be sputtered. The transferred energy to the atom is calculated with the binary elastic collision approximation. As described above following steps were followed.

4.4.2.1. Angular and energy distributions

Before showing the final results of the film growth simulation, an interesting initial point is the study of the angular and energy distributions of the silicon atoms when they arrive to the substrate. These distributions are obtained using the SIMTRA software with the input of the SRIM software. The angular distributions give the probability of one atom to arrive to the substrate with a particular direction expressed by the pair of angles $\{\theta, \varphi\}$. θ is the azimuthal angle and φ is the polar angle. In figure 4.7 these angles are represented, where the red line is the incoming direction of one atom from the target when they have passed through the gas. And the energy distributions give the probability of one atom to land onto the substrate with a particular energy E.

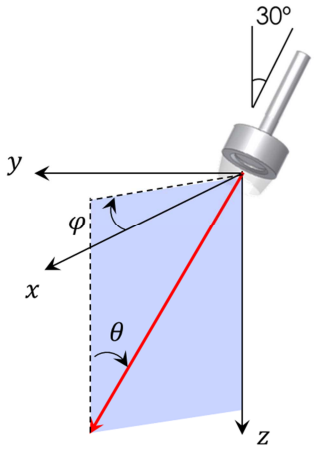

Figure 4.7: Angle definitions of an incoming atom during film growth.

So, an atom from the target can be characterized by $\{f(E), g(\theta, \varphi)\}$ being f and g probability distribution functions. In the software it has been supposed that the energy distribution is the same for every pair of angles and independent of the direction $\{\theta, \varphi\}$.

For the two different gas atmospheres, He + Ar and Ar, it has been necessary to calculate the angular and energy distributions in both locations, Z1 and Z2. The case of pure Ar atmosphere is a simple case because it is only one gas. In the case of a mixture of He + Ar, only the Ar contribution was taken into account, because in previous calculations with a He partial pressure of $1.7\ Pa$, was observed that the effect on the trajectories of Si atoms from the target is negligible due to a low atomic mass ratio between He and Si. However, Ar has an atomic mass higher than Si, so Ar can modify the trajectories of Si atoms from the target. Therefore, in the case of a mixture of He + Ar, only Ar has been considered with a partial pressure of $0.8\ Pa$ in the calculations of angular and energy distributions of Si atoms arriving to the substrate.

In figure 4.8 the angular distributions for the two gas atmospheres and for both locations of each deposition are presented.

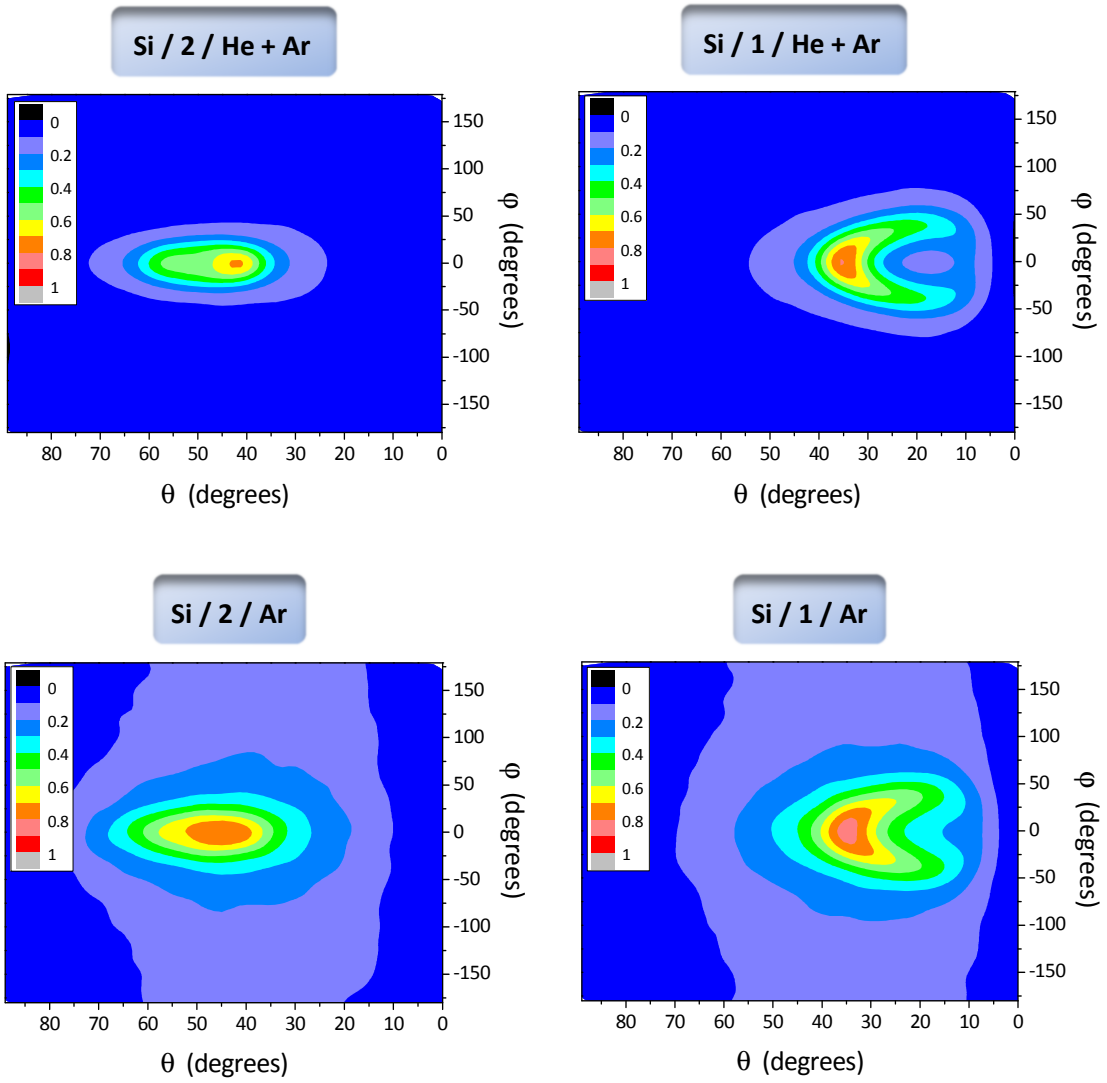

Figure 4.8: Angular distribution of Si atoms arriving to the substrate for the different locations and gas phase compositions.

Comparing the distributions in positions Z1 and Z2 for both gas atmospheres, it is observed that the distribution in Z1 is broader than in Z2. This fact is due to higher proximity of position Z1 to the magnetron, so the amount of Si atoms arriving to the substrate is higher and the possible directions are broader in Z1 than in Z2. The atoms reaching position Z2 have a higher directionality than in Z1.

Comparing the angular distributions for both gas atmospheres in a same location, it is shown that in the case of Ar atmosphere the distribution is broader than in the case of He + Ar atmosphere. The reason of this is the gas pressure. In the case of Ar atmosphere, the pressure is $1.4\ Pa$ while in the case of He + Ar, only the partial pressure of Ar ($0.8\ Pa$) is considered. High pressure means high probability of collisions between the Si and Ar atoms in the path of Si atoms from the target to the substrate. More collisions implies a higher loss of directionality of Si atoms arriving onto the substrate resulting in a broadener angular distribution.

For the energy distributions, the effect of the location of coating in the same gas atmosphere and the effect of the gas atmosphere in the same location of coating have been studied. To simplify the analysis are shown only in both zones for the case of Ar and in the case of Z2 for both atmospheres. The effects in the others cases are the same.

Figure 4.9 (a) shows the energy distributions comparing the location. It is observed that the energy values in Z1 are slightly higher than in Z2 as expected for the shorter distance to the magnetron in Z1 as compared to Z2. The atoms reach the substrate with higher energy in Z1. The effect for He + Ar atmosphere is similar.

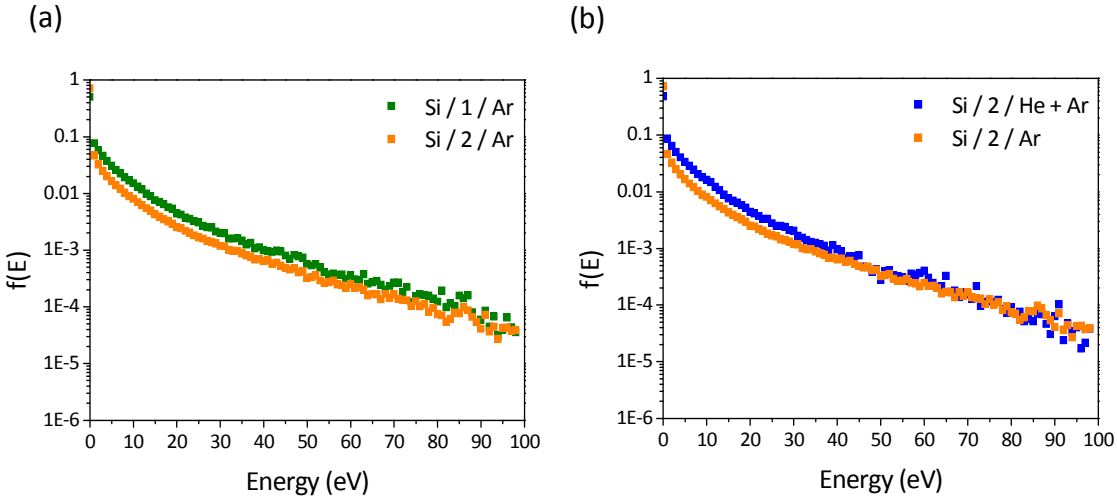

Figure 4.9: Energy distributions of Si atoms arriving to the substrate. Comparison between (a) Zones; (b) Gas atmospheres.

In figure 4.9 (b) the location is fixed at Z2, and the effect of gas atmosphere is shown. When a He + Ar atmosphere is used, the energy values are slightly higher than when Ar atmosphere is used. The reason is the same as for the angular distribution patterns, the gas pressure. In the case of the He + Ar atmosphere, as the He is not taken into account, the Ar partial pressure is smaller than in the case of pure Ar atmosphere. A lower pressure means less collisions between the Si and Ar atoms, and therefore, the Si atoms arrive to the substrate with higher energy.

4.4.2.2. Simulation of films' growth

Introducing in the NASCAM code the data described above about the angular and energy distribution of atoms arriving to the substrate, it is possible to simulate the film growth and therefore to analyze the resulting structure. The simulation of growth considers that no gas atoms are trapped in the film structure. As already mentioned another important fact is that NASCAM considers that for every pair of angles $\{\theta, \varphi\}$ (figure 4.7) the energy distribution is the same. In the simulation a substrate dimensions $\{x, y\}$ of 400×100 atoms was chosen, this corresponds to $120 \times 30\ nm^2$ approximately, and the number of Si atoms deposited is $2 \cdot 10^6$ atoms.

Figure 4.10 shows the structure of coatings obtained by simulation. To observe the porous structure more clear, a slice of the simulation in cross sectional view is presented in the XZ plane (the plane studied previously by SEM and TEM). The dimensions $\{x, y\}$ of these slices are 400×11 atoms.

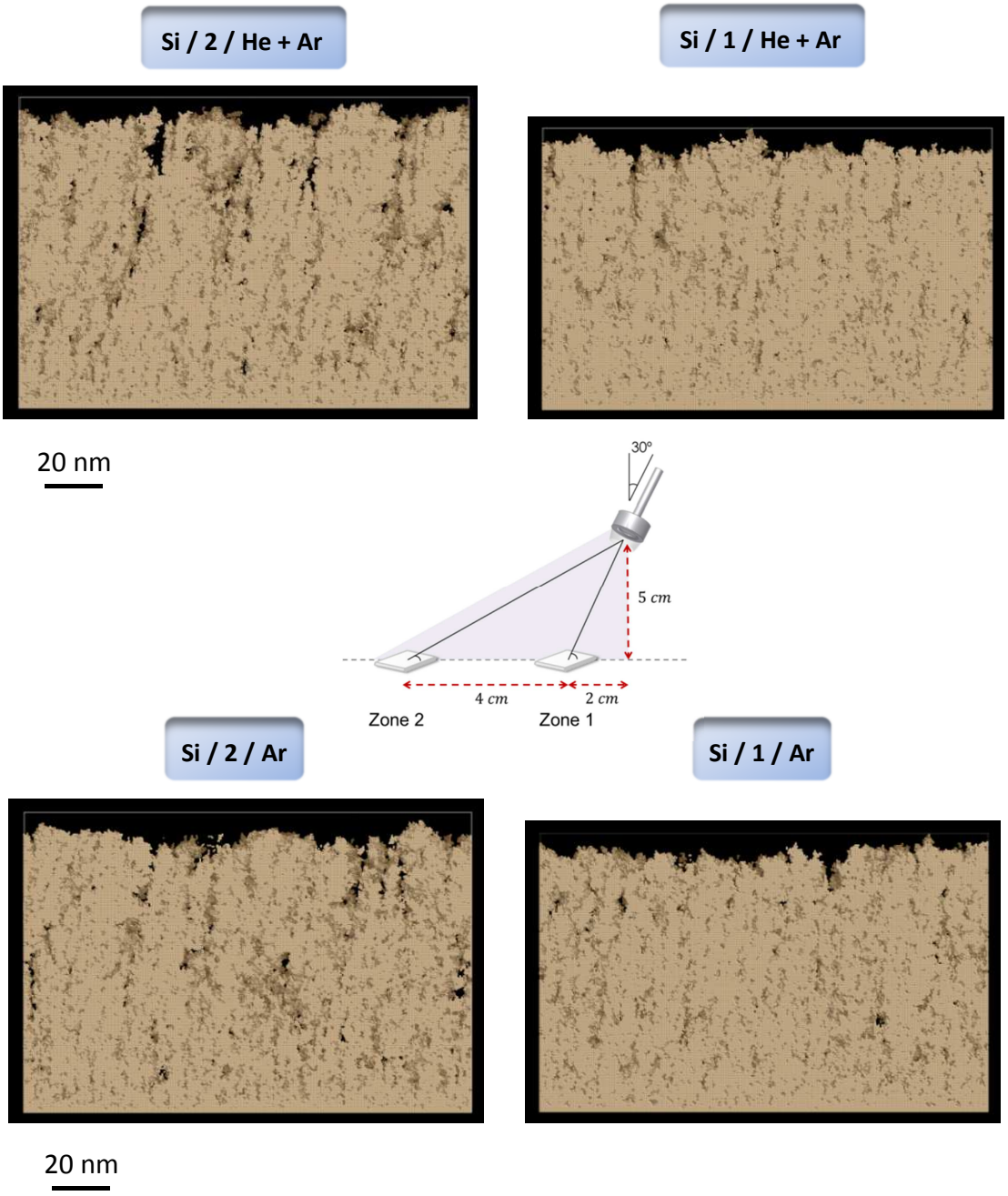

Figure 4.10: Simulation of films' growth obtained with NASCAM in cross section.

As shown in figure 4.10, the Z2 position seems more porous than Z1 for both gas atmospheres. In addition Z2 has a porous structure more tilted towards the magnetron than Z1. Comparing the same position, the simulation gives a higher tilt angle for the porous structure in coatings deposited with He + Ar. This fact is more notable in Z2. As it was explained before, in the simulation of coatings deposited with He + Ar, He was not taken into account, so the only difference between the simulation with He + Ar and Ar is the pressure of Ar, being higher in the case of pure Ar. This is the reason why the porosity tilt angle is higher in the case of He + Ar, because the number of collisions between the metal and gas atoms are lesser, and the directionality of incoming Si atoms is narrower.

The simulations can also give density values of the coatings which can be analyzed in a qualitative way. In figure 4.11 it is plotted the density of simulated coatings versus the deposition time. Data are plotted normalized to 1 at the maximum density value. In all cases the behavior is the same, the density decreases in the first few seconds and finally reaches a plateau which is considered the density value of coatings. The graph shows that using the same gas atmosphere, the density in position Z1 is higher than in Z2. This behavior was expected when the energy distributions of atoms arriving to the substrate is considered. Higher energy of the arriving atoms allows higher mobility on the surface to find a stable position filling the free sites making the coating more compact, and therefore, more dense. As described above in position Z1 the atoms arrive with higher energy than in Z2. This effect is observed experimentally too. According to table 4.2 the atomic density values of coatings, for the two gas atmospheres are higher in position Z1 than in Z2.

Other effect observed in figure 4.11 is that for the same location, Z1 or Z2, using He + Ar atmosphere, the simulated density is higher than using Ar. This effect is clearer in Z1. This fact can be caused again by the gas pressure considered in the calculations. As previously explained, low gas pressure (for the He + Ar case) means that the atoms arrive to the substrate with higher energy and therefore, the coating is denser. However, table 4.2 shows that the density in the coatings deposited with He + Ar is smaller than in coatings deposited with Ar. In this point simulation and experiment do not agree. Therefore, the

presence of He in the gas mixture should have an effect leading to the formation of porosity that was not considered in the simulation.

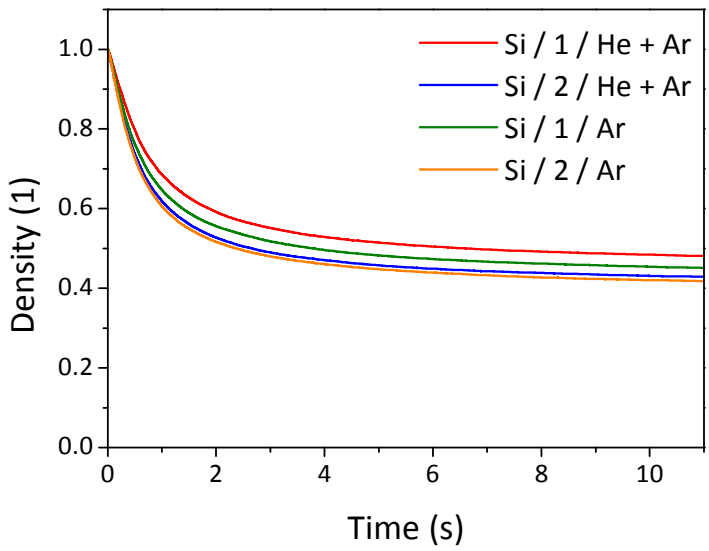

Figure 4.11: Simulation of the temporal evolution of density (normalized to 1 at maximum value) for each coating.

Analyzing the films simulation data showed in figure 4.10 by using the PORESTAT software, it is possible to represent the open porosity (porosity in contact with air) of the coatings under investigation as it is shown in figure 4.12.

Experimentally and theoretically, the porosity is higher in Z2 than in Z1. This result is confirmed by simulation in the images of figure 4.12. This fact agrees with the RBS results and EFTEM images previously presented, where the amount of oxygen is higher in Z2 than in Z1, and therefore, the open porosity in contact with air, is higher in Z2 than in Z1. For the comparison between He + Ar and Ar the results of PORESTAT, regarding open porosity, are congruent with the EFTEM images and can be explained by Ar partial pressure effects.

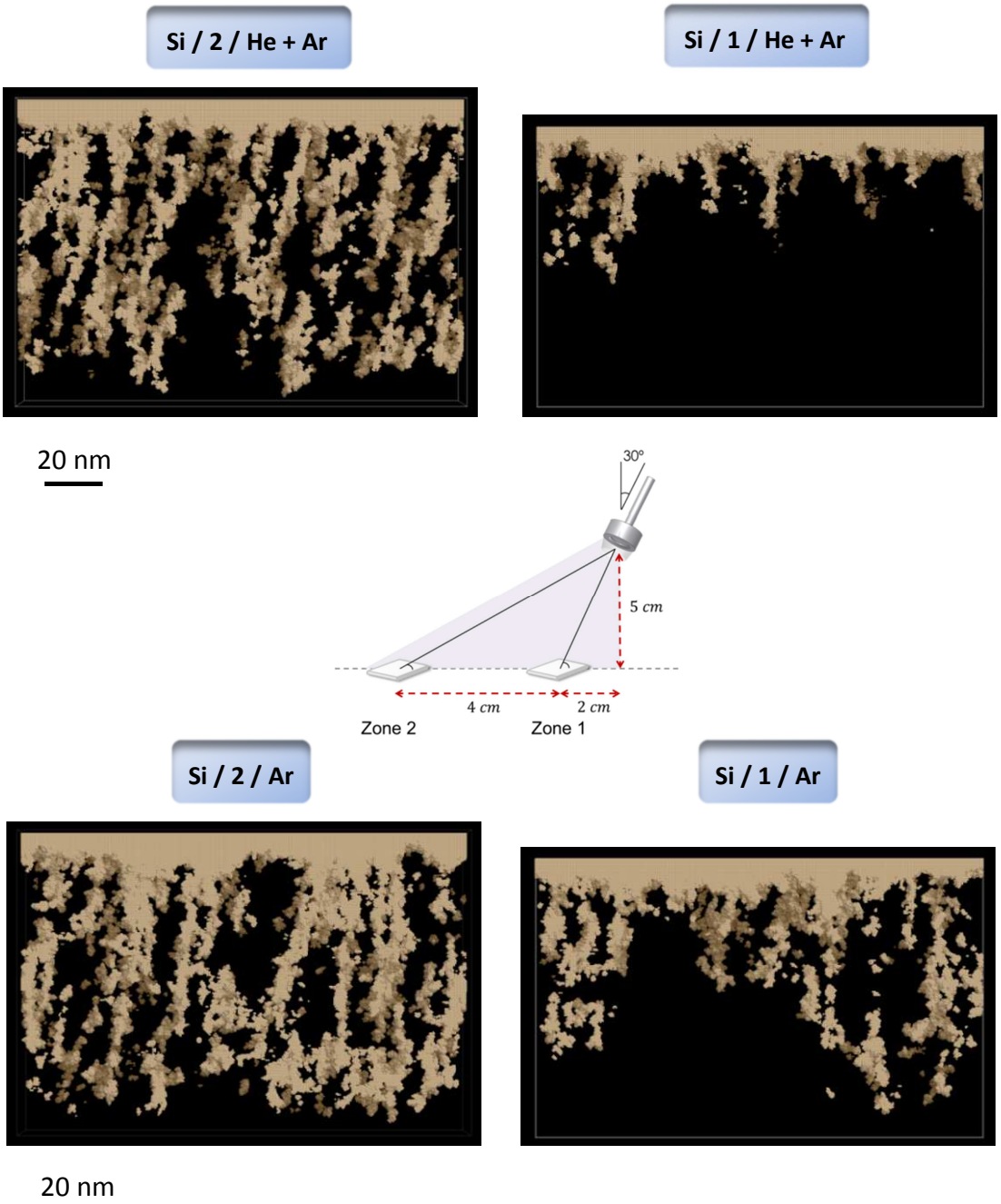

Figure 4.12: Open porosity of simulated coatings obtained by PORESTAT.

4.4.3. Analysis of closed porosity

In this section the closed porous structure of the coatings is studied in more detail. The PORESTAT software can evaluate the pore size of closed porosity using the simulation results obtained by NASCAM, and the obtained pore size distributions will be then compared with the measured data obtained from the TEM micrographs.

To measure experimentally the pore size using TEM micrographs, the same method that in previous chapters has been used. To compare with the PORESTAT results, the parameter named effective pore diameter will be used. Measuring the pore area obtained by PORESTAT, the pore is approximated by a circular shape. The diameter of the circle with an area equal to the pore area measured is the effective pore diameter.

In the figures 4.13 and 4.14 TEM micrographs of the coatings at higher resolution are presented where it is possible to observe in more detail the porous structure. In addition, the effective pore diameter distributions are added.

In the case of coatings deposited with Ar atmosphere it was possible to measure the pore size only for the coating growth in position Z1. In position Z2 it was impossible to clearly identify the small pores and the pore size distribution was rather arbitrary and inconclusive. For position Z1 the figure 4.13 presents numerous elongated small closed pores with sizes of around $2\ nm$ and below which are also clearly aligned. In the pore size distribution, the majority of the pores have an effective pore diameter around $2-3\ nm$. Regarding the shape, the pores are elongated and the microstructure can be defined as series of elliptical pores one after another, in some cases being difficult to determine when one pore ends and the following one begins. This is typical of columnar growth by magnetron sputtering for OAD deposition.

In the case of He + Ar mixture, the effective pore diameter ranges are about $3-6\ nm$ in Z1 and $2-7\ nm$ in Z2 with the majority falling around $4\ nm$ in both zones. Interesting aspect is the pore shape. The images presented in the figure 4.14 show elongated pores as well as rounded pores in both positions Z1 and Z2.

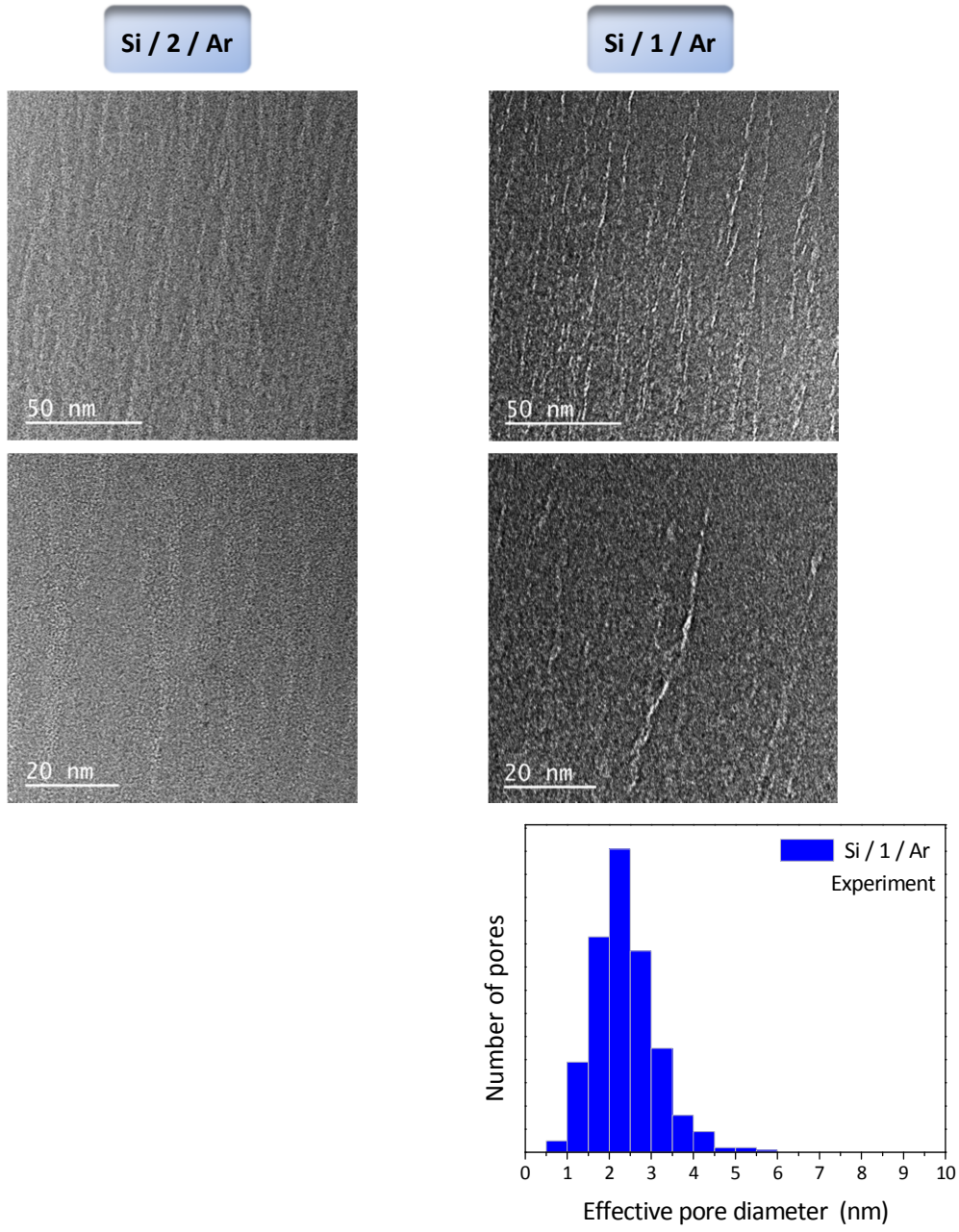

Figure 4.13: Pore details by TEM images and pore size distributions of the Si/1/Ar coating deposited with Ar as process gas.

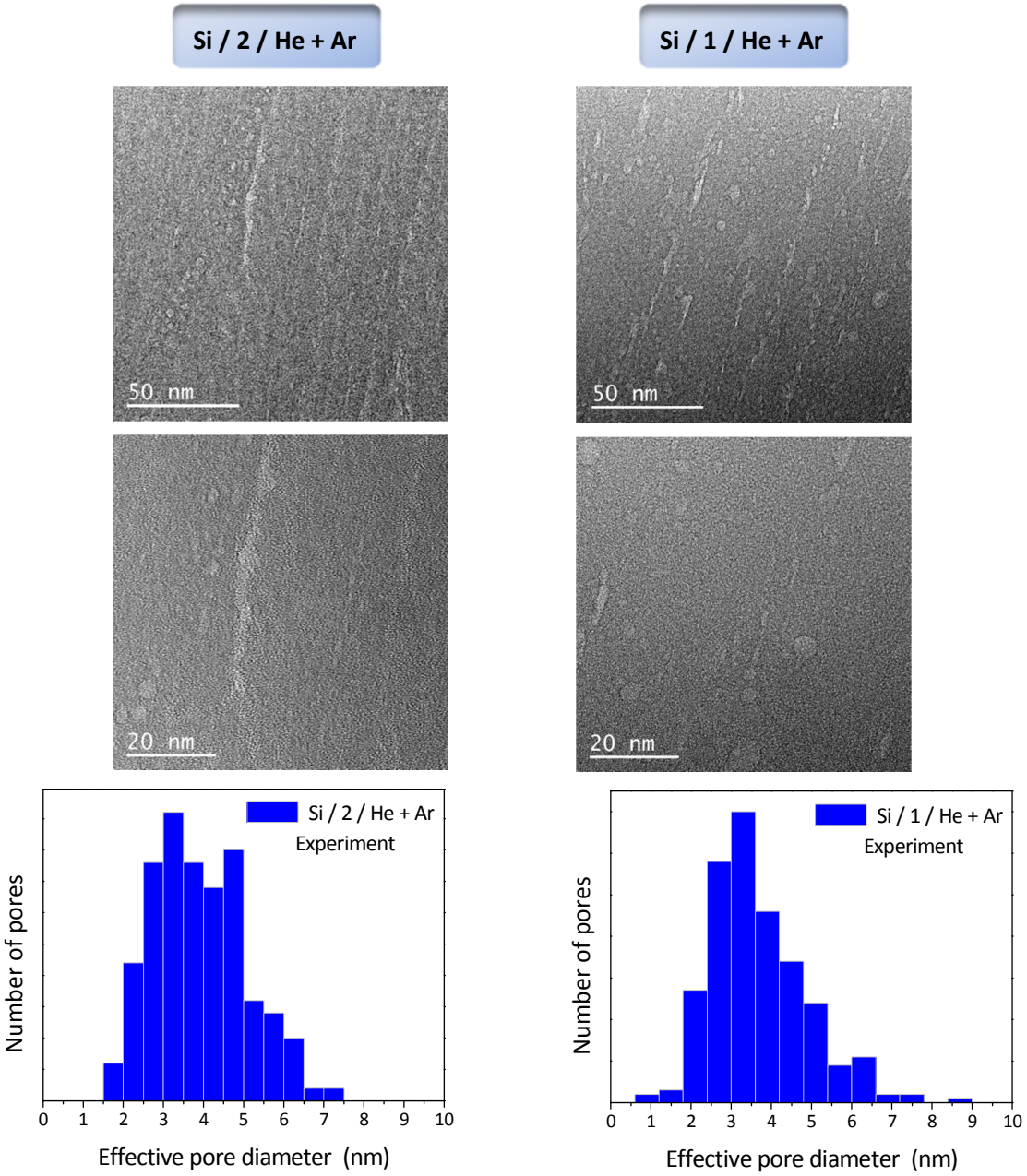

Figure 4.14: Pore details by TEM images and pore size distributions of coatings deposited with He + Ar as process gas.

Comparing both gas atmospheres, it seems that the presence of He in the plasma leads to rounder pores, as shown in our first paper [1], and has been also reported for DC sputtering of metals using He and Ar mixtures [20–22].

The next point is to study the pore size distribution obtained from the simulation results by the PORESTAT software. As already discussed the simulation results take into account the thermalization degree of sputtered particles by gas phase collisions and the typical shadowing effects under DC conditions. As it was explained previously in this chapter, an important parameter used in this PORESTAT analysis is the pore throat. In this case, the value of this parameter was considered as $\pi_t = 2\ nm$. This value has been chosen because is slightly higher than the minimum pore diameter detected by TEM. According to the IUPAC, this value is the critical pore size separating micropores and mesopores, therefore, the description would correspond to a pore connectivity analysis through mesopores.

In the following figure, it is presented the closed pore size distribution for both gas atmospheres and both zones, comparing the experimental and simulation results. These distributions give an idea about the effect of introducing He in the sputtering gas. For pure Ar, in zone 1 the pore size measured experimentally by TEM images fits very well with the simulation results. Therefore, shadowing effects completely explain the porosity, pore distribution and orientation. For the zone 2, as already discussed, it was not possible to get valuable experimental data.

In the case of He + Ar, although certain similarity is found in the results for the medium-large size pores, the results from the TEM and simulations seem to differ for the rest of the pore diameter range, so the surface shadowing effect mechanism cannot satisfactorily explain the pore structure of the films whenever He is introduced in the reactor, regardless of whether the growth takes place in position Z1 or in position Z2.

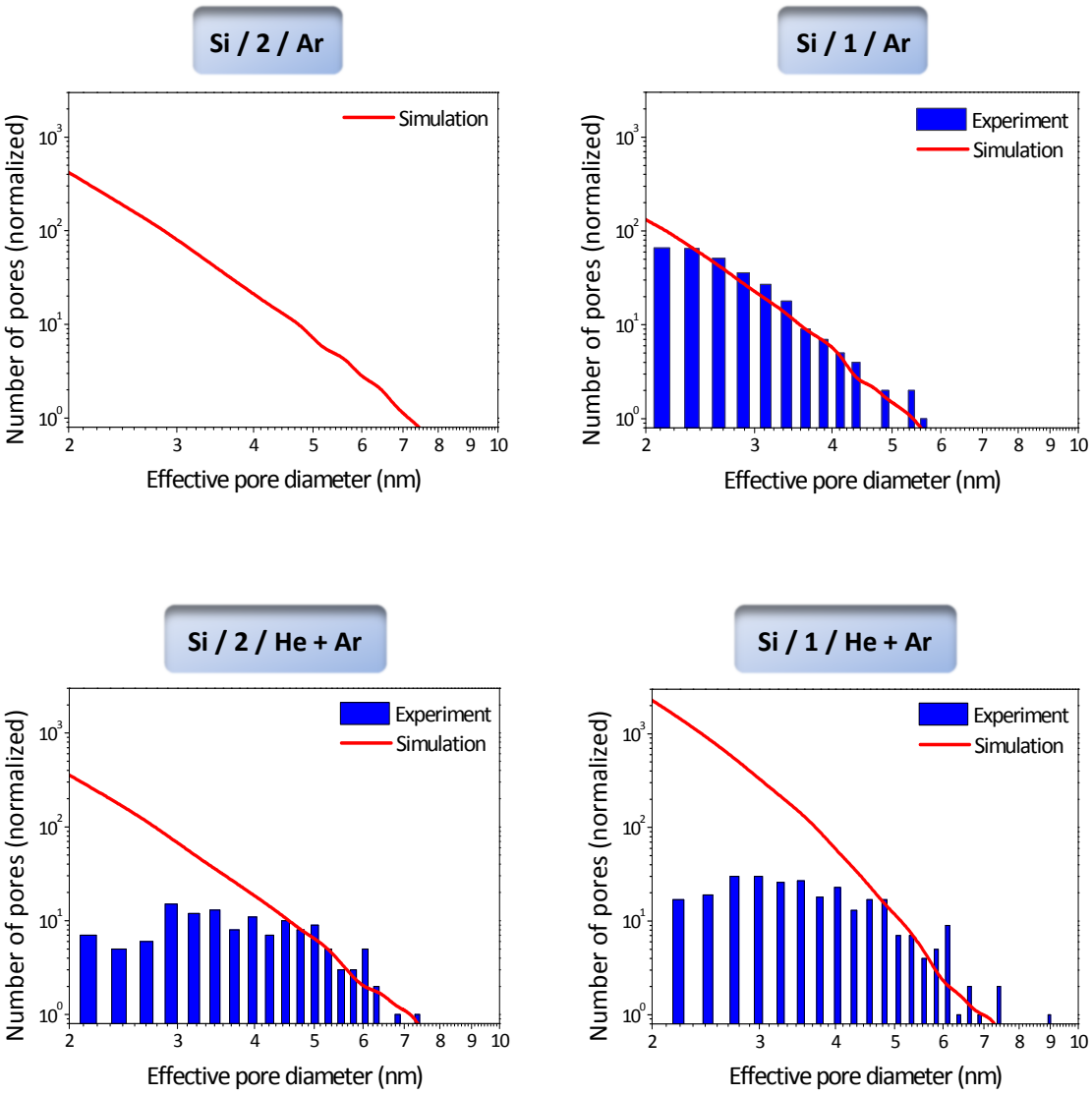

Figure 4.15: Pore size distributions for the investigated coatings. Comparison between experiments and simulations.

These results suggest that the He introduces a new process affecting the nanostructural development of the films. It is remarkable that if surface shadowing dominates the pore formation, smaller pores would be more abundant than larger ones. This fact suggests that

in the presence of He in the sputtering gas, a new nanostructuration process governs the pore dynamics that tend to merge small pores and turn them into larger occluded ones.

Related with this result there are many studies [15,18,19] on the behavior of embedded He atoms that, after being implanted, stay in metallic materials and promote the migration of point defects in the network in order to form He bubbles. This process, previously described in He implanted experiments, would explain the existence of larger pores in the higher magnification TEM images of our coatings as well as the rounder aspect of the pores. In this regard, the results presented in this chapter infer that such a mechanism is present, and it is relevant when He is employed for producing films by magnetron sputtering, even in the selected DC deposition conditions.

4.5. Conclusions

The microstructural evolution and pore formation in a-Si coatings deposited by magnetron sputtering has been studied by comparing TEM experimental results with computer simulations.

To understand the physical mechanisms taking place during the growth of the coatings, a simple Monte Carlo model (NASCAM) which only considers the surface shadowing mechanism was employed. For this reason the deposition conditions were carefully chosen, using low DC power conditions ($150\ W$) to avoid high plasma potentials and therefore avoiding positive ions to impinge on the film above any surface mobility threshold [29]. Coatings were produced in two positions inside the reactor, zone 1 (Z1) nearer and zone 2 (Z2) farther to the magnetron location. Also an oblique angle deposition geometry and two different sputtering gases (Ar or He + Ar) were employed.

The results presented in this chapter show how simulations reproduce and explain several experimental findings and also how the discrepancies can be interpreted:

- From TEM micrographs it was observed that the porosity grows tilted in the magnetron direction being the coatings in Z2 more porous than in Z1. This fact is characteristic of the OAD conditions and is a consequence of the shadowing effect clearly shown by the simulations.

- The RBS results show that in Z1 the amount of gas trapped in the coatings is higher than in Z2. As shown by simulation the more oblique incidence in Z2 causes a larger surface area making the desorption mechanisms more efficient.

- Using the simulation results from NASCAM, it was possible to obtain a pore size distribution with the PORESTAT software. Comparing these results with the experimental TEM study it was found that for pure Ar the simulation results in zone Z1 fit very well the experimental measurements, being possible to explain the size, shape and orientation of pores only by the shadowing effects. In fact elongated pores in a narrow size distribution of $2-3\,nm$ for the majority of pores were found. However, when He is introduced in the reactor, the simulation results do not fit well the experimental results. Only in medium-large pore size the model predicts well the experimental data but not for small pore sizes. This fact happens for both zones. So, the conclusion is that He introduces an effect on the porous structure by a new not considered mechanism which tends to merge small pores and form large ones. This mechanism could be similar to previously reported bubble formation processes in He implanted metals [15,18,19]. These processes have been associated with certain mobility of point defects in the Si network due to the low solubility of He in the material.

Finally it is worth to mention that under conditions of higher plasma potential, like the RF discharge used in this thesis, additional simulations tools need to be incorporated in order to consider the effect of He ions impingement, the surface mobility during film growth and the He insolubility promoting pore dynamics by migration of pore defects.

4.6. References

1. Godinho, V. *et al.* A new bottom-up methodology to produce silicon layers with a closed porosity nanostructure and reduced refractive index. *Nanotechnology* **24,** 275604 (2013).

2. Fernández-Camacho, A. & Godinho, V. Procedimiento de obtención de recubrimientos mediante pulverización catódica y recubrimiento obtenible. (2009). at <Spanin. P200930085, PCT/ES 2010/070245>

3. Godinho, V. *et al.* SiOxNy thin films with variable refraction index: Microstructural, chemical and mechanical properties. *Appl. Surf. Sci.* **256,** 4548–4553 (2010).

4. Godinho, V., Rojas, T. C. & Fernandez, A. Magnetron sputtered a-SiOxNy thin films: A closed porous nanostructure with controlled optical and mechanical properties. *Microporous Mesoporous Mater.* **149,** 142–146 (2012).

5. Pelliccione, M. & Lu, T.-M. *Evolution of thin film morphology: modeling and simulations*. (Springer, 2008).

6. Alvarez, R. *et al.* Growth regimes of porous gold thin films deposited by magnetron sputtering at oblique incidence: from compact to columnar microstructures. *Nanotechnology* **24,** 045604 (2013).

7. Alvarez, R. *et al.* On the microstructure of thin films grown by an isotropically directed deposition flux. *J. Appl. Phys.* **108,** 064316 (2010).

8. Garcia-Martin, J. M., Alvarez, R., Romero-Gomez, P., Cebollada, A. & Palmero, A. Tilt angle control of nanocolumns grown by glancing angle sputtering at variable argon pressures. *Appl. Phys. Lett.* **97,** 173103 (2010).

9. Thornton, J. High-Rate Thick-Film Growth. *Annu. Rev. Mater. Sci.* **7,** 239–260 (1977).

10. Lucas, S. & Moskovkin, P. Simulation at high temperature of atomic deposition, islands coalescence, Ostwald and inverse Ostwald ripening with a general simple kinetic Monte Carlo code. *Thin Solid Films* **518,** 5355–5361 (2010).

11. Moskovkin, P. & Lucas, S. Computer simulations of the early-stage growth of Ge clusters at elevated temperatures on patterned Si substrate using the kinetic Monte Carlo method. *Thin Solid Films* **536,** 313–317 (2013).

12. Alvarez, R. *et al.* Theoretical and experimental characterization of TiO2 thin films deposited at oblique angles. *J. Phys. -Appl. Phys.* **44,** 385302 (2011).

13. Alvarez, R. *et al.* Morphological evolution of pulsed laser deposited ZrO2 thin films. *J. Appl. Phys.* **107,** 054311 (2010).

14. Vasco, E., Zaldo, C. & Vazquez, L. Growth evolution of ZnO films deposited by pulsed laser ablation. *J. Phys.-Condens. Matter* **13,** L663–L672 (2001).

15. Wilson, W., Bisson, C. & Baskes, M. Self-Trapping of Helium in Metals. *Phys. Rev. B* **24,** 5616–5624 (1981).

16. Jager, W. *et al.* Density and Pressure of Helium in Small Bubbles in Metals. *J. Nucl. Mater.* **111,** 674–680 (1982).

17. Evans, J. H. Mechanisms of void coarsening in helium implanted silicon. *Nucl. Instrum. Methods Phys. Res. Sect. B-Beam Interact. Mater. At.* **196,** 125–134 (2002).

18. Morishita, K. Nucleation path of helium bubbles in metals during irradiation. *Philos. Mag.* **87,** 1139–1158 (2007).

19. Pizzagalli, L., David, M. L. & Bertolus, M. Molecular dynamics simulation of the initial stages of He bubbles formation in silicon. *Model. Simul. Mater. Sci. Eng.* **21,** 065002 (2013).

20. Jia, J., Shi, L., Lai, X. & Wang, Q. Preparation of Al thin films charged with helium by DC magnetron sputtering. *Nucl. Instrum. Methods Phys. Res. Sect. B Beam Interact. Mater. At.* **263,** 446–450 (2007).

21. Shi, L. Q., Liu, C. Z., Xu, S. L. & Zhou, Z. Y. Helium-charged titanium films deposited by direct current magnetron sputtering. *Thin Solid Films* **479,** 52–58 (2005).

22. Zheng, H. *et al.* Introduction of helium into metals by magnetron sputtering deposition method. *Mater. Lett.* **59,** 1071–1075 (2005).

23. Deng, A. H., Zhou, Y. L., Zhang, L. R. & Hou, Q. in *12th International Workshop on Slow Positron Beam Techniques (slopos12)* (eds. Buckman, S. J., Sullivan, J. P., Makochekanwa, C. & White, R.) **262,** 012017 (Iop Publishing Ltd, 2011).

24. NASCAM (NAnoSCAle Modeling) User's manual— Université de Namur. at <http://www.unamur.be/sciences/physique/pmr/telechargement/logiciels/nascam>

25. Ziegler, J. F., Ziegler, M. D. & Biersack, J. P. SRIM - The stopping and range of ions in matter (2010). *Nucl. Instrum. Methods Phys. Res. Sect. B-Beam Interact. Mater. At.* **268,** 1818–1823 (2010).

26. DRAFT - Design, Research And Feasibility of Thin Films at Ghent University/UGent. at <http://www.draft.ugent.be/>

27. Van Aeken, K., Mahieu, S. & Depla, D. The metal flux from a rotating cylindrical magnetron: a Monte Carlo simulation. *J. Phys. -Appl. Phys.* **41,** 205307 (2008).

28. PoreSTAT » nanoSCOPS. at <http://nanoscops.icmse.csic.es/software/porestat/>

29. Welzel, T. & Ellmer, K. Comparison of ion energies and fluxes at the substrate during magnetron sputtering of ZnO : Al for dc and rf discharges. *J. Phys. -Appl. Phys.* **46,** 315202 (2013).

30. Jensen, M. O. & Brett, M. J. Porosity engineering in glancing angle deposition thin films. *Appl. Phys. -Mater. Sci. Process.* **80,** 763–768 (2005).

31. Moreau, P., Brun, N., Walsh, C. A., Colliex, C. & Howie, A. Relativistic effects in electron-energy-loss-spectroscopy observations of the Si/SiO2 interface plasmon peak. *Phys. Rev. B* **56,** 6774–6781 (1997).

32. Jin, H., Oh, S. K., Kang, H. J. & Cho, M.-H. Band gap and band offsets for ultrathin (HfO2)(x)(SiO2)(1-x) dielectric films on Si(100). *Appl. Phys. Lett.* **89,** 122901 (2006).

Chapter 5

Design and Fabrication of Optical Multilayer Devices From Porous a-Si Coatings With Closed Porosity

5.1. Introduction

Up to now, the porous silicon coatings presented have been studied from a fundamental point of view investigating the formation of porosity, the stability of helium trapped in the coating, the effect on the coating structure of the deposition parameters, and the associated modification of the physical properties of the fabricated materials. In particular, in the chapter 3, it was analyzed the change in the refractive index using different

sputtering gases and deposition conditions, being possible to produce the thin films with tailored refractive index [1].

Using this ability, silicon multilayer structures as Bragg reflectors and optical microcavities will be designed in this chapter for functional applications. Note that the combination of silicon layers of different refraction index will lead in this case to single material devices.

A distributed Bragg reflector (DBR) is a 1D photonic structure composed by periodically alternating layers with different refractive index [2–5]. The periodic modulation of the refractive index gives raise to optical interference effects where light propagation is completely or partially inhibited (photonic band gap) at defined wavelength ranges [6]. This band gap is characterized by a high reflectance. When a disruption or controlled defect is introduced in the periodicity of a Bragg stack, a different optical device is designed, named optical microcavity (OMC) [7–10]. The reflectance spectrum will depend on the number of defects introduced and of its properties.

The critical parameters to control the properties of a DBR are the thickness and the refractive index of individual layers as well as the total number of layers. Controlling these parameters it is possible to change the range, the position of photonic band gap and the reflectance in this range. In the appendix V of this thesis, the theory on how to obtain the reflectance spectrum of a multilayer structure and the key parameters used is described in more detail. These calculations have been used in the present chapter to design the optical devices.

To use only one material to fabricate an optical device has several advantages compared with optical devices using different materials in each layer. In an optical device composed by layer's periods of different materials, the refractive indexes would be different however the conductivity and the thermal expansion of these materials are also different, being a handicap when these devices are exposed, for example, to temperature changes. Nevertheless, optical devices composed by periods of the same material where the physical properties are the same except the refractive index do not present this problem [11–13]. This is

the case of the optical devices designed herein, where only one material will be used, amorphous silicon.

Until now, silicon multilayer structures have been traditionally made using electrochemical methods in which by adjusting the current and time, highly porous and low porosity layers with low and high refractive indexes respectively are consecutively produced [14–19]. However, for high number or very thick layers this methodology provokes anisotropy of the etching rates during porous silicon formation that increases as deeper as the layer is formed. Also the chemical instability of the high porous layers that are easily oxidized can be a drawback for high quality layers [20]. To improve the chemical stabilization, thermal annealing processes were proposed [20–22]. However, using the methodology proposed in this thesis [1] to produce porous silicon coatings with closed porosity, these drawbacks are avoided and multilayers with high quality interfaces can be formed as it will be shown here.

The objective of this chapter is the design of optical devices, DBR and OMC using porous silicon coatings with different refractive index. The optical devices designed are centered in the near-IR region, making them suitable for filters at these wavelengths or for optical communications applications [23].

5.2. Preparation of the optical devices and characterization

Three different optical devices have been designed, two DBRs and one OMC. In every device two different layers of high refractive index contrast have been used; one denser layer, H_n, with high refractive index, n_H, and one porous layer, L_{n1} or L_{n2}, with lower refractive indexes, n_{L1} and n_{L2} respectively. As denser layer H_n, a coating deposited with Ar and with a substrate bias applied has been used. As porous layers two coatings deposited with He have been used; one of these with an applied substrate bias of $-100\,V$, L_{n2}, and the other without substrate bias, L_{n1}. The interest of the use of these two different porous layers will be explained later.

In the following table 5.1, the nomenclature of each device and the layers used to its fabrication are presented. The layers have been named according to the nomenclature in chapter 2.

Table 5.1: Summary of coatings used for each optical device.

Optical device	Porous layer	Denser layer	Active layer
DBR 1	L_{n1} Si/He	H_n Si/Ar/bias	---
DBR 2	L_{n2} Si/He/b 100	H_n Si/Ar/bias	---
OMC	L_{n2} Si/He/b 100	H_n Si/Ar/bias	L_{n2} Si/He/b 100

The active layer in the OMC is referred to the defect introduced in the structure.

The devices have been deposited on substrates placed as it is represented in the experimental setup on figure 5.1, using an oblique angle configuration with the magnetron head tilted $30°$ with the normal to the substrate and with the substrate located in a plane at $5\ cm$ vertical distance from the magnetron head.

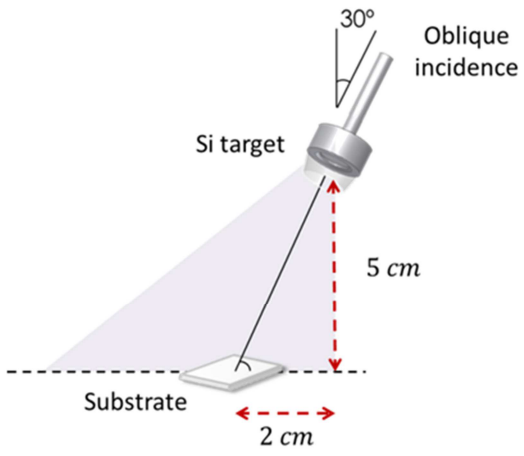

Figure 5.1: Schematic representation of the deposition geometry used.

Silicon (100) was used as substrate and it was used to study the structure of devices by SEM and TEM and to measure its optical properties. Most of the characterization techniques used in this chapter have been described in more detail in chapter 2.

To evaluate the morphology and to measure the thickness of the individual layers, SEM in the samples cross-section was used. However, to investigate in the nanoscale the structure of the device cross-sectional TEM was necessary. The chemical composition was analyzed by EDX and EELS inside the TEM. The refractive index of the individual layer was measured by ellipsometry. The optical properties of the device were studied measuring the experimental normal incidence specular reflectance spectra.

The reflectance measurements in the $1000 - 2500\ nm$ wavelength range were performed using a Fourier transform infrared spectrophotometer Bruker IFS-66 FTIR attached to a microscope which operate in reflection mode with a $4\times$ objective with 0.1 of numerical aperture (light cone angle $\pm\ 5.7°$).

5.3. Design's parameters of the optical devices

The general structures of the selected optical devices are presented in the figure 5.2. In the structure of the DBRs dense and porous layers were alternated, starting to deposit the dense layer and finishing with the dense layer again. In the case of the OMC, a porous layer is introduced as defect in the middle of the structure of the DBR. This defect is named active layer.

An important parameter for the design of these structures is the refractive index of the layers that form the optical devices and also the substrate's refractive index. This parameter has been measured in each individual layer by ellipsometry. In the figure 5.3 the refractive index and the extinction coefficient are plotted for the three individual layers used.

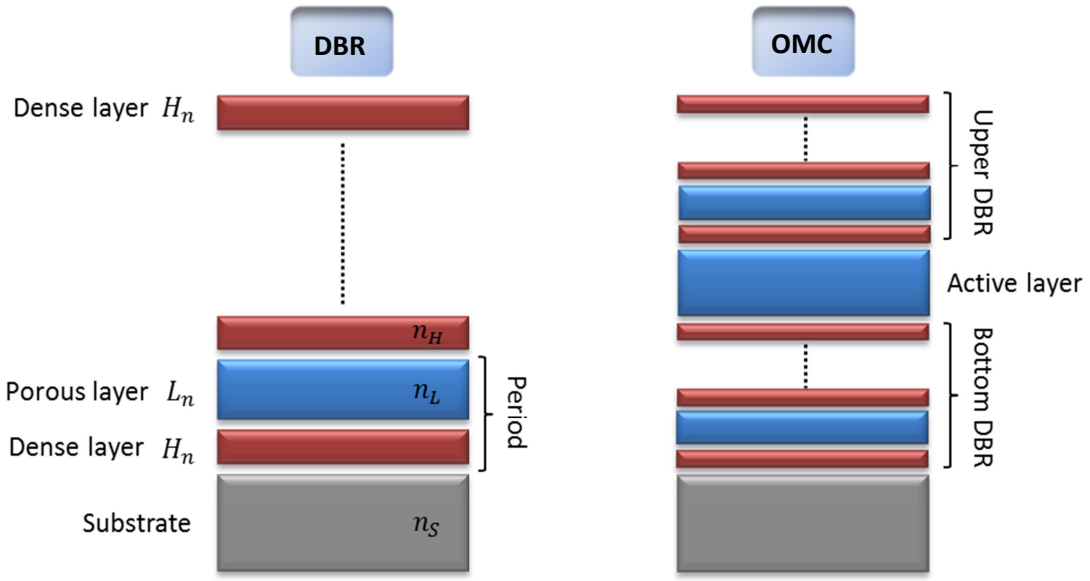

Figure 5.2: General structure of the selected optical devices.

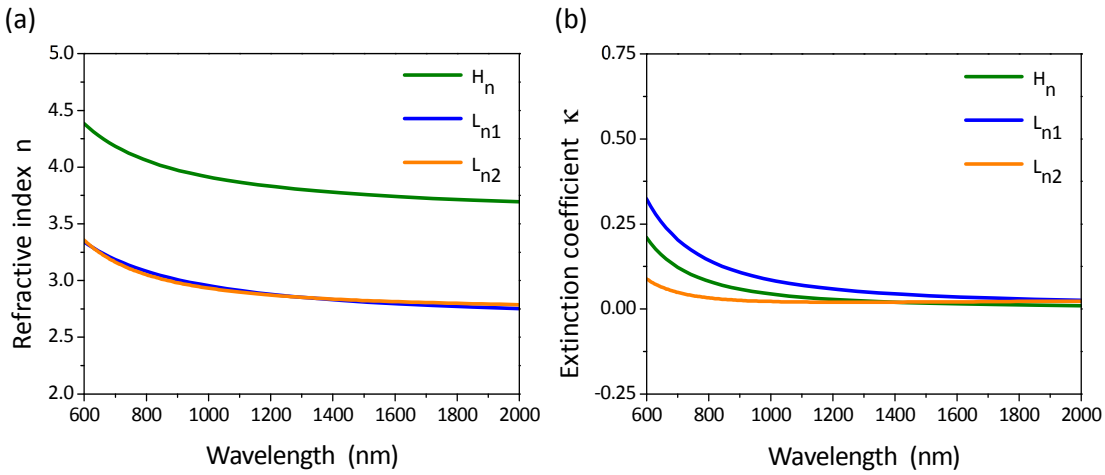

Figure 5.3: Optical properties of the individual layers used to fabricate the optical devices. (a) Refractive index. (b) Extinction coefficient.

The refractive index shows a significant difference between the dense coating, H_n, and the porous coatings, L_{n1} and L_{n2}, being as expected higher for dense than for porous coatings.

There is however no difference between both porous coatings.

The contrast index between dense and porous layers, defined as $\Delta n = n_H - n_L$, is high in the wavelength range measured here. This means that good optical properties of the optical devices are expected.

On the other hand, the extinction coefficient is very low in the near-IR region in the three coatings and therefore the absorption. This is the reason why this region was selected to design the optical devices.

The absorption of layers should be taken into account in the simulation of the optical behavior of the devices. In the following table are presented the complex refractive indexes, η, of the individual coatings expressed as $\eta = n + i\,\kappa$ and the refractive index of the substrate, at the resonant wavelength chosen (λ_0). The absorption of the substrate was negligible at the selected resonant wavelength [24], for this reason it has not been considered. The values presented in the table 5.2 have been used to simulate the optical response of the devices.

Table 5.2: Complex refractive index of layers and refractive index of substrate at the selected resonant wavelength λ_0.

Optical device	Resonant wavelength λ_0 (nm)	High complex refractive index (η_H)	Low complex refractive index (η_L)	Substrate refractive index (n_S)
DBR 1	1750	$3.72 + i\ 0.01$	$2.77 + i\ 0.03$	3.46
DBR 2	1750	$3.72 + i\ 0.01$	$2.80 + i\ 0.02$	3.46
OMC	1640	$3.74 + i\ 0.01$	$2.81 + i\ 0.02$	3.47

The optical devices have been designed using the quarter-wave configuration [25] where each optical layer thickness corresponds to one quarter of the resonant wavelength. In other words, the thicknesses of the dense t_H and porous t_L layers are given by:

$$t_H = \frac{\lambda_0}{4\, n_H} \qquad\qquad t_L = \frac{\lambda_0}{4\, n_L} \qquad [5.1]$$

being λ_0 the selected resonant wavelength, where the maximum reflectance is expected in the case of DBR.

The last parameter to design an optical device is the number of periods (pair of dense and porous layers). Using a code (see appendix V) to simulate the theoretical reflectance spectrum of multilayered structures, it has been possible to estimate the number of periods necessary to reach high reflectance values in the designed wavelength range. The details of the simulated reflectance data are presented in appendix V, as well as the simulation code used. Using the refractive indexes of the DBR 2 (without taking into account the absorption), the maximum reflectance reached at λ_0 is plotted in the following graph at different number of periods.

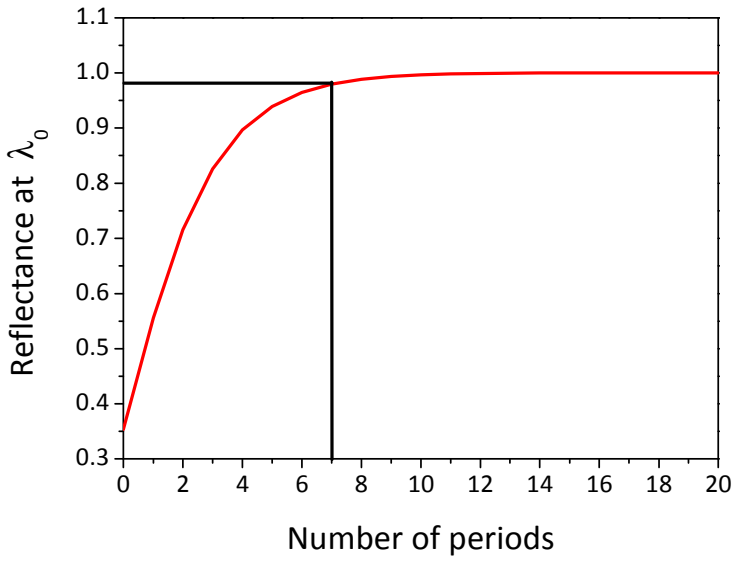

Figure 5.4: Variation of the maximum reflectance at λ_0 with the number of periods using the data of DBR 2.

From figure 5.4 it is observed that using 7 periods, a reflectance $\sim 98\ \%$ is reached. It is not worth to increase the number of periods because the corresponding increase in the reflectance is very low. So a good balance between number of periods and maximum reflectance is obtained with 7 periods. This value will be the number of periods for the design of DBR 1 and DBR 2. In the case of the OMC, has been estimated that 4 periods for the upper and bottom DBR are enough to get a low reflectance at the resonant wavelength.

Table 5.3 presents the theoretical thicknesses of the layers, calculated using the equations [5.1] for selected resonant wavelength, and the structure of the optical devices. For the case of the active layer, L_C , in the OMC the thickness of the active layer has been calculated as two times the thickness of the layer with low refractive index.

Table 5.3: Structure and thicknesses of layers for the three optical devices.

Optical device	Sequence of structure	t_H (nm)	t_{Ln1} (nm)	t_{Ln2} (nm)	t_{Lc} (nm)
DBR 1	$Substr-(H_nL_{n\,1})^7H_n-air$	118	158	---	---
DBR 2	$Substr-(H_nL_{n\,2})^7H_n-air$	118	---	156	---
OMC	$Substr-(H_nL_{n\,2})^4H_nL_c(H_nL_{n\,2})^4H_n-air$	110	---	146	292

Knowing all the parameters necessary to fabricate the optical devices, these are presented and studied in the next section.

5.4. OPTICAL DEVICES

5.4.1. DISTRIBUTED BRAGG REFLECTOR

Using the parameters presented in the previous section, two DBR have been fabricated. In figure 5.5 it is possible to observe their structure by SEM microscopy in the cross-section.

It is clearly observed the multilayered structure with 7 periods with similar thicknesses along the total thickness of the device. In both DBRs a sharp interface between dense and porous layers is shown.

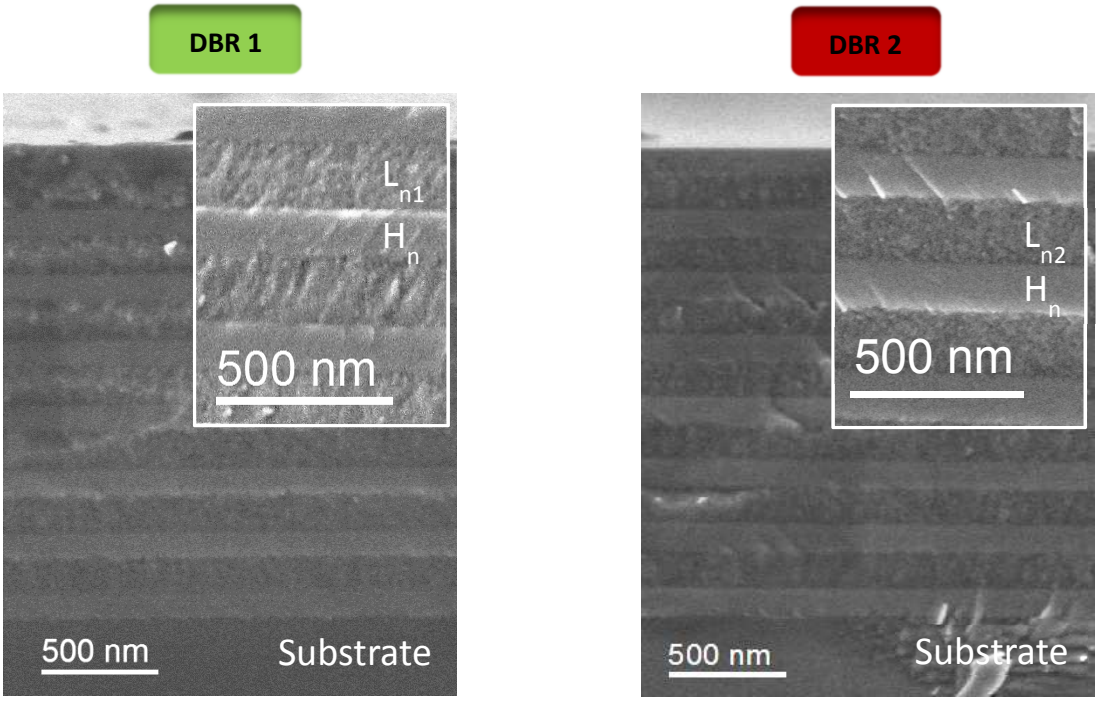

Figure 5.5: Cross sectional views of fabricated DBRs by SEM.

In more detail, figure 5.6 (a) presents a TEM micrographs of the multilayered structure of DBR 2 (similar to the one observed in DBR 1), and the structure of the porous layers in DBR 1 and DBR 2 (figures 5.6 (c) and (b) respectively). In these images it is shown the effect of the substrate bias on the porous layer. As it was explained in the chapter 3, when an OAD configuration is used the porous structure grows tilted in the magnetron direction (DBR 1, figure 5.6 (c)). However, when a substrate bias is applied using the same configuration, the porous structure grows in normal direction to the substrate, and this effect is presented in DBR 2, figure 5.6 (b). Following the same methodology reported in previous chapters, the pore size distribution in the porous layers was measured. For DBR 1 porous layer, the pore size obtained was similar to the one in the individual layer, with a major pore diameter

ranging between $3-58\,nm$ and the minor pore diameter in the $2-17\,nm$ range. (see figure 3.22 in chapter 3). For the layer used in DBR 2 a major pore diameter ranging between $4-30\,nm$ and the minor pore diameter between $3-10\,nm$ also similar to the one found for the individual layer produced using substrate bias.

Although in the figure 5.3 there was no significant difference in the refractive indexes of layers L_{n1} and L_{n2}, the interest in fabricating two DBRs with and without substrate bias during the growth of the porous layer, is for understanding the effect on the porous layer (grown without bias) when a bias is applied during the growth of the upper dense layer. By the SEM and TEM micrographs in figures 5.5 and 5.6, there is no effect on the porous structure. Later, in this section, it will be shown if there is some effect on the optical properties by comparing both devices DBR 1 and DBR 2.

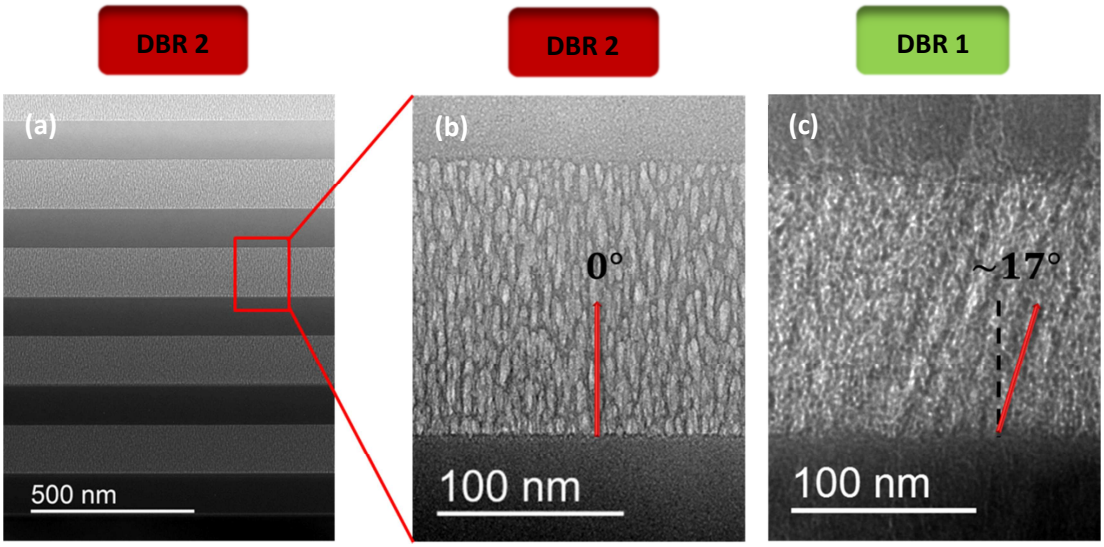

Figure 5.6: (a) TEM cross section view of multilayered structure of DBR 2 and detail of the porous structure in the porous layer in (b) DBR 2 and (c) DBR 1.

The quality of the optical response of a multilayer system depends greatly on the quality of the interface, and in this case, sharp interfaces are presented between the porous and dense layers as observed in previous microscopy images.

Also surface roughness is affecting the quality of the optical response. Roughness measurements have been done in the surface of each DBR, in table 5.4 the square mean roughness R_q values are presented.

Table 5.4: Square mean roughness coefficient of the DBRs surfaces.

Optical device	R_q of the surface (nm)
DBR 1	3.5 ± 2.6
DBR 2	1.8 ± 0.5

The roughness is very low in both DBRs, satisfying the condition $R_q \ll \lambda_0$. So the surface can be treated as optically smooth and therefore, specularly reflecting. Good optical properties are therefore expected in both DBRs.

The chemical characterization of these layers was performed and is shown here for DBR 2 as representative of the DBR devices combining STEM-ADF images with EDX and EELS analysis. In figure 5.7 (a) a STEM-ADF image of the multilayered structure is presented. In ADF images, the intensity I follows the equation below:

$$I \propto Z^2 t \qquad [5.2]$$

where Z is the atomic number of the material and t is the specimen thickness crossed by the electron beam. The darker areas in the figure correspond to lower Z value, in our case, the less dense layers (porous layers). Although the material of the porous and dense layers is the same, silicon, this fact can be understood considering that in the porous layer (L_n) the effective atomic number is smaller than in the dense layer (H_n).

Also, the influence of the TEM specimen thickness difference, related to cross-section sample's preparation, is observed from the substrate to the surface of the multilayer. For

this reason the layers near to the substrate are brighter than the layers farther from the substrate when comparing the same kind of layer H_n or L_n. This effect is shown in the evolution of the ADF signal on the line profile across the multilayer in the figure 5.7 (b).

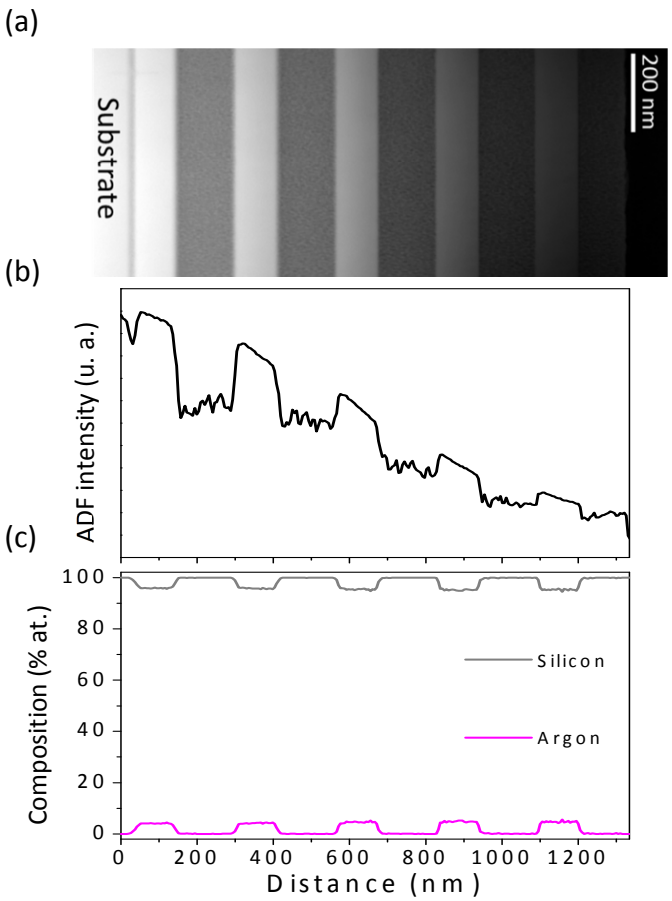

Figure 5.7: Chemical analysis. (a) STEM-ADF image of DBR 2. (b) ADF intensity profile. (c) Chemical composition of layers (by EDX).

The evolution of Si and Ar relative composition profiles extracted from the EDX spectra was measured using the standardless quantification method provided by the TIA software. In the figure 5.7 (c) the Si content is $100\ \%$ for the porous layers, because He is not taken into account. In dense layers (grown under Ar plasma), the Si amount decreases and the Ar

amount increases around $5\ at.\%$. This Ar content is similar to the quantity obtained by RBS ($6\ at.\%$) in the individual coating. The behavior is repeated through all the thickness of the multilayer structure where uniform thicknesses of dense and porous layers are pilled-up.

As it was proved in the work by Schierholz et al. [26] (see appendix IV), the individual porous coatings contain He trapped inside the pores. Using the same methodology, the presence of He is proved when the porous coatings are introduced in a multilayer structure.

Measuring the low-loss EELS spectra at different positions in the marked black line in the figure 5.8 (b), the He K-edge have been extracted as it is shown in the figure 5.8 (a).

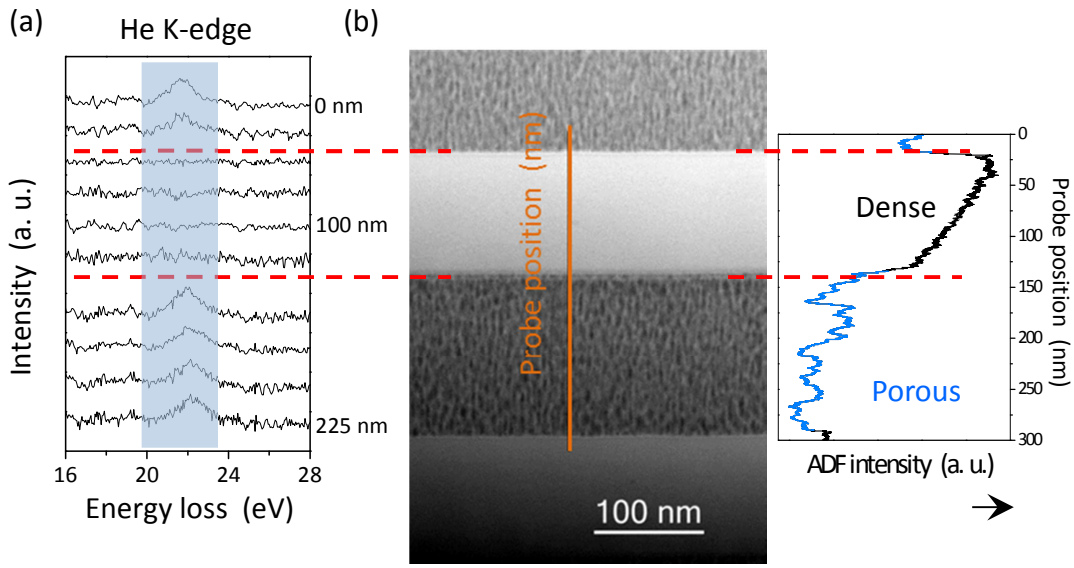

Figure 5.8: (a) He K-edge from low-loss EELS spectra. (b) STEM image showing a probe position line and corresponding ADF intensity.

In the figure 5.8 (b), each probe position across the marked line in nm corresponds to an EELS spectrum. At the positions 0 and $225\ nm$, placed in the porous layers it is possible to observe the He K-edge while at the $100\ nm$ position, placed in the dense layer, no He signal was detected. ADF profile was registered for these positions being the signal more intense in the dense layer and decreasing in the porous one.

All these results of the microstructural analysis confirm that the porous and dense layers integrated in the photonic structure are very similar to the individual coatings analyzed in chapter 3 with sharp defined interfaces as required for fabrication of optical devices.

Finally, the optical characterization of these two DBRs has been done measuring the reflectance spectrum. The experimental spectra were compared with simulated spectra using a code based on the transfer matrix method. As already mentioned this code is described in more detail in the appendix V.

The thicknesses of layers introduced in the simulation were the values obtained in the fabricated devices as measured in SEM images of the DBRs. These values, presented in the following table, are very similar to the desired theoretical values (after eq. [5.1]) showing the good control of the thickness that it is possible to obtain in the deposition equipment used.

Table 5.5: Comparison between experimental and theoretical thicknesses of layers.

Optical device		$t_H \ (nm)$	$t_{Ln1} \ (nm)$	$t_{Ln2} \ (nm)$
DBR 1	Theo.	118	158	---
	Exp.	112 ± 4	160 ± 5	---
DBR 2	Theo.	118	---	156
	Exp.	116 ± 8	---	158 ± 4

The experimental reflectance spectra were acquired in the near-IR range, $1000 - 2500 \, nm$, at normal incidence. The figure 5.9 shows the experimental and simulated spectra for DBR 1 and DBR 2.

Due to the good agreement of experimental and theoretically defined thicknesses, the experimental and simulated spectra are very similar too for both DBRs. It is possible to observe the high reflectance band characteristic of DBRs centered as expected at $1750 \, nm$. Besides, in both DRBs a high reflectance is obtained $\sim 95 \, \%$, as correspond to the contrast of indexes and the number of periods previously calculated.

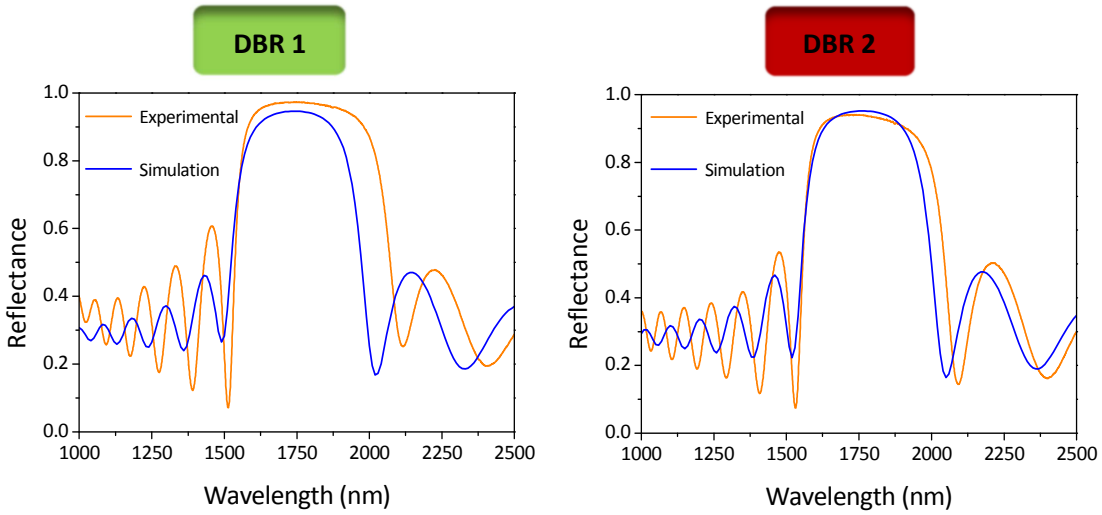

Figure 5.9: Experimental and simulated spectra of DBR 1 and DBR 2.

A difference between the simulated and experimental spectra is the band gap width. For both DBRs, the experimental band gap is broader than simulated. This may be due to the fact that the real part of the complex refractive indexes of the layers can be slightly different from the values introduced in the simulation, obtained from the individual coatings, or due to the experimental thicknesses values of the layers which have an associated error.

Coming back to the figure 5.9, in the case of the experimental spectrum of DBR 2, it is clearly observed that the center of the band gap is not symmetric (the band gap is not flat). This could be due to a change in the thickness of the same kind of layers, dense or porous, along the thickness of the device. The same effect takes place in a lesser extend in the case of DBR 1 where the band gap is not completely symmetric.

Anyhow, the fitting between the experimental and simulation spectra for both designed devices is very good. A band gap with high reflectance $\sim 95\ \%$ is obtained. This proving that the methodology presented in this thesis to obtain dense and porous layers is a good way to tailor-made fabrication of optical devices based in multilayered structures.

Taking advantage of the oblique angle geometry and exploiting the difference in thickness over a large area, consequence of the different distance to the magnetron, it is possible to design graded DBRs with a controlled position of the band gaps. This effect has been studied using the DBR 2. In the figure 5.10 is shown the experimental situation.

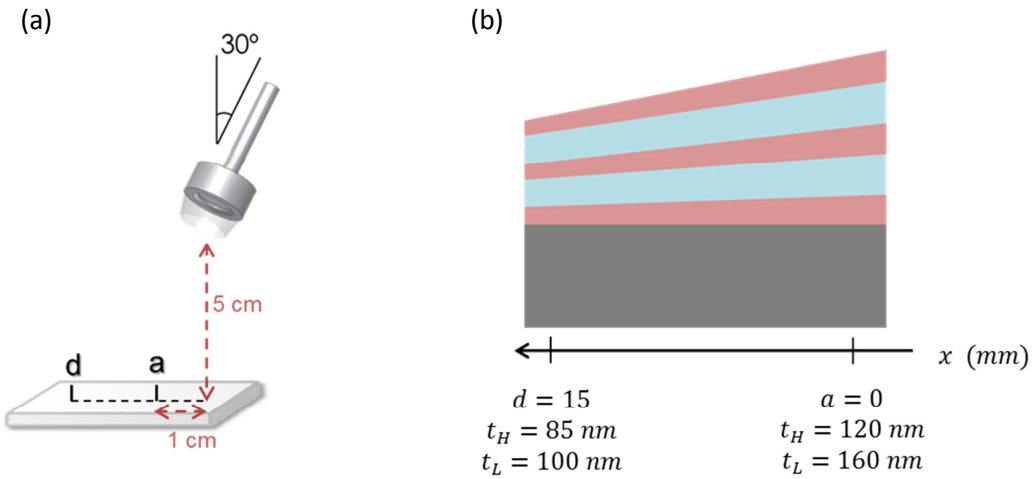

Figure 5.10: (a) Experimental setup. (b) Scheme of the effect on thickness in the coating with the distance to the magnetron.

The reflectance spectrum has been therefore measured in four different positions with a distance of $5\ mm$ between them, being a and d the nearest and the farther positions to the magnetron respectively (see figure 5.10 (a)). For this reason, in the figure 5.10 (b), it has been drawn the thickness of layers thicker in position a than in position d. In the next graph (figure 5.11) it is plotted the experimental reflectance spectrum for each position.

It is observed how the band gap position can be modified changing the position in respect to the magnetron. In positions nearer the magnetron the band gap is centered at higher wavelength and the maximum of reflectance is lower than in positions farther from the magnetron. The variation of these two parameters, resonant wavelength and maximum

reflectance at this wavelength, are plotted in the following graphs (figures 5.12 (a) and (b)) as a function of the distance to the magnetron.

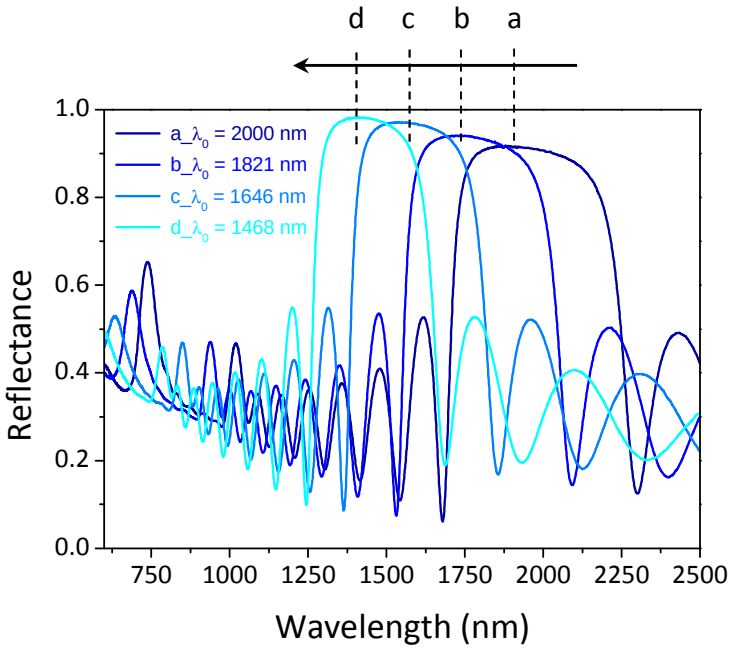

Figure 5.11: Variation of the reflectance spectrum with the distance to the magnetron.

The two effects are caused by the variation of the thickness of the layers as a function of the position respect to the magnetron (see figure 5.10 (b)). The thickness of layers using the quarter-wave configuration maximizes the reflectance value reached at λ_0 according to equation [5.1].

The relation between thicknesses and resonant wavelength is linearly growing, so, an increase in the thickness of layers implies an increase of the resonant wavelength. This explains the effect shown in figure 5.12 (a). Also the effect shown in figure 5.12 (b) can be understood as due to the higher absorption of light when the thickness of the layers increases.

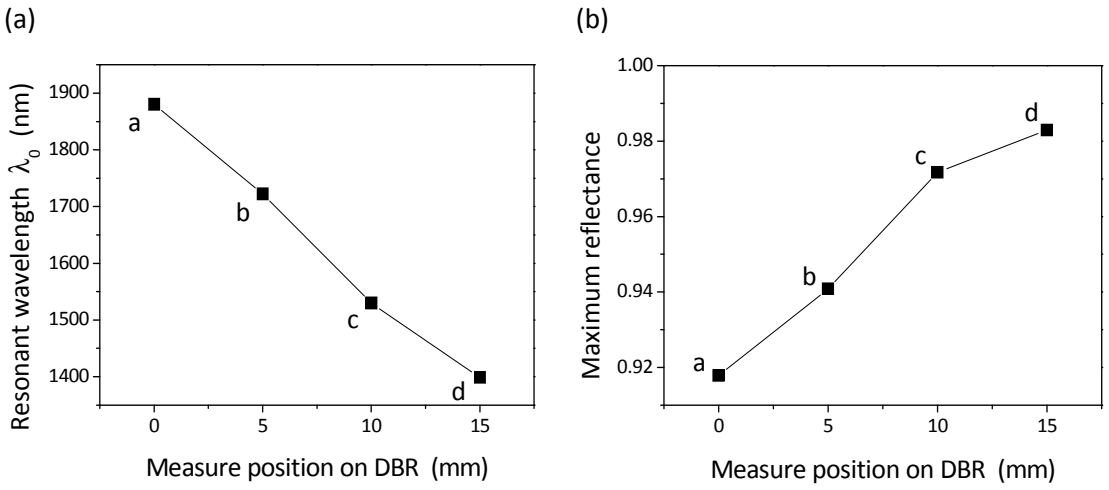

Figure 5.12: Effects of the sample's position respects to the magnetron on the reflectance spectrum. (a) Effect on the resonant wavelength λ_0 . (b) Effect on the maximum reflectance.

Another effect observed in the figure 5.11, is that the band gap width increases at positions nearer to the magnetron, or in other words, when the resonant wavelength increases. This fact is easy to explain analyzing the theoretical relation between the band gap width and the resonant wavelength given by the equation:

$$\Delta\lambda = \frac{4}{\pi}\,\lambda_0\, arcsin\left(\frac{n_H - n_L}{n_H + n_L}\right) \qquad [5.3]$$

where $\Delta\lambda$ is the band gap width. As it is observed, when the resonant wavelength increases, the band gap width increases too. Following the previous argument, the band gap width increases when the thickness of layers increases.

Finally it is interesting to notice that the low deposition temperatures characteristic of magnetron sputtering technology allows to deposit multilayers structures on different kind of substrates as polymers or flexible substrates. Recent works point to the relevance of developing flexible silicon photonic crystals [27].

In the figure 5.13, SEM images of two examples are shown, where the DBR 2 has been deposited on Teflon and kapton substrates. The same stacked structure can be deposited in these flexible substrates with a very good adhesion.

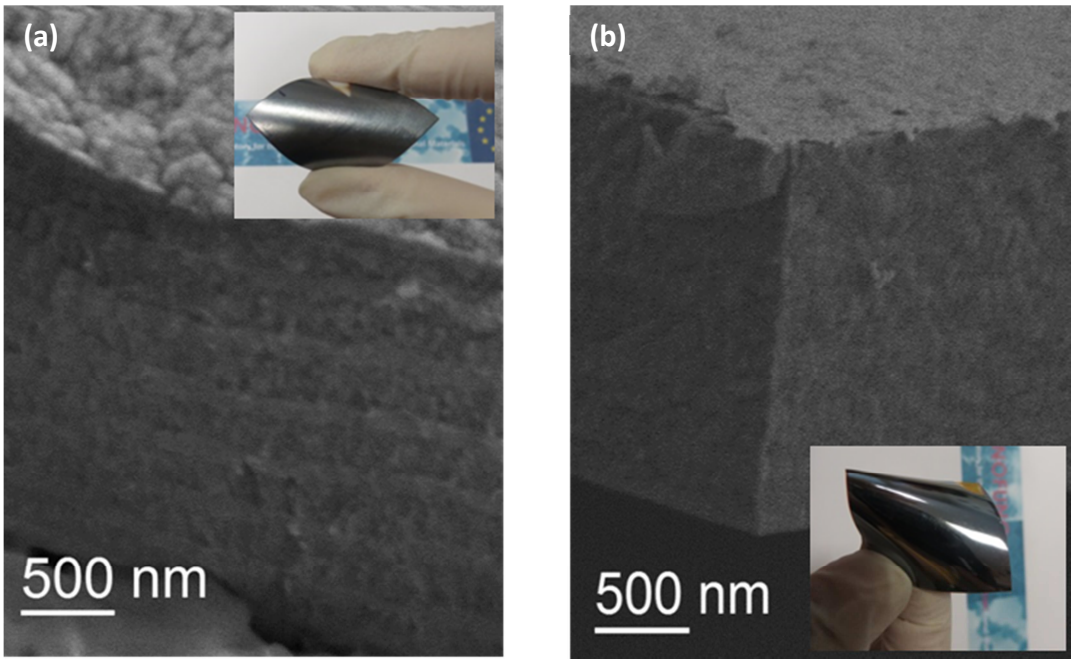

Figure 5.13: DBR 2 deposited on flexible substrates (a) Teflon. (b) Kapton.

The inset images in figure 5.13 show the good behavior of the coatings upon deformation of the flexible substrates, being an interesting property with application in flexible silicon electronics or photonics.

5.4.2. Optical microcavity

Another type of optical device designed and fabricated in this thesis is the optical microcavity (OMC). This multilayered structure is a DBR with defects in the periodicity. The breaking in the periodicity of the structure affects the reflectance spectrum which depends on the kind and number of defects.

In the microcavity designed herein only one defect has been introduced. The defect is a porous layer introduced in the middle of the DBR, having the porous layer the same nature that the porous layer used in the DBR (see figure 5.2). By simulation has been observed that when the defect or active layer has a thickness of two times the thickness of the porous layer of a DBR, the reflectance spectrum presents two band gaps with high reflectance separated by a narrow band with low reflectance. This kind of device can be used as a selector of frequencies due to the narrow band presenting low reflectance.

The DBRs have been designed with the quarter-wave configuration, meaning, the thicknesses of layers were calculated by equation [5.1], so the thickness of the active layer can be calculated as follows:

$$t_{Lc} = \frac{\lambda_0}{2\, n_L} \qquad [5.4]$$

The dense and porous layers used are the same as the ones used in the design of DBR 2, H_n and L_{n2} respectively. The simulations showed that 4 periods in the upper and bottom DBRs are enough to obtain a low reflectance at the resonant wavelength. The microcavity has been designed to present a minimum in the reflectance spectrum at $\lambda_0 = 1640\, nm$. In table 5.6 are presented the theoretical thickness calculated with the equations [5.1] and [5.4] and the experimental thickness measured on the SEM image of microcavity showed in the figure 5.14 (a).

Table 5.6: Comparison between experimental and theoretical thicknesses of layers in the OMC devices.

	$t_H\ (nm)$	$t_{Ln2}\ (nm)$	$t_{Lc}\ (nm)$
Theo.	110	146	292
Exp.	109 ± 5	151 ± 4	295 ± 7

Slightly differences are observed comparing the theoretical and the experimental thicknesses, showing again the good control on the thickness of layers obtained with the deposition methodology presented in this thesis.

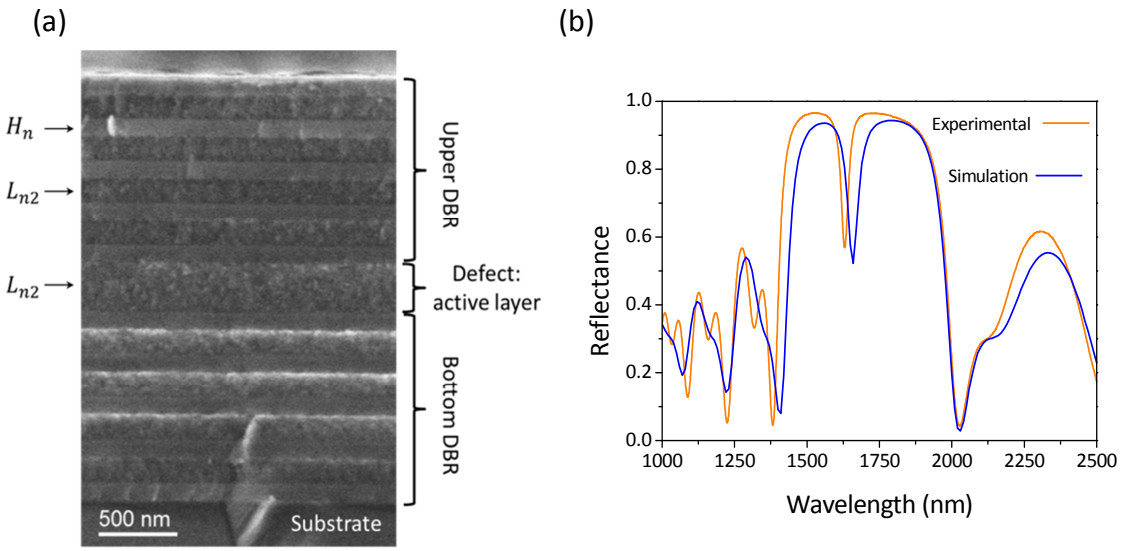

Figure 5.14: Optical microcavity. (a) SEM cross sectional view. (b) Reflectance spectra: experimental and simulated.

The image 5.14 (a) shows the different parts of the microcavity, two DBRs separated by an active layer. In the figure 5.14 (b), the experimental reflectance spectrum is plotted showing the two band gaps with high reflectance $\sim 97\ \%$ separated by a sharp band with low reflectance $\sim 57\ \%$ at $1630\ nm$, a little lower than the expected value, $1640\ nm$. Simulated spectra were calculated using the experimental thickness values (see figure 5.14 (b)) where the minimum reflectance in the cavity is located at $1660\ nm$ a little higher than the experimental. These differences between experimental and simulated spectra may be due to the difference between refractive indexes taken from individual layers and the ones in each particular device or uncertainty in the thickness of layers shown in the table 5.6. These results give an evaluation of the experimental errors (reproducibility control of the equipment). However, according to the figure 5.14 (b) the agreement between the experimental and simulated spectra can be considered as very good showing that, as in the case of DBR, this methodology to make porous and dense layers is also appropriated to design OMC devices.

For this kind of structures the quality factor Q is defined as follows:

$$Q = \frac{\lambda_0}{\Delta\lambda} \qquad [5.5]$$

where λ_0 is the resonant wavelength and $\Delta\lambda$ is the full width at half maximum (FWHM) of the resonance dip. In the following table are presented the quality factor values obtained in the experimental and simulated spectra shown in the figure 5.14 (b).

Table 5.7: Quality factor of OMC.

Quality factor Q	
Experimental	**Simulation**
56	47

Similar values are obtained for simulated and experimental spectra taking into account the uncertainty in the refractive indexes and the thicknesses of layers associated at the experimental conditions.

5.5. CONCLUSIONS

In this chapter it has been demonstrated the possibility to design optical devices as Bragg reflector (DBR) or optical microcavities (OMC) with a single material by magnetron sputtering. Single material optical devices are of interest for avoiding conductivity and thermal expansion changes at the multilayered interfaces.

With the methodology proposed in previous chapters it was shown the control of the refractive index in a-Si coatings only changing the sputtering gas (and eventually substrate bias parameters). Porous and denser coatings were prepared on demand in multilayered stacks.

Using a dense and two porous coatings, two DBRs and one OMC have been designed in the near-IR range. The denser coating deposited with Ar and substrate bias presents higher refractive index than the porous coatings deposited with He. The effect of substrate bias on the porous coating during the fabrication of the optical devices has been studied by depositing the porous layers in the DBR devices with and without substrate bias (DBR 1 and DBR 2 respectively).

The main difference between DBR 1 and DBR 2 is the porous structure of the porous layers with pores tilted in the magnetron direction for DBR 1 and pores oriented in the normal direction to the substrate for DBR 2. No significant difference has been found however in the refractive indexes of the two individual porous coatings in the near-IR range studied in this chapter.

The optical properties of these two DBRs have been analyzed measuring the specular reflectance in normal configuration. The experimental spectra have been compared with simulated spectra. The simulations have been performed considering the layers absorbent. Within the experimental errors variations are not significative in respect to fitting of experimental data.

The center of the band gap in experimental and simulated spectra is the same in both DBRs, $1750\ nm$, as expected from the similarity in refractive index for individual porous layers growth with and without substrate bias. The experimental band gap widths were higher than the simulated ones, most probably due to slight changes in the refractive indexes of layers in the DBR devices as compared to individual layers. The quality of fabricated DBR devices is very good due to sharp interfaces and good control of fabrication of the multilayered stack.

Taking advantage of the oblique angle deposition configuration used, the reflectance spectrum has been measured in different positions on the surface of DBR 2. At different positions it is possible to obtain a change in the resonant wavelength value and in the maximum of reflectance at each particular resonant wavelength. In positions nearer to the

magnetron, the resonant wavelength and the band gap width are higher than in positions nearer the magnetron, although the maximum of reflectance is lower in those positions.

Magnetron sputtering technology characterized by low deposition temperatures allows to deposit on different kind of substrates including sensible or flexible substrates. The DBR 2 has been deposited on Teflon and kapton, both flexible substrates, obtaining the same stacked structure with a good adhesion between the substrate and the multilayered structure even under deformation. These are interesting results with potential application for flexible silicon electronics or photonics.

A second type of optical device has been designed: a DBR 2 with a defect introduced in the middle of the structure to fabricate an OMC. The defect is a porous layer with the same nature of the porous layer used in the DBR but with a thickness two times the thickness of the porous layers. The experimental spectrum has been compared with simulated spectrum obtaining a good agreement. Also in this case it is demonstrated the good capabilities of our magnetron sputtering methodology to control the refractive indexes and thicknesses on multilayered stacks. Tailor-made optical devices have been fabricated with good quality and good agreement between obtained and predicted behavior.

5.6. References

1. Godinho, V. *et al.* A new bottom-up methodology to produce silicon layers with a closed porosity nanostructure and reduced refractive index. *Nanotechnology* **24,** 275604 (2013).

2. Guo, D.-L., Fan, L.-X., Wang, F.-H., Huang, S.-Y. & Zou, X.-W. Porous Anodic Aluminum Oxide Bragg Stacks as Chemical Sensors. *J. Phys. Chem. C* **112,** 17952–17956 (2008).

3. Rabaste, S. *et al.* Sol-gel fabrication of thick multilayers applied to Bragg reflectors and microcavities. *Thin Solid Films* **416,** 242–247 (2002).

4. Colodrero, S., Ocana, M. & Miguez, H. Nanoparticle-based one-dimensional photonic crystals. *Langmuir* **24,** 4430–4434 (2008).

5. Wu, Z., Lee, D., Rubner, M. F. & Cohen, R. E. Structural color in porous, superhydrophilic, and self-cleaning SiO2/TiO2 Bragg stacks. *Small* **3,** 1445–1451 (2007).

6. Yablonovitch, E. Photonic Crystals. *J. Mod. Opt.* **41,** 173–194 (1994).

7. Reece, P. J., Lerondel, G., Zheng, W. H. & Gal, M. Optical nicrocavities with subnanometer linewidths based on porous silicon. *Appl. Phys. Lett.* **81,** 4895–4897 (2002).

8. Weiss, S. M., Zhang, J., Fauchet, P. M., Seregin, V. V. & Coffer, J. L. Tunable silicon-based light sources using erbium doped liquid crystals. *Appl. Phys. Lett.* **90,** 031112 (2007).

9. Reece, P. J., Lerondel, G., Mulders, J., Zheng, W. H. & Gal, M. Fabrication and tuning of high quality porous silicon microcavities. *Phys. Status Solidi -Appl. Res.* **197,** 321–325 (2003).

10. Venturello, A. *et al.* Controlled light emission from dye-impregnated porous silicon microcavities. *J. Non-Cryst. Solids* **352,** 1230–1233 (2006).

11. Jang, S. J., Song, Y. M., Yeo, C. I., Park, C. Y. & Lee, Y. T. Highly tolerant a-Si distributed Bragg reflector fabricated by oblique angle deposition. *Opt. Mater. Express* **1,** 451–457 (2011).

12. Leem, J. W. & Yu, J. S. Broadband and wide-angle distributed Bragg reflectors based on amorphous germanium films by glancing angle deposition. *Opt. Express* **20,** 20576–20581 (2012).

13. Schubert, M. F., Xi, J.-Q., Kim, J. K. & Schubert, E. F. Distributed Bragg reflector consisting of high- and low-refractive-index thin film layers made of the same material. *Appl. Phys. Lett.* **90,** 141115 (2007).

14. Tokranova, N. A., Novak, S. W., Castracane, J. & Levitsky, I. A. Deep Infiltration of Emissive Polymers into Mesoporous Silicon Microcavities: Nanoscale Confinement and Advanced Vapor Sensing. *J. Phys. Chem. C* **117,** 22667–22676 (2013).

15. Kilian, K. A., Boecking, T., Gaus, K., Gal, M. & Gooding, J. J. Peptide-modified optical filters for detecting protease activity. *Acs Nano* **1,** 355–361 (2007).

16. Volk, J., Le Grand, T., Barsony, I., Gombkoto, J. & Ramsden, J. J. Porous silicon multilayer stack for sensitive refractive index determination of pure solvents. *J. Phys. -Appl. Phys.* **38,** 1313–1317 (2005).

17. Patel, P. N. & Mishra, V. Realization of porous silicon photonic bandgap optical sensor devices. *J. Optoelectron. Adv. Mater.* **16,** 269–275 (2014).

18. Ivanov, I. I. *et al.* Porous silicon Bragg mirrors on single- and multi-crystalline silicon for solar cells. *Renew. Energy* **55,** 79–84 (2013).

19. Harraz, F. A., El-Sheikh, S. M., Sakka, T. & Ogata, Y. H. Cylindrical pore arrays in silicon with intermediate nano-sizes: A template for nanofabrication and multilayer applications. *Electrochimica Acta* **53,** 6444–6451 (2008).

20. Huanca, D. R., Ramirez-Fernandez, F. J. & Salcedo, W. J. Porous silicon optical cavity structure applied to high sensitivity organic solvent sensor. *Microelectron. J.* **39,** 499–506 (2008).

21. Shtenberg, G., Massad-Ivanir, N., Fruk, L. & Segal, E. Nanostructured Porous Si Optical Biosensors: Effect of Thermal Oxidation on Their Performance and Properties. *ACS Appl. Mater. Interfaces* **6,** 16049–16055 (2014).

22. Bisi, O., Ossicini, S. & Pavesi, L. Porous silicon: a quantum sponge structure for silicon based optoelectronics. *Surf. Sci. Rep.* **38,** 1–126 (2000).

23. Zhang, H., Jia, Z., Lv, X. & Liu, Y. Design, analysis and optimization of porous silicon microcavity based on silicon-on-insulator at optical communication wavelengths. *Optik* **125,** 557–560 (2014).

24. Green, M. A. Self-consistent optical parameters of intrinsic silicon at 300 K including temperature coefficients. *Sol. Energy Mater. Sol. Cells* **92,** 1305–1310 (2008).

25. Rancourt, J. D. *Optical Thin Films*. (SPIE, 1996). at <http://ebooks.spiedigitallibrary.org/book.aspx?doi=10.1117/3.242743>

26. Schierholz, R. *et al.* STEM-EELS analysis reveals stable highdensity He in nanopores of amorphous silicon coatings deposited by magnetron sputtering. *Nanotechnology* **26,** 075703 (2015).

27. Xu, X. *et al.* Flexible Single-Crystal Silicon Nanomembrane Photonic Crystal Cavity. *Acs Nano* **8,** 12265–12271 (2014).

Chapter 6

Final Conclusions

The motivation of this thesis was the development of a magnetron sputtering methodology employing helium plasmas to produce porous silicon coatings with controlled porosity and refractive index. The relationship between deposition parameters, microstructure and final properties was comprehensively investigated through the chapters of this thesis; and in each chapter, conclusions are presented for the particular studies.

Here, a summary of the main conclusions obtained in this research work in agreement with the objectives proposed in chapter 1 is presented.

- A new bottom-up methodology has been developed to deposit amorphous silicon coatings using helium as sputtering gas by magnetron sputtering technique. The coating deposited in this way present a particular structure with closed porosity. Controlling the deposition parameters it is possible to deposit coatings with tailored refractive index. Several deposition parameters have been studied.

    - Deposition gas: the choice of the inert deposition gas is essential for the introduction of closed porosity in amorphous silicon coatings. Using He as deposition gas a closed pores structure, containing the deposition gas inside the pores is obtained, presenting a decreased refractive index when compared with dense coatings deposited with Ar.

    - Deposition geometry: with the deposition conditions investigated in this thesis, changing the vapor flux direction it is possible to modify the orientation of pores which appear in the vapor flux direction, respecting the well-known tangent rule for OAD.

    - Helium pressure: depositing in OAD configuration, the orientation of pores can be changed modifying the He pressure; an increase of He pressure provokes a decrease in the pore tilt angle as the Si atoms arriving to the substrate lose directionality due to high number of collisions with gas atoms in the plasma. Besides, it has been observed a decrease in the He amount trapped in the coating when the pressure was increased.
    - RF Power supplied: increasing the RF power supplied to the target increases the energy of the atoms and ions impinging on the substrate, which results, in the case of OAD geometry investigated in this thesis, in

a pore orientation angle close to the deposition geometry. An increase in the pore size has been observed when the power supplied was increased. Besides, a change in the pore shape was observed obtaining rounded pores at low power and more elongated pores at higher power. Although the pore size was increased for the higher power conditions a decrease in He amount trapped in the pores was observed, that could be motivated by a higher desorption of He atoms on the films due to higher energy of the Si atoms arriving to the films and displacing the He atoms.

- Substrate bias: in OAD configuration, when a substrate bias is applied, the ions bombardment during deposition improves the adatom mobility and the shadowing effects characteristic of OAD disappear, the pores are oriented in normal direction regarding the substrate. Besides, the pore shape is more elongated when a bias is applied. When high voltage is applied (in this work $-200\ V$) the kinetics of formation of a nanocrystalline phase, composed by closed pores and silicon crystals imbibed in an amorphous matrix, is induced. This nano-composite phase contains less He than the amorphous phase due to a decrease of pore size and most probably in the amount of closed pores.

- Deposition temperature: although it was not possible to investigate a wide range of substrate temperatures due to experimental restrains, 3 positions of interest in the well-known Thorton's model were investigated for OAD of the porous silicon coatings. For $T_h = \frac{T_s}{T_m} < 0.3$, Zone I of Thorton's model, the structure is governed by low atom mobility and shadowing effects. Besides the structure of the coatings exhibits high porosity oriented in the magnetron direction. For $T_h \approx 0.3$, atomic diffusion is allowed, promoting the formation of a

dense layer close to the substrate where the temperature effects are stronger. For $T_h > 0.3$ surface diffusion is allowed resulting in a denser layer closed to the substrate. The RBS shows a decrease in the He amount incorporated in the coatings.

It was proved that He is located inside the pores. By STEM-EELS technique it has been possible to estimate the He density and pressure inside the pore obtaining pressure results in the order of GPa, similar to the ones reported in bibliography for He implanted. The He stability inside closed porosity has been proved by RBS spectra of a same coating measured in different dates, from several months until 2 years since deposition. No changes were observed in the He amount trapped in the coating, showing the high stability of these new porous coatings.

Annealing treatments show that the pore structure filled with He is stable at least at $300°C$. However, a reduction in the He amount was measured at $550°C$ with a $5\ at.\%$ trapped in the coating.

- To understand the physical mechanisms taking place in the growth of Si closed pores structure coatings, a simple Monte Carlo (NASCAM) based on shadowing effects was employed. The computer simulation tools were used to compare with the experimental results. Measuring the pore size obtained by computer simulation it was concluded that in the case of the coatings deposited with Ar, simulation and experiments agree very well showing that the formation of porosity is governed by the shadowing effects. However, in the case of the coatings deposited with He + Ar the results differ in the range of small pores concluding that the shadowing mechanism cannot satisfactorily explain the pore structure when He is added. Therefore, He seems to introduce a new process affecting the nanostructural development of the films. This process tends to merge small pores and form large

ones and it has been associated with certain mobility of point defects in the Si network due to the low solubility of He in the material.

- The possibility to employ the methodology presented in this thesis for producing photonic structures was explored. Two types of single material optical devices were designed: distributed Bragg reflector (DBR) and an optical microcavity (OMC). The optical multilayers are composed by alternated dense and porous silicon coatings with different refractive index just by changing the deposition gas, for applications in the near-IR range. A good control of the layers thickness with high refractive index contrast and sharp interfaces is demonstrated. The reflectance spectrum of each device was measured and compared with the theoretical spectrum obtaining a good agreement between them. This fact shows that the new methodology studied in this thesis is very adequate to fabricate optical devices.

  Furthermore, the characteristics of magnetron sputtering technique allow to deposit on flexible substrates. This has been proved on Teflon and kapton substrates. Taking advantage of the deposition geometry also gradient Bragg reflectors can be designed using this methodology. The method presented is very versatile allowing deposition over large surfaces and different substrates like over glass or polymers.

Appendix I

Characterization techniques

The characterization techniques used in this thesis will enumerated in this appendix.

Ellipsometry measurements

Optical characterization of the coatings was performed by ellipsometry on samples deposited on quartz substrates. The measurements were executed in a *UVISEL spectroscopic ellipsometer from HORIBA Jobin Yvon* with an incidence angle of $60°$ and a wavelength range of $300 - 2100\,nm$. The data were analyzed using the Deltapsi2 software developed by HORIBA Jobin Yvon.

Scanning electron microscopy (SEM)

Scanning electron microscopy was performed to study the morphology and thickness of samples in a high resolution FEG (field emission gun) microscope, *HITACHI S4800*. Samples grown on silicon substrates were used for the SEM analysis. Cross section samples were obtained by cleavage of the silicon pieces. More details about the preparation of the samples are shown in chapter 2.

Transmission electron microscopy (TEM)

For the transmission electron microscopy observations with selected area electron diffraction analysis (TEM/SAED) two microscopes were used: a *Philips CM200* operating at $200\,kV$ and a *Tenai F30* operating at $300\,kV$. The samples analyzed by TEM were grown on silicon substrates. Cross section observations were obtained by cleavage of the silicon pieces. More details about the preparation are presented in the chapter 2.

Scanning transmission electron microscopy (STEM) and Electron energy loss spectroscopy (EELS)

The composition of the coatings in the nanoscale was evaluated inside the *Tecnai F30* microscope. To get information about the composition of the individual pores at the nanoscale, the scanning mode (STEM) was used with a probe size of less than $1\,nm$. Spatially resolved electron energy loss spectra (EELS) were recorded in the low-loss range over $2048\,channels$ ($0.05\,eV/channel$), with integration time of $0.05\,s$. In this range in addition to the plasmon peaks, the He K-edge at $22\,eV$ is accessible for quantification. Experimental details of these analyses are given in appendix IV.

Rutherford backscattering spectroscopy (RBS)

The composition of the films was evaluated by Rutherford Backscattering Spectroscopy (RBS).

In this thesis two facilities were used:

- National Center of Accelerators (CNA Sevilla, Spain) using a $3\,MV$ tandem accelerator. The RBS spectra were obtained using two different energies, 1.0 and $2.3\,MeV$ for proton beam and a surface barrier detector set at $165°$. The lower energy is necessary to separate the Si signal coming from the substrate and from the film, in order to obtain the sample thickness. The higher energy is required to obtain the He content, because of the energy range where the $^4He(p,p_0)^4He$ cross section is available. To obtain the thickness and composition of the coatings, both spectra were simulated simultaneously for every coating using the SIMNRA code[1] .
- PMR-LARN Laboratory (University of Namur) using a $2\,MV$ tandetrom accelerator ALTAIS. The energy used was $2.5\,MeV$. The thickness and chemical composition of the coatings were deduced by means of the Sim Target 1.0 [2] and SIMNRA 6.06 [1] codes. Non-Rutherford cross-sections were computed by SigmaCalc on the IBANDL database [3] at detection angles of $165°$ and $170°$.

Samples grown on silicon and carbon glass substrates were used in this technique.

Reflectance measurements

The specular reflectance measurements were performed using a near-infrared spectrometer *Bruker IFS-66 FTIR.* In the $1000 - 2500\ nm$ wavelength range, the Fourier transform infrared spectrophotometer was attached to a microscope operating in reflection mode with a $4\times$ objective with 0.1 of numerical aperture (light cone angle $\pm\ 5.7°$). Samples grown on silicon substrates were used for the reflectance measurements.

X-ray photoelectron spectroscopy (XPS)

The X-ray photoelectron spectroscopy equipment was a *Leybold Heraus LH10 Spectrometer* working in the constant analyzer energy mode with a pass-energy of $50\ eV$. The samples were analyzed with Al K_α radiation. The binding energy reference was taken as the main component of the C $1s$ peak at $284.6\ eV$ for adventitious carbon. For quantification the XPS spectra were subjected to background subtraction (Shirley background) and sensitivity factors supplied by the instrument manufacturer were used. The analysis was done on samples grown on silicon substrates.

X-ray diffraction (XRD)

To evaluate the crystallinity, X-ray diffraction (XRD) measurements were done using a *PANalytical X'Pert PRO diffractometer* in Bragg-Brentano $\theta - \theta$ configuration in the interval $10° - 90°$ with a step of $0.05°$ and with a time of $4\ s$ in every step. The radiation used was K_α of Cu with a wavelength of $\lambda = 1.54056$ Å. The measurements were done on samples deposited on quartz substrates.

REFERENCES

1. Mayer, M. in *Application of Accelerators in Research and Industry, Pts 1 and 2* (eds. Duggan, J. L. & Morgan, I. L.) **475,** 541–544 (Amer Inst Physics, 1999).

2. Aeken K V. DRAFT - Design, Research And Feasibility of Thin Films at Ghent University/UGent. at <http://www.draft.ugent.be/>

3. Gurbich, A. F. Evaluated differential cross-sections for IBA. *Nucl. Instrum. Methods Phys. Res. Sect. B-Beam Interact. Mater. At.* **268,** 1703–1710 (2010).

Appendix II

Magnetron sputtering

This appendix will be dedicated to present an overview on the deposition technique used to prepare the coatings presented in this thesis.

Sputtering Deposition

Sputtering deposition is a physical vapor deposition technique in which a target is bombarded with energetic ions provoking the ejection of the atoms from the target that are finally deposited on a substrate forming a layer. This most common form of sputtering is a plasma-based sputtering. The plasma is formed by the partial ionization of a gas applying an electric discharge between the target (cathode) and the substrate to be covered (anode). In the figure 1 (a) the sputtering process is sketched showing the different components of the plasma: ions, electrons, neutral atoms and photons. These last ones give the color to the plasma.

When the energy of the formed ions is high enough, the interaction with the target surface creates a collision cascade and some of the momentum is transferred to the surface atoms which can be ejected – **sputtered**. These ejected atoms travel some distance until reaching the substrate and condensate forming a thin film. Most of the transferred energy appears as heat in the target surface and near surface. Generally in sputtering the targets are actively cooled, minimizing the radiant heat and preventing also diffusion processes in case of alloy compounds. Figure 1 (b) presents some of the most significant events that occur on a bombarded target. In addition to sputtering, some of the bombarding particles are reflected as high energy neutrals and some are implanted on the surface. Also ejected secondary electrons can interact with the gas atoms through inelastic collisions increasing the ionization probability and creating more ions necessary to sustain the plasma [1].

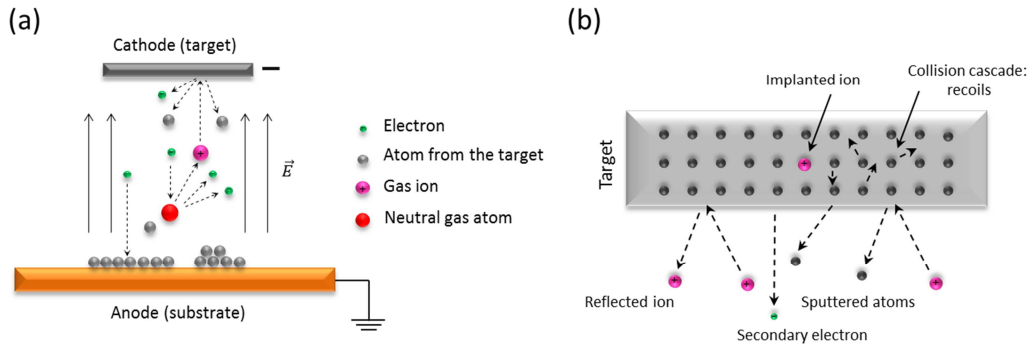

Figure 1: (a) Sputtering process and plasma components, (b) Events that occur on the bombarded target.

A measure of the removal of surface target atoms is the sputtering yield Y, defined as the ratio between the number of sputter-ejected atoms and the number of incident projectiles [1].

The number of sputtered atoms depends on the energy, mass and incident angle of the bombarding ion on the target, and also on the target material, its surface binding energy and crystallographic orientation. The sputtered atoms travel through the plasma in vapor phase and when they arrive to the substrate they condensate and are deposited.

Possible ways to increase the ionization probability are by one hand to increase the number of gas atoms increasing the gas pressure or to increase the applied potential. However these measures have some disadvantages. The deposition rate is reduced at higher gas pressure by ion-electron recombination and sputtered atoms collisions in the gas phase, producing also poor quality of the film. Increased potential will also increase energy consumption.

Magnetron Sputtering

In conventional sputtering, the electrons that are ejected from the cathode are accelerated away from the cathode and not all are efficiently used for sustaining the discharge. A good solution to improve deposition process is the use of an adequate magnetic field, deflecting

the secondary electrons to keep them near the target surface. The confinement of electrons causes that the same electron participates in ionization events several times increasing the number of ions created and therefore the number of sputtered atoms and secondary electrons by the impact on the target. These secondary electrons would be trapped by the magnetic field and so on. This configuration, named **magnetron sputtering**, allows generating stable plasma with high density of ions, increasing the deposition rate. Figure 2 shows a representation of the magnetron sputtering process as it has been used in this thesis for the fabrication of thin films.

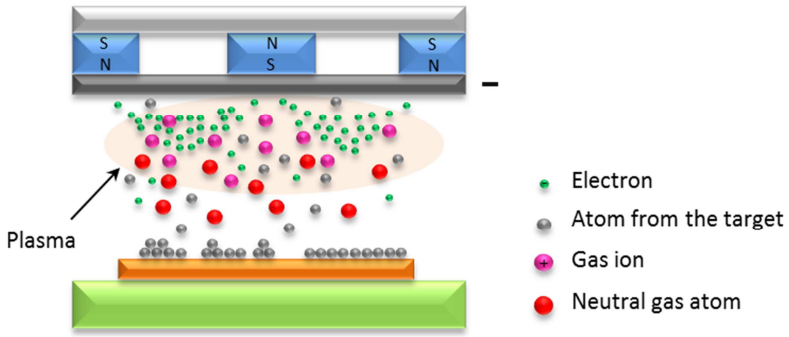

Figure 2: Magnetron sputtering process. The plasma is confined near the target producing higher deposition rates.

The most common magnetron configuration is the planar magnetron source, where the sputter-erosion path is a closed circle on a flat target denominated “race track”. Figure 3 shows the magnet configuration and a representation of the magnetic field lines and their intensity for the magnetron source used in this thesis. This representation was done by Romain Tonneau (University of Namur, Belgium) based on magnetic field measurements carried out in Seville using a magnetic field probe.

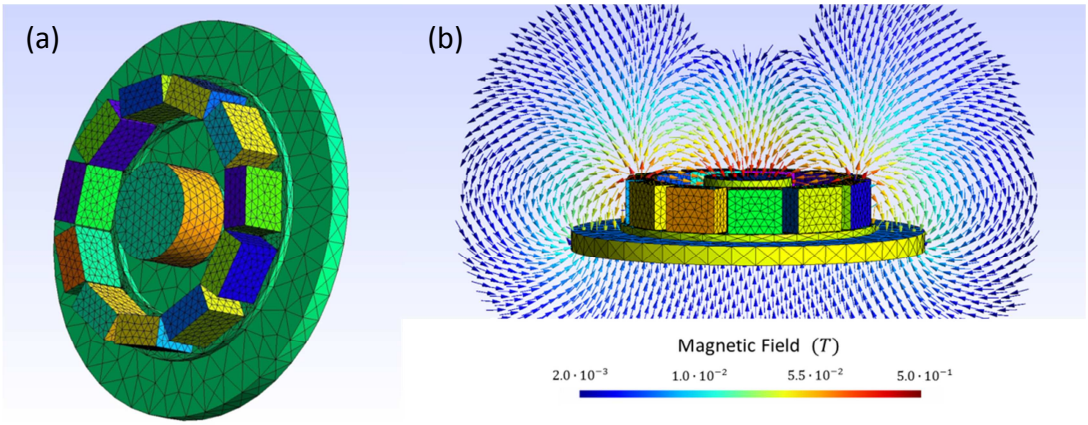

Figure 3: (a) Magnet position and (b) Magnetic field lines and its intensity for the magnetron source used in this thesis (2" magnetron from Thin Film Consulting).

Also two magnet configurations are possible depending on the magnets strength. In balanced magnet configuration (the one used in this work), the magnets strength and dimensions are the same resulting in strongly confined plasma near the target region. Therefore, only a few charged particles reach the substrate. This configuration prevents the bombardment of the substrate by energetic particles. However, the plasma confinement near the target can be detrimental in activating reactive gases in reactive sputtering deposition, or in situations where it is advantageous to deliver more energy to the substrates. In these situations unbalanced magnet configuration is used, being possible to use magnets with different strength and/or dimensions increasing the plasma's density near to the substrate [2].

External bias voltage can be applied to the substrate in order to increase the particles' energy towards the substrate. If a negative bias is applied, the ions are attracted to the substrate and the electrons repelled, while a positive bias has the opposite effect. Biased coatings are generally denser when compared to the typical columnar growth of non-biased films. Negative bias was also applied in this thesis in some experiments.

It is worth to mention that magnetron sputtering configuration has a drawback related with the irregular erosion of the target. The plasma's density is higher where the magnetic field

lines are parallel to the target, so, in this area, the "race track" is formed wasting the target. This may affect the film uniformity and requires frequent replacement of the target. To improve target utilization, rotating cylindrical magnetrons, employing cylindrical tubular targets have been developed [2].

Commonly sputtering deposition occurs in the presence of inert gases like argon or helium, this is the case of the coatings deposited during this thesis. When a reactive gas (as nitrogen or oxygen) is added to the discharge it is possible to deposit a broad variety of compound materials, controlling the composition of the coatings. This is called reactive sputtering. However, the introduction of a reactive gas in contact with the target leads to the formation of compound material poisoning the target's surface, usually with sputtering rates lower than the one of the pure target [3].

Compound materials can also be prepared by the use of alloy targets or co-deposition from different targets.

There are several modes of powering magnetrons: direct current (DC), radio frequency (RF), pulsed DC and recently high-power impulse magnetron sputtering (HIPIMS).

The direct current (DC) mode is the simplest and least expensive and have been applied successfully in metallic targets. However, for semiconductor or insulating targets, this mode fails, due to the accumulation of positive charge on the target interrupting the sputtering process and producing strong arcing. Besides, only a small fraction of the gas is converted to ions resulting in a low deposition rate, so, high gas pressure is necessary to increase the deposition rate this affecting the film quality.

A solution to these problems is to apply a voltage variable with the time with a frequency ω. If the polarity of the target is changed with the time the positive charge accumulation on the target is avoided. This is the named alternate current (AC) sputtering mode.

At low frequency ω, the electrons and ions can follow the variation of electric field, and it would be as a DC mode, sputtering the target with electrons or with ions depending of the

polarity of the target in every instant. At high frequencies, when the alternating signal is applied to the cathode, generating plasma, then the plasma acts as a rectifier that generates an average negative voltage at the smaller of both electrodes, which is in general the target. This negative voltage is called the self-bias. Due to the different masses, electrons can react to the variation of electric field, while ions are too heavy are only affected by the self-bias voltage V_{sb} that accelerates them to the target. In the following figure it is represented a typical voltage variation with the time in AC mode at high frequencies.

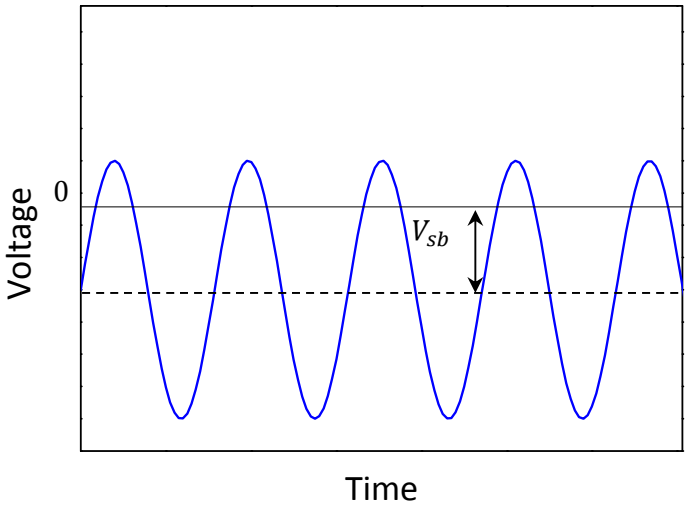

Figure 4: AC voltage on the target and self-bias V_{sb}.

Usually, the frequency value used is $13.56\ MHz$ in the radiofrequency range. The AC mode in this range is named radiofrequency (RF) mode. Both DC and RF modes have been employed in this thesis.

So, in the case of RF mode, the electrons are oscillating back and forth colliding more times with the gas atoms before they are lost, and therefore, increasing the ionization degree compared with the DC mode. This means that it is possible to work with lower gas pressure increasing the deposition rate because there are less collisions between the sputtered

atoms and the gas atoms. Since the target is capacitively connected to the plasma it makes no difference whether the target is of conductive or electrically isolating material. In spite of these advantages for RF mode in many industrial applications the DC mode is preferred for its easier up-scaling.

In pulsed DC mode the applied voltage is pulsed at a much lower frequency, typically $50 - 250\ kHz$ depending on the application [2]. The discharge voltage is cycled between high negative to perform sputtering and low positive voltage to attract the electrons. Figure 5 shows the events occurring in the different parts of the cycle. An optimal control of the different cycle parts can be the use of dual magnetron sputtering, switching between negative and positive voltage between two targets.

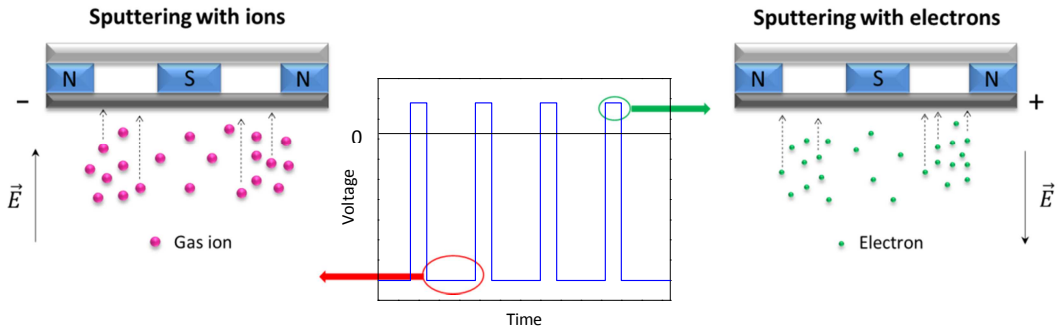

Figure 5: Pulsed DC mode showing the sputtering with ions or with electrons depending of the cycle of the voltage applied.

HIPIMS uses a large energy impulse on a very short period, typically $100\ \mu s$. This method results in high density plasma with a high ionization degree of the sputtered material [2].

Magnetron sputtering presents important advantages over other deposition processes, among them, the possibility of depositing films in a wide variety of substrates even substrates sensible to temperature like polymers, the sputtering conditions can be easily reproduced from run to run. It is a low cost process without the need of chemical

precursors avoiding toxic emissions of by- products. One of the major advantages of the magnetron sputtering process is the easiness to scale up to industrial processes.

References

1. Mattox, D. M. *Handbook of Physical Vapor Deposition (PVD) Processing*. (William Andrew, 2010).

2. Martin, P. M. *Handbook of Deposition Technologies for Films and Coatings: Science, Applications and Technology*. Chapter 5. (William Andrew, 2009).

3. Sproul, W. D., Christie, D. J. & Carter, D. C. Control of reactive sputtering processes. *Thin Solid Films* **491,** 1–17 (2005).

Appendix III

Morphology and microstructure of thin films: Structure-zone models

The formation of a thin film has several stages, starting with the condensation of the atoms on the substrate when they arrive in vapor phase. Next, the atoms condensed on the substrate form stable nucleus and these nuclei grow and join other nuclei, forming islands and finally a continuous film.

Depending of the incident energy of the arrived atom, it can be adsorbed or desorbed on the substrate. The probability of one atom to be adsorbed on the substrate is described by the *sticking coefficient* S_C, defined as the ratio between the number of atoms adsorbed and the number of atoms arrived to the substrate. S_C varies between 0 and 1 and it depends of the nature of the atoms, the surface of the substrate and the deposition parameters.

When an atom is adsorbed on the substrate and it has enough energy to overcome the diffusion barriers, it can move on the surface changing its position.

The jump rate (change of position) follows the Arrhenius law for thermally activated processes:

$$\nu = \nu_0 \, e^{-E_D/k_B T} \qquad [1]$$

where k_B is the Boltzmann's constant, T is the absolute temperature in kelvins, E_D is the barrier energy to change the position and ν_0 is the attempt rate, estimated as:

$$\nu_0 = \frac{2\, k_B T}{h} \qquad [2]$$

being h the Planck's constant.

While the diffusion of the atoms takes place, they can encounter other atoms. Then, they can cluster and form nuclei. In the figure 1 is shown this situation [1,2].

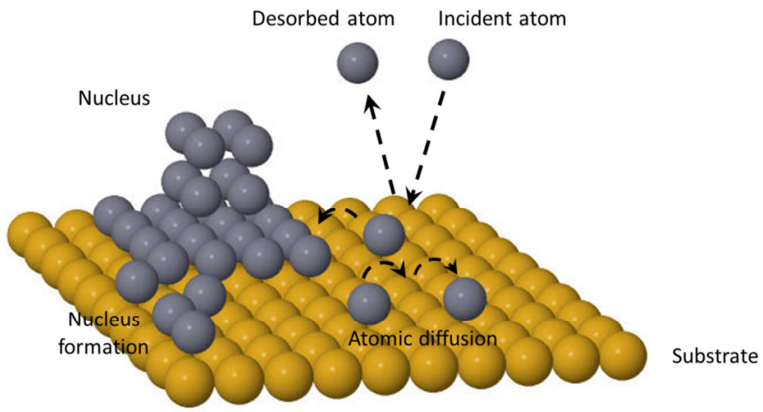

Figure 1: Representation of nucleus formation, atomic diffusion and atomic desorption. Adapted from [2].

The formation of nuclei can take place by adding atoms in vapor phase and therefore growing the nuclei (see figure 2 (a)) or by adding atoms just deposited on the surface. In the last one way there are three different processes for it [1,3]:

- Ostwald ripening mechanism: large nucleus grow at the expenses of the smaller ones. This mechanism is influenced by the size and chemical potential of the nuclei. See figure 2 (b).
- Sintering: the neck formed between two growing nuclei allows faster growth and merging. See figure 2 (c).
- Cluster migration: the nuclei can move on the surface substrate, rotate or jump to each other at sufficient high temperature. The coalescence occurs by collisions between individual nuclei. See figure 2 (d).

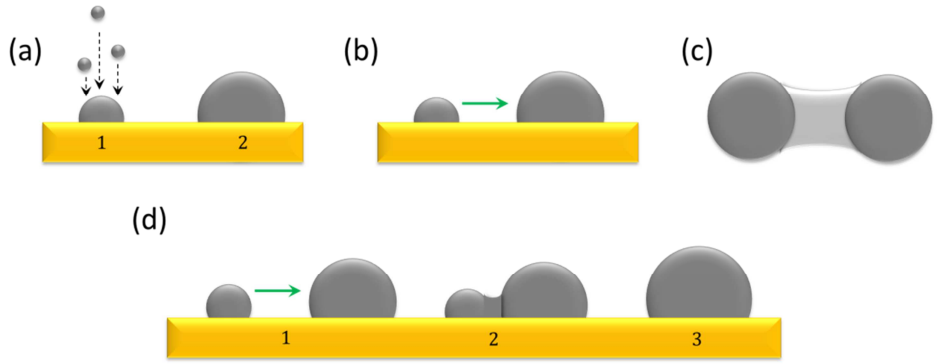

Figure 2: Different mechanism on the growth of nuclei. (a) Adding atoms in vapor phase. (b) Ostwald ripening. (c) Sintering. (d) Cluster migration. Adapted from [1].

Depending on the balance between desorption and nucleation it is possible to distinguish three different cases [1]:

- *Predominant desorption:* the atoms arrive to the substrate and they are desorbed, therefore no film is formed. If the temperature of substrate is sufficient high, a monolayer could be formed.
- *Nucleation without atomic diffusion:* the atoms arrive to the substrate and they stay in the same site of impingement, therefore there is no atomic diffusion forming amorphous coatings with low density. This process is favored by low incident energy of the atoms, low temperature of substrate or high deposition rate.
- *Nucleation with atomic diffusion:* the atoms deposited on the substrate can move on it reaching more energetically stable sites. This situation takes place at high incident energy of atoms or at medium-high temperature of substrate. In this case, depending of the binding energy E_{bin} between the atoms deposited and the energy interaction E_{ads} between the atoms deposited and the surface of substrate, three different modes of nucleation and growth can be observed.

The description of these three models follows [1,4]:

a) Volmer – Weber ($E_{bin} > E_{ads}$): the atoms deposited tend to join between them forming islands. See figure 3 (a).

b) Frank - Van der Merwe ($E_{bin} < E_{ads}$): the atoms deposited have more affinity to join with the atoms of the substrate resulting in a growth of film layer by layer. See figure 3 (b).

c) Stranski - Krastanov: this mode is a mixture between the two modes explained above. Firstly a growth layer by layer takes place and next a growth in island. See figure 3 (c).

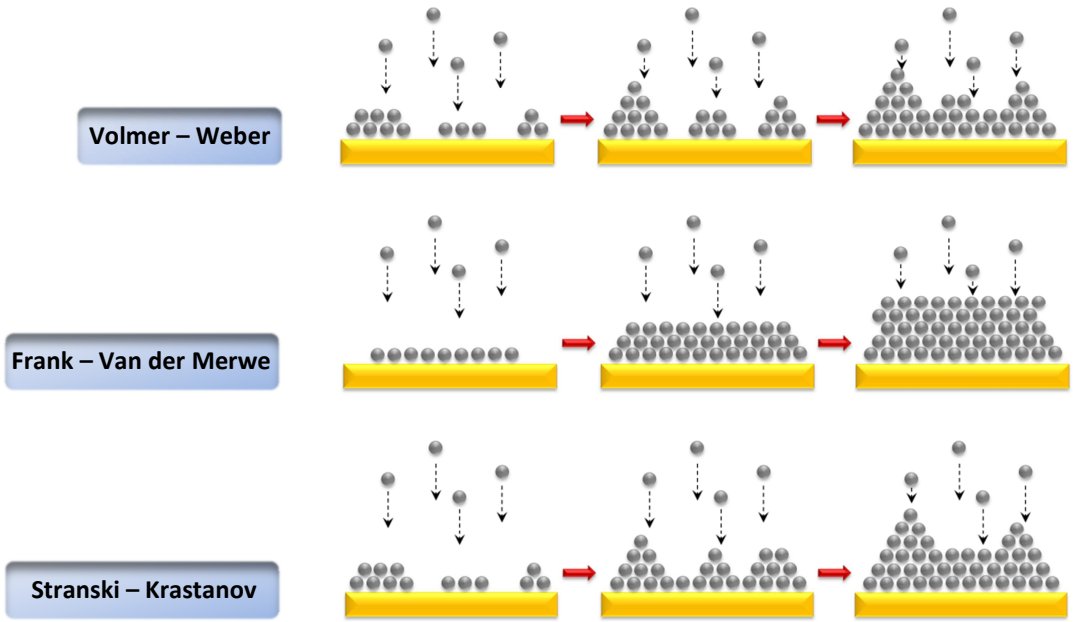

Figure 3: Different growth modes [1].

The final properties of the coating depend of the morphology and microstructure of the coating.

As a way to illustrate the evolution of the microstructure as a function of different deposition conditions, over the years different models have been developed which the microstructure with the different deposition parameters. They are known as structure zone

models (SZM), although they are not really models, they are simplistic representations of expected film microstructure trends versus deposition parameters. Not all the parameters are included in these zone models, so their representations can only serve for rough orientation due to each combination of substrate, film material, and deposition conditions represents a unique system. Nevertheless they illustrate the common features of films grown under certain deposition parameters.

As the microstructure of coatings is strongly influenced by the temperature or surface mobility on the growing surface, the structure zone models (SZMs) are commonly represented as a function of the homologous temperature T_h defined as the ratio between the substrate temperature T_s and the melting temperature of the deposited material T_m in kelvins.

The first model for structure versus T_h, was proposed by Movchan and Demchisin [5] in 1969 for very thick films deposited by evaporation. Based on the analysis of many samples, their model divides the film growth in three different zones:

- Zone I ($T_h < 0.3$): it is characterized by a low atom mobility on the substrate or film leading a continued nucleation of grains. This results in a fine-grained structure of textured grains, pointing in the direction of the arriving vapor. Originating a columnar structure separated with voids and mainly caused by statistical roughening and self-shadowing effects. This shadowing effect is more pronounced when the atoms arrive to the substrate in oblique angle α as it is shown in the figure 4.

  The figure 4 shows the shadow region where the deposition of atoms is not possible forming the voids between the columns. In these conditions the relation between the deposition angle α and the columnar angle β is given by the tangent rule [6]:

$$\tan\alpha = 2\ \tan\beta \qquad [3]$$

This relation fits well the experimental observations when $\alpha < 60°$ but provides a poor description otherwise. Nevertheless, in the literature exist other models to predict the columnar tilt angle [7–11].

In this zone, the orientation of the nuclei defines the orientation of the columns and can be predicted by a ballistic deposition model.

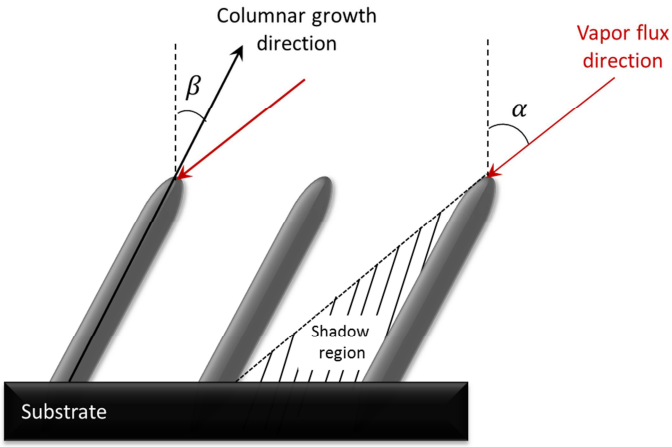

Figure 4: Columnar growth in OAD conditions and shadowing effect. (α- deposition angle, β- column growth direction).

- Zone II $(0.3 < T_h < 0.5)$: At higher temperature diffusion is allowed leading to uniform columnar grains. This zone it is characterized by columnar grains separated by dense intercrystalline boundaries presenting a surface with a smooth appearance. The grain size increases with T_h. The surface ends of the grains lead to a faceted surface.
- Zone III $(0.5 < T_h < 1)$: At even higher temperature bulk diffusion and recrystallization leads to dense films with large grains. The microstructure consists in equiaxed grains with a polyhedral structure. The grain diameters increase with T_h.

In the following figure is shown a representation of this model.

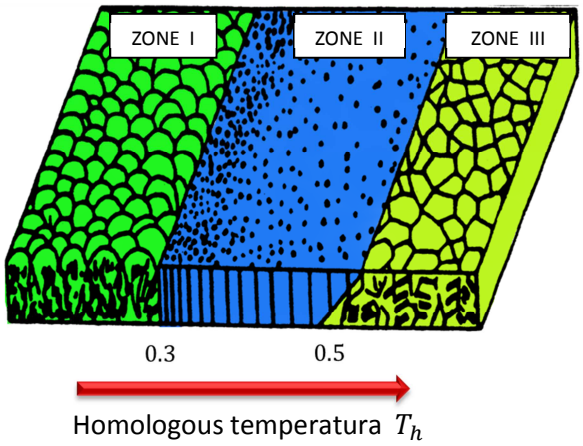

Figure 5: Structure zone model proposed by Movchan and Demchisin.

In 1977 with the broad use of magnetron sputtering Thornton [12] modified the model proposed by Movchan and Demchisin adding a new variable, the innert gas pressure (argon)). At low pressure sputtered particles experience almost no collisions before arriving to the substrate. However, at higher deposition pressures the sputtered atoms suffer collisions and their energy distribution is altered. In his model Thornton introduced a transition zone named zone T between the zones I and II.

On zone I of Thornton's model, shadowing processes are responsible for the columnar growth. Higher sputtering gas pressures extend this zone to higher temperatures due to gas scattering and decreased surface mobility due to gas adsorption and collisions on the surface. In zone T the coating has a fibrous morphology and this is considered to be a transition zone between zone I and zone II. This structure forms due to the energetic bombardment at low gas pressures and high temperature, which erodes the peaks and fill-in the valleys. In zone II the growth process is dominated by adatom surface diffusion, allowing the densification of intercolumnar boundaries. However, the basic columnar morphology remains. The grain size increases and the surface features tend to be faceted.

In zone III bulk diffusion allows recrystallization, grain growth and densification. Often a highly modified columnar morphology is detectable, with columns of single crystals [13]. In the figure 6 is sketched this structure zone model with the different main processes.

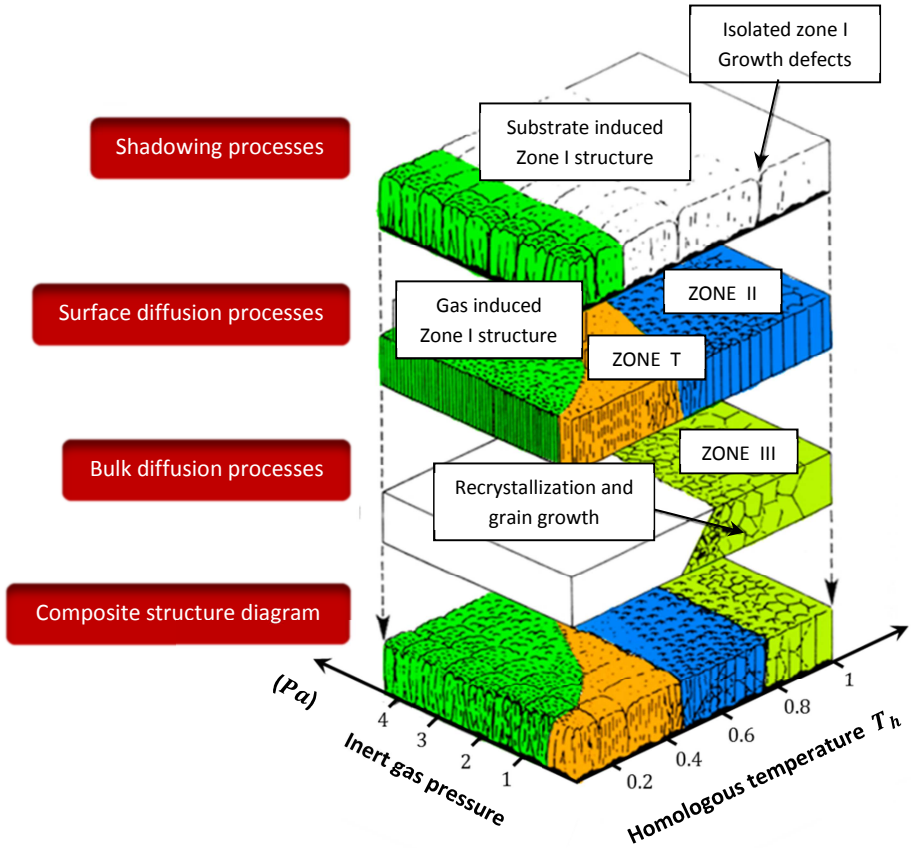

Figure 6: Thornton's structure zone model.

This model was revised by Messier et al. [14] in 1983 replacing the inert gas pressure and introducing a parameter which affect to the induced mobility in a more fundamental manner than the inert gas pressure. This parameter is the substrate floating potential V_s. This substrate floating potential can accelerate the positive ions in the plasma to bombard the substrate and its value affects the growth of the coating and therefore the final

microstructure. The particularity in this model is that the zone T can be small or may even not exist at sufficiently low V_s values. In the figure 7 a representation of this model is presented.

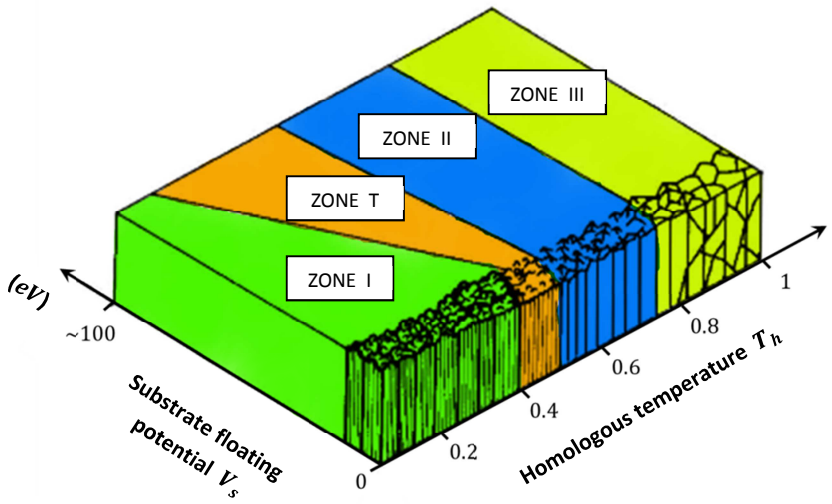

Figure 7: Messier's structure zone model.

Besides the structure of coatings with low atomic diffusion ($T_h < 0.5$) was investigated considering the effects of ion bombardment as well as the substrate temperature. The model proposed takes into account the thickness evolution recognizing three general structural units: nano-, micro- and macro-columns. These three levels of physical structure are considered as subzones of the zone I. In the figure 8 are sketched these structural units.

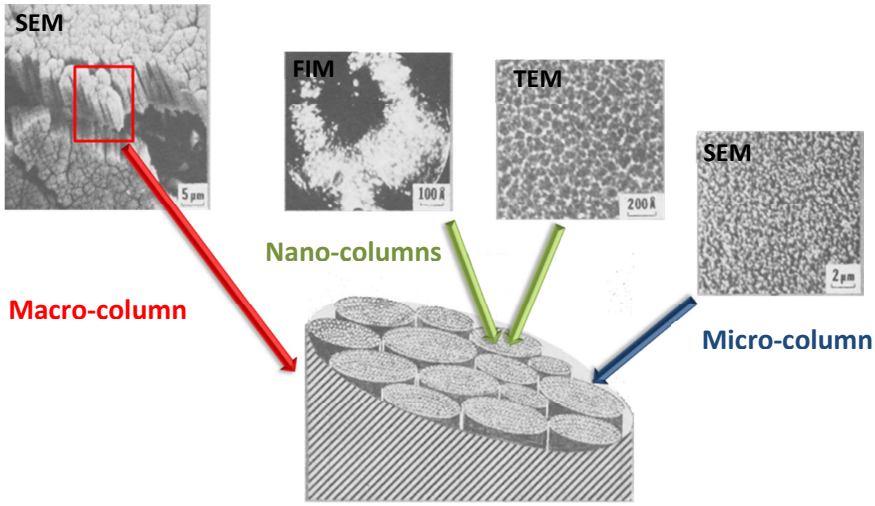

Figure 8: Structural units of a film grown under low mobility conditions (zone I).

In 2006, Mahieu et al. [15] reported a structure zone model with a revision in the zone I, the zone with lowest adatom mobility. The model is divided in five zones.

- Zone Ia: The atoms have very low mobility, and they stick at the same place where they hit the substrate. This is known as ballistic deposition. The only parameter affecting the growth is the incoming direction of the atoms. A columnar structure separated by voids is obtained mainly caused by shadowing effect, resulting in a coating with a density lower than the density of bulk material.
- Zone Ib: Under the same deposition condition as in the zone Ia but with continuous bombardment by energetic species (delivery of kinetic energy to the film). The voids are filled by particles and a more dense columnar structure is obtained. The film is amorphous–like. It is not possible to pass from zone Ia into zone Ib by increasing the temperature. The increase of temperature does not result in filling the voids, leading to other kind of structure (zone Ic). The mobility of atoms is controlled by direct impact not by thermal effects.

- Zone Ic: It takes place the self-shadowing diffusion where the atoms cannot diffuse from one column (grain) to another. The voids between columns are filled due to the increased mobility of atoms and the columns are separated by grain boundaries. The columns can only compete with each other by shadowing.
- Zone T: The diffusion of atoms from one grain to another is allowed. The competitive growth of neighboring grains should occur in an evolutionary way. The immobility of grain boundary is still prohibited. V-shaped and faceted columns are proposed.
- Zone II: A columnar structure with approximately straight columns throughout the whole film thickness will be formed. Due to rapid surface diffusion and the appearance of crystallization, shadowing has a minor influence on growth. Increasing the temperature increases the effect of recrystallization and restructuring, thus increasing the lateral size of the resulting columns.

In the following figure is represented the structure in every zone:

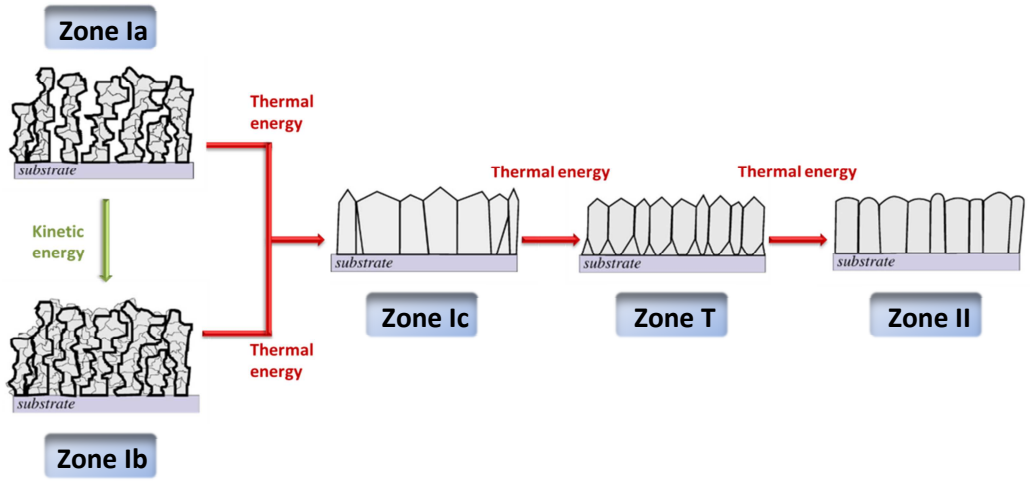

Figure 9: Structure zone model proposed by Mahieu et al.

Due to the development of new deposition and characterization techniques, it is necessary to modify the previous SZMs to include new deposition parameters in the model. High

power impulse magnetron sputtering (HIPIMS) is a novel deposition technology with a great interest in industrial applications. To include the deposition parameters related in this tech nique, recently in the year 2010, a new model has been proposed by Anders [16]. This model is an extension and modification of the Thornton´s model in which several changes have been proposed:

- Replace the linear T_h axis with a generalized temperature T^* which includes T_h and a temperature shift caused by the potential energy of particles arriving on the surface.
- Replace the linear pressure axis with a logarithmic axis for a normalized energy E^*, describing displacement and heating effects caused by the kinetic energy of bombarding particles.
- The z-axis represents the net film thickness t^* indicating the thickness reduction by densification and sputtering or the representation of " negative thickness values" by ion etching.

In the figure 10, it is represented the sketch of this model.

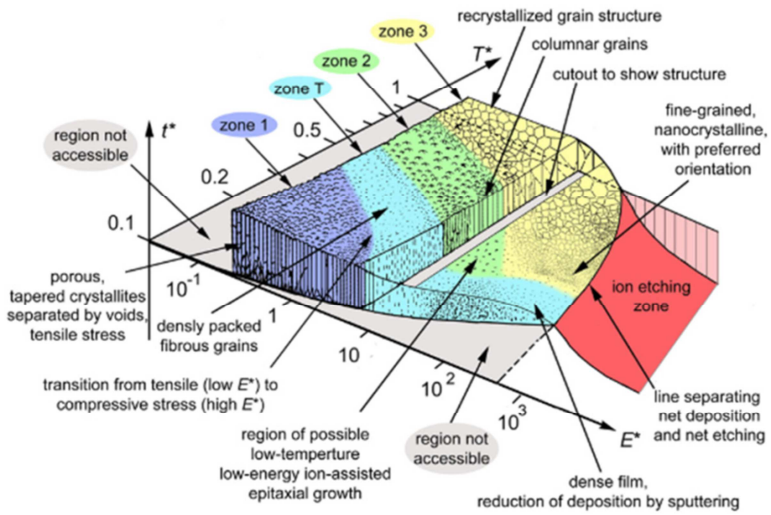

Figure 10: Structure zone model proposed by Anders.

References

1. Saraiva, M. Sputter Deposition of MgO Thin Films: The Effect of Cation Substitution. (Universiteit Gent, 2012). at <http://vs08154.virtualserver.priorweb.be/File/1204_PhD_Saraiva_reduced.pdf>

2. NASCAM (NAnoSCAle Modeling) User's manual— Université de Namur. at <http://www.unamur.be/sciences/physique/pmr/telechargement/logiciels/nascam>

3. Barna, P.B. and Adamik, M. *Science and Technology of Thin Films*. (World Scientific Publishing Co.Pte.Ltd., 1995).

4. Venables, J., Spiller, G. & Hanbucken, M. Nucleation and Growth of Thin-Films. *Rep. Prog. Phys.* **47,** 399–459 (1984).

5. Movchan, B. & Demchish.av. Study of Structure and Properties of Thick Vacuum Condensates of Nickel, Titanium, Tungsten, Aluminium Oxide and Zirconium Dioxide. *Phys. Met. Metallogr.-Ussr* **28,** 83–& (1969).

6. Nieuwenhuizen, JM. & Haanstra, H. Microfractography of Thin Films. *Philips Tech. Rev.* **27,** 87–& (1966).

7. Lichter, S. & Chen, J. Model for Columnar Microstructure of Thin Solid Films. *Phys. Rev. Lett.* **56,** 1396–1399 (1986).

8. Meakin, P. Ballistic Deposition Onto Inclined Surfaces. *Phys. Rev. A* **38,** 994–1004 (1988).

9. Tait, R., Smy, T. & Brett, M. Modeling and Characterization of Columnar Growth in Evaporated-Films. *Thin Solid Films* **226,** 196–201 (1993).

10. Hodgkinson, I., Wu, Q. H., Knight, B., Lakhtakia, A. & Robbie, K. Vacuum deposition of chiral sculptured thin films with high optical activity. *Appl. Opt.* **39,** 642–649 (2000).

11. Alvarez, R. *et al.* Theoretical and experimental characterization of TiO2 thin films deposited at oblique angles. *J. Phys. -Appl. Phys.* **44,** 385302 (2011).

12. Thornton, J. High-Rate Thick-Film Growth. *Annu. Rev. Mater. Sci.* **7,** 239–260 (1977).

13. Mattox, D. M. *Handbook of Physical Vapor Deposition (PVD) Processing*. (William Andrew, 2010).

14. Messier, R., Giri, A. & Roy, R. Revised Structure Zone Model for Thin-Film Physical Structure. *J. Vac. Sci. Technol. -Vac. Surf. Films* **2,** 500–503 (1984).

15. Mahieu, S., Ghekiere, P., Depla, D. & De Gryse, R. Biaxial alignment in sputter deposited thin films. *Thin Solid Films* **515,** 1229–1249 (2006).

16. Anders, A. A structure zone diagram including plasma-based deposition and ion etching. *Thin Solid Films* **518,** 4087–4090 (2010).

Appendix IV

STEM-EELS analysis reveals stable high-density He in nanopores of amorphous silicon coatings deposited by magnetron sputtering

Nanotechnology 26 (2015) 075703 (10pp)

doi: 10.1088/0957-4484/26/7/075703

Roland Schierholz[a,b,*], Bertrand Lacroix[a], Vanda Godinho[a], Jaime Caballero-Hernández[a], Martial Duchamp[c] and Asunción Fernández[a,*]

[a] Instituto de Ciencia de Materiales de Sevilla, CSIC-Univ. Sevilla, Avda. Américo Vespucio 49, 41092 Sevilla, Spain

[b] Institut für Energie- und Klimaforschung, Grundlagen der Elektrochemie (IEK9), Forschungszentrum Jülich GmbH, 52425 Jülich, Germany

[c] Ernst Ruska-Centre for Microscopy and Spectroscopy with Electrons, Forschungszentrum Jülich GmbH, 52425 Jülich, Germany

* rolandschierholz@gmx.de, asuncion@icmse.csic.es

Abstract

A broad interest has been showed recently on the study of nanostructuring of thin films and surfaces obtained by low-energy He plasma treatments and He incorporation via magnetron sputtering. In this paper spatially resolved electron energy-loss spectroscopy (EELS) in a scanning transmission electron microscope (STEM) is used to locate and characterize the He state in nanoporous amorphous silicon coatings deposited by magnetron sputtering. A dedicated MATLAB program was developed to quantify the helium density inside individual pores based on the energy position shift or peak intensity of the He K-edge. A good agreement was observed between the high density ($\sim 35 - 60\ at/nm^3$) and pressure ($0.3 - 1.0\ GPa$) values obtained in nanoscale analysis and the values derived

from macroscopic measurements (the composition obtained by proton backscattering spectroscopy coupled to the macroscopic porosity estimated from ellipsometry). This work provides new insights into these novel porous coatings, providing evidence of high-density He located inside the pores and validating the methodology applied here to characterize the formation of pores filled with the helium process gas during deposition. A similar stabilization of condensed He bubbles has been previously demonstrated by high-energy He ion implantation in metals and is newly demonstrated here using a widely employed methodology, magnetron sputtering, for achieving coatings with a high density of homogeneously distributed pores and He storage capacities as high as $21\ at.\%$.

Keywords: spatially resolved EELS, spectrum imaging, magnetron sputtering, amorphous porous silicon coatings, closed nanopores, condensed He bubbles, reduced refractive index

Introduction

The introduction of porosity in nanomaterials has been a topic of increasing interest over the last decade, and research efforts have been focused on the synthesis and characterization of newly designed porous and nanostructured materials. A fundamental understanding of the nanostructure permits the control and design of porous materials with tailored functionalities. Among many others, porous silicon currently remains one of the most actively researched materials for diverse applications such as sensors, photonic devices, microelectronics and solar energy conversion [1–6]. Being fully compatible with the established microelectronics technology, the most attracting feature of porous silicon is the wide range of refractive indexes that can be achieved by varying the percentage of porosity. In a recent work, we proposed a new bottom-up approach to prepare porous silicon coatings by magnetron sputtering as an alternative route to the traditional electrochemical-based processes [7]. In that work, we demonstrated the possibility of producing porous silicon coatings with tailored refractive indices (from 3.75 to 4.75 at $500\ nm$) using magnetron sputtering with He or Ar as the process gas [7,8]. In addition to the advantages of the well-known industrial scale-up of the magnetron sputtering process, our

procedure provides many possibilities for the design and production of various devices alternating for example dense and porous layers, intrinsic or doped silicon, etc. [7]. The low-refractive-index coatings produced exhibit a microstructure of closed pores that can be oriented to the coating's growing direction. In this previous work [7], the incorporation of a high He amount (up to $30\ at.\%$) inside the coatings was detected by proton backscattered spectroscopy, and it was proposed that He was most likely trapped inside the closed pores during deposition [7,8]. In fact, in another previous paper, we used spatially resolved electron energy-loss spectroscopy (EELS) in a scanning transmission electron microscope (STEM) to demonstrate that amorphous porous SiN_xO_y coatings can be prepared by magnetron sputtering, revealing closed pores containing molecular N_2 inside [9].

At this point of the research, the challenge in the present work is to investigate the location of the He in the porous Si coatings as well as to quantify the helium with nano-scale resolution using the STEM/EELS methodology available in the TEM facilities of our laboratory. The incorporation of He in metals has been well investigated due to its importance in nuclear technology. Ion implantation has been used to re-create the conditions of the reactors mainly to investigate damage caused in materials. In these works, the extremely low solubility of He in metals has been reported to be the cause of the formation of He bubbles during ion implantation [10–12]. In most of these works, helium implanted in crystalline materials leads to the formation at a certain depth of a layer of largely dispersed bubbles with diameters ranging from 2 to $25\ nm$. EELS was used for the evaluation of helium density inside these bubbles. The first approach was to use the blue shift of the He $1s \rightarrow 2p$ transition as a function of He density [10,13]. Later, spatially resolved EELS was reported to be able to record spectra of single bubbles by several authors [12,14–16]. The advantage here is that the helium density can be retrieved at the nanoscale using two different methods. One method uses the integrated intensity under the He K-edge, and the other uses the already mentioned energy shift of the $1s \rightarrow 2p$ transition. A description of both methods is given in reference [12] (and the references therein). The first aim of the work presented here was to apply a similar STEM/EELS methodology to confirm that the He incorporated in the amorphous silicon coatings prepared by magnetron sputtering remains

inside the closed pores and, if so, to characterize the physical parameters (density, pressure) of He. Both goals were accomplished, as described in this paper, and an *ad hoc* MATLAB routine was also developed. Additionally, we compare the values for the He density obtained inside the microscope to the values estimated from macroscopic measurements. Note that our results presented in this paper reveal similar stabilization of condensed He in the nanopores (He densities of $\sim 30 - 50\ at/nm^3$) as that previously demonstrated in bubbles formed by high-energy He ion implantation in metals [12,14–16]. A high amount of He can therefore be stored and stabilized at room temperature inside the closed pores. To store a similar density in a macroscopic tank at room temperature, pressures of approximately $1\ kbar$ would be required [17].

To re-create the conditions of the cold plasma in contact with the nuclear reactor walls, some researchers have artificially introduced He in different metals using also magnetron sputtering in He/Ar mixtures [18–20]. More recently the exposure to He plasmas and He incorporation via magnetron sputtering have also been presented as a route for nanostructuring metals [21–23]. In all these articles, although the presence of He and nanopores was reported by TEM images, no quantification of the He condensed state was provided. At this point, it is important to emphasize the relevance of the present work that newly demonstrates that coatings can be prepared by magnetron sputtering containing a high density of homogeneously distributed pores filled with helium in a condensed state.

Experimental

Deposition details

In our previous work [7] we showed the dependence of the pore size and distribution on several deposition parameters of the magnetron sputtering deposition. Based on this information, a deposition power of $300\ W$ in radiofrequency (RF) was selected in this paper to obtain rather large and separated pores to facilitate the individual pore analysis by

STEM/EELS (see the micrograph shown in figure 1). The magnetron head was placed at a $30°$ angle to the normal of the substrate at a distance of $5\ cm$ (see the inset in figure 1 left).

For comparison purposes a dense coating was also deposited using $150\ W$ in RF-mode and a substrate bias of $100\ V$. Both, the dense and porous amorphous silicon coatings, were deposited from a pure Si target (Kurt J Lesker $99.999\ \%$ pure). Before deposition the base pressure was $10^{-4} Pa$. The porous coating was deposited at p(He)$= 4.8\ Pa$, while the dense coating was deposited at p(Ar)$= 1.3\ Pa$. Silicon (100) and quartz were used as substrates. Table 1 summarizes the deposition conditions and labels for the studied samples.

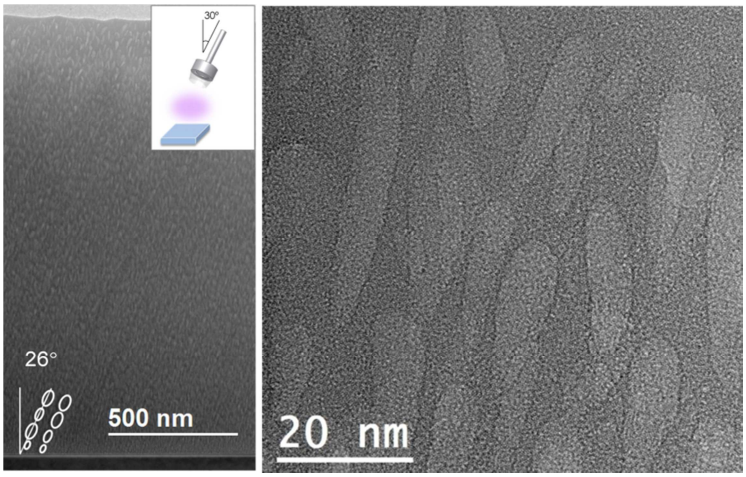

Figure 1: Left: TEM cross-sectional view of sample a-pSi(300). Insets: Deposition geometry and pore orientation schemes. Right: Details of high resolution showing pores shapes.

Table 1: Deposition parameters and deposition rate calculated from SEM measurements.

Sample	RF power (W)	Dep. gas	Pressure (Pa)	Sub. bias (V)	Dep. rate (nm/min)
a-pSi(300)	300	He	4.8	---	28.7
a-Si(150)(bias)	150	Ar	1.3	100	13

Characterization of the coatings

The thickness of the coatings was examined using scanning electron microscopy (HITACHI S-4800 SEM-FEG) working at $2\ kV$ on fractured samples without any conductive coating.

The microstructure of the coatings was investigated by transmission electron microscopy (TEM) using a FEI Tecnai F30 microscope operated at $300\ kV$ equipped with a Gatan GIF Quantum 963 energy filter at the Laboratory of Nanoscopies and Spectroscopies (LANE-ICMSE, Sevilla, Spain). Cross-sectional TEM specimens of the coatings deposited on Si substrates were prepared using the conventional approach by mechanical polishing and dimple grinding followed by Ar^+ ion milling until electron transparency was attained. The quantitative STEM/EELS analysis of individual nano-pores of highly porous coatings requires the preparation of thin lamella of less than $100\ nm$ thickness, which should include closed filled pores. However, overlap of pores should be avoided, and very small pores will make the STEM/EELS analysis of individual pores more difficult. In this sense the porous sample deposited at $300\ W$ is very adequate as shown in figure 1.

The compositions of the thin films were evaluated using proton backscattering spectrometry (p-BS) at the National Center for Accelerators (CNA, Sevilla, Spain) using a $3\ MV$ tandem accelerator. The spectra were obtained using two different energies, 1.0 and $2.3\ MV$, for the proton beam and a surface barrier detector set at $165°$. To obtain the thickness and composition of the films, both spectra were simultaneously simulated for every sample using the SIMNRA code [24] (see more details in reference [7])

The optical characterization was performed on coatings on quartz substrates in a UVISEL spectroscopic ellipsometer from HORIBA Jobin Yvon with an incidence angle of $60°$ and a wavelength range of $563 - 1550\ nm$. The data were analyzed using the Deltapsi2 software developed by HORIBA Jobin Yvon.

STEM-EELS spectrum imaging data analysis

Annular dark field scanning transmission electron micrographs (ADF-STEM) and spatially resolved electron energy loss-spectra (EELS) were recorded simultaneously in the Tecnai F30 on single pores of various diameters. The spectrum images were acquired in the low-loss region with a pixel size of $1\ nm$ using subpixel scanning ($16 * 16$). At each position, an EELS spectrum of $2048\ pixels$ of length with energy dispersion of $0.05\ eV/channel$ was recorded using an integration time between 0.05 and $0.07\ s$.

The He K-edge peak corresponding to the $1s$ to $2p$ transition was placed at approximately $22\ eV$ on the high energy tail of the Si plasmon at approximately $17\ eV$ [25]. To process the EELS spectrum image dataset and extract the He signal, a MATLAB program was developed based on the method described in reference [12]. A version of this program is provided in the supporting information section. First, the raw data were aligned with the zero loss peak (ZLP) and subjected to multivariate statistical analysis (MSA) [26] to remove the statistical noise. The plural scattering distribution was then removed from the spectra using Fourier-log multiple scattering deconvolution (Program FLOG [27]). The specimen thickness map was calculated using the log-ratio method [27] using the mean free path calculated using the IMFP routine [27]. Using our experimental conditions, a mean free path of $\lambda = 145\ nm$ was obtained using the Malis equation [28]. The contribution of the Si plasmon was fitted with the function given in eq. 1 from reference [29]:

$$I = \frac{a\ E}{\left(E^2 - E_p^2\right)^2 + \left(E\ \Delta E_p\right)^2} \qquad [1]$$

Here, E_p represents the plasmon energy, ΔE_p corresponds to the peak width, and a represents the amplitude. To improve the He signal extraction, a second peak was required at energies higher than $23\ eV$. This contribution may be due to surface oxide SiO_2 or carbon contamination (both at approximately $24\ eV$). These two plasmon contributions were fitted simultaneously to the data in two ranges (from 16 to $20.5\ eV$ and from 23.5 to $40\ eV$) on both sides of the He-K edge. During the fit, the E_p value of the second plasmon was fixed

between 23 and 25 eV. The sum of these two contributions (Si and SiO_2 plasmon) is referred to as the background signal for the He-K edge. After subtraction of the background signal, the residual signal was fitted in the He K-edge range from 20.5 to 23.5 eV. For the He $1s \rightarrow 2p$ transition, a simple Gaussian function was used for fitting as this function was reported to yield good results [12]. An example of the fitting procedure will be shown below in the "Results and Discussion" section (figure 3 (c)).

To quantify the atomic density of He at each position of the spectrum image, two methods were used. In Method 1 [12], the He density n_{He} is given by:

$$n_{He} = \frac{I_{He}}{I_{ZLP}} \frac{1}{d\,\sigma_{He}} \quad [2]$$

where I_{ZLP} and I_{He} are the integrated intensities of the zero loss peak (ZLP) and the He K-edge, respectively. σ_{He} is the cross-section of the He $1s \rightarrow 2p$ transition, which was calculated using the program Sigmak3 [27]. For our experimental conditions (acceleration voltage of $300\,keV$, convergence semi-angle $\alpha = 12.4\,mrad$, collection semi-angle $\beta = 9.6\,mrad$, and integration range of 3 eV), we obtained $\sigma_{He} = 6.4 \cdot 10^{-24}\,m^2$. d is the pore thickness at the pixel position. This latter value was evaluated as the complement of the specimen thickness at each particular pixel compared with the value at a reference pixel outside the pores. This method was suggested in references [14,15] and was cross-checked using the STEM-ADF image contrast assuming a uniform ellipsoidal volume of the pores perpendicular to the growing direction. The results of I_{He} and I_{ZLP} were stored in 2D maps, and the map of He density was calculated using these parameters.

To confirm these measurements, another method (Method 2) was used for comparison. This method relies on the linear relationship between the blue energy shift (ΔE_{He}) of the He K-edge compared with its position for the free atom (21.218 eV, reference [30]) and the helium density (n_{He}):

$$\Delta E = C \times n_{He} + \delta \quad [3]$$

where C and δ are constants. The energy shift is attributed to the short-range Pauli repulsion between electrons of the neighboring atoms [13]. In this work, we assume that the He density inside the pores will follow a similar linear law. In the literature, some discrepancies in C and δ values can be observed [10,12,14,15], and we used two extreme values of C. Method 2(a) uses $\Delta E = 0.015\, n_{He} + 0.45$ [15], and Method 2(b) uses $\Delta E = 0.044\, n_{He} + 0.07\, eV$ [14]. Finally, the He pressure p_{He} inside the pores can be estimated from the n_{He} values provided by the two methods using a suitable equation of state (EOS) [11,12] depending on the He density range.

Results and discussion

Porous silicon coating with reduced refractive index

Figure 1 shows the microstructure of the investigated porous coating (a-pSi(300), which consists of a highly porous structure of closed pores oriented in the magnetron direction (figure 1, left). The high-resolution TEM image (figure 1, right) shows the shape of the pores in detail and reveals the amorphous structure of the Si-matrix. With a RF power of $300\ W$ supplied to the magnetron, an increase in pore size is observed compared with the coatings reported in the previous work [7]. Pores with diameters ranging from 2 to $60\ nm$ can be observed for the a-pSi(300) coating. The pores exhibit similar minor diameters as the ones in previous samples [7] (average size of $9 \pm 2\ nm$), while the major diameters are larger.

The proton backscattering (p-BS) spectrum of this sample is compared with that of the dense sample in figure 2. A strong signal corresponding to He inside the coating is observed in the porous sample, corresponding to a He amount of $21\ at.\%$ (see table 2). In addition to Si, the dense sample, a-Si(150)(bias), which was deposited under Ar atmosphere with a voltage applied to the substrate, shows a small signal corresponding to the incorporation of Ar. The incorporation of Ar in samples deposited by magnetron sputtering with an applied substrate bias has been reported previously by other authors [31]; nevertheless, this incorporation does not result in the introduction of porosity (details concerning the microstructure of this dense coating are provided in reference [7]).

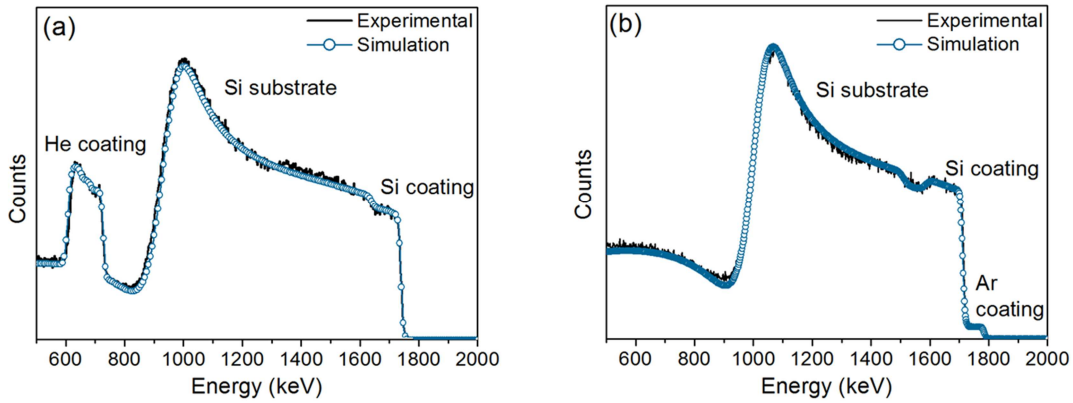

Figure 2: Proton backscattering spectroscopy of (a) porous sample a-pSi(300) and (b) dense sample a-Si(150)(bias).

Table 2: Thickness and chemical composition as given by p-BS.

Sample	Thickness $(10^{15}\ at/cm^2)$	Si $(\%\ at.)$	He $(\%\ at.)$	Ar $(\%\ at.)$
a-pSi(300)	11000	79	21	---
a-Si(150)(bias)	9500	94	---	6

The introduction of porosity leads to a decrease of both the refractive index and extinction coefficient. Table 3 summarizes the values of the refractive indices and damping constants of both coatings at $605\ nm$. Using the effective medium approximations [32], one can express the relative electrical permittivity of the porous coating, a heterogeneous media ($\varepsilon_{r,eff}$), as a function of the dielectric constants of the continuous matrix ($\varepsilon_{r,c}$) and dispersed phase ($\varepsilon_{r,d}$) and the volume fraction (ϕ) occupied by the pores (eq. 4, reference [32]):

$$\varepsilon_{r,eff} = \varepsilon_{r,c}\left(1 - \frac{3\,\phi\,(\varepsilon_{r,c} - \varepsilon_{r,d})}{2\,\varepsilon_{r,c} + \varepsilon_{r,d} + \phi\,(\varepsilon_{r,c} - \varepsilon_{r,d})}\right) \qquad [4]$$

We calculated the dielectric constant, $\varepsilon = n^2 - k^2$, using the values of n and k measured by ellipsometry at $605\ nm$, as listed in Table 3 and derived a porosity of $22\ \%$ for the

porous coating a-pSi(300) assuming that the dielectric constant of the matrix is similar to that of a-Si(150)(bias) and setting $\varepsilon_{r,d}$ for the pores to 1 [33].

Table3: Refractive index at $605\ nm$ and porosity fraction calculated from effective medium approach in equation 4. The porosity is calculated using a-Si(150)(bias) as reference for the matrix.

Sample	n $(605\ nm)$	k $(605\ nm)$	ε_r $(605\ nm)$	ϕ (%)
a-pSi(300)	3.74	0.1	13.98	22.2
a-Si(150)(bias)	4.38	0.25	18.86	

Extraction of the He EELS signal and evaluation of physical parameters (density, pressure)

In figure 1, it is possible to observe some isolated pores in which the spatially resolved EELS analysis could be performed. Figure 3 (a) presents the ADF-STEM signal acquired in parallel with the spectrum image, which encloses an isolated pore. Therefore, an EELS spectrum corresponds to each one of the $1 \times 1\ nm^2$ pixels in the image. In the ADF signal, the matrix with higher atomic number and scattering cross section appears bright, and the pores appear dark. In figure 3 (b), three EELS spectra corresponding to three selected pixels at the center, the border and outside of the pore are presented with a vertical shift for comparison purposes.

For the selected pixel $(16,10)$, which corresponds to a zone outside the pore, the low loss spectrum contains a peak corresponding to the Si plasmon at $17\ eV$ [25]. Moving toward the pore, pixel $(5,10)$ at the border, a small peak at approximately $22\ eV$ begins to appear that becomes stronger at the center of the pore, pixel $(6,13)$. This superimposed peak corresponds to the He K edge [25], confirming the presence of He inside the pores.

To characterize the physical parameters of He in the coating, the signal of the He K-edge at each position was extracted from the EELS spectra following the procedure described in detail in section 2.3 (see also the MATLAB program in the supporting information). To illustrate the method, fits of the background signal for the matrix position outside $(16,10)$ and inside $(6,13)$ the pore are presented in figures 3 (c) and 3 (d). This background signal

includes the peak of the Si plasmon as well as another peak for the surface SiO_2 component. The figures also show the residual signal obtained by subtraction of the background and experimental spectra. Note that the He signal at approximately $22\ eV$ is clearly visible in the residual signal inside the pore (figure 3 (d)), while a flat line is observed above $16\ eV$ for the position outside the pore (figure 3 (c)). These results clearly validate our fitting procedure for the extraction of the He signal. The two additional features in the residual signal at energies of approximately 5 to $10\ eV$ (figure 3 (c)) and 10 to $15\ eV$ (figure 3 (d)) can be attributed to the Si/SiO_2 interface plasmon [16,34] and the cavity plasmons [16], respectively.

Figure 4 illustrates the methods used to evaluate the He density inside the pores. Using our MATLAB routine (see supporting information) and following the procedures described above, the extracted helium signal was fit with a Gaussian function (figure 3 (d)), and the corresponding integrals of the He intensity (I_{He}) and energy shift (ΔE_{He}) relative to the He free atom value were stored in 2D maps (see figures 4 (a) and 4 (e)). As demonstrated on the elemental intensity map (figure 4 (a)), helium is located inside the nanopore volume. The local specimen thickness at each pixel position is indicated in figure 4 (b). The pore thickness map (figure 4 (c)) was prepared by selecting the pixel $(17,9)$ as a reference for the specimen thickness ($t_{ref} = 38.8\ nm$). In this case, a maximum value of $6.5\ nm$ was observed for the pore thickness, which is comparable to the minor axis of the ellipsoidal pore ($7\ nm$) measured on the ADF-image in figure 3 (a). Using the results of the He intensity and pore thickness, it was possible to prepare the helium density map as described in Method 1 (see eq. 2) and presented in figure 4 (d). By considering only the pixels close to the pore center (to avoid surface effects) [14], the density inside the pore ranges from 25 to $54\ at/nm^3$, and a mean density of $36\ at/nm^3$ was measured. The decreasing of n_{He} from the top to the bottom of the pore can be explained by He desorption under electron irradiation, as reported by David et al. [15,16] during STEM recording of the spectrum imaging data.

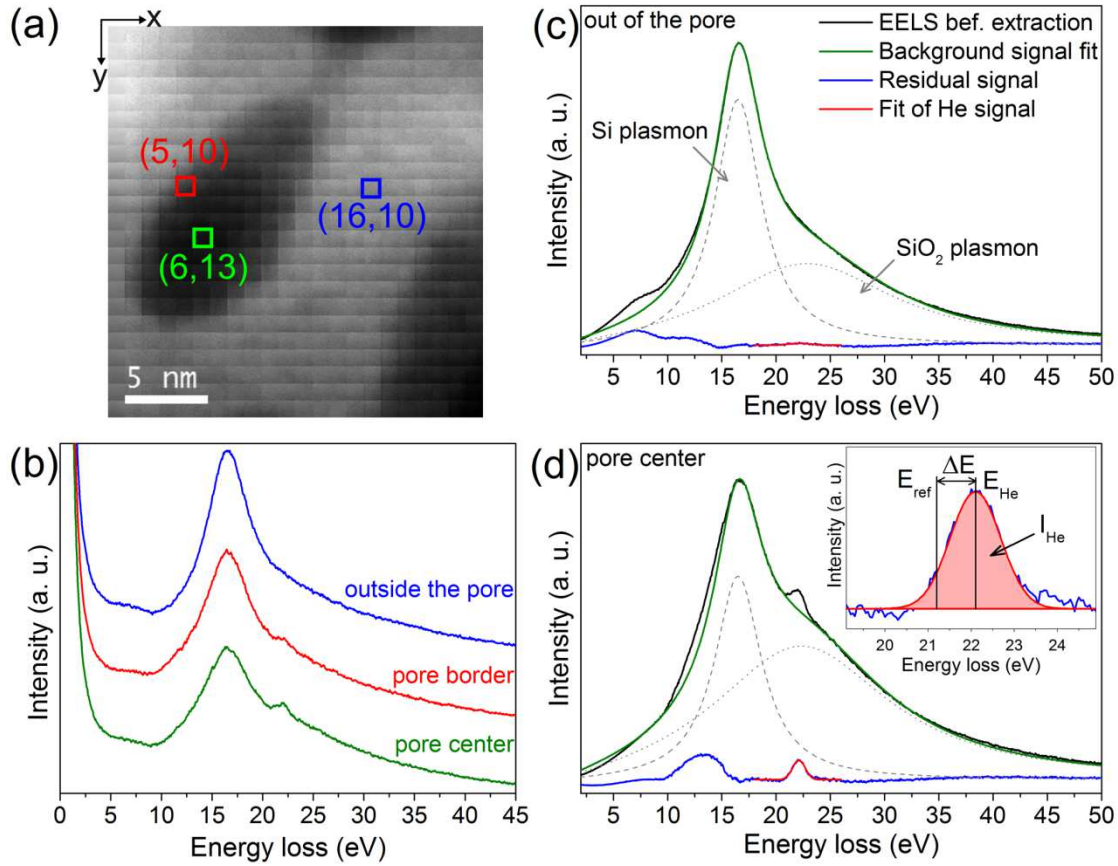

Figure 3: (a) STEM-ADF image recorded in the vicinity of one isolated pore. (b) Low loss EELS spectra plotted for the various (x,y) positions indicated in (a) (at the center, at the border and outside the pore). (c) and (d) Fitting analysis of the EELS spectra recorded outside and inside the pore. The green line corresponds to the fit of the main background signal (the dashed lines are the Si and SiO_2 fitted components). The blue curve represents the residual signal containing the He K-edge at approximately 22 eV (only visible inside the pore). The fit of the He K-edge using a Gaussian function is plotted in red (see also details in the inset in (d)).

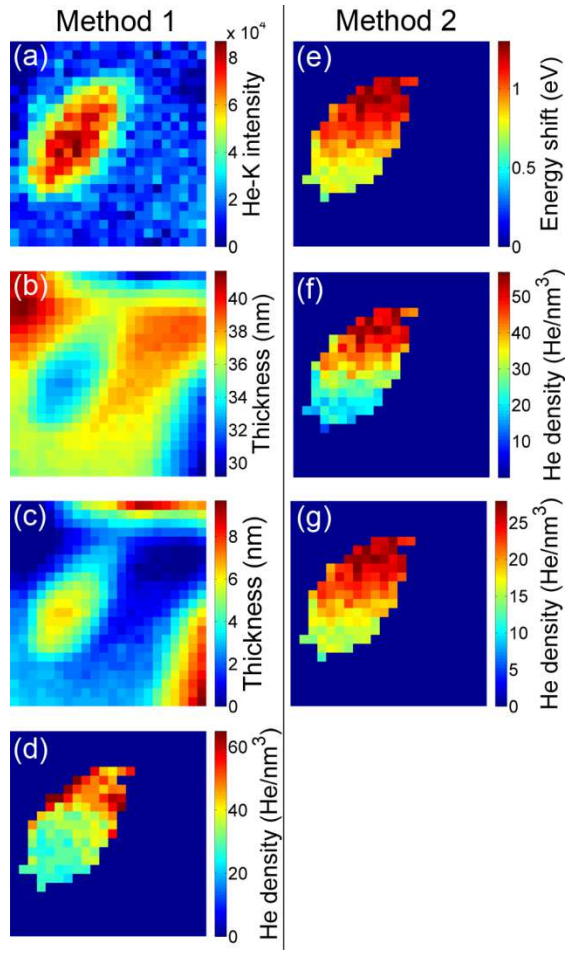

Figure 4: (a) Helium elemental map (He-K edge integrated intensity I_{He} map). (b) Specimen thickness map. (c) Pore thickness map. The pixel (17,9), close to the center of the spectrum image was selected as a reference for the specimen thickness ($t_{ref} = 38.8\ nm$). (d) He density map n_{He} obtained using Method 1. (e) Energy shift map of the He-K edge, ΔE_{He}, relative to the free atom energy ($21.218\ eV$). (f) He density map n_{He} obtained using Method 2a. (g) He density map n_{He} obtained using Method 2 (b). To improve the clarity, the pixels outside the pore (of low He-K intensity) have been removed in (d), (e), (f) and (g).

Following Method 2 (described in section 2.3), figure 4 (e) shows the local energy shift ΔE of the He K-edge from the value of the free atoms [30]. Figures 4 (f) and 4 (g) present the corresponding He-density maps calculated according to eq. 3 using Methods 2 (a) [15] and 2

(b) [14]. By comparing figures 4 (d), 4 (f) and 4 (g), a good agreement between the He density obtained using Methods 1 and 2 (a) is observed.

Table 4 summarizes the n_{He} values obtained in two different pores using the above mentioned methods for the characterization of the He state in porous a-Si coatings deposited by magnetron sputtering. For the two pores, a good agreement is observed for the He density using Methods 1 and 2 (a), which provides a good indication of the reliability of our procedure. Even if different authors agree on the linear character of ΔE and n_{He} dependence, the values given for C vary significantly [10,12,14,15]. For our density range (approximately $20 - 70\ at/nm^3$), we believe that the system is better described using Method 2 (a) because the law given by David *et al.* [15] was established for a significant number of recorded data in the $20 - 100\ at/nm^3$ range. The law given by Taverna *et al.* [14] (Method 2 (b)) was determined using smaller He densities, $10 - 40\ at/nm^3$, and thus does not completely describe our system. This idea is supported by Lucas and co-workers [13], who observed that the C value is also dependent on temperature and density.

Table 4: He density and pressure measured inside two studied pores. The maximum, minimum and mean values of the He density were determined over a selection of pixels close to the center of the pores to avoid surface effects [14]. Pore#1 refers to the pore presented in figures 3 and 4, and Pore#2 refers to another pore analyzed for comparison.

Pore	Method	n_{He} max (at/nm^3)	p_{He} max (GPa)	n_{He} min (at/nm^3)	p_{He} min (GPa)	n_{He} mean (at/nm^3)	p_{He} mean (GPa)
Pore#1	1	54 ± 20	0.8	25 ± 7	0.2	36 ± 20	0.3
	2 (a)	54 ± 24	0.8	18 ± 12	0.1	36 ± 10	0.3
	2 (b)	27 ± 11	0.2	15 ± 9	0.1	21 ± 4	0.1
Pore#2	1	76 ± 35	2.0	31 ± 7	0.3	45 ± 35	0.5
	2 (a)	76 ± 32	2.0	39 ± 20	0.4	59 ± 9	1.0
	2 (b)	35 ± 12	0.3	22 ± 10	0.1	29 ± 4	0.2

Knowing the density of He inside the pores, the internal pressure becomes a relevant parameter to be determined. At higher atomic densities, the ideal gas law is inaccurate.

Walsh [12] discussed different semi-empirical equations of states (EOSs) to calculate the He pressure inside the pores from the measured n_{He}. For our density range, the Trinkaus EOS [11] is the most suitable. The maximum, minimum and mean He density values described before were used to calculate the He pressure, and the results are presented in table 4. Using Method 1 and 2 (a) for the first pore (Pore#1, presented in figures 3 and 4), a mean pressure of $0.3\ GPa$ was determined, and the pressure locally reaches up to $0.8\ GPa$. In the second pore investigated (Pore#2), higher mean pressure values of 0.5 and $1\ GPa$ were observed, and the pressure locally reaches up to $2\ GPa$. These differences in the two pores are not necessarily significant considering the large uncertainties of the He density measurements that mainly originate from the difficulty of accurately measuring the local pore thickness and from He desorption during the measurements. Nevertheless, these local measurements provide a good indication that the He pressure inside the pore is in the GPa range, which is several orders of magnitude higher than the pressure in the deposition chamber, $p_{He} = 4.8\ Pa$.

Therefore, the obtained values should be taken as representative values of the He state in the coatings. To our knowledge, these results reveal for the first time that He can be stabilized in a condensed state inside the nano-pores of amorphous silicon coatings prepared by magnetron sputtering.

Comparison with macroscopic results

The methodology presented in the previous section is based on the direct nanoscale detection of the He signal in the amorphous silicon coatings. The use of spatially resolved EELS with nanometer-scale resolution coupled with the analysis of the data cube matrix allowed us to measure the He density inside the pores with nanometer resolution. As additional information, we propose here a strategy to determine an average value of the He density inside the pores using macroscopic measurements.

Accordingly, one must first assume a homogeneous distribution of pores in the coating and considering the porosity fraction, $\phi = 22\ \%$, calculated using the Maxwell-Garnett

equation (eq. 4) and presented in table 3, $1\,nm^3$ of the porous coating corresponds to $0.22\,nm^3$ of the pore volume (and $0.78\,nm^3$ of the dense matrix). Considering the density of dense crystalline silicon, we can calculate a reference value of 50 Si atoms per nm^3 for the dense matrix. The total number of Si atoms in $1\,nm^3$ of porous silicon is therefore $0.78 \times 50 = 39$ Si atoms. Knowing the coating composition as measured by p-BS ($79\,\%$ Si and $21\,\%$ He), the He amount per nm^3 of porous silicon coating is 10 atoms of He. From the results in the previous section, evidence is provided that all the He is inside the pores; therefore, a He concentration inside the pores of $45.5\,at/nm^3$ can be calculated. This average value calculated from macroscopic measurements is in good agreement with our mean values obtained at the nanoscale using EELS on different pores (see table 4). The macroscopic value is most likely overestimated because the density of crystalline silicon was assumed for the calculation.

Conclusions

Spatially resolved EELS was used here for the first time on a-Si coating with closed porosity formed during deposition by magnetron sputtering, demonstrating the helium trapping inside the pores. A good compromise between the adequate deposition conditions and proper TEM sample preparation (thin enough for analysis without pores overlapping but not too thin to have individual closed pores in the field of view) is relevant for the use of the methodology present in this work.

The MATLAB program developed to extract the He signal proved to be a valuable procedure, and the results of the integrated He-K peak intensity and energy shift were used to calculate the He density, n_{He}, inside the pores in the form of 2D maps. This program is provided in the supporting information section of this article. A good agreement was observed between the results of Method 1 and Method 2 (a), demonstrating the reliability of the analysis. The He pressure inside the pores was calculated, being very high in the GPa range, while the He working gas pressure during deposition was only a few Pa.

A strategy is proposed to provide a rough estimate of the He density in the pores from the bulk proton backscattering measurements coupled to porosity estimations from ellipsometry. The results are on the same order of magnitude as those calculated from spatially resolved EELS measurements.

This study provides new insights on the trapping of gas inside closed porosity formed by magnetron sputtering deposition. Amorphous silicon coatings can be prepared containing a high density of homogeneously distributed pores with He storage capacities as high as $21\ at.\%$ at room temperature using a widely used methodology such as magnetron sputtering. In our previous work [7], we also described other experimental deposition parameters that could be used to obtain more than $30\ at.\%$ He. Our work newly demonstrates that He is located inside the nano-pores in a condensed state for coatings prepared by magnetron sputtering. Several applications can be envisaged considering that magnetron sputtering is also one of the most common methods in the vacuum-based deposition coating industry. The tuning of the refraction index was already mentioned as fundamental for optical application devices. The electron excitation of liquid helium produces emission in the vacuum-UV. A possible application of the materials characterized in the present work can be as alternative sources to classical VUV light sources [17]. The extension of the method to other materials is currently under investigation in our laboratory.

Acknowledgments

This work was supported by the EU 7FP (project Al-NanoFunc CT-REGPOT-2011-1-285895 and Integrated Infrastructure Initiative Ref.312483-ESTEEM2); the CSIC (PIE 201060E102, PIE 201460E018); the Spanish Ministry MINECO (projects CSD2008–00023 and CTQ2012-32519); and Junta de Andalucía (TEP217 and PE2012-TEP862). The authors also acknowledge the collaboration with the Ernst Ruska-Centre of the Forschungszentrum Jülich within the ER-C proposal A-084.

Supporting Information

A version of the program for the STEM-EELS data analysis running with MATLAB is available as supporting information. This program is a user-friendly and semi-automated program that was developed to map the composition of helium confined in small cavities (pores and bubbles) formed in a silicon matrix. For more information, the reader is invited to read the user manual, which is also available in the supporting information. For any publication results from analysis performed using this program, please cite the present article.

Online supplementary data available from **stacks.iop.org/NANO/26/075703/mmedia**

References

1. Becker, C. *et al.* Large-area 2D periodic crystalline silicon nanodome arrays on nanoimprinted glass exhibiting photonic band structure effects. *Nanotechnology* **23,** 135302 (2012).

2. Jin, H. & Liu, G. L. Fabrication and optical characterization of light trapping silicon nanopore and nanoscrew devices. *Nanotechnology* **23,** 125202 (2012).

3. Zhang, K., Seo, J.-H., Zhou, W. & Ma, Z. Fast flexible electronics using transferrable silicon nanomembranes. *J. Phys. -Appl. Phys.* **45,** 143001 (2012).

4. Spinelli, P., Verschuuren, M. A. & Polman, A. Broadband omnidirectional antireflection coating based on subwavelength surface Mie resonators. *Nat. Commun.* **3,** 692 (2012).

5. Qu, Y. *et al.* Electrically Conductive and Optically Active Porous Silicon Nanowires. *Nano Lett.* **9,** 4539–4543 (2009).

6. Ge, M. *et al.* Scalable preparation of porous silicon nanoparticles and their application for lithium-ion battery anodes. *Nano Res.* **6,** 174–181 (2013).

7. Godinho, V. *et al.* A new bottom-up methodology to produce silicon layers with a closed porosity nanostructure and reduced refractive index. *Nanotechnology* **24,** 275604 (2013).

8. Godinho, V. *et al.* On the formation of the porous structure in nanostructured a-Si coatings deposited by dc magnetron sputtering at oblique angles. *Nanotechnology* **25,** 355705 (2014).

9. Godinho, V., Rojas, T. C. & Fernandez, A. Magnetron sputtered a-SiOxNy thin films: A closed porous nanostructure with controlled optical and mechanical properties. *Microporous Mesoporous Mater.* **149,** 142–146 (2012).

10. Jager, W. *et al.* Density and Pressure of Helium in Small Bubbles in Metals. *J. Nucl. Mater.* **111,** 674–680 (1982).

11. Trinkaus, H. Energetics and Formation Kinetics of Helium Bubbles in Metals. *Radiat. Eff. Defects Solids* **78,** 189–211 (1983).

12. Walsh, C. A., Yuan, J. & Brown, L. M. A procedure for measuring the helium density and pressure in nanometre-sized bubbles in irradiated materials using electron-energy-loss spectroscopy. *Philos. Mag. -Phys. Condens. Matter Struct. Defects Mech. Prop.* **80,** 1507–1543 (2000).

13. Lucas, A., Vigneron, J., Donnelly, S. & Rife, J. Theoretical Interpretation of the Vacuum Ultraviolet Reflectance of Liquid-Helium and of the Absorption-Spectra of Helium Microbubbles in Aluminum. *Phys. Rev. B* **28,** 2485–2496 (1983).

14. Taverna, D. *et al.* Probing physical properties of confined fluids within individual nanobubbles. *Phys. Rev. Lett.* **100,** 035301 (2008).

15. David, M.-L., Pailloux, F., Mauchamp, V. & Pizzagalli, L. In situ probing of helium desorption from individual nanobubbles under electron irradiation. *Appl. Phys. Lett.* **98,** 171903 (2011).

16. David, M.-L. *et al.* In situ controlled modification of the helium density in single helium-filled nanobubbles. *J. Appl. Phys.* **115,** 123508 (2014).

17. Lucas, A., Donnelly, S., Vigneron, J. & Rife, J. Vacuum Ultraviolet Spectroscopy of High-Pressure Helium Microbubbles in Metals. *Surf. Sci.* **126,** 66–79 (1983).

18. Jia, J., Shi, L., Lai, X. & Wang, Q. Preparation of Al thin films charged with helium by DC magnetron sputtering. *Nucl. Instrum. Methods Phys. Res. Sect. B Beam Interact. Mater. At.* **263,** 446–450 (2007).

19. Shi, L. Q., Liu, C. Z., Xu, S. L. & Zhou, Z. Y. Helium-charged titanium films deposited by direct current magnetron sputtering. *Thin Solid Films* **479,** 52–58 (2005).

20. Zheng, H. *et al.* Introduction of helium into metals by magnetron sputtering deposition method. *Mater. Lett.* **59,** 1071–1075 (2005).

21. Tanyeli, I., Marot, L., van de Sanden, M. C. M. & De Temmerman, G. Nanostructuring of Iron Surfaces by Low-Energy Helium Ions. *Acs Appl. Mater. Interfaces* **6,** 3462–3468 (2014).

22. Kajita, S. *et al.* Helium plasma implantation on metals: Nanostructure formation and visible-light photocatalytic response. *J. Appl. Phys.* **113,** 134301 (2013).

23. Iyyakkunnel, S. *et al.* Morphological Changes of Tungsten Surfaces by Low-Flux Helium Plasma Treatment and Helium Incorporation via Magnetron Sputtering. *Acs Appl. Mater. Interfaces* **6,** 11609–11616 (2014).

24. Mayer, M. in *Application of Accelerators in Research and Industry, Pts 1 and 2* (eds. Duggan, J. L. & Morgan, I. L.) **475,** 541–544 (Amer Inst Physics, 1999).

25. Ahn, C.C. & Krivanek, O.L. *EELS Atlas*. (Gata, 1983).

26. Bonnet, N. Multivariate statistical methods for the analysis of microscope image series: applications in materials science. *J. Microsc.-Oxf.* **190,** 2–18 (1998).

27. Egerton, R. F. *Electron Energy-Loss Spectroscopy in the Electron Microscope*. (Springer US, 2011). at <http://link.springer.com/10.1007/978-1-4419-9583-4>

28. Malis, T., Cheng, S. & Egerton, R. Eels Log-Ratio Technique for Specimen-Thickness Measurement in the Tem. *J. Electron Microsc. Tech.* **8,** 193–200 (1988).

29. Duchamp, M. *et al.* Electron energy-loss spectroscopy of boron-doped layers in amorphous thin film silicon solar cells. *J. Appl. Phys.* **113,** 093513 (2013).

30. H. G. Kuhn. *Atomic Spectra*. at <http://archive.org/details/AtomicSpectra_369>

31. Williams, D. *et al.* Nitrogen, Oxygen, and Argon Incorporation During Reactive Sputter Deposition of Titanium Nitride. *J. Vac. Sci. Technol. B* **5,** 1723–1729 (1987).

32. Navid, A. & Pilon, L. Effect of polarization and morphology on the optical properties of absorbing nanoporous thin films. *Thin Solid Films* **516,** 4159–4167 (2008).

33. Schmidt, J. W. & Moldover, M. R. Dielectric permittivity of eight gases measured with cross capacitors. *Int. J. Thermophys.* **24,** 375–403 (2003).

34. Moreau, P., Brun, N., Walsh, C. A., Colliex, C. & Howie, A. Relativistic effects in electron-energy-loss-spectroscopy observations of the Si/SiO2 interface plasmon peak. *Phys. Rev. B* **56,** 6774–6781 (1997).

Appendix V

Calculation of reflectance on multilayered structures: Theory and application

In this appendix, it will be exposed an overview about the theory to calculate the reflectance of supported thin films using the method named “transfer matrix method”. The appendix is divided in two parts. In the first part, the method will be applied to the calculation of reflectance in a single layer and then, will be extended to the case of multilayer structures. Besides this, the particular multilayer structure (DBR), studied in chapter 6, will be also analyzed. In the second part, the computational code to obtain the reflectance spectrum for a general multilayer structure will be presented.

Part I: Calculation of the reflectance in thin films

Simple case: One layer

The problem presented is how to calculate the reflectance of a single layer with a complex refractive index η deposited on a substrate with a complex refractive index η_S. This situation is sketched in figure 1.

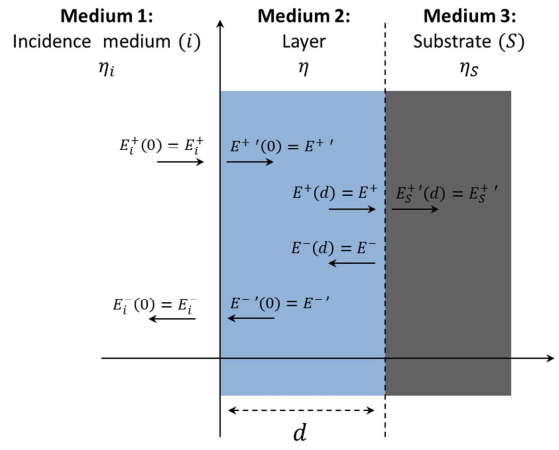

Figure 1: Simple case: one layer.

In this figure, the transmitted and reflected electric fields in each medium are represented. The electric field representation has been chosen, but similar treatment can be done with the magnetic field.

The method exposed herein for calculating the reflectance spectrum is a matrix method named transfer matrix method [1,2]. This method is based to associate a matrix to every interface, separation between two media (transmission matrix), and to every bulk of layer (propagation matrix) obtaining the matrix of every layer.

In the case of an interface $i-j$, the relation between electric fields in each face of the interface is:

$$\begin{pmatrix} E_i^+ \\ E_i^- \end{pmatrix} = D_{ij} \begin{pmatrix} E_j^+ \, ' \\ E_j^- \, ' \end{pmatrix} \qquad [1]$$

being D_{ij} the transmission matrix between the media i and j defined as:

$$D_{ij} = D_i^{-1} D_j \qquad [2]$$

The expression of the D matrices depend on the polarization (parallel ∥ or perpendicular ⊥). In a medium j, the general expression of these matrices are:

- Parallel polarization: $(D_j)_{\parallel} = \begin{pmatrix} \cos\theta_j & -\cos\theta_j \\ \eta_j & \eta_j \end{pmatrix}$
- Perpendicular polarization: $(D_j)_{\perp} = \begin{pmatrix} 1 & 1 \\ -\eta_j \cos\theta_j & \eta_j \cos\theta_j \end{pmatrix}$

[3]

where η_j is the complex refractive index of the medium expressed as $\eta_j = n_j + i\,\kappa_j$, being the real part n_j the refractive index and the complex part κ_j the extinction coefficient. θ_j is the propagation angle of radiation on the medium.

The expressions of the D matrices can be obtained applying the continuity conditions of the electric fields (or magnetic fields) in the interface for each polarization.

Using the definition [2], a compact expression of the transmission matrix, taking into account the Fresnel equations is:

$$D_{ij} = \frac{1}{t_{ij}} \begin{pmatrix} 1 & r_{ij} \\ r_{ij} & 1 \end{pmatrix} \quad [4]$$

r_{ij} and t_{ij} are the reflection and transmission coefficients in the interface $i-j$ respectively. This expression is valid for both polarizations.

The relation between the electric fields in a medium j is:

$$\begin{pmatrix} E_j^{+\prime} \\ E_j^{-\prime} \end{pmatrix} = P_j \begin{pmatrix} E_j^{+} \\ E_j^{-} \end{pmatrix} \quad [5]$$

where P_j is the propagation matrix which expression is:

$$P_j = \begin{pmatrix} e^{-i\beta_j} & 0 \\ 0 & e^{i\beta_j} \end{pmatrix} \quad [6]$$

β_j is the phase difference gained by the radiation with a wavelength λ when goes through the thickness of layer d_j. The expression to calculate it is:

$$\beta_j = \frac{2\,\pi}{\lambda}\,\eta_j\,d_j\cos\theta_j \quad [7]$$

In the figure 1, knowing the relation between electric fields in an interface and through the thickness of a layer or medium it is possible to calculate the relation between electric fields in the medium 1 (incident medium) and in the medium 3 (substrate) with the expression:

$$\begin{pmatrix} E_i^{+} \\ E_i^{-} \end{pmatrix} = M \begin{pmatrix} E_S^{+\prime} \\ E_S^{-\prime} \end{pmatrix} \quad [8]$$

M is named the matrix of layer. The expression of this matrix is the matrix product:

$$M = D_i^{-1} D\,P\,D^{-1} D_S \quad [9]$$

Seeing the figure 1, the reflection coefficient r of the layer is defined as the relation between the reflected electric field and the incident electric field.

$$r = \frac{E_i^-}{E_i^+} \quad [10]$$

Using the expression [4], the reflection coefficient in a medium j when the radiation arrives from a medium i is:

$$r_{ij} = \frac{D_{ij}[2,1]}{D_{ij}[1,1]} \quad [11]$$

Extending this expression to the case of a layer, the reflection coefficient is:

$$r = \frac{M[2,1]}{M[1,1]} \quad [12]$$

The reflectance is defined as:

$$R = |r|^2 \quad [13]$$

As there are two polarizations, parallel and perpendicular, the reflection coefficient will be:

$$r = \frac{1}{2}(r_{\parallel} + r_{\perp}) \quad [14]$$

Finally, the reflectance of the layer will be:

$$R = \frac{1}{4}\left|r_{\parallel} + r_{\perp}\right|^2 \quad [15]$$

GENERALIZATION TO A PERIODIC MULTILAYERED STRUCTURE

In the case of a periodic multilayer structure, the methodology explained in the previous section can be extended to calculate the reflectance of this particular structure. The situation is showed in the figure 2. The multilayer structure is composed by N periods. Each period is composed by two layers with different complex refractive indexes η_1 and η_2 and thicknesses d_1 and d_2 respectively.

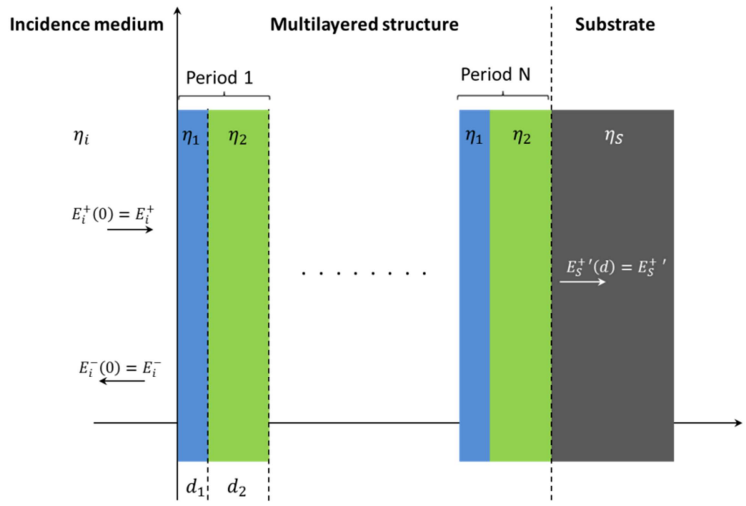

Figure 2: Periodic multilayered structure.

The relation between electric field in the incident medium and the electric field in the substrate is:

$$\begin{pmatrix} E_i^+ \\ E_i^- \end{pmatrix} = M \begin{pmatrix} E_S^{+\prime} \\ E_S^{-\prime} \end{pmatrix} \qquad [16]$$

Following the same reasoning that in the previous case, the M matrix is:

$$M = D_i^{-1} \left(\prod_{j=1}^{2} D_j \, P_j \, D_j^{-1} \right)^N D_S \qquad [17]$$

The reflection coefficient and the reflectance are obtained in the same way that in the previous case, taking into account the expression [12] for both polarizations and [15].

SOLUTION OF A PARTICULAR CASE: HIGH REFLECTANCE MULTILAYERED STRUCTURE

As application of the theory explained above, the Bragg reflector (DBR) designed in the chapter 6 is analyzed to obtain the reflectance expression at the resonant wavelength. This DBR is composed by a multilayer with 7 periods, however, herein, the results will be generalized at N periods. Every period is formed by two layers, one layer with high refractive index n_H and another layer with lower refractive index n_L. On this multilayer one layer more with high refractive index n_H is added to the multilayer structure. The sketch of the multilayer is showed in the figure 3.

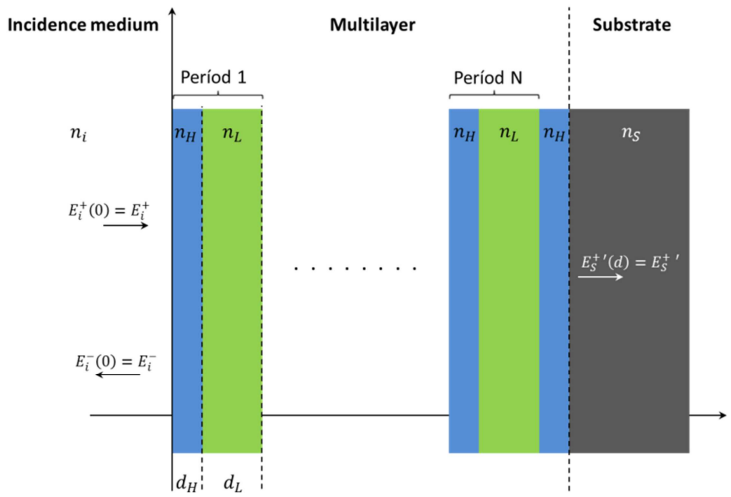

Figure 3: Particular case: High reflectance multilayered structure.

In a first approximation the absorption of the layers and the substrate will be considered negligible for the particular range of near-IR. So, it will be only taken into account the real part of the complex refractive index. The radiation will be at normal incidence to the surface, $\theta_i = 0°$, so there is no difference between both polarizations.

For this type of devices in order to get a high reflectance at λ_0, resonant wavelength, the necessary conditions are [3]:

$$\beta_H = \frac{\pi}{2} \qquad \beta_L = \frac{\pi}{2} \qquad [18]$$

Observing the expression [7], these conditions are satisfied if:

$$d_H = \frac{\lambda_0}{4\, n_H} \qquad d_L = \frac{\lambda_0}{4\, n_L} \qquad [19]$$

The thickness of the layer with high refractive index n_H is lower than the thickness of the layer with low refractive index n_L. This configuration is named quarter-wave configuration. Although it is presented herein the particular case without absorption in the layers, when the absorption is considered, for calculating the thickness of layers in [19] the real part of the complex refractive index will be used.

As in the previous sections the M matrix for the multilayer structure is:

$$M = D_i^{-1}\,(D_H\, P_H\, D_H^{-1}\, D_L\, P_L\, D_L^{-1})^N\, D_H\, P_H\, D_H^{-1}\, D_S \qquad [20]$$

Developing the matrix product using the expressions for the D and P matrices presented in [3] and [6] respectively, it is obtained the expression:

$$M = C \begin{pmatrix} -\, n_S\, n_i\, n_L^{2\,N} - \, n_H^{2(N+1)} & n_S\, n_i\, n_L^{2\,N} - \, n_H^{2(N+1)} \\ -\, n_S\, n_i\, n_L^{2\,N} + \, n_H^{2(N+1)} & n_S\, n_i\, n_L^{2\,N} + \, n_H^{2(N+1)} \end{pmatrix} \qquad [21]$$

C is a constant which depends of n_H, n_L and N.

The reflection coefficient is obtained by the ratio between the elements $M[2,1]$ and $M[1,1]$, obtaining:

$$r = \frac{\frac{n_S\, n_i}{n_H^2}\left(\frac{n_L}{n_H}\right)^{2\,N} - 1}{\frac{n_S\, n_i}{n_H^2}\left(\frac{n_L}{n_H}\right)^{2\,N} + 1} \qquad [22]$$

In this case it is not necessary to distinguish between parallel and perpendicular polarizations, because for normal incidence ($\theta_i = 0°$), $D_{\parallel} = D_{\perp}$.

With this result, finally, the reflectance expression at the resonant wavelength λ_0 is:

$$R = |r|^2 = \left(\frac{\frac{n_S\, n_i}{n_H^2} \left(\frac{n_L}{n_H}\right)^{2N} - 1}{\frac{n_S\, n_i}{n_H^2} \left(\frac{n_L}{n_H}\right)^{2N} + 1} \right)^2 \qquad [23]$$

This is the maximum reflectance reached. The maximum reflectance of the multilayer structure depends of the refractive index of layers, substrate and incident medium as well as the number of periods. To show more clear this dependence, the parameters of the DBR 2 studied in chapter 6 are used, $n_i = 1$, $n_H = 3.72$, and $n_S = 3.46$ at $\lambda_0 = 1750\, nm$. Introducing these values in the expression [23], the dependence of the reflectance with the variable $\frac{n_L}{n_H}$ at different number of periods N is showed in the figure 4.

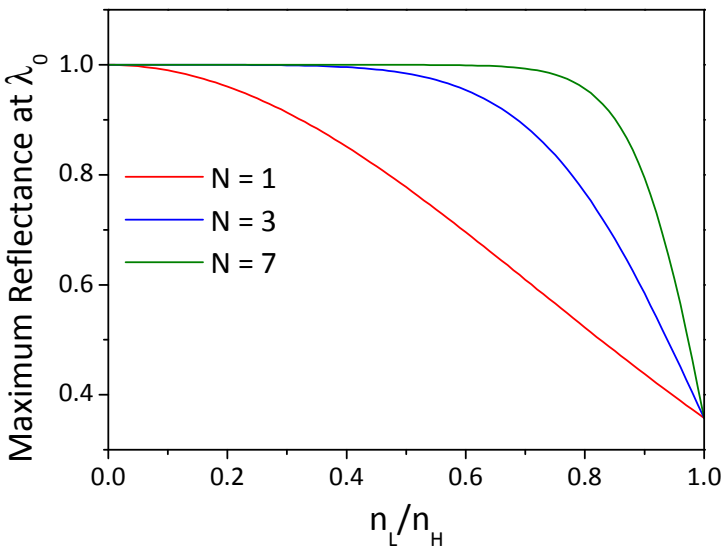

Figure 4: Effect on the maximum reflectance at λ_0 (1750 nm) of ratio of refractive index of layers and the number of periods.

When the ratio of the refractive indexes of layers increases, the maximum reached reflectance is lower. This means that to get a high maximum reflectance, high contrast of refractive indexes is necessary. If the layers do not have a high difference between the refractive indexes, it is possible to compensate this fact increasing the number of periods. This behavior is showed in the figure 4 too. At the same ratio of refractive indexes, the maximum reflectance increases when the number of periods is increased, satisfying that $\lim_{N\to\infty} R(N) = 1$.

To complete this analysis, in the following figure it is shown a typical reflectance spectrum of a Bragg reflector.

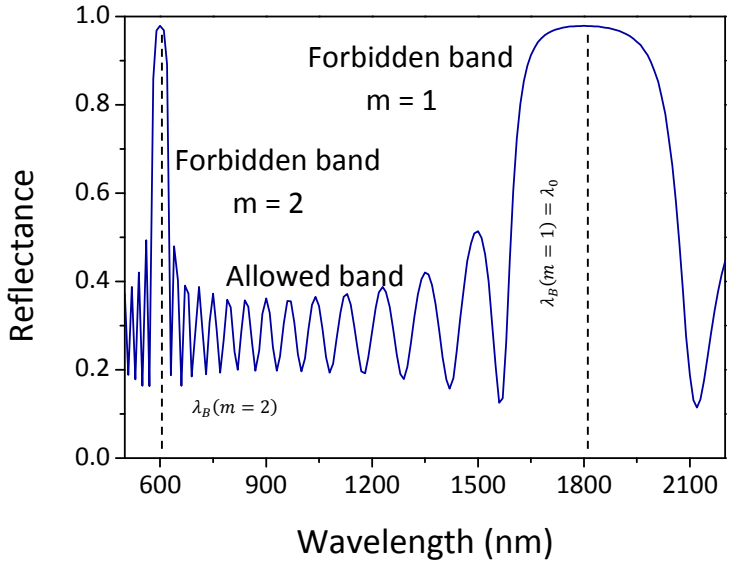

Figure 5: Example of a reflectance spectrum of a high reflectance multilayered structure.

The main characteristics of this reflectance spectrum are the stopping bands, ranges of wavelength with a high reflectance where the propagation of photons is forbidden. Between two stopping bands there is an allowed band where the photons can pass through

the structure. The position of the forbidden band centers are defined by the following relation:

$$(2m-1)\lambda_B = 2\,(n_L d_L + n_H d_H) \qquad [24]$$

where m is an integer number named the order of the forbidden band. λ_B is the wavelength where the center of the band is located. When $m = 1$, λ_B is the resonant wavelength λ_0 of the device.

Besides, the width of the forbidden bands changes with the order m being narrower when m increases. The relation between the width of the forbidden band and the resonant wavelength at order m is given by:

$$\Delta\lambda = \frac{4}{\pi}\,\lambda_B\, arcsin\left(\frac{n_H - n_L}{n_H + n_L}\right) \qquad [25]$$

This relation show that the forbidden band width depends of the refractive index of the layers. A high contrast in the refractive index means a broader forbidden band.

PART II: CODE TO CALCULATE THE THEORETICAL REFLECTANCE SPECTRA OF THE DESIGNED MULTILAYERS

A code based on the transfer matrix method [1,2,4] to obtain the theoretical reflectance spectra of optical devices has been developed in this thesis and will be presented here. The code is valid to calculate the reflectance spectra in one layer or in different multilayer structures.

The code has been developed using the computational software Mathematica 9.0. However, the code is valid if other version of Mathematica is used. The code is divided in two parts:

- The first part is the input parameters part where the particular parameters of the structure (one layer or multilayer) are introduced. It is possible to change the resonant wavelength, wavelength spectrum range and step, the refractive index of every layer, substrate and incident medium, the incidence angle of radiation and the thickness of the layers. The numerical values can be changed but it is recommendable does not change the letters and symbols. Besides, in the case of a multilayer, it is possible to modify the structure of the multilayer (order of layers and number of periods) changing the value of several coefficients. The meaning of each coefficient is explained in the table 1.

Table 1: Meaning of structure coefficients.

	Coefficient	Meaning
Upper DBR	**a1**	The number of periods composed by HL layers. The possible values are in the range $[0, \infty)$. The number must be integer.
	b1	The number of periods composed by LH layers. The possible values are in the range $[0, \infty)$. The number must be integer.
	c1	A single H layer can be added under a previous HL layers. The possible values are 0 (no H layer) or 1 (H layer).
	d1	A single L layer can be added under a previous LH layers. The possible values are 0 (no L layer) or 1 (L layer).
Active layer	**e**	An active layer (disruption in the periodicity of Bragg reflector) can be added in the case of an optical microcavity (OMC). The possible values are 0 (no C layer) or 1 (C layer)
Bottom DBR	**a2**	This coefficient is thought if an OMC is designed. The meaning is the number of periods composed by HL layers under the active layer. The possible values are in the range $[0, \infty)$. The number must be integer.
	b2	This coefficient is thought if an OMC is designed. The meaning is the number of periods composed by LH layers under the active layer. The possible values are in the range $[0, \infty)$. The number must be integer.
	c2	A single H layer can be added under previous HL layers. The possible values are 0 (no H layer) or 1 (H layer).
	d2	A single L layer can be added under a previous LH layers. The possible values are 0 (no L layer) or 1 (L layer).

As an example, in the table 2 different structures with the coefficient values are presented.

Table 2: Examples of different structures and the values of the structure coefficients.

Structure	Coefficient values
Air-$(HL)^7$-Substrate	a1 = 7, b1 = 0, c1 = 0, d1 = 0, e = 0, a2 = 0, b2 = 0, c2 = 0, d2 = 0
Air-$(HL)^4$H-Substrate	a1 = 4, b1 = 0, c1 = 1, d1 = 0, e = 0, a2 = 0, b2 = 0, c2 = 0, d2 = 0
Air-$(HL)^3$-Lc-$(HL)^2$H-Substrate	a1 = 3, b1 = 0, c1 = 0, d1 = 0, e = 1, a2 = 2, b2 = 0, c2 = 1, d2 = 0
Air-H-Substrate (single layer)	a1 = 0, b1 = 0, c1 = 1, d1 = 0, e = 0, a2 = 0, b2 = 0, c2 = 0, d2 = 0
Air-$(LH)^3$L-Lc-$(HL)^2$H-Substrate	a1 = 0, b1 = 3, c1 = 0, d1 = 1, e = 1, a2 = 2, b2 = 0, c2 = 1, d2 = 0

In the layers' thickness part, the expression can be removed to put a numerical value in nanometers.

- The second part is the code itself. It will be only necessary to modify the expression of refraction angle in the layers in the case of the calculation of the reflectance spectra with an incident angle different of zero and with a structure different of Air-$(HL)^n$H-Substrate for a DBR device or Air-$(HL)^n$H-Lc-$(HL)^n$H-Substrate for a OMC device.

Green letters divide the code in two parts: input parameters and program. It is not necessary to write them in the code. Red letters indicate the title of every part. It is not necessary to write them in the code. Blue letters help to understand the mean of each code line. They are not written in the code. The numbers at the beginning of the every code line are only a guide. They must not be written in the code. To run the code, it is necessary to write the black text in the order presented.

A limitation is that the code supposes the refractive index do not change with the wavelength. In the case of a single layer, the refractive index can be chosen at the middle of the wavelength range. In the case of DBR, the refractive index of layers can be chosen at the resonant wavelength. Besides, the code was designed to simulate the reflectance spectrum for structures with two different layers in each period as a maximum.

In the following lines, the code lines are presented.

"Input Parameters"

"Wavelength (nm)"

1 "Resonant wavelength" $\lambda 0 = 1550$

2 "Minimum spectral wavelength" $\lambda \min = 1000$

3 "Maximum spectral wavelength" $\lambda \max = 2700$

4 "Wavelength step" $p = 10$

5 $\text{nmax} = 1 + \frac{\lambda \max - \lambda \min}{p}$

6 "Wavelength values λ" $\lambda = \text{Table}\,[\lambda \min + p\,(n-1), \{n, 1, \text{nmax}\}]$

"Structure"

7 $a1 = 7$

8 $b1 = 0$

9 $c1 = 1$

10 $d1 = 0$

11 $e = 0$

12 $a2 = 0$

13 $b2 = 0$

14 $c2 = 0$

15 $d2 = 0$

"Incidence Angle (radians)"

16 $\theta i = 0\ \pi$

"Refractive Indexes"

17 "H layer (high index)" $\eta h = 3.50 + i\ 0.01$

18 "L layer (low index)" $\eta l = 2.60 + i\ 0.02$

19 "C layer (cavity index)" $\eta c = 2.60 + i\ 0.02$

20 "Incidence medium" $\eta i = 1.00 + i\ 0.00$

21 "Substrate" $\eta s = 3.48 + i\ 0.01$

"Layers' Thickness (nm)"

22 "H layer" $dh = \frac{\lambda 0}{4\ \mathrm{Re}[\eta h]}$

23 "L layer" $dl = \frac{\lambda 0}{4\ \mathrm{Re}[\eta l]}$

24 "C layer" $dc = \frac{\lambda 0}{4\ \mathrm{Re}[\eta c]}$

"Program"

"Refraction Angle in the layer (radians)"

25 "H layer" $\theta h = \mathrm{ArcSin}\left[\frac{\mathrm{Re}[\eta i]}{\mathrm{Re}[\eta h]}\ \mathrm{Sin}[\theta i]\right]$

26 "L layer" $\theta l = \mathrm{ArcSin}\left[\frac{\mathrm{Re}[\eta h]}{\mathrm{Re}[\eta l]}\ \mathrm{Sin}[\theta h]\right]$

27 "C layer" $\theta c = \mathrm{ArcSin}\left[\frac{\mathrm{Re}[\eta h]}{\mathrm{Re}[\eta c]}\ \mathrm{Sin}[\theta h]\right]$

28 "Substrate" $\theta s = \mathrm{ArcSin}\left[\frac{\mathrm{Re}[\eta h]}{\mathrm{Re}[\eta s]}\ \mathrm{Sin}[\theta h]\right]$

"Phase difference in the layer"

29 "H layer" $\beta h = \frac{2\ \pi}{\lambda}\ \eta h\ dh\ \mathrm{Cos}\ [\theta h]$

30 "L layer" $\beta l = \frac{2\pi}{\lambda}\, \eta l\, dl\, Cos\,[\theta l]$

31 "C layer" $\beta c = \frac{2\pi}{\lambda}\, \eta c\, dc\, Cos\,[\theta c]$

"D Matrices S polarization (⊥)"

32 "Incidence medium" $DiS = \begin{pmatrix} 1 & 1 \\ \eta i\, Cos[\theta i] & -\eta i\, Cos[\theta i] \end{pmatrix}$

33 "H layer" $DhS = \begin{pmatrix} 1 & 1 \\ \eta h\, Cos[\theta h] & -\eta h\, Cos[\theta h] \end{pmatrix}$

34 "L layer" $DlS = \begin{pmatrix} 1 & 1 \\ \eta l\, Cos[\theta l] & -\eta l\, Cos[\theta l] \end{pmatrix}$

35 "C layer" $DcS = \begin{pmatrix} 1 & 1 \\ \eta c\, Cos[\theta c] & -\eta c\, Cos[\theta c] \end{pmatrix}$

36 "Substrate" $DsS = \begin{pmatrix} 1 & 1 \\ \eta s\, Cos[\theta s] & -\eta s\, Cos[\theta s] \end{pmatrix}$

"Inverse D Matrices S polarization (⊥)"

37 "Incidence medium" $DIS = Inverse[DiS]$

38 "H layer" $DHS = Inverse[DhS]$

39 "L layer" $DLS = Inverse[DlS]$

40 "C layer" $DCS = Inverse[DcS]$

"D Matrices P polarization (∥)"

41 "Incidence medium" $DiP = \begin{pmatrix} Cos[\theta i] & Cos[\theta i] \\ \eta i & -\eta i \end{pmatrix}$

42 "H layer" $DhP = \begin{pmatrix} Cos[\theta h] & Cos[\theta h] \\ \eta h & -\eta h \end{pmatrix}$

43 "L layer" $DlP = \begin{pmatrix} Cos[\theta l] & Cos[\theta l] \\ \eta l & -\eta l \end{pmatrix}$

44 "C layer" $DcP = \begin{pmatrix} Cos[\theta c] & Cos[\theta c] \\ \eta c & -\eta c \end{pmatrix}$

45 "Substrate" $DsP = \begin{pmatrix} Cos[\theta s] & Cos[\theta s] \\ \eta s & -\eta s \end{pmatrix}$

"Inverse D Matrices P polarization (∥)"

46 "Incidence medium" $DIP = Inverse[DiP]$

47 "H layer" DHP = Inverse[DhP]

48 "L layer" DLP = Inverse[DlP]

49 "C layer" DCP = Inverse[DcP]

"P matrix (H layer)"

50 $Ph = \begin{pmatrix} \text{Exp}[-i\,\beta h] & 0 \\ 0 & \text{Exp}[i\,\beta h] \end{pmatrix}$

"Value list of the element [1,1] of P matrix (H layer)"

51 phr = Table[Ph[[1, 1, j]], {j, 1, nmax}]

"Value list of the element [2,2] of P matrix (H layer)"

52 phl = Table[Ph[[2, 2, j]], {j, 1, nmax}]

"P matrix (H layer) composed with two previous value tables"

53 $sh = \text{Table}\left[\begin{pmatrix} phr[[j]] & 0 \\ 0 & phl[[j]] \end{pmatrix}, \{j, 1, nmax\}\right]$

"M matrix (H layer) S polarization (⊥)"

54 $MhS = \text{Table}\left[DhS.\begin{pmatrix} sh[[j, 1, 1]] & 0 \\ 0 & sh[[j, 2, 2]] \end{pmatrix}.DHS, \{j, 1, nmax\}\right]$

"M matrix (H layer) P polarization (∥)"

55 $MhP = \text{Table}\left[DhP.\begin{pmatrix} sh[[j, 1, 1]] & 0 \\ 0 & sh[[j, 2, 2]] \end{pmatrix}.DHP, \{j, 1, nmax\}\right]$

"M matrix (H layer) power to c1 S polarization (⊥)"

56 $MhSc1 = \text{Table}\left[\text{MatrixPower}\left[\begin{pmatrix} MhS[[j,1,1]] & MhS[[j,1,2]] \\ MhS[[j,2,1]] & MhS[[j,2,2]] \end{pmatrix}, c1\right], \{j, 1, nmax\}\right]$

"M matrix (H layer) power to c1 P polarization (∥)"

57 $MhPc1 = \text{Table}\left[\text{MatrixPower}\left[\begin{pmatrix} MhP[[j,1,1]] & MhP[[j,1,2]] \\ MhP[[j,2,1]] & MhP[[j,2,2]] \end{pmatrix}, c1\right], \{j, 1, nmax\}\right]$

"M matrix (H layer) power to c2 S polarization (⊥)"

58 $MhSc2 = \text{Table}\left[\text{MatrixPower}\left[\begin{pmatrix} MhS[[j,1,1]] & MhS[[j,1,2]] \\ MhS[[j,2,1]] & MhS[[j,2,2]] \end{pmatrix}, c2\right], \{j, 1, nmax\}\right]$

"M matrix (H layer) power to c2 P polarization (∥)"

59 $$\text{MhPc2} = \text{Table}\left[\text{MatrixPower}\left[\begin{pmatrix}\text{MhP}[[j,1,1]] & \text{MhP}[[j,1,2]] \\ \text{MhP}[[j,2,1]] & \text{MhP}[[j,2,2]]\end{pmatrix}, \text{c2}\right], \{j, 1, \text{nmax}\}\right]$$

"P matrix (L layer)"

60 $$\text{Pl} = \begin{pmatrix}\text{Exp}[-\text{i}\,\beta\text{l}] & 0 \\ 0 & \text{Exp}[\text{i}\,\beta\text{l}]\end{pmatrix}$$

"Value list of the element [1,1] of P matrix (L layer)"

61 $$\text{plr} = \text{Table}[\text{Pl}[[1, 1, j]], \{j, 1, \text{nmax}\}]$$

"Value list of the element [2,2] of P matrix (L layer)"

62 $$\text{pll} = \text{Table}[\text{Pl}[[2, 2, j]], \{j, 1, \text{nmax}\}]$$

"P matrix (L layer) composed with two previous value tables"

63 $$\text{sl} = \text{Table}\left[\begin{pmatrix}\text{plr}[[j]] & 0 \\ 0 & \text{pll}[[j]]\end{pmatrix}, \{j, 1, \text{nmax}\}\right]$$

"M matrix (L layer) S polarization (⊥)"

64 $$\text{MlS} = \text{Table}\left[\text{DlS}.\begin{pmatrix}\text{sl}[[j, 1, 1]] & 0 \\ 0 & \text{sl}[[j, 2, 2]]\end{pmatrix}.\text{DLS}, \{j, 1\ , \text{nmax}\}\right]$$

"M matrix (L layer) P polarization (∥)"

65 $$\text{MlP} = \text{Table}\left[\text{DlP}.\begin{pmatrix}\text{sl}[[j, 1, 1]] & 0 \\ 0 & \text{sl}[[j, 2, 2]]\end{pmatrix}.\text{DLP}, \{j, 1\ , \text{nmax}\}\right]$$

"M matrix (L layer) power to d1 S polarization (⊥)"

66 $$\text{MlSd1} = \text{Table}\left[\text{MatrixPower}\left[\begin{pmatrix}\text{MlS}[[j,1,1]] & \text{MlS}[[j,1,2]] \\ \text{MlS}[[j,2,1]] & \text{MlS}[[j,2,2]]\end{pmatrix}, \text{d1}\right], \{j, 1, \text{nmax}\}\right]$$

"M matrix (L layer) power to d1 P polarization (∥)"

67 $$\text{MlPd1} = \text{Table}\left[\text{MatrixPower}\left[\begin{pmatrix}\text{MlP}[[j,1,1]] & \text{MlP}[[j,1,2]] \\ \text{MlP}[[j,2,1]] & \text{MlP}[[j,2,2]]\end{pmatrix}, \text{d1}\right], \{j, 1, \text{nmax}\}\right]$$

"M matrix (L layer) power to d2 S polarization (⊥)"

68 $$\text{MlSd2} = \text{Table}\left[\text{MatrixPower}\left[\begin{pmatrix}\text{MlS}[[j,1,1]] & \text{MlS}[[j,1,2]] \\ \text{MlS}[[j,2,1]] & \text{MlS}[[j,2,2]]\end{pmatrix}, \text{d2}\right], \{j, 1, \text{nmax}\}\right]$$

"M matrix (L layer) power to d2 P polarization (∥)"

69 $$\text{MlPd2} = \text{Table}\left[\text{MatrixPower}\left[\begin{pmatrix}\text{MlP}[[j,1,1]] & \text{MlP}[[j,1,2]]\\ \text{MlP}[[j,2,1]] & \text{MlP}[[j,2,2]]\end{pmatrix}, \text{d2}\right], \{j, 1, \text{nmax}\}\right]$$

"P matrix (C layer)"

70 $$\text{Pc} = \begin{pmatrix}\text{Exp}[-\text{i}\,\beta c] & 0\\ 0 & \text{Exp}[\text{i}\,\beta c]\end{pmatrix}$$

"Value list of the element [1,1] of P matrix (C layer)"

71 $$\text{pcr} = \text{Table}[\text{Pc}[[1, 1, j]], \{j, 1, \text{nmax}\}]$$

"Value list of the element [2,2] of P matrix (C layer)"

72 $$\text{pcl} = \text{Table}[\text{Pc}[[2, 2, j]], \{j, 1, \text{nmax}\}]$$

"P matrix (C layer) composed with two previous value tables"

73 $$\text{sc} = \text{Table}\left[\begin{pmatrix}\text{pcr}[[j]] & 0\\ 0 & \text{pcl}[[j]]\end{pmatrix}, \{j, 1, \text{nmax}\}\right]$$

"M matrix (C layer) S polarization (⊥)"

74 $$\text{McS} = \text{Table}\left[\text{DcS}.\begin{pmatrix}\text{sc}[[j, 1, 1]] & 0\\ 0 & \text{sc}[[j, 2, 2]]\end{pmatrix}.\text{DCS}, \{j, 1\ , \text{nmax}\}\right]$$

"M matrix (C layer) P polarization (∥)"

75 $$\text{McP} = \text{Table}\left[\text{DcP}.\begin{pmatrix}\text{sc}[[j, 1, 1]] & 0\\ 0 & \text{sc}[[j, 2, 2]]\end{pmatrix}.\text{DCP}, \{j, 1\ , \text{nmax}\}\right]$$

"M matrix (C layer) power to e S polarization (⊥)"

76 $$\text{McSe} = \text{Table}\left[\text{MatrixPower}\left[\begin{pmatrix}\text{McS}[[j,1,1]] & \text{McS}[[j,1,2]]\\ \text{McS}[[j,2,1]] & \text{McS}[[j,2,2]]\end{pmatrix}, \text{e}\right], \{j, 1, \text{nmax}\}\right]$$

"M matrix (C layer) power to e P polarization (∥)"

77 $$\text{McPe} = \text{Table}\left[\text{MatrixPower}\left[\begin{pmatrix}\text{McP}[[j,1,1]] & \text{McP}[[j,1,2]]\\ \text{McP}[[j,2,1]] & \text{McP}[[j,2,2]]\end{pmatrix}, \text{e}\right], \{j, 1, \text{nmax}\}\right]$$

"M matrix (HL layers) S polarization (⊥)"

78 $$\text{MhlS} = \text{Table}\left[\begin{pmatrix}\text{MhS}[[j,1,1]] & \text{MhS}[[j,1,2]]\\ \text{MhS}[[j,2,1]] & \text{MhS}[[j,2,2]]\end{pmatrix}.\begin{pmatrix}\text{MlS}[[j,1,1]] & \text{MlS}[[j,1,2]]\\ \text{MlS}[[j,2,1]] & \text{MlS}[[j,2,2]]\end{pmatrix}, \{j, 1, \text{nmax}\}\right]$$

"M matrix (HL layers) P polarization (∥)"

79 $$\text{MhlP} = \text{Table}\left[\begin{pmatrix}\text{MhP}[[j,1,1]] & \text{MhP}[[j,1,2]]\\ \text{MhP}[[j,2,1]] & \text{MhP}[[j,2,2]]\end{pmatrix}\cdot\begin{pmatrix}\text{MlP}[[j,1,1]] & \text{MlP}[[j,1,2]]\\ \text{MlP}[[j,2,1]] & \text{MlP}[[j,2,2]]\end{pmatrix},\{j,1,\text{nmax}\}\right]$$

"M matrix (HL layers) power to a1 S polarization (⊥)"

80 $$\text{MhlSa1} = \text{Table}\left[\text{MatrixPower}\left[\begin{pmatrix}\text{MhlS}[[j,1,1]] & \text{MhlS}[[j,1,2]]\\ \text{MhlS}[[j,2,1]] & \text{MhlS}[[j,2,2]]\end{pmatrix},\text{a1}\right],\{j,1,\text{nmax}\}\right]$$

"M matrix (HL layers) power to a1 P polarization (∥)"

81 $$\text{MhlPa1} = \text{Table}\left[\text{MatrixPower}\left[\begin{pmatrix}\text{MhlP}[[j,1,1]] & \text{MhlP}[[j,1,2]]\\ \text{MhlP}[[j,2,1]] & \text{MhlP}[[j,2,2]]\end{pmatrix},\text{a1}\right],\{j,1,\text{nmax}\}\right]$$

"M matrix (HL layers) power to a2 S polarization (⊥)"

82 $$\text{MhlSa2} = \text{Table}\left[\text{MatrixPower}\left[\begin{pmatrix}\text{MhlS}[[j,1,1]] & \text{MhlS}[[j,1,2]]\\ \text{MhlS}[[j,2,1]] & \text{MhlS}[[j,2,2]]\end{pmatrix},\text{a2}\right],\{j,1,\text{nmax}\}\right]$$

"M matrix (HL layers) power to a2 P polarization (∥)"

83 $$\text{MhlPa2} = \text{Table}\left[\text{MatrixPower}\left[\begin{pmatrix}\text{MhlP}[[j,1,1]] & \text{MhlP}[[j,1,2]]\\ \text{MhlP}[[j,2,1]] & \text{MhlP}[[j,2,2]]\end{pmatrix},\text{a2}\right],\{j,1,\text{nmax}\}\right]$$

"M matrix (LH layers) S polarization (⊥)"

84 $$\text{MlhS} = \text{Table}\left[\begin{pmatrix}\text{MlS}[[j,1,1]] & \text{MlS}[[j,1,2]]\\ \text{MlS}[[j,2,1]] & \text{MlS}[[j,2,2]]\end{pmatrix}\cdot\begin{pmatrix}\text{MhS}[[j,1,1]] & \text{MhS}[[j,1,2]]\\ \text{MhS}[[j,2,1]] & \text{MhS}[[j,2,2]]\end{pmatrix},\{j,1,\text{nmax}\}\right]$$

"M matrix (LH layers) P polarization (∥)"

85 $$\text{MlhP} = \text{Table}\left[\begin{pmatrix}\text{MlP}[[j,1,1]] & \text{MlP}[[j,1,2]]\\ \text{MlP}[[j,2,1]] & \text{MlP}[[j,2,2]]\end{pmatrix}\cdot\begin{pmatrix}\text{MhP}[[j,1,1]] & \text{MhP}[[j,1,2]]\\ \text{MhP}[[j,2,1]] & \text{MhP}[[j,2,2]]\end{pmatrix},\{j,1,\text{nmax}\}\right]$$

"M matrix (LH layers) power to b1 S polarization (⊥)"

86 $$\text{MlhSb1} = \text{Table}\left[\text{MatrixPower}\left[\begin{pmatrix}\text{MlhS}[[j,1,1]] & \text{MlhS}[[j,1,2]]\\ \text{MlhS}[[j,2,1]] & \text{MlhS}[[j,2,2]]\end{pmatrix},\text{b1}\right],\{j,1,\text{nmax}\}\right]$$

"M matrix (LH layers) power to b1 P polarization (∥)"

87 $$\text{MlhPb1} = \text{Table}\left[\text{MatrixPower}\left[\begin{pmatrix}\text{MlhP}[[j,1,1]] & \text{MlhP}[[j,1,2]]\\ \text{MlhP}[[j,2,1]] & \text{MlhP}[[j,2,2]]\end{pmatrix},\text{b1}\right],\{j,1,\text{nmax}\}\right]$$

"M matrix (LH layers) power to b2 S polarization (⊥)"

88 $$\text{MlhSb2} = \text{Table}\left[\text{MatrixPower}\left[\begin{pmatrix}\text{MlhS}[[j,1,1]] & \text{MlhS}[[j,1,2]] \\ \text{MlhS}[[j,2,1]] & \text{MlhS}[[j,2,2]]\end{pmatrix}, \text{b2}\right], \{j, 1, \text{nmax}\}\right]$$

"M matrix (LH layers) power to b2 P polarization (∥)"

89 $$\text{MlhPb2} = \text{Table}\left[\text{MatrixPower}\left[\begin{pmatrix}\text{MlhP}[[j,1,1]] & \text{MlhP}[[j,1,2]] \\ \text{MlhP}[[j,2,1]] & \text{MlhP}[[j,2,2]]\end{pmatrix}, \text{b2}\right], \{j, 1, \text{nmax}\}\right]$$

"M matrix (all layers) S polarization (⊥)"

90 $$\text{MS} = \text{Table}\left[\text{DIS} \cdot \begin{pmatrix}\text{MhlSa1}[[j,1,1]] & \text{MhlSa1}[[j,1,2]] \\ \text{MhlSa1}[[j,2,1]] & \text{MhlSa1}[[j,2,2]]\end{pmatrix} \cdot \begin{pmatrix}\text{MlhSb1}[[j,1,1]] & \text{MlhSb1}[[j,1,2]] \\ \text{MlhSb1}[[j,2,1]] & \text{MlhSb1}[[j,2,2]]\end{pmatrix} \cdot \begin{pmatrix}\text{MhSc1}[[j,1,1]] & \text{MhSc1}[[j,1,2]] \\ \text{MhSc1}[[j,2,1]] & \text{MhSc1}[[j,2,2]]\end{pmatrix} \cdot \begin{pmatrix}\text{MlSd1}[[j,1,1]] & \text{MlSd1}[[j,1,2]] \\ \text{MlSd1}[[j,2,1]] & \text{MlSd1}[[j,2,2]]\end{pmatrix} \cdot \begin{pmatrix}\text{McSe}[[j,1,1]] & \text{McSe}[[j,1,2]] \\ \text{McSe}[[j,2,1]] & \text{McSe}[[j,2,2]]\end{pmatrix} \cdot \begin{pmatrix}\text{MhlSa2}[[j,1,1]] & \text{MhlSa2}[[j,1,2]] \\ \text{MhlSa2}[[j,2,1]] & \text{MhlSa2}[[j,2,2]]\end{pmatrix} \cdot \begin{pmatrix}\text{MlhSb2}[[j,1,1]] & \text{MlhSb2}[[j,1,2]] \\ \text{MlhSb2}[[j,2,1]] & \text{MlhSb2}[[j,2,2]]\end{pmatrix} \cdot \begin{pmatrix}\text{MhSc2}[[j,1,1]] & \text{MhSc2}[[j,1,2]] \\ \text{MhSc2}[[j,2,1]] & \text{MhSc2}[[j,2,2]]\end{pmatrix} \cdot \begin{pmatrix}\text{MlSd2}[[j,1,1]] & \text{MlSd2}[[j,1,2]] \\ \text{MlSd2}[[j,2,1]] & \text{MlSd2}[[j,2,2]]\end{pmatrix} \cdot \text{DsS}, \{j, 1, \text{nmax}\}\right]$$

"M matrix (all layers) P polarization (∥)"

91 $$\text{MP} = \text{Table}\left[\text{DIP} \cdot \begin{pmatrix}\text{MhlPa1}[[j,1,1]] & \text{MhlPa1}[[j,1,2]] \\ \text{MhlPa1}[[j,2,1]] & \text{MhlPa1}[[j,2,2]]\end{pmatrix} \cdot \begin{pmatrix}\text{MlhPb1}[[j,1,1]] & \text{MlhPb1}[[j,1,2]] \\ \text{MlhPb1}[[j,2,1]] & \text{MlhPb1}[[j,2,2]]\end{pmatrix} \cdot \begin{pmatrix}\text{MhPc1}[[j,1,1]] & \text{MhPc1}[[j,1,2]] \\ \text{MhPc1}[[j,2,1]] & \text{MhPc1}[[j,2,2]]\end{pmatrix} \cdot \begin{pmatrix}\text{MlPd1}[[j,1,1]] & \text{MlPd1}[[j,1,2]] \\ \text{MlPd1}[[j,2,1]] & \text{MlPd1}[[j,2,2]]\end{pmatrix} \cdot \begin{pmatrix}\text{McPe}[[j,1,1]] & \text{McPe}[[j,1,2]] \\ \text{McPe}[[j,2,1]] & \text{McPe}[[j,2,2]]\end{pmatrix} \cdot \begin{pmatrix}\text{MhlPa2}[[j,1,1]] & \text{MhlPa2}[[j,1,2]] \\ \text{MhlPa2}[[j,2,1]] & \text{MhlPa2}[[j,2,2]]\end{pmatrix} \cdot \begin{pmatrix}\text{MlhPb2}[[j,1,1]] & \text{MlhPb2}[[j,1,2]] \\ \text{MlhPb2}[[j,2,1]] & \text{MlhPb2}[[j,2,2]]\end{pmatrix} \cdot \begin{pmatrix}\text{MhPc2}[[j,1,1]] & \text{MhPc2}[[j,1,2]] \\ \text{MhPc2}[[j,2,1]] & \text{MhPc2}[[j,2,2]]\end{pmatrix} \cdot \begin{pmatrix}\text{MlPd2}[[j,1,1]] & \text{MlPd2}[[j,1,2]] \\ \text{MlPd2}[[j,2,1]] & \text{MlPd2}[[j,2,2]]\end{pmatrix} \cdot \text{DsP}, \{j, 1, \text{nmax}\}\right]$$

"Reflection coefficient (all layers) S polarization (⊥)"

92 $$\text{rS} = \text{Table}\left[\frac{\text{MS}[[j,2,1]]}{\text{MS}[[j,1,1]]}, \{j, 1, \text{nmax}\}\right]$$

"Reflection coefficient (all layers) P polarization (∥)"

93 $$\text{rP} = \text{Table}\left[\frac{\text{MP}[[j,2,1]]}{\text{MP}[[j,1,1]]}, \{j, 1, \text{nmax}\}\right]$$

"Mean reflection coefficient"

```
94    r = Table[1/2 (rS[[j]] + rP[[j]]), {j, 1, nmax}]
```

"Reflectance"

```
95    R = Table[Re[r[[j]] Conjugate[r[[j]]]], {j, 1, nmax}]
```

"Pair {Wavelength, Reflectance}"

```
96    Rdata = Table[{λ[[j]], R[[j]]}, {j, 1, nmax}]
```

"Reflectance Spectrum Plot"

```
97    ListPlot[Rdata, Joined → True]
```

"Table {Wavelength, Reflectance}"

```
98    TableForm[Rdata]
```

The interesting output data are the three final lines, where it is obtained the pair {Wavelength, Reflectance}, the plot of reflectance versus wavelength and the pair {Wavelength, Reflectance} in a columnar way, easily to export to a txt file for example.

References

1. Yonte Sanchidrián, T. Fundamentos geométricos de la óptica de multicapas: memoria para optar al grado de Doctor. ([Universidad Complutense], Servicio de Publicaciones, 2006).

2. Young, N. & Kowal, J. Optically Active Fluorite Films. *Nature* **183,** 104–105 (1959).

3. Rancourt, J. D. *Optical Thin Films*. (SPIE, 1996). at <http://ebooks.spiedigitallibrary.org/book.aspx?doi=10.1117/3.242743>

4. Das, K. C. *et al.* Surface and interface studies of RF sputtered HfO2 thin films with working pressure and gas flow ratio. *J. Mater. Sci.-Mater. Electron.* **26,** 6025–6031 (2015).

Resumen en español

Control de la Microestructura en Recubrimientos de Silicio Poroso con Porosidad Cerrada para Aplicaciones Funcionales

1. Introducción

Los materiales basados en silicio siguen siendo hoy en día claves para el desarrollo de la tecnología moderna. Así, los continuos avances en dispositivos fotónicos, microelectrónica y energía solar [1–4] han puesto una vez más la atención en el silicio poroso [5–7].

El silicio poroso fue descubierto de forma accidental en 1950 por el matrimonio Uhlir [8] que trabajando en un nuevo método electroquímico para la producción de obleas de silicio para microelectrónica, observaron que las obleas de silicio no eran uniformemente disueltas en soluciones de HF, apareciendo finos canales que se propagaban preferencialmente en la dirección (100) de las mismas.

Sin embargo, no fue hasta la década de los 90 en la que el interés en este nuevo material se generalizó debido a su particular estructura que presenta un incremento de la banda prohibida en relación a la del silicio [9]. Además en la misma época Canham [10] reportó una fuerte fotoluminiscencia en el visible a temperatura ambiente en obleas de silicio dopado tipo p anodizadas en soluciones de HF. También se han reportado propiedades electroluminiscentes de este nuevo material [11,12].

El interés en la investigación en silicio poroso ha crecido de forma apreciable desde los años 90. Aplicaciones en diodos de silicio o dispositivos capaces de guiar, modular o detectar luz, compatibles con la actual tecnología basada en silicio hacen del silicio poroso un material de interés actual. En este contexto, y motivado por trabajos anteriores desarrollados en el grupo de investigación, en esta tesis se presenta una nueva metodología para la producción de silicio poroso por magnetrón sputtering.

1.1. Procesos para la formación de silicio poroso

Teniendo en cuenta la aplicación, el coste del material y del proceso, la estabilidad química requerida, producción a gran escala, etc., se han investigado diferentes procesos para la producción de silicio poroso.

Éstos se pueden clasificar en dos grupos: *top-down (de arriba abajo)*, en el que se empieza desde una oblea de silicio sólido (figura 1.1 (a)) y *bottom-up (de abajo arriba)*, donde los átomos o conjunto de átomos de silicio son depositados sobre un sustrato obteniendo una estructura porosa (figura 1.1 (b)).

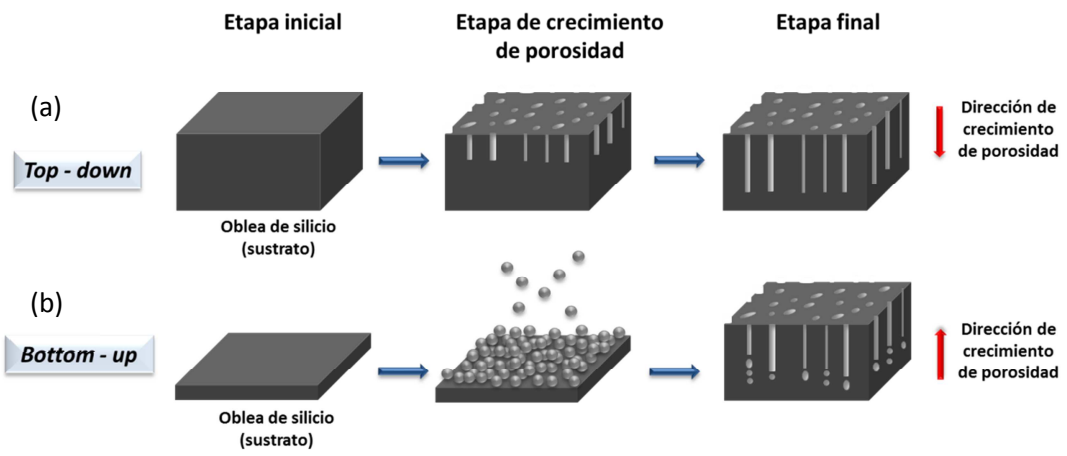

Figura 1.1: Diferentes procesos de producción de silicio poroso. (a) Top-down. (b) Bottom-up.

Tradicionalmente el silicio poroso se obtiene mediante un proceso top-down, por anodizado electroquímico en soluciones de HF, el cual bajo condiciones adecuadas de corriente y concentración de electrolito, se genera porosidad abierta en la oblea de silicio. En la figura 1.2 se muestran varios ejemplos de estructuras de silicio poroso [13].

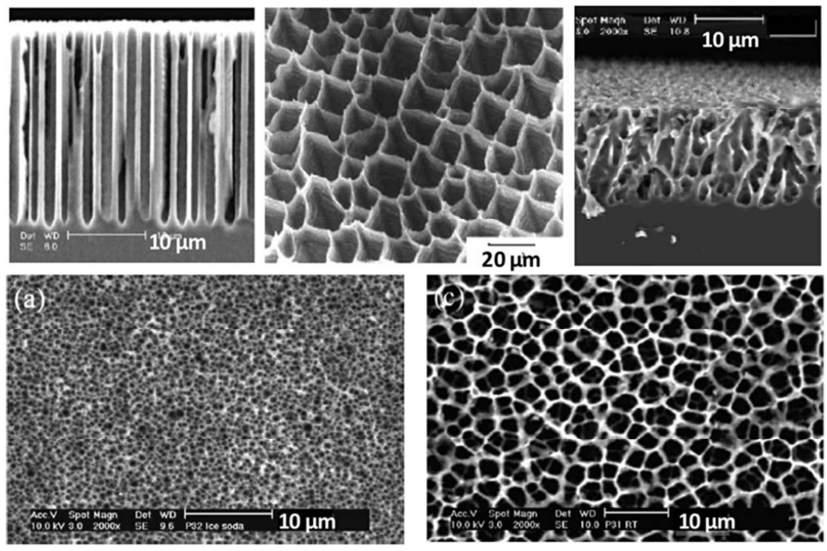

Figura 1.2: Ejemplos de estructuras de silicio poroso obtenidas por el método de anodizado electroquímico [13].

Sin embargo, el silicio poroso obtenido de esta forma presenta efectos de envejecimiento que deterioran sus propiedades originales. Tratamientos térmicos de oxidación superficial han sido propuestos para garantizar su estabilidad, aunque aumentando el coste de producción. Por otro lado, para la aplicación y procesamiento del silicio poroso como capa fina se hace necesario el uso de procedimientos de transferencia del material a otro tipo de sustrato [14]. Estos procedimientos son normalmente complexos, presentando limitaciones de tamaño y naturaleza de los sustratos de transferencia.

Así, los métodos de deposición de películas delgadas son considerados como buenas alternativas para la producción de recubrimientos de silicio poroso, en especial cuando se requieren sustratos poliméricos o de vidrio.

Teniendo en cuenta todos estos aspectos, esta tesis propone una nueva metodología bottom-up para producir recubrimientos de silicio poroso con porosidad cerrada mediante la técnica de deposición por magnetron sputtering.

1.2. Nueva metodología para la obtención de silicio poroso con porosidad cerrada mediante magnetron sputtering

Una de las propiedades más interesantes del silicio poroso es la facilidad de alterar su índice de refracción modificando su porosidad. En trabajos previos realizados en el grupo NanoMatMicro se mostró como recubrimientos porosos de SiO_xN_y depositados por la técnica de magnetron sputtering bajo unas determinadas condiciones, presentaban una estructura con porosidad cerrada en la que se detectó señal del gas de deposición en el interior. Esta porosidad permitía modificar el índice de refracción del recubrimiento [15,16]. Además, se observó una estructura similar en recubrimientos de silicio utilizando helio como gas de deposición [17].

Por otro lado, el comportamiento insoluble del He introducido en diferentes metales mediante implantación iónica ya ha sido investigado por su relevancia en problemas de física nuclear. Se observó que el He implantado tiende a acumularse en pequeñas burbujas [18].

Este hecho junto con los trabajos previamente citados ha motivado el desarrollo de esta nueva metodología para producir recubrimientos de silicio poroso mediante magnetron sputtering presentando porosidad cerrada y propiedades ópticas controladas.

En el siguiente apartado se plantean los objetivos a perseguir en esta tesis.

1.3. Objetivos y planteamiento de la tesis

La motivación de esta tesis es el desarrollo una nueva metodología para producir recubrimientos de silicio poroso con porosidad cerrada por magnetron sputtering, siendo de gran interés el estudio de la formación y control de la microestructura porosa así como el efecto de ésta sobre las propiedades finales del material.

El trabajo presentado en esta tesis se desarrolla en diferentes apartados con objetivos definidos en cada uno de ellos.

Apartado 2: Detalles experimentales

En este apartado se describen los materiales y la cámara de deposición utilizados. También se presentan las condiciones generales de deposición y la nomenclatura utilizada para los recubrimientos estudiados a lo largo de la tesis.

Apartado 3: Nueva metodología bottom-up para producir recubrimientos de silicio poroso por magnetron sputtering

Este apartado es fundamental para el desarrollo de la metodología presentada en la tesis. Se estudia el efecto de los diferentes parámetros de deposición sobre la microestructura final del recubrimiento, tamaño, forma y distribución de la porosidad así como la cantidad y presión del gas de proceso atrapado en los poros. El control microestructural y químico se obtiene mediante un chequeo exhaustivo de los parámetros de deposición: potencia aplicada al blanco, composición y presión del gas de síntesis, geometría de deposición y condiciones del sustrato (bias y temperatura). La correlación entre las condiciones de deposición y los análisis microestructurales y químicos permite proponer un modelo empírico para el

crecimiento de recubrimientos de porosidad cerrada por magnetrón sputtering frente a los diferentes parámetros de deposición.

Apartado 4: Estudio de la formación de nanoestructuras en recubrimientos de silicio poroso amorfo (a-pSi) por simulación

Este apartado tiene como objetivo, con la ayuda de una potente herramienta como es la simulación Monte Carlo, entender los fundamentos que controlan el crecimiento de recubrimientos con porosidad cerrada en presencia de He. Para la deposición de los recubrimientos se han utilizado unas condiciones de deposición específicas de acuerdo a las limitaciones de los modelos teóricos de los que se dispone. Se hace uso del software NASCAM para simular el crecimiento de recubrimientos depositados con diferentes gases o mezcla de gases de sputtering. Los resultados de la simulación son comparados con resultados experimentales.

Apartado 5: Diseño y fabricación de dispositivos ópticos multicapa mediante el uso de recubrimientos de silicio poroso con porosidad cerrada

Como posible aplicación de los recubrimientos depositados por la metodología presentada, poniendo en evidencia la versatilidad del método, en este apartado se han diseñado dos tipos dispositivos fotonicos (un refractor de Bragg distribuido (DBR) y una microcavidad óptica (OMC))empleando capas porosas de bajo índice de refracción (n_L) y capas densas de alto (n_H). Mediante la comparación de los espectros de reflectancia experimental y teórico, en el rango de interés de cada uno de los dispositivos, se mostrará si la metodología desarrollada a lo largo de esta tesis es adecuada para el diseño de este tipo de dispositivos.

Apartado 6: Conclusiones finales

De los resultados obtenidos en los apartados previos se presentan unas conclusiones finales como cierre de este resumen de la tesis.

2. Condiciones experimentales

2.1. Materiales

A continuación se presentan el blanco y los gases de sputtering usados, así como los sustratos utilizados.

Blanco: Silicio monocristalino (suministrador: Kurt J. Lesker, 99.999% de pureza) de $2''$ de diámetro y $0.125''$ de grosor.

Tabla 2.1: Gases de sputtering.

Gas de sputtering	Pureza	Impurezas *		
		H_2O	O_2	C_nH_m
Helio	99.999 %	$\leq 3\ ppm$	$\leq 2\ ppm$	$\leq 0.5\ ppm$
Argón	99.999 %	$\leq 3\ ppm$	$\leq 2\ ppm$	$\leq 0.1\ ppm$

* ppm: partes por millón.

Tabla 2.2: Sustratos.

Tipo de sustrato	Suministrador	Propiedad estudiada / Técnica
Silicio (100)	A.C.M.	Microestructura (microscopía electrónica) y composición química (RBS y XPS)
Cuarzo	SICO Technology GmbH	Índice de refracción (Elipsometría)
Vidrio de carbono	Goodfellow	Composición química (RBS)
Teflon	Goodfellow	Prueba de concepto de la metodología de deposición
Kapton	Goodfellow	Prueba de concepto de la metodología de deposición

2.2. Cámara de deposición

En la figura 2.1 se presenta un esquema de la cámara de deposición utilizada.

Se trata de un sistema no comercial compuesto por dos bombas de vacío (rotatoria y turbomolecular) separadas de la cámara por una válvula de guillotina. La presión de vacío es medida por un sensor *full range* y la presión del gas de sputtering por un sensor de capacitancia. La cámara dispone de un sistema de calentamiento formado por cuatro placas cerámicas que permiten calentarla antes de la deposición para reducir al máximo la cantidad de agua adsorbida en las paredes interiores.

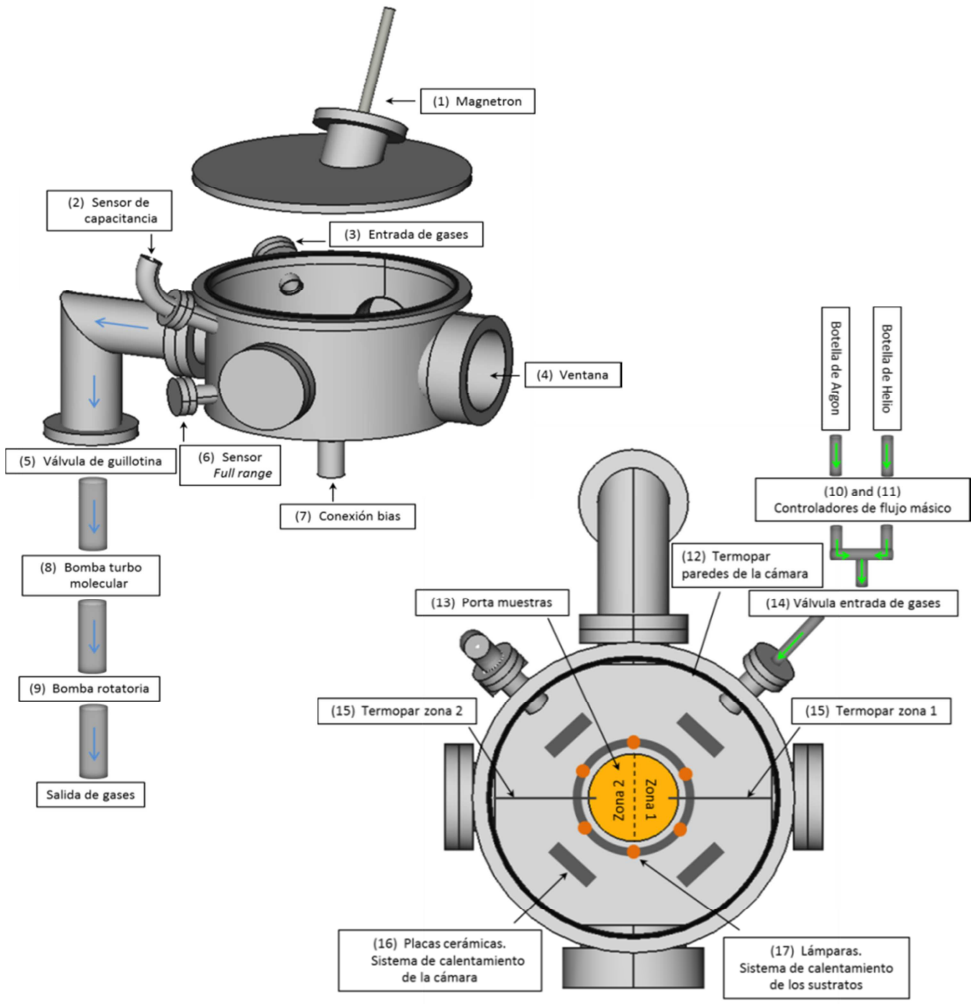

Figura 2.1: Cámara de deposición con los diferentes componentes.

El magnetron está inclinado $30°$ respecto al porta muestras que esta eléctricamente aislado de la cámara y al que es posible aplicar un voltaje (bias). Además cuenta con un sistema de calentamiento de los sustratos.

En la figura 2.2 se representa la posición de los sustratos utilizada con respecto al magnetron, zona 1 y zona 2.

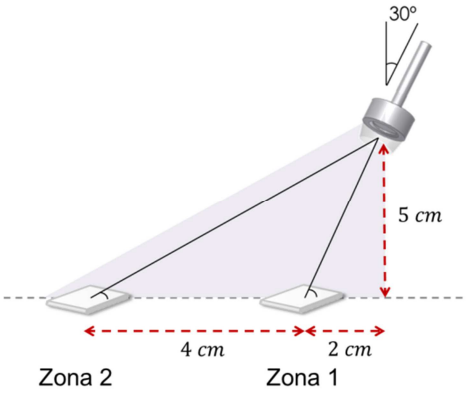

Figura 2.2: Posición relativa de las dos zonas donde se colocan los sustratos respecto al magnetron.

2.3. Condiciones generales de deposición y nomenclatura de los Recubrimientos

En todos los recubrimientos depositados, se alcanzó una presión de vacío en la cámara después del calentamiento de $1 \cdot 10^{-4}\ Pa$. Además, antes de la deposición los sustratos se calientan a $50°C$ durante una hora y el blanco se limpia durante $15\ min$ en las mismas condiciones de deposición que las usadas para cada recubrimiento. A continuación se describen la nomenclatura y las condiciones de deposición empleadas en los diferentes apartados.

Apartado 3:

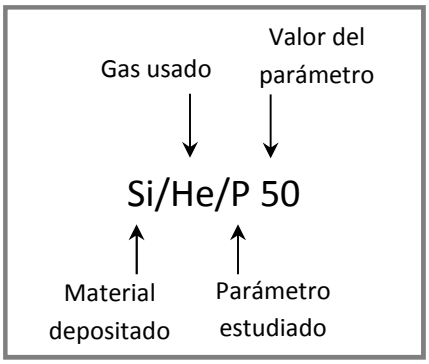

Abreviatura	Parámetro
P	Potencia
pr	Presión de gas
b	Bias
h	Temperatura de deposición

Tabla 2.3: Condiciones de deposición de los recubrimientos descritos en el apartado 3.

Parámetro deposición	Nombre recubrimiento	Gas	Ángulo incidencia**	Modo / Potencia (W)	Presión (Pa)	Bias (V)	Temperatura sustrato $(°C)$
ÁNGULO INCIDENCIA	**Recubrimiento poroso (a-pSi) ***	He	0°	RF 150	1.33	0	---
	Si/He		30°		4.8		
GAS	**Si/He**	He	30°	RF 150	4.8	0	---
	Si/Ar	Ar					
POTENCIA	**Si/He/P 50**	He	30°	RF 50	4.8	0	---
	Si/He/P 150			RF 150			
	Si/He/P 300			RF 300			
PRESIÓN DE GAS	**Si/He/pr 2.7**	He	30°	RF 150	2.7	0	---
	Si/He/pr 2.9				2.9		
	Si/He/pr 4.8				4.8		
	Si/He/pr 9.0				9.0		
	Si/He/pr 23.8				23.8		
	Si/He/pr 54.6				54.6		
BIAS	**Si/He/b 0**	He	30°	RF 150	9.0	0	---
	Si/He/b 100					−100	
	Si/He/b 200					−200	

TEMP. DEP.	Si/He/h As dep Si/He/h 200 Si/He/h 300	He	30°	RF 150	2.7	0	--- 200 300
OTROS	Recubrimiento denso (a-Si) * Si/Ar/bias	Ar	0° 30°	RF 150	1.33 1.5	0 −100	---

* Estos recubrimientos fueron crecidos en otra cámara de deposición con una geometría de incidencia normal.
**Ángulo medido respecto de la vertical.

Tabla 2.4: Recubrimientos analizados en el estudio de la estabilidad térmica.

Recubrimento	Temperatura de calentamiento $(°C)$
Si/He/h As dep	---
Si/He/HT-300C	300
Si/He/HT-550C	550

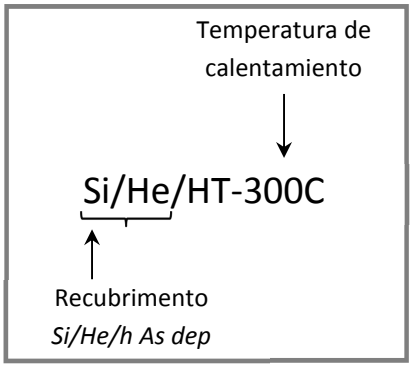

Apartado 4:

Tabla 2.5: Recubrimientos estudiados en el apartado 4.

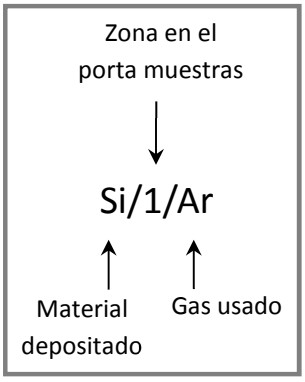

Recubrimiento	Zona en el porta muestras	Modo / Potencia (W)	Presión (Pa)
Si / 1 / He + Ar	1	DC 150	He: 1.7 Ar: 0.8
Si / 2 / He + Ar	2	DC 150	He: 1.7 Ar: 0.8
Si / 1 / Ar	1	DC 150	1.4
Si / 2 / Ar	2	DC 150	1.4

Apartado 5:

Tabla 2.6: Recubrimientos usados en el diseño de los dispositivos ópticos.

Dispositivo óptico *	Recubrimientos	Secuencia
DBR 1	L_{n1}: Si/He H_n: Si/Ar/bias	Sust-$(H_nL_{n1})^7H_n$-aire
DBR 2	L_{n2}: Si/He/b 100 H_n: Si/Ar/bias	Sust-$(H_nL_{n2})^7H_n$-aire
OMC	L_{n2}: Si/He/b 100 H_n: Si/Ar/bias L_c: Si/He/b 100	Sust-$(H_nL_{n2})^4H_n$-L_c-$(H_nL_{n2})^4H_n$-aire

* *DBR:* reflector de Bragg distribuido. *OMC*: Microcavidad óptica.

3. NUEVA METODOLOGÍA BOTTOM-UP PARA PRODUCIR RECUBRIMIENTOS DE SILICIO POROSO POR MAGNETRON SPUTTERING

En este apartado de la tesis se pretende demostrar la posibilidad de producir recubrimientos de silicio poroso con porosidad cerrada, proponiendo de esta forma una nueva metodología *bottom-up* para la producción de recubrimientos de silicio poroso. Para ello, se estudiará la influencia de diferentes parámetros de deposición (presión y naturaleza del gas de sputtering, potencia de deposición, temperatura y voltaje aplicado a los sustratos y geometría de deposición) sobre la estructura final del recubrimiento y su efecto sobre las propiedades ópticas, demostrando así la posibilidad de producir recubrimientos con propiedades ópticas a medida.

3.1. RECUBRIMIENTOS DE SILICIO POROSO AMORFO CON POROSIDAD CERRADA POR MAGNETRON SPUTTERING

Los resultados previos obtenidos en el grupo NanoMatMicro utilizando helio como gas de sputtering han sido el punto de partida para el desarrollo de esta nueva metodología para la producción de recubrimientos de silicio poroso con índice de refracción controlado.

La figura 3.1 describe la cámara de deposición utilizada en estos estudios previos y que se empleó también en esta sección para la producción de los dos tipos de recubrimientos de silicio. Uno de ellos depositado con helio resultando una estructura con porosidad cerrada (a-pSi) y otro depositado con Ar y de estructura más densa (a-Si). En la tabla 3.1 se muestran las condiciones de deposición utilizadas para ambos recubrimientos.

Tabla 3.1: Condiciones de deposición.

Condiciones de deposición	
Potencia RF (W)	150
Distancia blanco – sustrato (cm)	10
Presión de base (Pa)	$1 \cdot 10^{-4}$
Presión de gas (Pa)	1.33
Gases de deposición	Ar, He

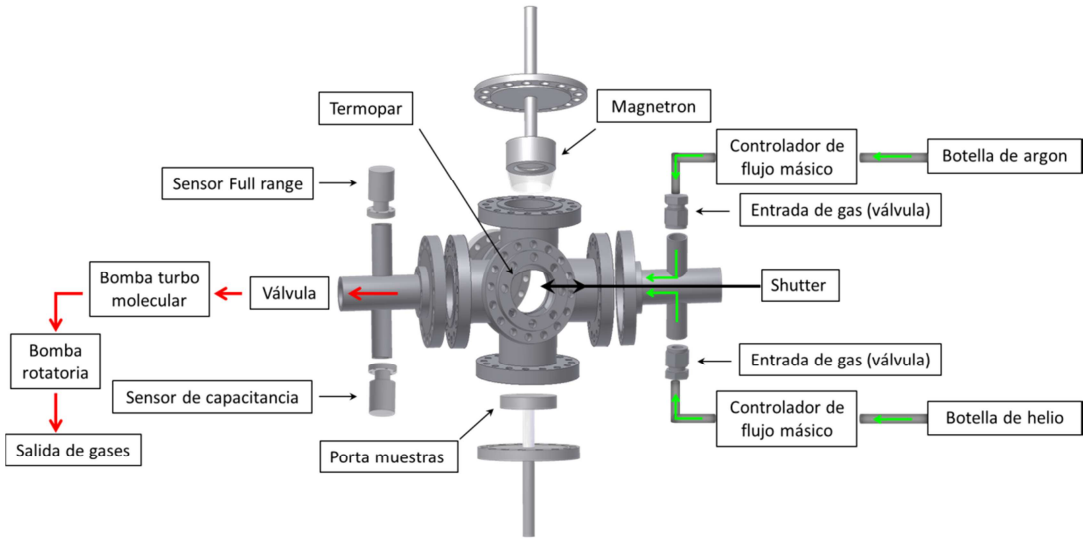

Figura 3.1: Cámara de deposición utilizada para depositar los recubrimientos (denso y poroso) analizados en esta sección.

En la figura 3.2 se muestran imágenes de microscopía electrónica de los recubrimientos denso y poroso. En el caso del recubrimiento poroso (figura 3.2 (a) y (b)) se puede observar como la porosidad está alineada en la dirección de crecimiento del recubrimiento con un

tamaño de poro que varía entre 10 y $50\ nm$.También se muestra el carácter amorfo de estos recubrimientos dado por el patrón de difracción de electrones.

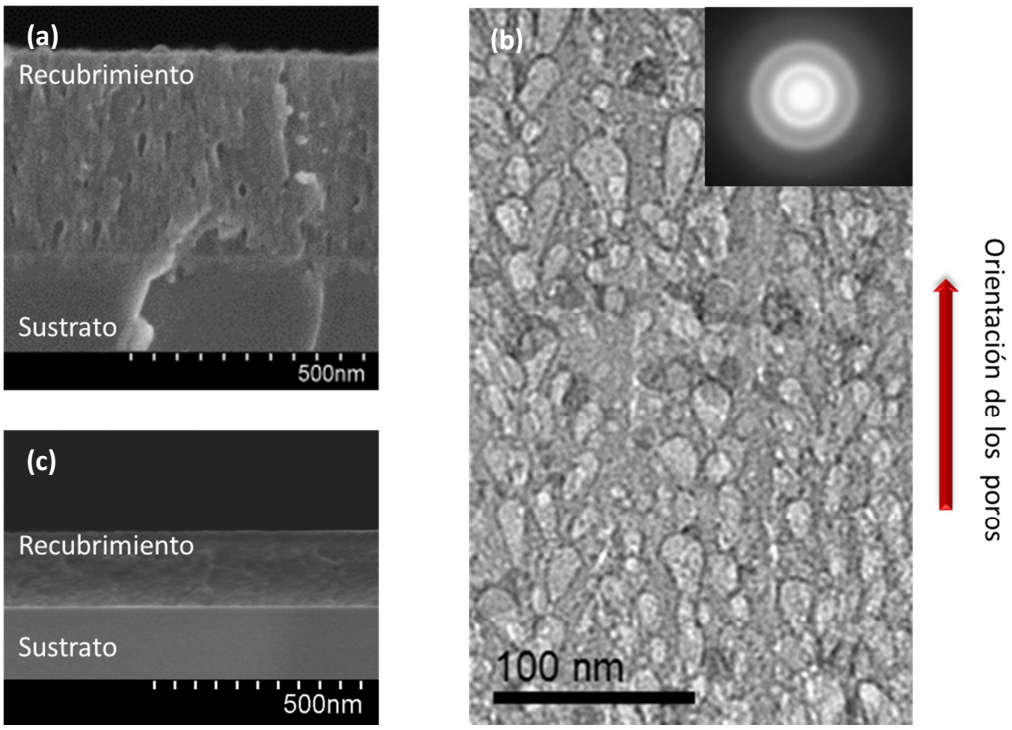

Figura 3.2: (a) Sección transversal por SEM del recubrimiento de silicio poroso amorfo (a-pSi). (b) Sección transversal por TEM de la misma muestra y patrón de difracción de electrones. (c) Sección transversal por SEM del recubrimiento de silicio denso (a-Si).

La composición química de los recubrimientos fue estudia por medio de las técnicas de XPS y RBS. Los resultados de XPS indican que las capas presentan composición similar y están formadas mayoritariamente de silicio metálico (Si^0), con una fuerte oxidación superficial como confirman los resultados de RBS. En la figura 3.3 (a) se muestran los espectros de XPS para las muestras porosa y densa en el que se observan los picos Si 2p correspondientes al óxido de silicio (SiO_2) y al silicio metálico (Si^0).

El espectro de RBS obtenido a $1983\,keV$ de la muestra porosa (a-pSi), figura 3.3 (b), presenta un pico correspondiente al He ($\sim 14\,\%\,at.$), comprobando de esta forma su incorporación. Este pico no se observa en las capas depositadas con Ar.

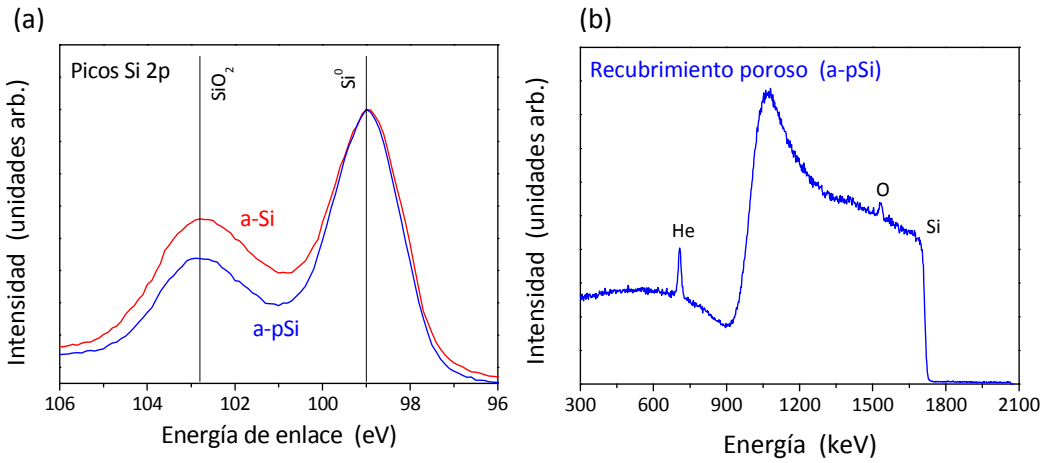

Figura 3.3: (a) Espectros de XPS. Picos Si 2p de los recubrimientos poroso (a-pSi) y denso (a-Si). (b) Espectro de RBS del recubrimiento poroso (a-pSi) depositado con He.

La introducción de porosidad permite variar el índice de refracción de los materiales. En la tabla 3.2 se presentan los valores del índice de refracción a $500\,nm$, obtenidos por elipsometria para las películas estudiadas en comparación con valores de la literatura. La introducción de porosidad cerrada permite una importante disminución del índice de refracción (de 4.9 a 3.6) para recubrimientos con composición similar.

Tabla 3.2: Índices de refracción de los recubrimientos poroso y denso a $500\,nm$ comparados con los valores en la literatura de [19].

	Material	Índice de refracción n $(\lambda = 500\,nm)$
	Recubrimiento poroso (a-pSi)	3.6
	Recubrimiento denso (a-Si)	4.9
Valores en la literatura	**Silicio cristalino c-Si**	$\mathbf{3.49}$ [19]
	Silicio amorfo a-Si	$\mathbf{4.90}$ [19]
	Silicio poroso pSi	$\mathbf{1-3.5}$ [19]

Los resultados presentados en esta sección han permitido confirmar y reproducir experimentalmente los resultados preliminares obtenidos en el grupo. Estas son las bases para desarrollo de la nueva metodología para la producción de recubrimientos de Si poroso. A continuación se detalla de forma sistemática la influencia de los diferentes parámetros de deposición en la estructura de los recubrimientos. Con los resultados obtenidos se propone un diagrama descriptivo del crecimiento de estos recubrimientos porosos en función de los parámetros de deposición.

3.2. Influencia de los parámetros de deposición en recubrimientos de silicio poroso amorfo

3.3.1. Geometría de deposición. Deposición a ángulo oblicuo

La geometría de deposición es un parámetro determinante para el crecimiento y evolución microestructural en procesos de PVD. En condiciones de baja temperatura de deposición ($\frac{T_{sustrato}}{T_{fusión\ material}} < 0.3$) la estructura de los recubrimientos depositados por magnetrón sputtering viene determinada por la baja movilidad de adatomos y efectos de sombra que dan origen a un crecimiento de estructuras columnares (más detalles en el apéndice III). En sistemas de deposición de ángulo oblicuo, los primeros átomos que se depositan sobre el sustrato forman núcleos sobre los cuales los átomos que llegan a continuación se depositan, produciendo zonas de sombra en las cuales no se deposita material. Este mecanismo da origen a estructuras columnares orientadas. Modificando el ángulo de incidencia de los átomos es posible producir diferentes tipos de estructuras porosas con porosidad abierta. En el caso de la metodología desarrollada en esta tesis se cumplen las condiciones de baja movilidad de adatomos. Así, se observa una orientación de la porosidad en la dirección de crecimiento de las capas cuando se utilizan unas condiciones de deposición con el magnetrón en posición vertical (como es el caso de los resultados presentados en la sección anterior). En esta sección se estudia la influencia del ángulo de deposición sobre la estructura de recubrimientos porosos depositados en atmosfera de helio. Se ha utilizado la cámara de deposición descrita en apartado 2 de este resumen con la geometría de deposición mostrada en la figura 3.4.

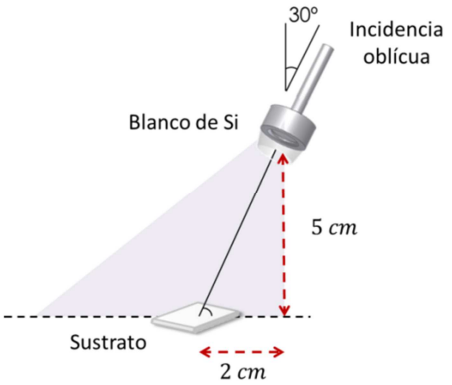

Figura 3.4: Representación de la geometría de deposición utilizada.

La tabla 3.3 presenta las condiciones experimentales utilizadas en esta sección.

Tabla 3.3: Condiciones de deposición utilizadas en ángulo oblicuo.

Condiciones de deposición	
Potencia RF (W)	150
Distancia blanco – sustrato (cm)	5
Presión de base (Pa)	$1 \cdot 10^{-4}$
Presión de gas (Pa)	4.8
Gas de deposición	He

En la figura 3.5 se muestra la estructura resultante del recubrimiento poroso depositado con las anteriores condiciones de deposición. Se observa porosidad cerrada, inclinada un ángulo β_p (véase figura 3.5(c)) con respecto a la normal al sustrato. Aunque este ángulo es menor que el ángulo de deposición α, se cumple la relación entre ángulos dada por la regla de la tangente [20] (más detalles en el apéndice III). De esta forma se muestra que cambiando el ángulo del magnetrón con respecto al sustrato es posible orientar la porosidad cerrada. Esta estrategia puede ser interesante a la hora de modificar las propiedades ópticas de los recubrimientos porosos.

La geometría de ángulo oblicuo presentada en esta sección se utilizará en los estudios presentados en las secciones siguientes.

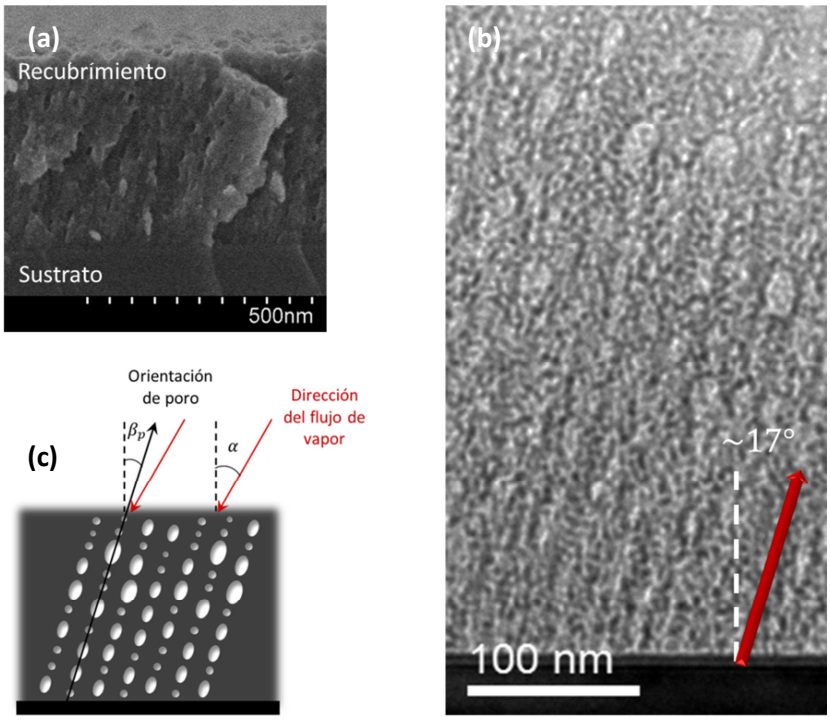

Figura 3.5: (a) Sección transversal por SEM del recubrimiento de silicio poroso amorfo. (b) Sección transversal por TEM del mismo recubrimiento. (c) Orientación de los poros en deposición a ángulo oblicuo (α – ángulo de deposición, β_p – dirección de alineación de los poros).

3.3.2. Gas de sputtering

El gas de proceso afecta no solo al rendimiento de pulverización (sputtering yield) y las propiedades del plasma, sino también a la llegada del material a los sustratos [21–23]. La relación entre las masas atómicas del gas de bombardeo y del material a depositar influye en la transferencia de energía y momento en los procesos de colisión en el plasma modificando la trayectoria de los átomos que llegan al sustrato para formar el recubrimiento. Por otra parte masa del gas de sputtering afecta también a la generación de los diferentes iones en la descarga del plasma, que a su vez afectan la trayectoria de los átomos en el plasma.

Varios autores han investigado los efectos de diferentes gases inertes en las propiedades del plasma en descargas RF [22–27]. Sin embargo en estos trabajos no se discute la influencia de gases inertes, en procesos de magnetrón sputtering en ángulo oblicuo, en la microestructura de las películas delgadas.

En esta sección el efecto de la naturaleza del gas inerte, He y Ar, en la microestructura de recubrimientos depositados en ángulo oblicuo, bajo condiciones similares de presión y potencia ha sido investigado. En la tabla 3.4 se presentan las condiciones de deposición empleadas.

Tabla 3.4: Condiciones de deposición de los recubrimientos depositados con diferente gas de sputtering.

Recubrimiento	Gas de sputtering	Potencia RF (W)	Presión de gas (Pa)	Velocidad de deposición * (nm/min)
Si / He	He	150	4.8	15
Si / Ar	Ar	150	4.8	32

*Calculadas a partir de los espesores obtenidos por imágenes de SEM en sección transversal.

En la figura 3.6 las micrografías de SEM en visión planar y sección transversal muestran la morfología de los recubrimientos. También se presentan los resultados de TEM en sección transversal.

La velocidad de deposición calculada a partir de los resultados de SEM (tabla 3.4) indica, tal como sería de esperar, una menor velocidad de deposición para los recubrimientos depositados con He. El He presenta un rendimiento de pulverización menor que el Ar.

El uso de diferentes gases inertes de síntesis propicia la formación de diferentes estructuras como se puede observar en la figura 3.6. El uso de He da lugar a una estructura porosa con poros cerrados que crecen inclinados debido a geometría de deposición como ya se ha explicado en el apartado anterior. Sin embargo, el uso de Ar genera una estructura columnar con una orientación normal al sustrato en la que se aprecian espacios intercolumnares. La pérdida de direccionalidad en el caso de la deposición con Ar puede deberse a la presión de deposición y a la elevada masa del Ar con respecto a la del Si. En los

procesos de colisión en el plasma los átomos de Si se dispersan, perdiendo energía y dirección, llegando al sustrato de forma aleatoria.

El He presenta un rendimiento de pulverización muy bajo, sin embargo los átomos de He presentan estados metaestables de energía superior a la de los presentados por los átomos de Ar. Los resultados de microscopia electrónica muestran una superficie más plana en el caso de los recubrimientos fabricados con He, que puede deberse al impacto en la capa en crecimiento de átomos e iones de energía más elevada.

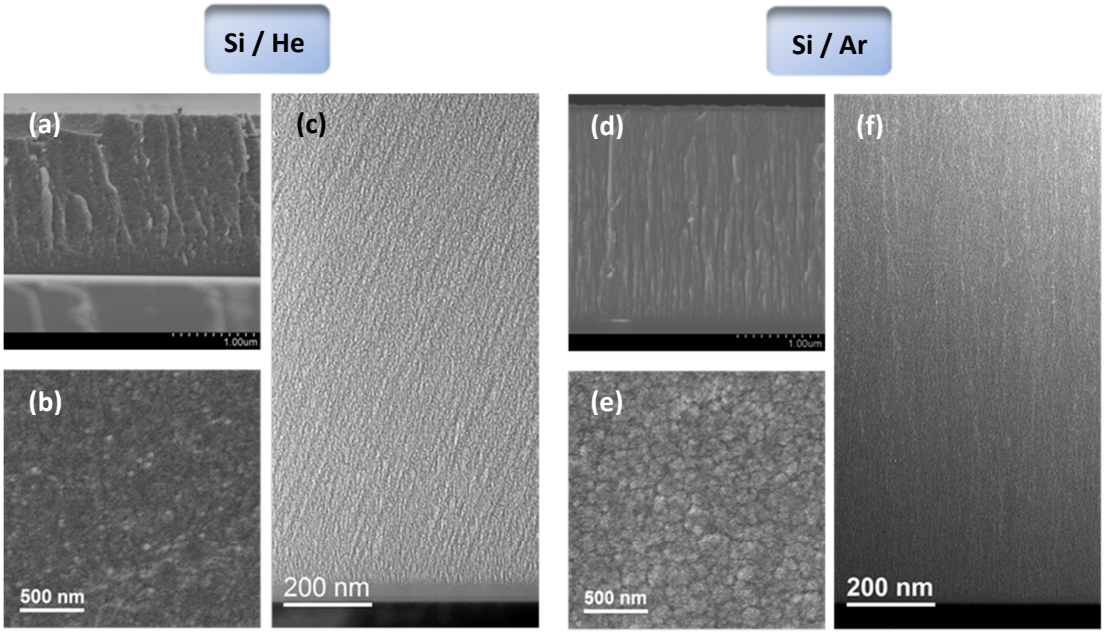

Figura 3.6: (a) y (d) Sección transversal por SEM. (b) y (e) Vista de la superficie por SEM. (c) y (f) Sección transversal por TEM de los recubrimientos depositados utilizando helio y argón respectivamente.

3.3.3. Presión de helio

La presión del gas de proceso es el parámetro de mayor influencia sobre la trayectoria y de los átomos de material, provenientes del blanco. Las partículas arrancadas del blanco colisionan con los átomos del gas en su trayectoria hacia el sustrato de forma que cuanto mayor la presión, mayor es el número de colisiones. Estas colisiones modifican la energía,

dirección y momento de los átomos arrancados del blanco y por lo tanto la morfología y la microestructura de las capas.

En deposición en ángulo oblicuo los efectos de sombra solo son posibles para flujos de partículas colimados (valores típicos de presión para deposición por evaporación de $0.133\ Pa$ para una distancia fuente-sustrato de $45\ cm$). En esta tesis el efecto de la presión de He en la morfología y microestructura de películas delgadas de silicio poroso se investigó para una distancia magnetrón-sustrato de $5\ cm$ y a una potencia de $150\ W$ RF, utilizando presiones de trabajo de 2.7 a $54.6\ Pa$. El rango de presiones seleccionado está limitado por las condiciones experimentales. Para presiones inferiores a $2.7\ Pa$ no es posible mantener la descarga y para presiones superiores a $54.6\ Pa$ el sistema de vacío no es capaz de mantener constante la presión con el consecuente paro de la bomba turbomolecular.

En la figura 3.7 se muestra la morfología de los recubrimientos estudiados en función de la presión de deposición. A presiones más bajas se obtienen superficies más planas, mientras que para presiones de trabajo más elevadas la superficie de los recubrimientos es más rugosa. Este efecto puede asociarse a una más baja energía de los iones de He para presiones más altas, al igual que se observa para otros gases inertes [22,23].

En la deposición convencional en ángulo oblicuo, utilizando Ar, se ha reportado que la presión ejerce un efecto significativo sobre el ángulo que presentan las columnas [28]. En este trabajo se observa un efecto similar en el ángulo de alineación de los poros. Para bajas presiones de trabajo, la inclinación de los poros es similar a la inclinación del magnetrón ($\sim 30°$); y disminuye con el aumento de la presión, alcanzando valores prácticamente constantes para presiones superiores a $20\ Pa$.

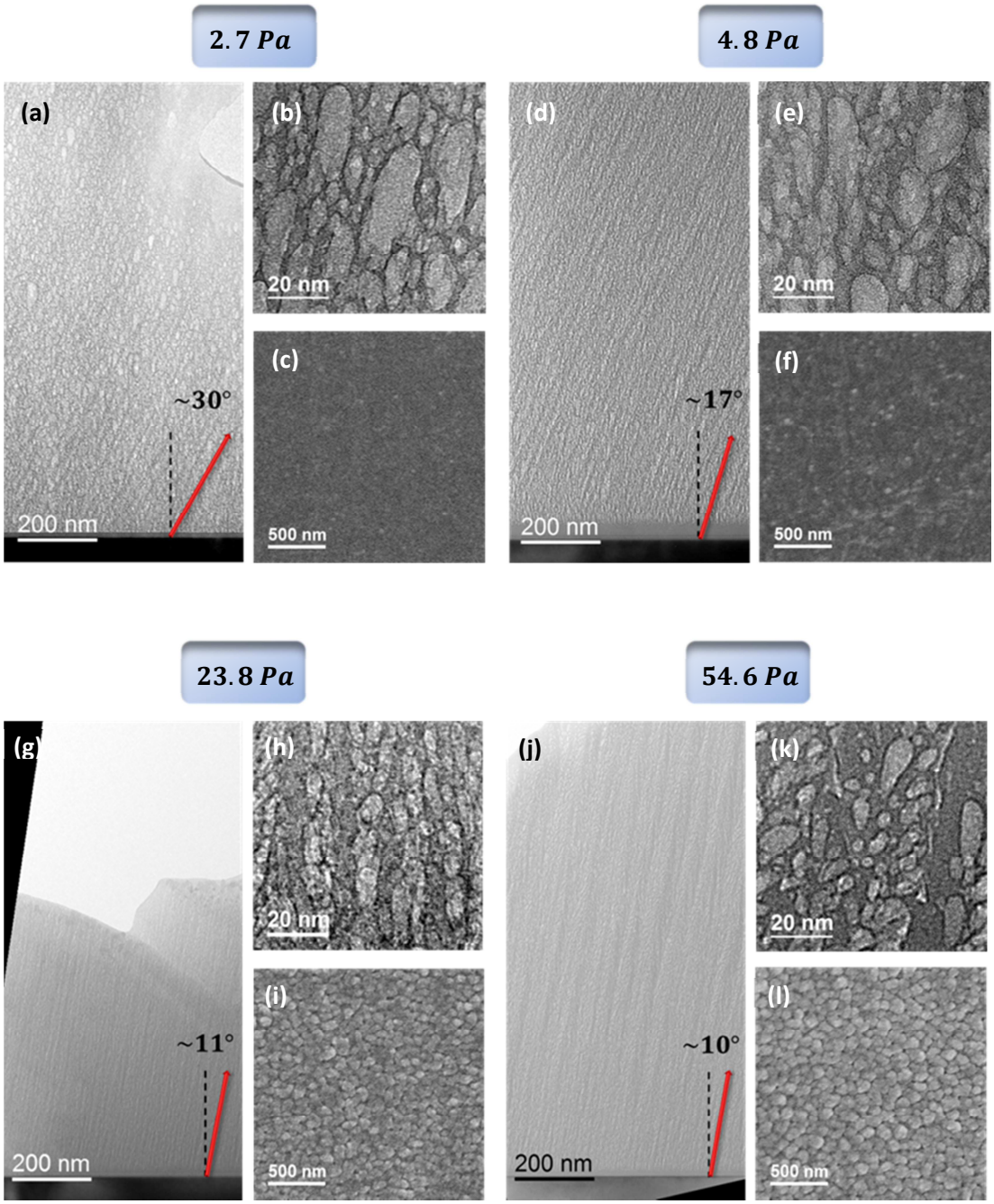

Figura 3.7: (a), (d), (g) y (j) Sección transversal por TEM. (b), (e), (h) y (k) Detalle de los poros por TEM. (c), (f), (i) y (l) Vista de la superficie por SEM de los recubrimientos depositados a diferentes presiones de He.

La figura 3.8 (a) presenta la variación del ángulo de los poros en función de la presión de He. Este efecto se debe a que el recogido libre medio (λ) de los átomos que dejan el blanco es inversamente proporcional a la presión. Cuando la presión aumenta, la probabilidad de que un átomo arrancado del blanco colisione con átomos del gas de proceso aumenta disminuyendo el recogido libre medio. Para elevados valores de λ la trayectoria de los átomos arrancados del blanco no se ve afectada por la presión debido al bajo número de colisiones que sufren. Por otro lado para valores elevados de presión se alcanza un elevado grado de termalización y los átomos que llegan al sustrato han perdido su direccionalidad debido al elevado número de colisiones con los átomos del gas.

Por último, es importante señalar el efecto de la presión de trabajo sobre la cantidad de He atrapado en los recubrimientos. En la figura 3.8 (b) se observa una clara disminución de la cantidad de He atrapado al aumentar la presión de deposición.

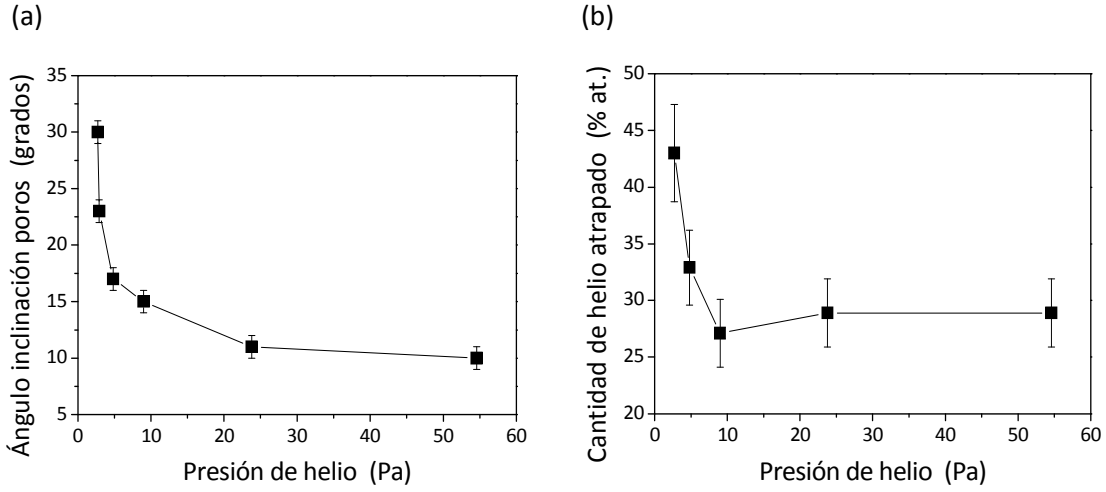

Figura 3.8: (a) Ángulo de orientación de los poros. (b) Cantidad de He atrapado en los recubrimiento de Si, en función de la presión de He durante la deposición.

Se observa una acentuada disminución de la cantidad de He atrapado en los recubrimientos de Si para presiones de He entre 2 y $10\,Pa$. Para valores superiores de presión de deposición la cantidad de He atrapada se mantiene prácticamente constante en el rango

investigado. En definitiva, un cambio en la presión de helio se traduce en una modificación del ángulo de alineación de los poros así como en la cantidad de helio atrapado en el recubrimiento.

3.3.4. Potencia aplicada

Al igual que la presión de gas de proceso, la potencia de sputtering permite modificar la energía con la que los átomos arrancados del blanco llegan al sustrato. A fin estudiar el efecto de la potencia de descarga RF en la nanoestructura porosa, se han depositado recubrimientos de silicio empleando diferentes potencias y utilizando He como gas de sputtering manteniendo fija la presión. En la tabla 3.5 se presentan las condiciones de deposición utilizadas para los recubrimientos estudiados.

Tabla 3.5: Efecto de la potencia aplicada. Condiciones de deposición de los recubrimientos.

Recubrimiento	Potencia RF (W)	Presión de He (Pa)	Velocidad de deposición * (nm/min)
Si/He/P 50	50	4.8	2
Si/He/P 150	150	4.8	15
Si/He/P 300	300	4.8	28

*Calculadas a partir de los espesores obtenidos por imágenes de SEM en sección transversal.

Como cabría esperar la velocidad de deposición aumenta significativamente con el aumento de la potencia aplicada. En la figura 3.9 (de (a) a (f)) se presentan micrografías de barrido de las capas en superficie y sección transversal. El aumento de la potencia aplicada al blanco no produce efectos significativos en porosidad de los recubrimientos. Se observa que la superficie de las muestras depositadas a potencia más elevada es menos rugosa, siendo una consecuencia de la elevada energía de los átomos e iones que bombardean el sustrato. Aumentando la potencia en RF resulta en un aumento del "DC-self bias" (ver apéndice II) aumentando de esta forma el bombardeo iónico durante el crecimiento de la capa.

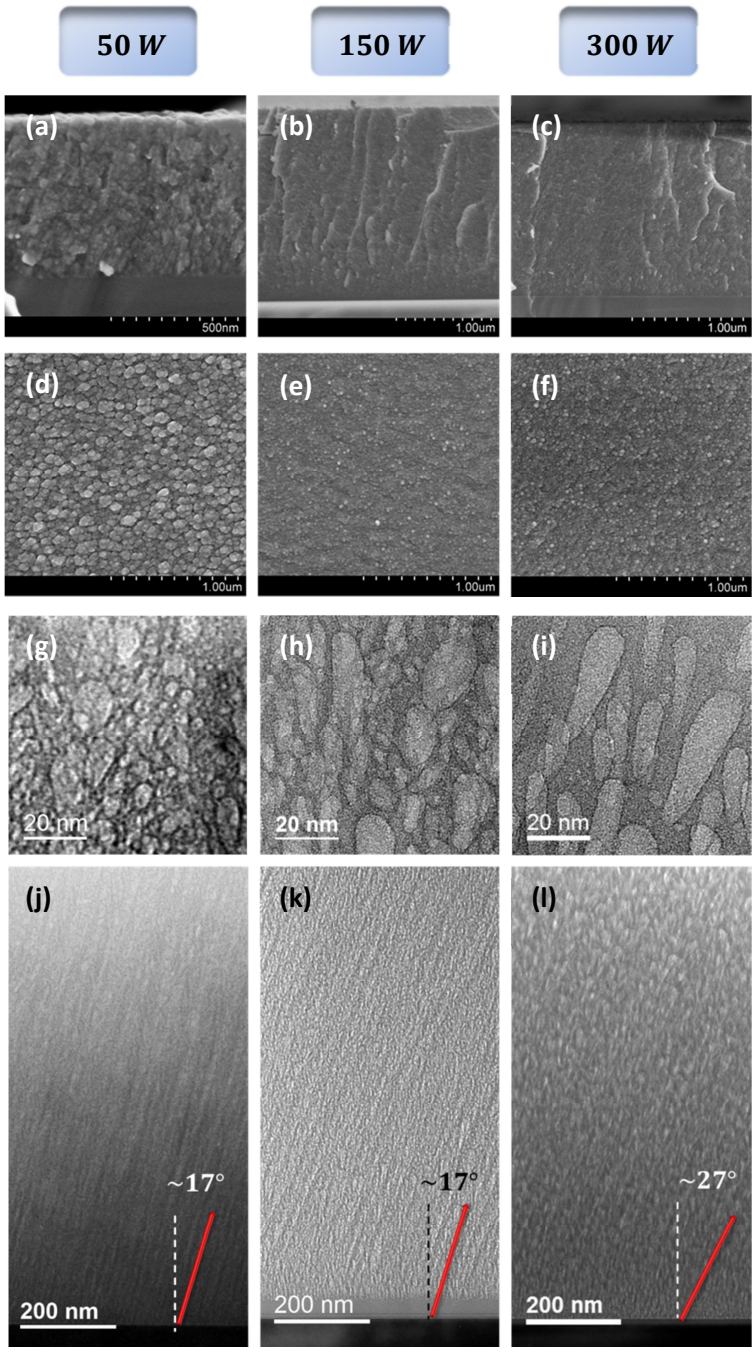

Figura 3.9: Efecto de la potencia aplicada (50, 150 y 300 W respectivamente) en recubrimientos porosos observados. Micrografías SEM: vista superficie (a), (b) y (c) y sección transversal (d), (e), (f). Detalle de los poros por micrografías TEM a diferentes potencias. (g), (h) y (i) .Sección transversal de los recubrimientos (j), (k) y (l).

La porosidad de los recubrimientos y su orientación se muestra en detalle en la figura 3.9 de (g) a (l). Se destaca un cambio en el ángulo de alineación de los poros en la muestra depositada a $300\,W$ con respecto a las muestras depositadas a potencias inferiores. La pérdida de direccionalidad en los recubrimientos depositados a 50 y $150\,W$, puede deberse a un menor bombardeo iónico y menor energía de los átomos arrancados.

También se observa un efecto tanto en el tamaño como en la forma de los poros. Medidas del tamaño de poro reflejan un incremento, tanto en su diámetro mayor como menor para potencias más elevadas. El recubrimiento depositado a menor potencia ($50\,W$) tiene un diámetro mayor medio de poro entorno a $11\,nm$ mientras que para la muestra depositada a mayor potencia ($300\,W$) se observa un diámetro mayor medio entorno a $22\,nm$. También se aprecia un cambio en la forma del poro teniéndose poros más redondeados a baja potencia y cambiando a una forma más alargada a altas potencias.

Cabe esperar que estos cambios en el tamaño medio de poros tengan efecto sobre propiedades que dependan directamente de la porosidad como es el caso del índice de refracción. Las propiedades ópticas de los recubrimientos se han investigado por elipsometría. En la figura 3.10 se observa la variación del índice de refracción con la longitud de onda (en el rango de 600 a $2000\,nm$) para las muestras depositadas a las distintas potencias estudiadas. Un aumento del índice de refracción tiene lugar cuando se aumenta la potencia en el rango de 150 a $300\,W$.

La composición de esto recubrimientos se investigó p-RBS para evaluar el efecto de la potencia sobre la cantidad de He atrapada en los poros cerrados. Los resultados se presentan en la tabla 3.6.

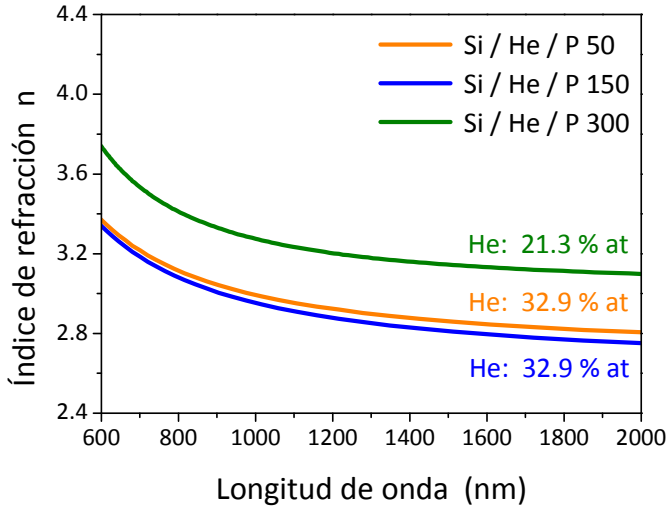

Figura 3.10: Efecto de la potencia sobre el índice de refracción.

Tabla 3.6: Efecto de la potencia de deposición en la cantidad de He atrapado en los recubrimientos.

Coating	Si (% at.)	He (% at.)	O (% at.)
Si/He/P 50	64.7	32.9	2.4
Si/He/P 150	64.7	32.9	2.4
Si/He/P 300	78.7	21.3	---

Los recubrimientos se componen mayoritariamente de Si y He con una pequeña contaminación de O en el caso de los recubrimientos depositados a bajas potencias.

Por otra parte se observa que a pesar de un mayor tamaño de poro, la muestra depositada a $300\ W$ presenta menor cantidad de He incorporado. Esta reducción en la incorporación de He puede deberse a una desorción de los átomos de He en la capa debida a la alta energía de los átomos de Si que se depositan, desplazando los átomos de He.

Los resultados presentados en las secciones anteriores asumen, con base a trabajos previos [15], que la cantidad de He incorporada en los recubrimientos se encuentra dentro de los poros, sin embargo no se ha mostrado hasta ahora evidencia experimental que lo

corrobore. Se hacen necesarias técnicas de análisis a la nano escala como es el caso de STEM/EELS, que permitan identificar y caracterizar el He atrapado en los recubrimientos. Para este estudio se utilizó la muestra depositada a $300\,W$, ya que esta presenta poros grandes y relativamente dispersos, facilitando el análisis de un solo poro. Micrografías de campo oscuro con detector anular (ADF-STEM) y espectros EELS con elevada resolución lateral se han registrado simultáneamente en poros aislados de diferente tamaño. La figura 3.11 presenta la imagen ADF-STEM adquirida junto con los espectros EELS en el rango de bajas energías. A cada pixel de $1 \times 1\,nm^2$ corresponde un espectro EELS. En las imágenes ADF, la matriz de silicio de mayor número atómico presenta mayor intensidad correspondiendo a las zonas más claras en la imagen y los poros a las zonas más oscuras.

En la figura 3.11 (b) se presentan los espectros EELS en el rango de bajas energías para tres pixeles seleccionados en el centro, borde y fuera de un poro. El espectro correspondiente al pixel $(16,10)$, fuera del poro, presenta un pico a $17\,eV$ característico del plasmon del Si. En el borde del poro (pixel $(5,\,10)$) otro pico a $22\,eV$ aparece aumentando de intensidad en la posición $(6,13)$ o sea en el centro del poro. Este pico corresponde al borde K del He, confirmando de este modo la presencia de He dentro del poro. En el apéndice IV [29] se presenta un análisis más detallado del estado del He dentro de los poros.

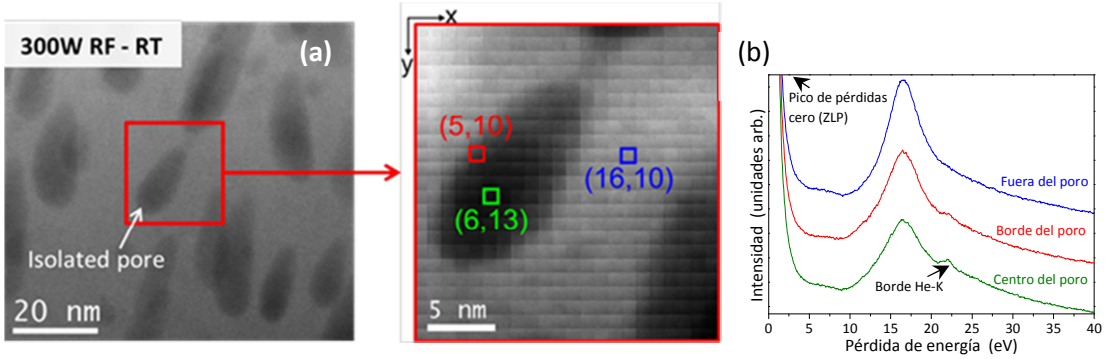

Figura 3.11: (a) Imagen ADF-STEM de la capa porosa mostrando los poros en negro, (b) Espectros EELS en el rango de bajas energías correspondientes a los pixeles marcados en (a).

3.3.5. Bias en el sustrato

La aplicación de un voltaje (bias) al sustrato altera los campos eléctricos cerca del sustrato, modificando el flujo y energía de los átomos a depositar. Al polarizar negativamente el sustrato, los iones positivos del plasma son acelerados hacia el sustrato con energías muy elevadas [21,30]. El efecto de la polarización en la deposición de estructuras porosas se ha investigado aplicando diferente de voltaje al sustrato durante la deposición. En la tabla 3.7 se presentan las condiciones de preparación de las muestras estudiadas.

Tabla 3.7: Condiciones de deposición de los recubrimientos preparados bajo diferente voltaje bias.

Recubrimiento	Voltaje bias (V)	Presión de He (Pa)	Potencia RF (W)	Tiempo de deposición (min)	Espesor (nm)	Razón de deposición efectiva* (nm/min)
Si/He/b 0	$flotante$	9.0	150	120	1700	14
Si/He/b 100	-100	9.0	150	120	1300	11
Si/He/b 200	-200	9.0	150	180	1300	7

* Calculadas a partir de los espesores obtenidos por imágenes de SEM.
**Razón de deposición efectiva = espesor total del recubrimiento depositado / tiempo de deposición.

Se observa una reducción de la velocidad efectiva de deposición con el aumento del voltaje aplicado al sustrato ya que al aumentar el voltaje se producen efectos de sputtering de la propia capa. Es conocido que recubrimientos depositados con bias presentan estructuras más densas y compactas [31]. Para estudiar el efecto del bias en las estructuras porosas se han analizado los recubrimientos por microscopia electrónica. La figura 3.12 muestra las imágenes obtenidas por TEM en la sección transversal de las capas.

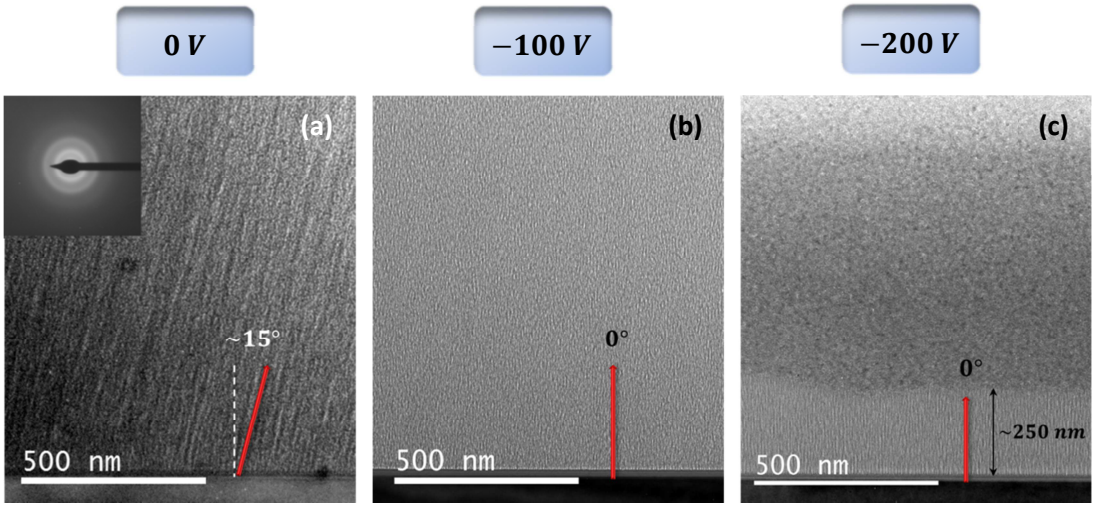

Figura 3.12: Efecto del voltaje bias sobre el crecimiento de la estructura en recubrimientos con porosidad cerrada. (a) $0\ V$. (b) $-100\ V$. (c) $-200\ V$.

En el recubrimiento depositado sin bias, los poros están inclinados en la dirección del magnetron, con un tamaño de poro que varía entre 3 y $54\ nm$. Sin embargo, con la aplicación de un bias de $-100\ V$ los poros se alinean perpendicularmente al sustrato siendo más estrechos y alargados con tamaños que varían entre 4 y $30\ nm$ en sus diámetros mayores. El bombardeo iónico favorece la movilidad de los adatomos y los efectos de sombra desaparecen, sin embargo los recubrimientos mantienen la porosidad cerrada.

Aplicando un voltaje más alto, $-200\ V$, se observan dos tipos estructuras porosas, como se muestra en la figura 3.12 (c). Una fase amorfa compuesta por poros alineados verticalmente y una fase nano-composite formada por cristales de silicio y poros cerrados embebidos en una matriz amorfa. En la figura 3.13 se muestra en detalle las diferentes zonas de la capa. La difracción de electrones de los cristales (figura 3.13 (c)) coincide con la del silicio cristalino, corroborándose que se trata de cristales de silicio. La aplicación de voltajes elevados al sustrato induce la cinética de formación de una fase nanocristalina. Efectos similares se han observado en la literatura [32–34].

La incorporación de He en estos recubrimientos se ha estudiado mediante RBS. Para los recubrimientos depositados sin polarización y con bias de $-100\,V$, la composición es uniforme a lo largo de todo el espesor del recubrimiento con un contenido en He de 27.0 y $37.6\,\%\,at.$ respectivamente, observándose un incremento de la cantidad de He incorporado con el bias aplicado.

Sin embargo, a voltajes más altos, $-200\,V$, hay una disminución de la cantidad de He atrapado en el recubrimiento, siendo de 18.2 y $12.5\,\%\,at.$ en las fases amorfa y nano-composite respectivamente. La reducción de la cantidad de He incorporado puede deberse a una reducción en el tamaño de poro así como en la cantidad de poros cerrados.

Hay que resaltar que los cambios microestructurales observados con el aumento de bias no se observan con el aumento de la temperatura del sustrato que se discutirá a continuación.

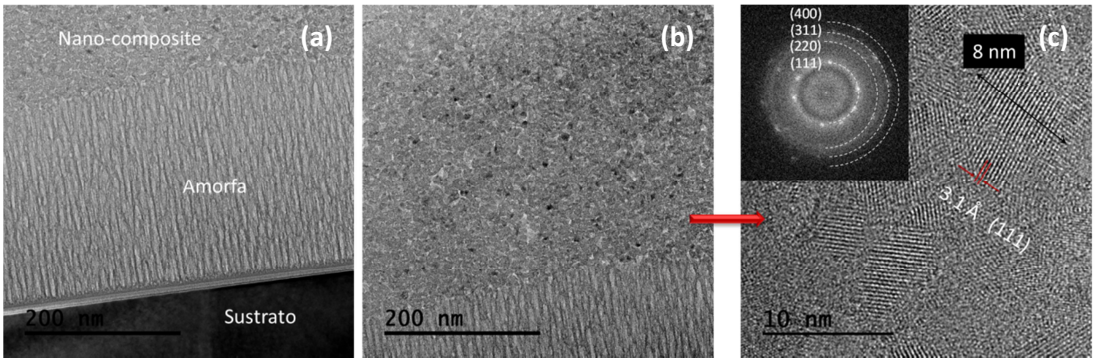

Figura 3.13: Efecto del bias sobre la estructura porosa del recubrimiento *Si/He/b 200*. (a) y (b) Fases amorfa y nano-composite. (c) Micrografía de alta resolución de la fase nano-composite mostrando los cristales de silicio y patrón de difracción de electrones.

3.3.6. Temperatura de deposición

Aunque la gran mayoría de la investigación en deposición en ángulo oblicuo se centre en deposición a baja temperatura, limitando de este modo la cinética de difusión superficial y favoreciendo los efectos de sombra; los diagramas tradicionales de estructuras de zonas

para el crecimiento de películas delgadas clasifican la microestructura en función de la temperatura homologa ($T_h = \frac{T_s}{T_m}$). En este apartado, se ha investigado la influencia de la temperatura de deposición, la cual mejora la movilidad de los adátomos, en la microestructura porosa. Para ello se han depositado recubrimientos a diferentes temperaturas de deposición. La elección de temperaturas aplicadas al sustrato está limitada por el dispositivo experimental siendo la temperatura máxima de $300°C$, sin embargo estas temperaturas se ajustan a las zonas I (*Si/He/h 0*), T (*Si/He/h 200*) y II del modelo de Thornton [35] (ver más detalles en el apéndice III). En la siguiente tabla se muestran las condiciones de deposición utilizadas.

Tabla 3.8: Condiciones de los recubrimientos depositados a diferentes temperaturas de deposición.

Recubrimiento	Temperatura de deposición $(°C)$	Presión de He (Pa)	Potencia RF (W)	Razón de deposición (nm/s)	T_s/T_m *
Si/He/h 0	---	2.7	150	0.23	0.23
Si/He/h 200	200	2.7	150	0.18	0.28
Si/He/h 300	300	2.7	150	0.14	0.34

* T_m para silicio cristalino: $1683.15\ K$.

En la figura 3.14 las imágenes de TEM muestran la estructura de los recubrimientos.

La muestra sin calentamiento *Si/He/h 0* (figura 3.14 (a)) muestra la típica estructura de poros cerrados inclinados en la dirección del magnetrón cuyo tamaño varía entre 3 y $43\ nm$ en el diámetro mayor. En este caso $T_h < 0.3$, Zona I del modelo de Thornton, la estructura se rige por efectos de sombra y de baja movilidad atómica.

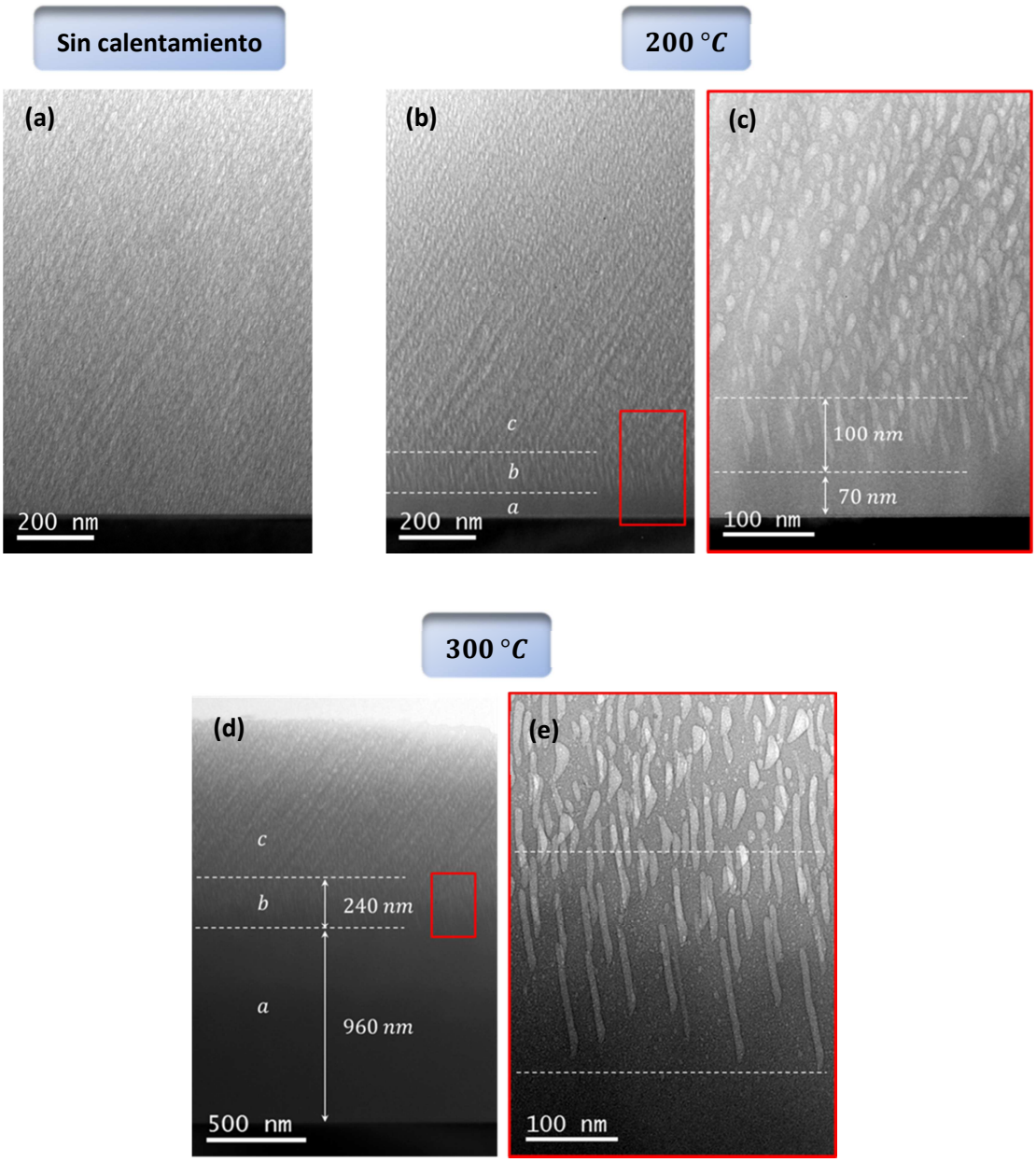

Figura 3.14: Sección transversal de los recubrimientos por TEM. (a) *Si/He/h 0*. (b) y (c) *Si/He/h 200*. (d) y (e) *Si/He/h 300*.

Cuando se aumenta la temperatura de deposición a $200\,°C$, $T_h \approx 0.3$ la difusión atómica está permitida, formándose una capa densa junto al sustrato (región a), en la cual el He no queda atrapado y es desorbido (figuras 3.14 (b) y (c)) debido a la alta temperatura y por

tanto no hay formación de poros. Sobre esta zona se observa una región porosa (región b) de poros alargados cuyo tamaño varía entre 36 y $70\,nm$. Esta formación de poros alargados puede estar relacionada con una mayor movilidad del He que es térmicamente activada. El He, al intentar escapar del recubrimiento, forma poros más alargados. A cierta distancia del sustrato, debido a la baja conductividad térmica del silicio, la temperatura no es suficiente para modificar la estructura, y una capa porosa (región c), similar a la formada en la muestra sin calentamiento, es formada con poros cuyo tamaño varía entre 4 y $54\,nm$ en su diámetro mayor.

En la muestra depositada a más alta temperatura, $300\,°C$, (figuras 3.14 (d) y (e)), se obtiene una estructura similar a la formada en la muestra *Si/He/h 200*. Se diferencian en que en este caso el espesor de la región a es mayor y que los poros formados en la región b son de mayor tamaño $\sim 170\,nm$. La capa porosa en la región c está formada por poros con un tamaño entre 4 y $83\,nm$ en su diámetro mayor.

La composición de los recubrimientos fue analizada por p-RBS para evaluar el efecto de la temperatura de deposición en la cantidad de He incorporado al recubrimiento. El recubrimiento depositado sin calentamiento tiene incorporado un $44\,\%\,at.$ de He, mientras que en los recubrimientos depositados con temperatura, en la región a (capa densa) no se detectó la presencia de He. En las regiones b y c, para la muestra *Si/He/h 200*, alrededor de un $41\,\%\,at.$ está formado por He. En el caso de la muestra a más alta temperatura, *Si/He/h 300*, este porcentaje de He es reducido a un $22\,\%\,at.$. Un aumento de la temperatura de deposición promueve la movilidad del He en la capa y menor cantidad es incorporado al recubrimiento.

3.3. Estabilidad de los recubrimientos porosos

A la hora de incorporar de este tipo de recubrimientos en dispositivos reales se cuestiona la estabilidad no solo de estas estructuras porosas sino también del He en el recubrimiento. Se ha investigado la estabilidad del He en la de estructura porosa realizando medidas de RBS a una misma muestra en distintas fechas, separadas algunos meses incluso hasta 2

años. En la figura 3.15 se muestran los espectros de RBS. Una cantidad de He de alrededor de $\sim 32\ \%\ at.$ es incorporada al recubrimiento, la cual no cambia hasta dos años después.

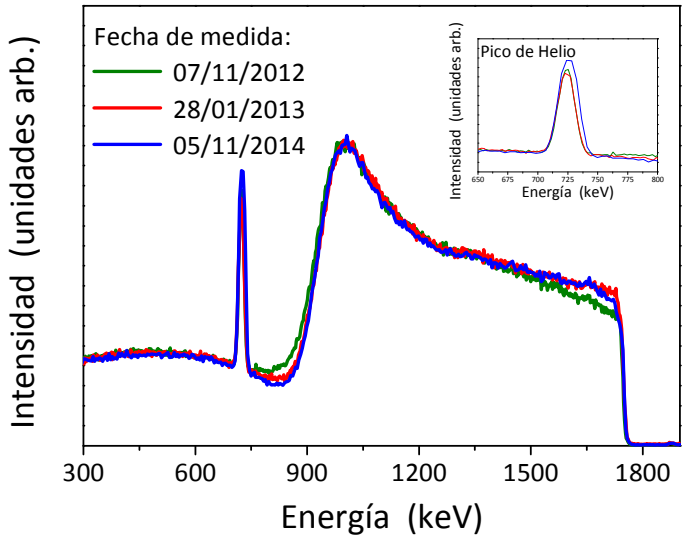

Figura 3.15: Espectros de RBS de una muestra porosa medidos en distintos instantes de tiempo.

Por otro lado, trabajos previos sobre implantación de He en materiales demostraron la coalescencia de los poros y la liberación de He por medio de tratamientos térmicos [36,37]. Siguiendo esta misma línea, se han realizado, sobre un recubrimiento poroso, tratamientos térmicos a diferentes temperaturas. El objetivo es observar el efecto sobre la estructura y sobre la cantidad de He atrapado en el recubrimiento. Una muestra porosa, *Si/He/As dep,* fue depositada utilizando He a una presión de $2.7\ Pa$ y una potencia de $150\ W$ RF con una distancia entre el blanco y el sustrato de $5\ cm$. El calentamiento se realizó en un horno bajo un flujo de He de $100\ ml/min$, aplicando una rampa de calentamiento de $10°C/min$ hasta alcanzar la temperatura deseada que se mantuvo durante $120\ min$. Se han elegido dos temperaturas de calentamiento, 300 y $550°C$, por debajo de la temperatura de cristalización para recubrimientos de silicio amorfo [38]. El efecto de la temperatura sobre la estructura ha sido analizado a través de medidas de difracción de rayos X (XRD). En la figura 3.16 se muestran los espectros de difracción.

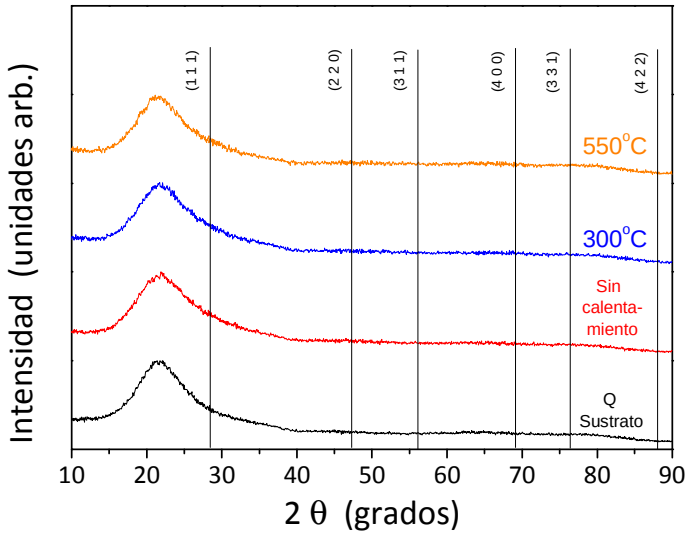

Figura 3.16: Espectros de difracción de rayos X para los recubrimientos porosos depositados sin calentamiento, a 300 y $550°C$, así como del sustrato.

Como puede verse, las muestras conservan el carácter amorfo después de los diferentes tratamientos térmicos. Tampoco se dan cambios significativos en la porosidad. La muestra depositada sin calentamiento (*Si/He/As dep*) muestra un tamaño de poro comprendido entre 3 y $60\ nm$, mientras que para las dos muestras sometidas a tratamiento térmico (*Si/He/HT-300C* y *Si/He/HT-550C*) entre 3 y $70\ nm$ (figura 3.17).

La composición química ha sido estudiada mediante medidas de RBS. En la siguiente tabla se muestra la composición para cada uno de los recubrimientos estudiados.

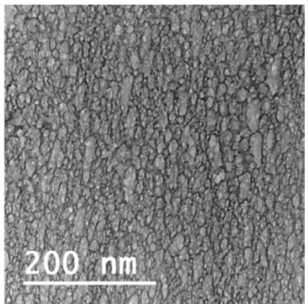

Tabla 3.9: Composición química por RBS de los recubrimientos bajo tratamiento térmico.

Recubrimiento	Espesor ($\cdot 10^{15}\ at/cm^2$)	Si ($\%\ at.$)	He ($\%\ at.$)	O ($\%\ at.$)
Si/He/As dep	7930	54.9	43.4	1.7
Si/He/HT-300C	7256	56.8	41.2	2.0
Si/He/HT-550C	5390	89.8	5.1	5.1

Figura 3.17: Imagen TEM en sección transversal de la muestra tratada a $550°C$. Composición química por RBS de los recubrimientos tras tratamiento térmico.

Como se observa, hasta una temperatura de $300°C$, los recubrimientos presentan una composición similar, con un alto porcentaje de He ($\sim 40\ \%\ at.$). Sin embargo, a $550°C$ un fuerte decrecimiento en el contenido de He es observado ($\sim 5\ \%\ at.$). Esto demuestra que el He dentro de los poros permanece estable hasta una temperatura de $300°C$.

3.4. Diagrama de estructura de zonas para recurbimientos de silicio poroso con porosidad cerrada por magnetrón sputtering

La correlación entre las condiciones de deposición y los análisis microestructurales y químicos permite proponer a modo de resumen un modelo empírico para el crecimiento de recubrimientos de porosidad cerrada por magnetrón sputtering frente a los diferentes parámetros.

Gas de sputtering: $P = 150\ W$ RF, $p = 4.8\ Pa$

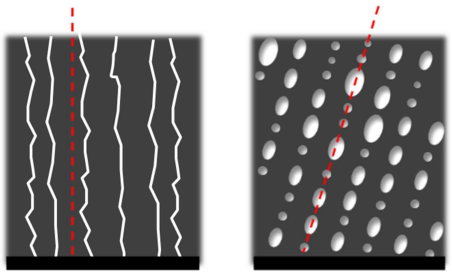

Argón *Helio*

Geometría de deposición: $P = 150\ W$ RF

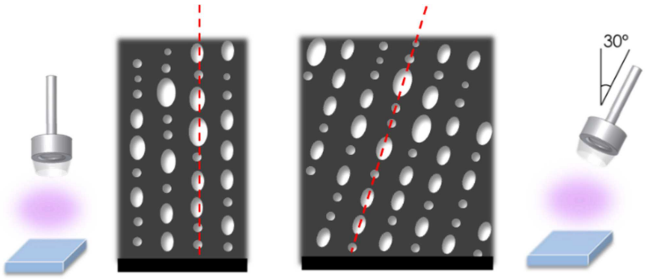

Presión de helio: $P = 150\ W$ RF

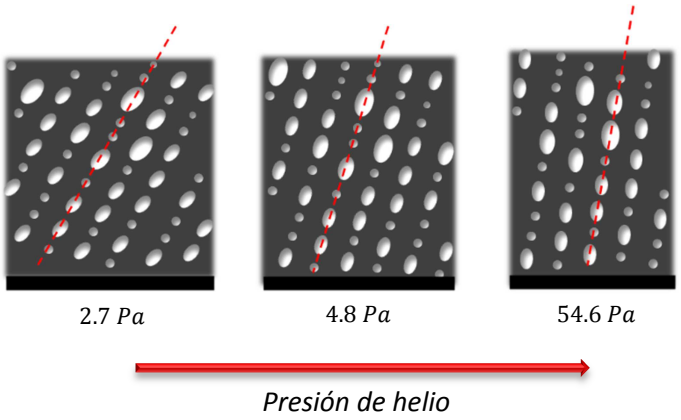

Potencia: $p = 4.8\ Pa$

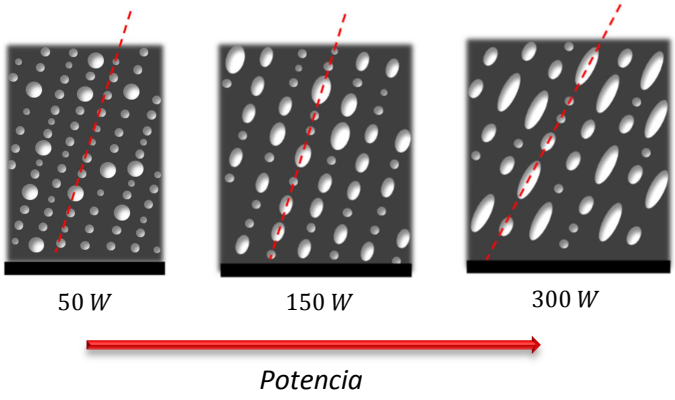

Bias: $P = 150\ W$ RF, $p = 9.0\ Pa$

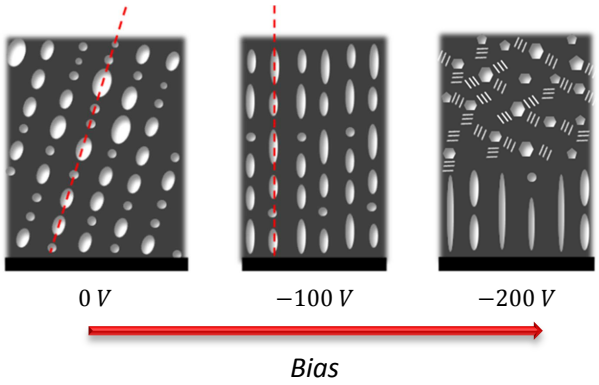

Temperatura de deposición: $P = 150\ W$ RF, $p = 2.7\ Pa$

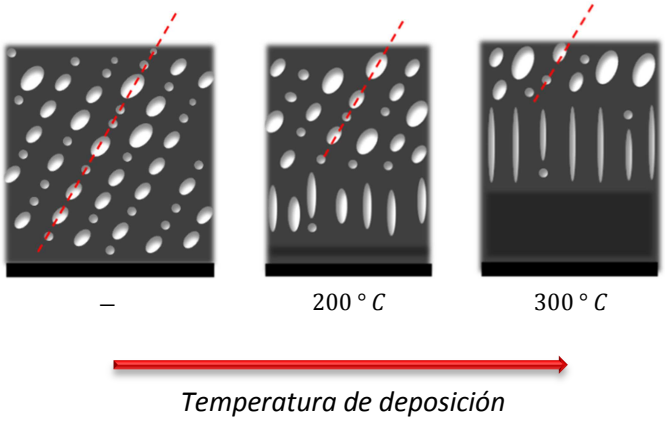

4. Estudio de la formación de nanoestructuras en recubrimientos de silicio poroso mediante simulación

Como ya ha sido demostrado en apartados anteriores, los parámetros de deposición y el gas de sputtering juegan un papel importante en el desarrollo de estructuras con porosidad cerrada. Con el objetivo de entender, desde un punto de vista fundamental, los fenómenos que causan la formación de las diferentes estructuras, se utilizarán herramientas de simulación. La ventaja de ello es que los procesos físicos que la simulación tiene en cuenta son conocidos, así, comparando experimento y simulación es posible entender los

fenómenos que determinan las diferentes estructuras obtenidas en distintas condiciones de deposición y usando diferentes gases de síntesis.

4.1. Software para la simulación

Para simular la formación del recubrimiento y entender la influencia de los procesos atómicos en la formación de la nanoestructura, se ha utilizado el software NASCAM [39,40]. Dicho software está basado en simulación cinética tridimensional Monte Carlo (kMC) que modela agregación balística. El modelo simula la evolución temporal de los adátomos depositados considerando que estos llegan a la superficie (sustrato o capa) con unas distribuciones angulares y de energía específicas. Una vez estos adátomos son depositados, dependiendo de su energía y la estructura de enlace pueden darse procesos de movilidad superficial.

Para la realización de la simulación, se han seguido diferentes pasos. En primer lugar se han calculado las distribuciones angulares y de energía de los átomos arrancados del blanco. Para ello se empleó el software SRIM [41]. En el segundo paso el transporte de los átomos provenientes del blanco a través del gas de sputtering hasta alcanzar el sustrato es simulado usando el software SIMTRA [42]. Con dicho software se obtienen las distribuciones angulares y de energía de los átomos al llegar al sustrato. SIMTRA sólo considera átomos neutros, por lo que la contribución de los iones del plasma a la formación del recubrimiento no es tenida en cuenta. Y tercero, introduciendo la información obtenida en los pasos anteriores en NASCAM, éste último simulará el crecimiento del recubrimiento en tres dimensiones. Finalmente, para analizar la estructura porosa del recubrimiento simulado, se usó el software PORESTAT [43], el cuál es capaz de diferenciar entre porosidad abierta y cerrada.

4.2. Detalles experimentales de los recubrimientos estudiados

Debido a que SIMTRA no tiene en cuenta el efecto de los iones en el plasma, para reducir su influencia sobre el crecimiento del recubrimiento, se aplicará una potencia de $150\,W$ en modo DC al blanco durante la deposición. Para estudiar el efecto de los gases, se han

depositado recubrimientos bajo dos atmósferas distintas: Ar y mezcla de He y Ar. Finalmente, la geometría de deposición es analizada también depositando en condiciones de ángulo oblicuo en dos zonas distintas, zona 1 (Z1) y zona 2 (Z2), mostradas en la figura 2.2 de este resumen. En la siguiente tabla se muestran las condiciones de deposición de los recubrimientos estudiados.

Tabla 4.1: Condiciones de deposición de los recubrimientos estudiados.

Recubrimiento	Zona en el porta muestras	Modo / Potencia (W)	Presión (Pa)	Razón de deposición * (nm/s)
Si/1/Ar	1	DC 150	1.4	0.85
Si/2/Ar	2	DC 150	1.4	0.34
Si/1/He + Ar	1	DC 150	He: 1.7 Ar: 0.8	0.63
Si/2/He + Ar	2	DC 150	He: 1.7 Ar: 0.8	0.31

* Valores calculados a partir de los espesores obtenidos por imágenes de SEM en sección transversal.

Con las condiciones de deposición elegidas, en ambas zonas se tiene una temperatura suficientemente baja de forma que los procesos activados térmicamente tienen una eficiencia muy limitada en comparación con los efectos de sombra [35].

4.3. Caracterización microestructural: Comparación entre resultados experimentales y simulación

4.3.1. Resultados experimentales

En la figura 4.1 se presentan imágenes de la sección transversal de los recubrimientos obtenidas por TEM, en donde destaca el efecto de la geometría de deposicion. Debido a la posición inclinada del magnetron, los recubrimientos presentan una estructura porosa inclinada en la dirección del magnetron.

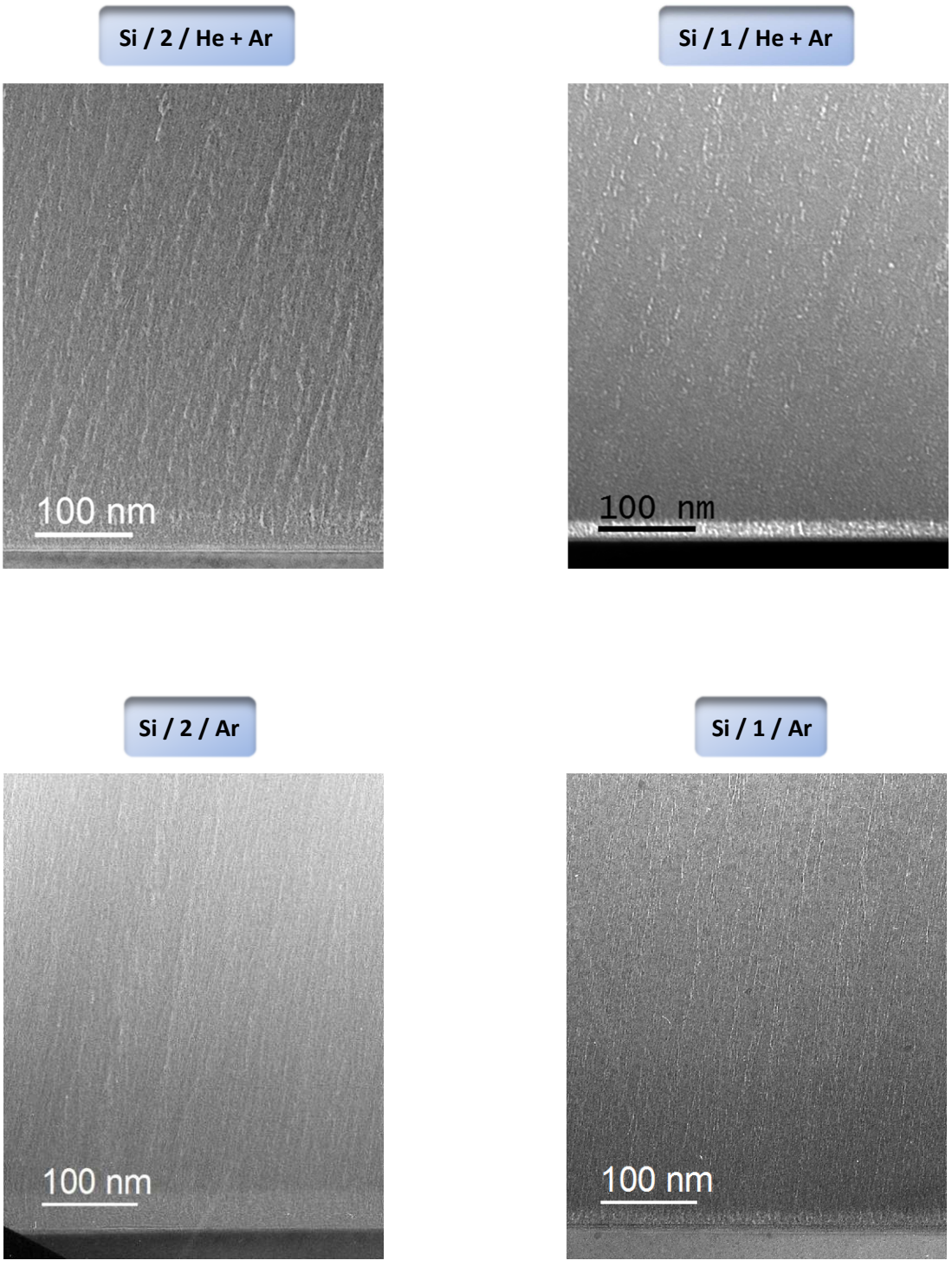

Figura 4.1: Sección transversal de los recubrimientos depositados con ambos gases y zonas obtenidos por TEM.

4.3.2. Simulación del crecimiento de los recubrimientos

En la simulación del crecimiento de los recubrimientos sólo se ha tenido en cuenta los efectos de sombra ya que a las temperaturas de crecimiento experimentales, los efectos térmicos son despreciables.

Además, para el caso del cálculo de las distribuciones angulares y de energía de los átomos arrancados del blanco así como durante el transporte a través del gas de sputtering, en los recubrimientos simulados con una mezcla de He y Ar, sólo se tuvo en cuenta la contribución del Ar debido a su mayor masa atómica, despreciando la contribución del He con una masa menor que el Si. Así, la única diferencia en cuanto a gases de sputtering en las simulaciones es la presión de Ar.

Con esto en mente, en la figura 4.2 se presentan las imágenes de la estructura simulada por NASCAM de los recubrimientos en sección transversal con unas dimensiones de 400×11 átomos, en el mismo plano que el mostrado en la figura 4.1.

La simulación muestra que la zona 2 parece ser más porosa que la zona 1 independientemente del gas de sputtering usado. También la zona 2 muestra una estructura porosa más inclinada hacia el magnetron que la zona 1. Atendiendo a una misma zona, la simulación hecha para la mezcla He y Ar (en la que la influencia del He ha sido despreciada) muestra una estructura más inclinada que la simulación hecha con sólo Ar.

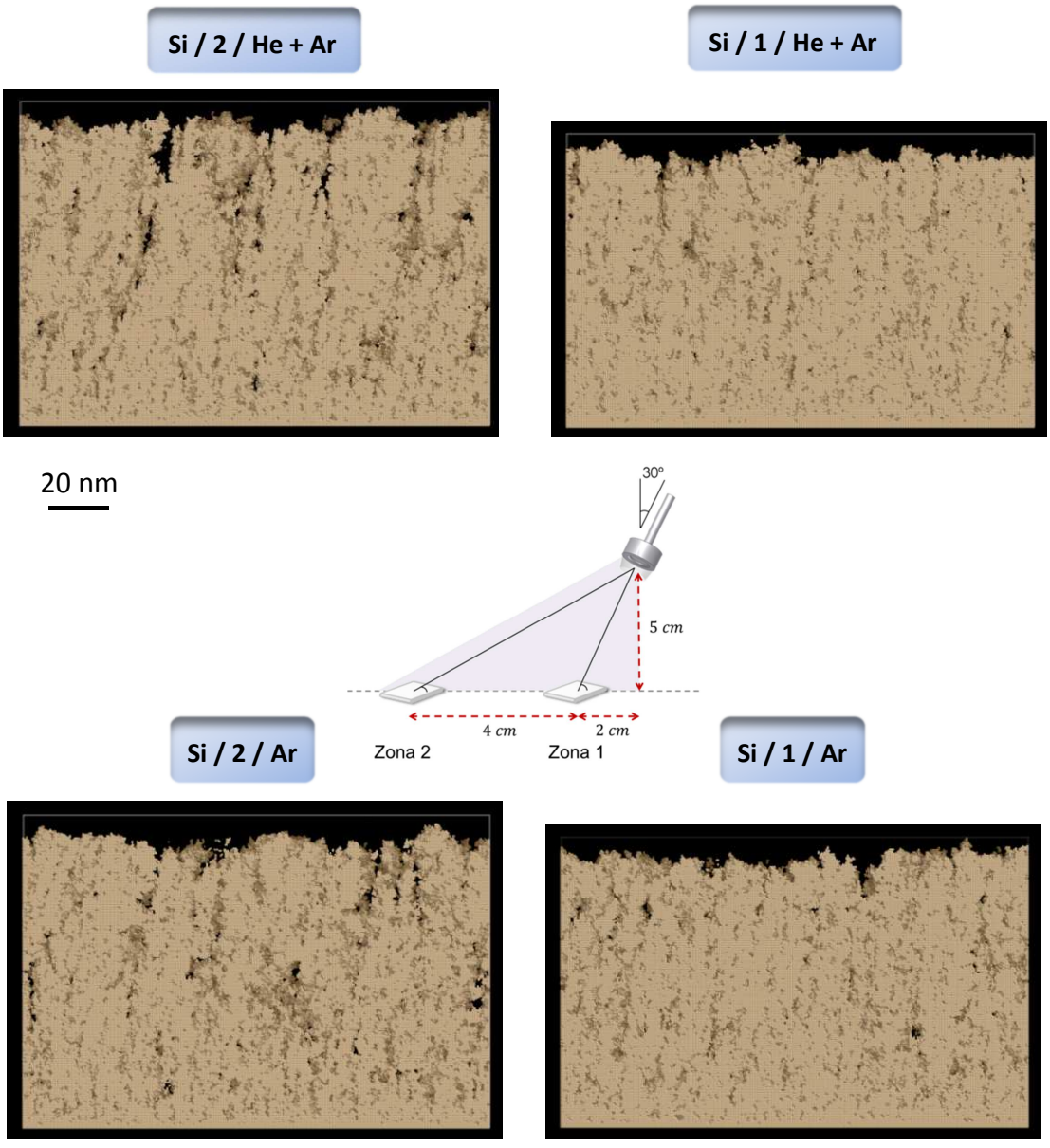

Figura 4.2: Simulación de la estructura de los recubrimientos en sección transversal con NASCAM.

4.3.3. Análisis de la porosidad cerrada

Una vez presentada la simulación para cada uno de los recubrimientos, se estudió la porosidad cerrada de éstos y se comparó con los resultados experimentales.

En las figuras 4.3 y 4.4 se presentan imágenes TEM de alta resolución mostrando el tipo de poros presentes en cada recubrimiento. Además se ha medido su tamaño presentado en forma de distribución de diámetro de poro efectivo. Dicho diámetro de poro efectivo es definido como el diámetro que debería tener el poro si fuese circular para tener un área igual a la medida experimentalmente.

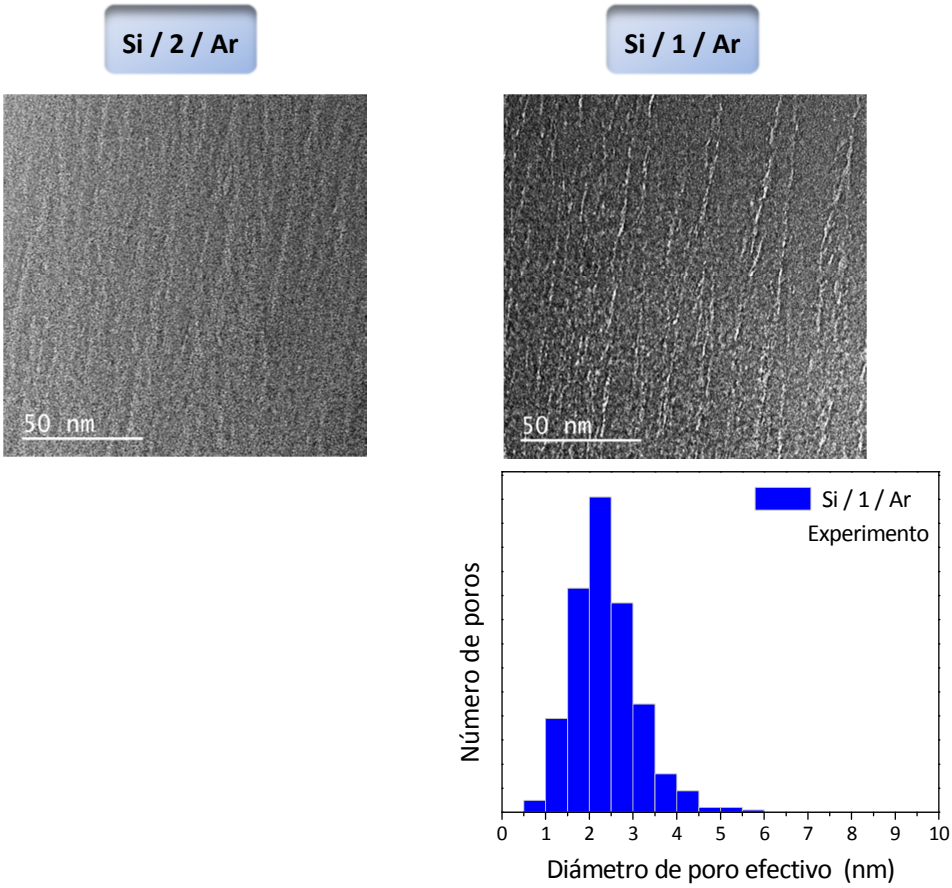

Figura 4.3: Detalle de la porosidad por TEM y distribución de tamaño de poro del recubrimiento depositado con Ar en la zona 1.

En el caso de los recubrimientos depositados con Ar (figura 4.3) no ha sido posible medir el tamaño de poro en la zona 2 debido a que las medidas obtenidas eran arbitrarias e inconcluyentes. Sin embargo, en la zona 1 cabe destacar poros pequeños y alargados con un tamaño en torno a $2\,nm$ alineados uno detrás de otro. Este tipo de porosidad es la típica en recubrimientos con estructura columnar en condiciones de deposición oblicua como es el caso.

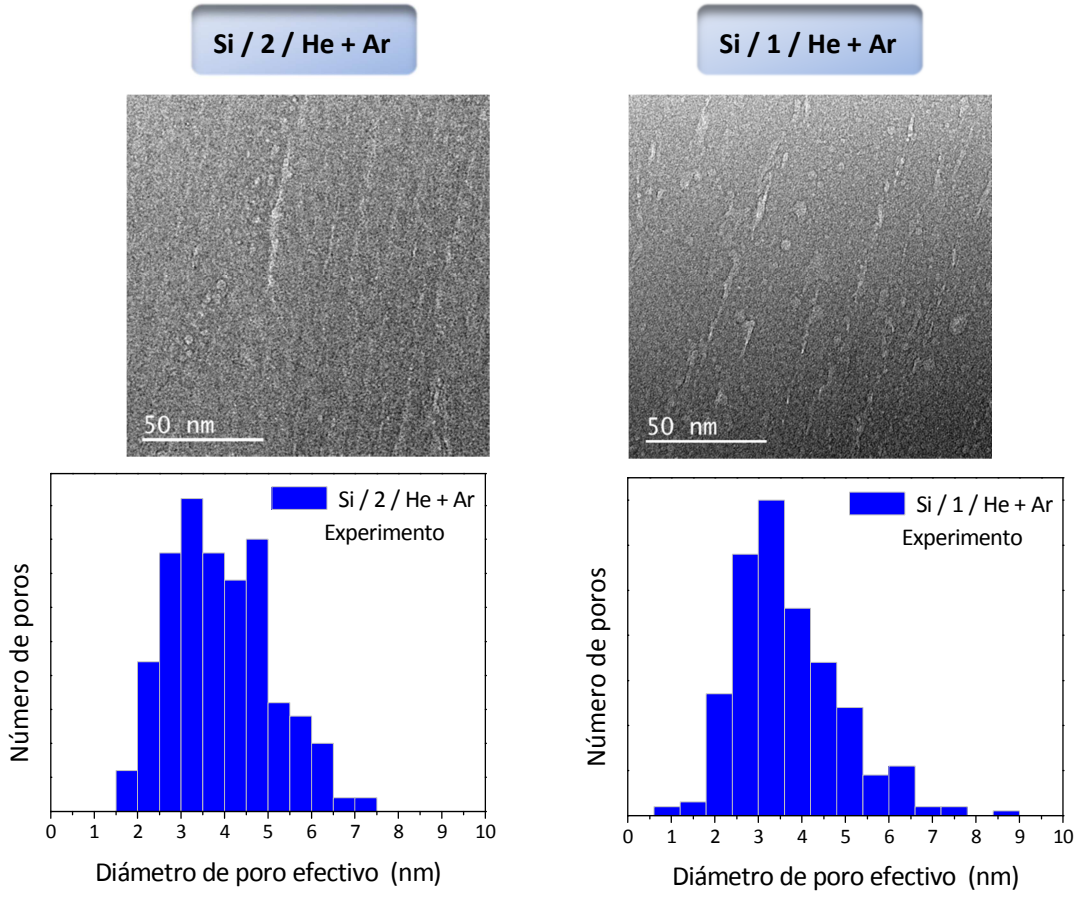

Figura 4.4: Detalle de la porosidad por TEM y distribuciones de tamaño de poro de los recubrimientos depositados con He + Ar en ambas zonas.

En los recubrimientos depositados con la mezcla He + Ar (figura 4.4) se observa un tamaño medio de poro en torno a $4\,nm$ en ambas zonas, sin embargo, el aspecto destacable es la

forma de los poros, que como se muestra en la figura 4.4, los hay alargados como en el caso de los recubrimientos preparados con Ar, pero también los hay más redondeados.

Así, parece ser que la presencia de He en el gas de sputtering da lugar a la formación de poros redondeados como ya fue reportado en un trabajo previo [44]. Este hecho también ha sido reportado en el caso de sputtering de metales usando una mezcla de He y Ar [45–47].

Mediante el uso del software PORESTAT se ha medido, a partir de los resultados obtenidos por NASCAM el tamaño de poro de los recubrimientos. Las distribuciones de tamaño de poros cerrados en comparación con los resultados experimentales se presentan en las figuras 4.5 y 4.6.

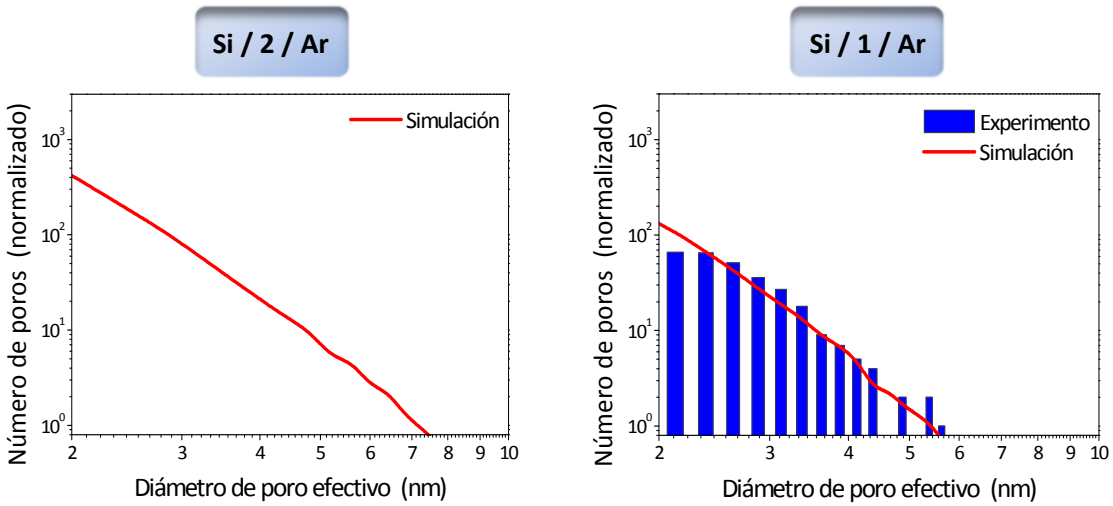

Figura 4.5: Distribuciones de tamaño de poro de los recubrimientos depositados con Ar. Comparación entre experimento y simulación.

Como se observa en la figura 4.5, para el caso de los recubrimientos depositados con Ar, el ajuste entre los datos experimentales y la simulación del tamaño de poro en la zona 1 es muy bueno, demostrando así que los efectos de sombra explican completamente la porosidad producida en estas condiciones de deposición (distribución de tamaño y

orientación de los poros). En la zona 2, como ya ha sido explicado anteriormente, no se ha podido medir experimentalmente el tamaño de los poros.

En el caso de los recubrimientos depositados con la mezcla He + Ar (figura 4.6) se observa cierta similitud para mayor tamaño de poros, sin embargo, para poros pequeños los resultados de la simulación difieren de los experimentales en ambas zonas. Lo que indica que los efectos de sombra no pueden explicar completamente la estructura porosa obtenida. La presencia de He en la mezcla de gases introduce un nuevo proceso en el desarrollo de la estructura del recubrimiento por el cual los poros pequeños tienden a unirse formando poros de mayor tamaño. Este tipo de proceso podría ser similar a los ya reportados sobre la formación de burbujas durante la implantación de metales con He [37,48,49]. Estos procesos están asociados a cierta movilidad de los defectos en la red debido a la baja solubilidad del He en el material.

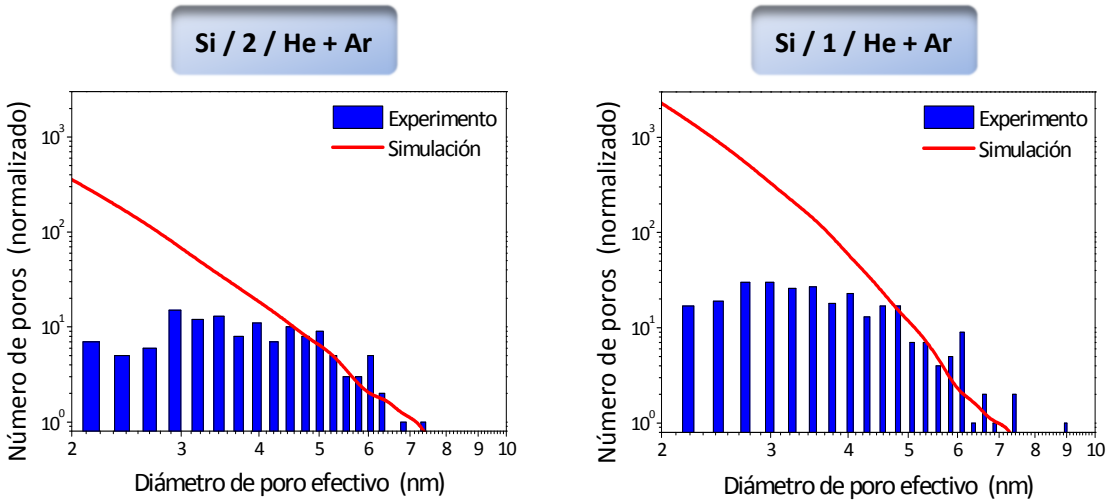

Figura 4.6: Distribuciones de tamaño de poro de los recubrimientos depositados con mezcla He + Ar. Comparación entre experimento y simulación.

5. Diseño y fabricación de dispositivos ópticos multicapa mediante el uso de recubrimientos de silicio poroso con porosidad cerrada

En los apartados anteriores, se han estudiado recubrimientos de silicio poroso con porosidad cerrada desde un punto de vista fundamental, investigando la formación de la porosidad, la estabilidad del He atrapado en la estructura así como el efecto de los parámetros de deposición sobre las propiedades físicas de los recubrimientos. En particular, se ha mostrado como es posible modificar el índice de refracción cambiando el gas de sputtering [44]. En este apartado con base a los resultados anteriores se pasará a diseñar estructuras multicapa como reflectores de Bragg distribuidos (DBR) [50–53] o microcavidades ópticas (OMC) [54–57] utilizando un único material, silicio.

Las propiedades de estos dispositivos ópticos, como la posición de la banda fotónica prohibida y la reflectancia en esta banda, pueden ser modificadas controlando parámetros críticos como el espesor de las capas individuales que componen la estructura multicapa, el índice de refracción de cada una de ellas y el número total de capas depositadas (ver apéndice V).

Así el objetivo planteado es el diseño de dos reflectores de Bragg y una microcavidad óptica utilizando recubrimientos de silicio con diferente índice de refracción a partir de la metodología ya presentada.

5.1. Dispositivos ópticos estudiados y parámetros de diseño

En el diseño de los dispositivos se han usado dos tipos de capas: una densa H_n de alto índice de refracción n_H y una porosa $L_{n\,1}$ o $L_{n\,2}$ de bajo índice de refracción $n_{L\,1}$ o $n_{L\,2}$ respectivamente. La capa activa utilizada en el caso del diseño de la OMC es del mismo tipo que la capa porosa $L_{n\,2}$. En la tabla 5.1 se muestran las capas utilizadas en cada dispositivo, cuyas condiciones de deposición fueron presentadas en la tabla 2.3 de este resumen.

La localización de los sustratos en el porta muestras para la fabricación de los dispositivos ha sido la zona 1 (ver figura 2.2 de este resumen).

Tabla 5.1: Capas utilizadas en el diseño de cada dispositivo.

Dispositivo óptico	Capa porosa	Capa densa	Capa activa
DBR 1	L_{n1} Si/He	H_n Si/Ar/bias	---
DBR 2	L_{n2} Si/He/b 100	H_n Si/Ar/bias	---
OMC	L_{n2} Si/He/b 100	H_n Si/Ar/bias	L_{n2} Si/He/b 100

La longitud de onda de diseño λ_0 ha sido elegida en el rango del infrarrojo cercano aprovechando que la absorción en este rango es muy baja. Para el caso de los DBRs, la estructura de los dispositivos se obtiene alternando capas densa y porosa con un período de 7 bicapas depositando primero la capa densa y terminando de nuevo con una capa densa. Mientras que el período fue de 4 para los DBR que componen la OMC separados por la capa activa. Los espesores de las capas fueron elegidos tales que el espesor óptico de cada capa fuese un cuarto de la longitud de onda de diseño del dispositivo. Para el caso de la capa activa, el espesor óptico fue de un medio.

Los índices de refracción de las capas utilizadas (densa y porosas) en cada dispositivo así como sus espesores y la estructura del dispositivo se presentan en las siguientes tablas.

Tabla 5.2: Índices de refracción de las capas densa y porosas y del sustrato a la longitud de onda de diseño.

Dispositivo óptico	Longitud de onda de diseño $\lambda_0\ (nm)$	Alto índice de refracción complejo (η_H)	Bajo índice de refracción complejo (η_L)	Índice de refracción del sustrato (n_S)
DBR 1	1750	$3.72 + i\ 0.01$	$2.77 + i\ 0.03$	3.46
DBR 2	1750	$3.72 + i\ 0.01$	$2.80 + i\ 0.02$	3.46
OMC	1640	$3.74 + i\ 0.01$	$2.81 + i\ 0.02$	3.47

Tabla 5.3: Estructura de los dispositivos y espesores de las capas.

Dispositivo óptico	Secuencia de la estructura	$t_H{}^*$ (nm)	$t_{Ln1}{}^*$ (nm)	$t_{Ln2}{}^*$ (nm)	$t_{Lc}{}^*$ (nm)
DBR 1	$Sustr-(H_nL_{n\,1})^7H_n-aire$	112 ± 4	160 ± 5	---	---
DBR 2	$Sustr-(H_nL_{n\,2})^7H_n-aire$	116 ± 8	---	158 ± 4	---
OMC	$Sustr-(H_nL_{n\,2})^4H_nL_c$ $-(H_nL_{n\,2})^4H_n-aire$	109 ± 5	---	151 ± 4	295 ± 7

*Calculados a partir de los espesores obtenidos por imágenes de SEM en sección transversal.

En la siguiente figura se muestra la estructura del DBR 2 y en más detalle la estructura porosa de las capas utilizadas en los DBR 1 y DBR 2 obtenidas por TEM.

El efecto de aplicación de bias durante la deposición de la capa porosa queda presente en la figura anterior, en la que la aplicación del bias (DBR 2) hace que la porosidad se presente en dirección perpendicular al sustrato, mientras que cuando el bias no es aplicado (DBR 1) la porosidad esta inclinada en la dirección del magnetron. Además también queda mostrado que el efecto de aplicación de bias durante la deposición de la capa densa no afecta a la estructura de las capas porosas anteriormente depositadas, ya se hubiese aplicado bias o no en la deposición de estas últimas.

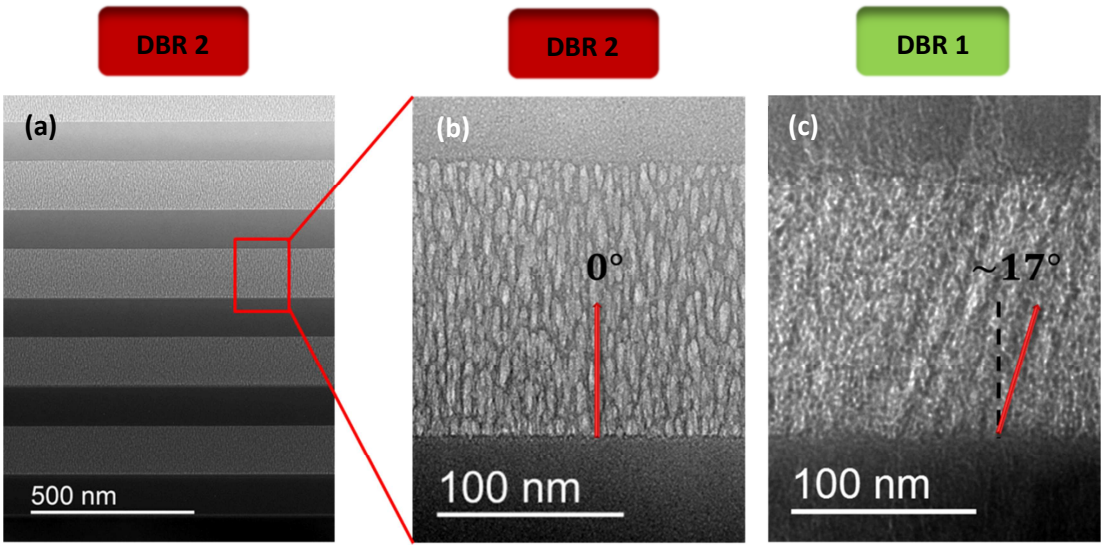

Figura 5.1: (a) Sección transversal por TEM de la estructura multicapa DBR 2 y detalle de la estructura porosa en (b) DBR 2 y (c) DBR1.

La reflectancia de los dispositivos DBR fue medida en el rango del infrarrojo cercano, $1000 - 2500\ nm$, y comparada con la teórica obtenida mediante simulación del espectro introduciendo los valores de índices de refracción y espesores mostrados en las tablas 5.2 y 5.3 respectivamente. La figura 5.2 muestra dichos espectros para cada uno de los DBRs diseñados.

En ambos DBRs puede verse el buen acuerdo entre el espectro teórico y el experimental, con el centro de la banda prohibida en la posición a la que se había diseñado y con una alta reflectancia en esa posición. Las ligeras diferencias entre los espectros teórico y experimental pueden ser debidas a los errores asociados a la medición de los espesores de las capas componentes. Aún con estas diferencias, queda mostrado el buen control del espesor de las capas individuales que se alcanza, y por tanto la calidad de los dispositivos ópticos fabricados con la metodología propuesta.

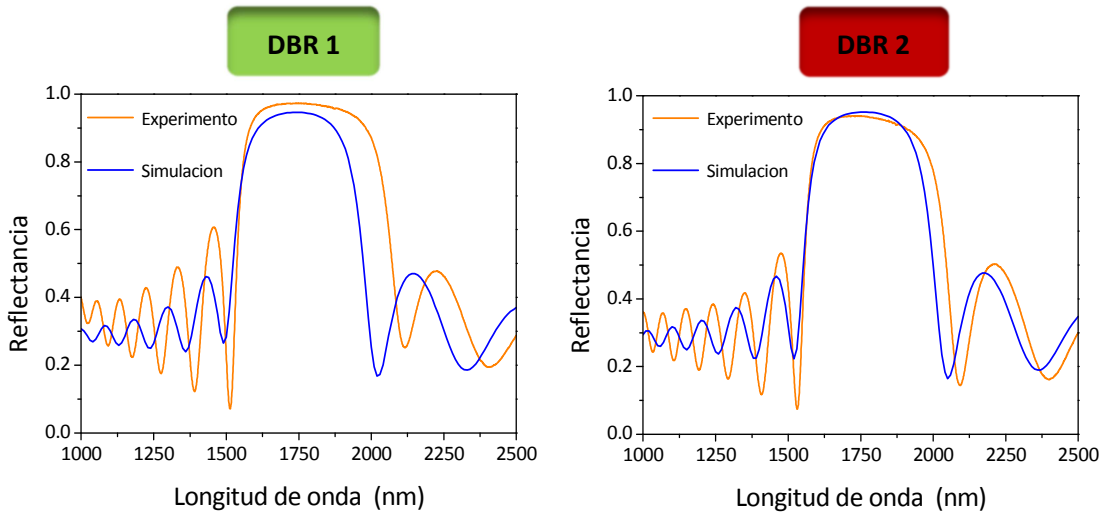

Figura 5.2: Espectros de reflectancia teórica y experimental de los dispositivos DBR 1 y DBR 2.

Una de las ventajas de la deposición en ángulo oblicuo (OAD) es la diferencia de espesor con la distancia al magnetron. Aprovechando esta ventaja experimental se ha fabricado un DBR (con las mismas condiciones que el DBR 2) el cual posee un gradiente de espesor de las capas que lo forman con la distancia al magnetron. El esquema experimental se muestra en la figura 5.3 (a) y (b) así como el efecto sobre el espectro de reflectancia, figura 5.3 (c), mostrando un desplazamiento de la posición de la banda prohibida así como en la anchura de la banda.

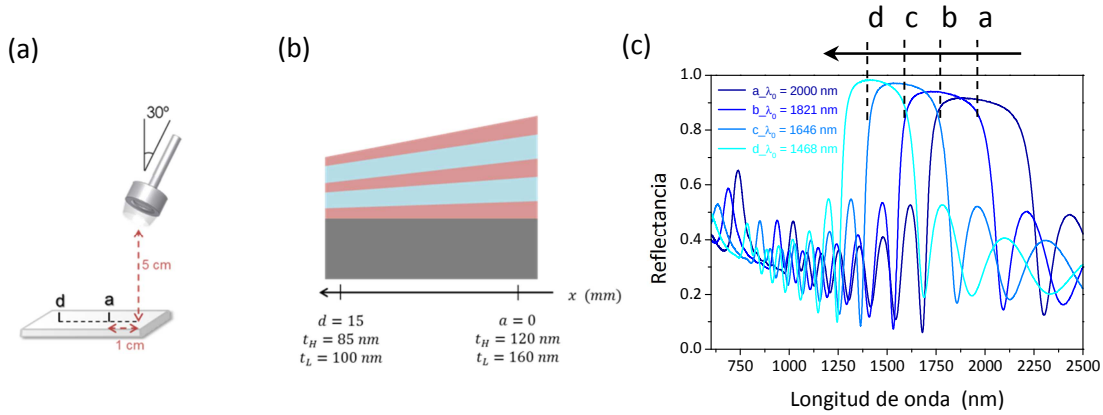

Figura 5.3: (a) Geometría de deposición. (b) Efecto sobre el espesor de las capas en función de la distancia al magnetrón. (c) Espectro de reflectancia de los recubrimientos obtenidos.

La técnica de magnetron sputtering también se caracteriza por temperaturas de deposición bajas, que permiten depositar sobre una amplia variedad de sustratos, tales como sustratos flexibles o polímeros. En la siguiente figura se muestra un dispositivo DBR depositado en las mismas condiciones que el DBR 2 sobre dos tipos de sustratos flexibles, teflón (figura 5.4 (a)) y kapton (figura 5.4 (b)).

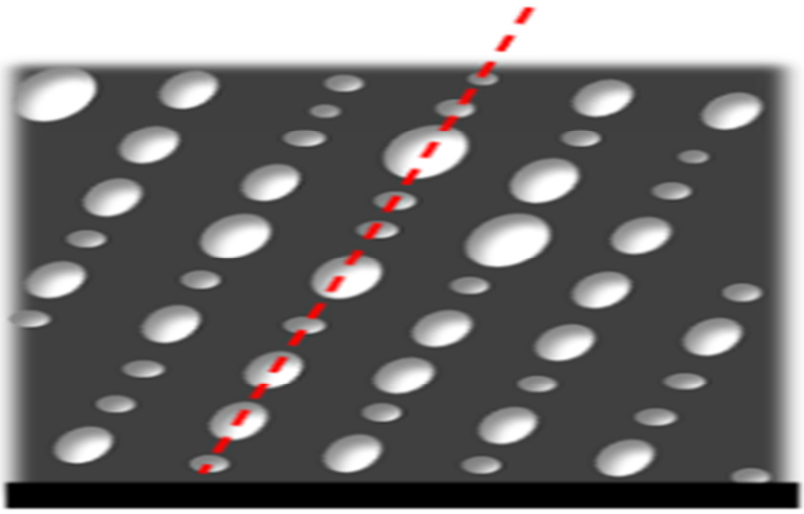

Figura 5.4: DBR 2 depositado sobre diferentes sustratos flexibles. (a) Teflon. (b) Kapton.

En la figura 5.5 (a) se presenta la estructura de la microcavidad óptica diseñada obtenida por SEM en la que se distinguen tanto las capas densa y porosa, así como la capa activa en el centro de la estructura.

Igual que en los casos de los DBRs presentados anteriormente, el espectro de reflectancia medido experimentalmente es comparado con el espectro teórico, mostrando un buen acuerdo entre ambos tanto en la posición del pico de la microcavidad como en la anchura de este.

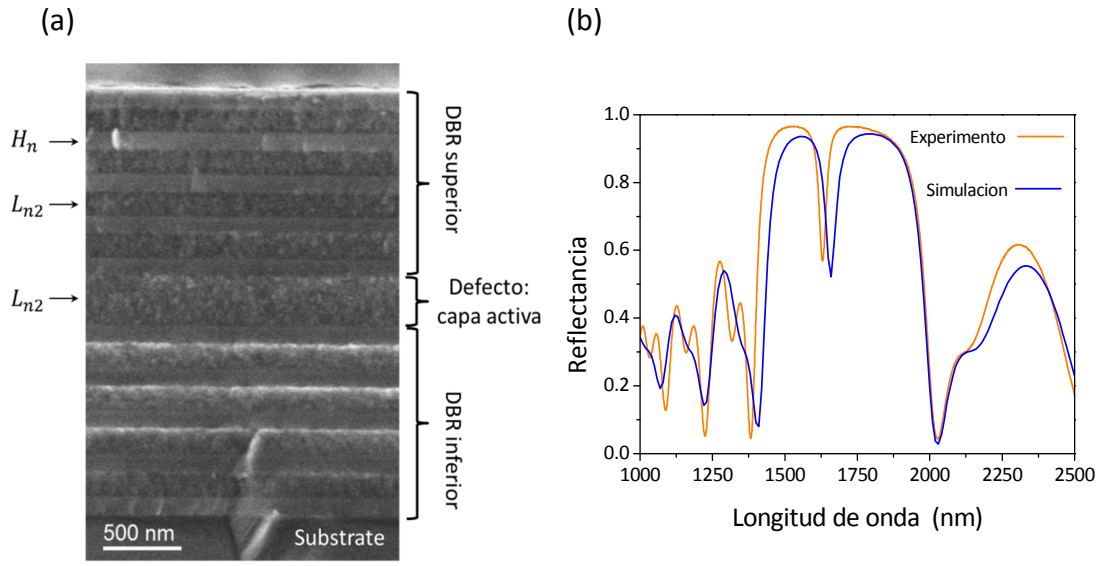

Figura 5.6: Microcavidad óptica (a) Vista sección transversal por SEM. (b) Espectros de reflectancia teórico y experimental.

6. Conclusiones finales

El objetivo principal de esta tesis ha sido el desarrollo de una nueva metodología para producir recubrimientos de silicio poroso utilizando plasmas de helio mediante la técnica de magnetron sputtering. Dicha metodología permite un control de la porosidad y por tanto del índice de refracción del recubrimiento. En los diferentes apartados que componen este resumen se han estudiado las relaciones entre los parámetros de deposición, microestructura y propiedades finales. De forma más concreta se pasará a exponer las conclusiones particulares obtenidas en cada uno de los apartados:

- La nueva metodología desarrollada permite producir recubrimientos amorfos de silicio poroso utilizando helio como gas de sputtering con una particular estructura de poros cerrados. El control de los parámetros de deposición permite modificar la porosidad para fabricar recubrimientos con índices de refracción a medida. Los parámetros de deposición estudiados son:

- Gas de deposición: el uso de He permite una estructura de poros cerrados en cuyo interior se encuentra el gas, mientras que el Ar da lugar a una estructura más densa y por tanto con un índice de refracción mayor.
- Geometría de deposición: en condiciones de deposición a ángulo oblicuo, cambiando la dirección del flujo de vapor es posible modificar la orientación de los poros los cuales aparecen orientados en la misma dirección que el flujo de vapor, cumpliéndose la regla de la tangente.
- Presión de helio: en configuración de ángulo oblicuo, un incremento de la presión de helio da lugar a una disminución del ángulo de orientación de los poros. Esto se debe al aumento de colisiones entre los átomos de gas y los átomos de Si a depositar, perdiendo estos últimos su direccionalidad al llegar al sustrato. Además, la cantidad de He atrapado en el recubrimiento disminuye con la presión de gas durante la deposición.
- Potencia RF: con una geometría de ángulo oblicuo, el incremento de potencia orienta los poros hacia una dirección más cercana a la dirección de la geometría de deposición. Además se observa un incremento en el tamaño de poro con el incremento de la potencia cambiando de poros redondeados a poros más alargados. También se ha observado un menor contenido de He en el recubrimiento a la potencia más alta, que podría ser debido a la alta desorción de los átomos de He que son desplazados al llegar al sustrato los átomos de Si con más energía.
- Bias en el sustrato: en configuración de ángulo oblicuo, la aplicación de bias da lugar a un crecimiento de la porosidad en dirección normal al sustrato con poros con una forma más alargada. Esto es debido al aumento de la movilidad atómica al aplicar bias que provoca la desaparición de los efectos sombra. Para valores de

bias mayores ($-200\,V$) se forma una fase nano-composite compuesta por poros cerrados y cristales de Si embebidos en la matriz amorfa. La fase nano-composite contiene menor cantidad de He que la fase amorfa.

- Temperatura de deposición: se han depositado recubrimientos a diferentes temperaturas pertenecientes a las zonas I, T y II del modelo de Thornton. En la zona I ($T_h = \frac{T_s}{T_m} < 0.3$), en la que la estructura es dominada la baja movilidad atómica y los efectos de sombra, se tiene una estructura con la porosidad orientada en la dirección del magnetron. En la zona T ($T_h \approx 0.3$), en la que la difusión atómica tiene lugar, se forma una capa densa junto al sustrato seguido por una capa porosa. En la zona II ($T_h > 0.3$), donde se dan efectos de difusión atómica superfical, se da la misma estructura que en la zona T con una capa densa de mayor espesor.

Además se demuestra que el He atrapado en el recubrimiento se encuentra dentro de los poros a una presión del orden de GPa. Se prueba la estabilidad del He en el recubrimiento no observándose diferencia en su contenido a lo largo del tiempo.

Mediante tratamiento térmico se muestra que la estructura de poros con He es estable al menos hasta $300°C$. A $550°C$ se observa una fuerte disminución de la cantidad de He en el recubrimiento.

- Para entender los mecanismos físicos en la formación de la estructura porosa de recubrimientos de Si, se utilizaron herramientas de simulación (NASCAM) basadas en el efecto sombra. La comparación de las medidas de tamaño de poro dadas por la simulación con las obtenidas de recubrimientos experimentales muestra que en deposiciones en atmósfera de Ar, el efecto de sombra explica completamente la formación de la porosidad. Sin embargo, en deposiciones en atmósfera de He + Ar, experimento y simulación difieren en el rango de poros pequeños. Así se concluye

que el He introduce un nuevo mecanismo en el desarrollo de la porosidad distinto del efecto sombra.

- Con la metodología presentada se diseñan dos tipos de dispositivos ópticos: un reflector de Bragg distribuido (DBR) y una microcavidad óptica (OMC). Estos dispositivos están formados por la alternancia de capas de alto y bajo índice de refracción (recubrimientos densos y porosos). Se obtiene un buen acuerdo entre los espectros de reflectancia experimental y teórico.

  También se demuestra la posibilidad de utilizar dicha metodología para depositar sobre sustratos flexibles como teflón y kapton. Por último se presenta el diseño de un DBR con un gradiente de espesor, modificando así la posición del pico de Bragg dependiendo del espesor de las capas componentes.

7. Referencias

1. Becker, C. *et al.* Large-area 2D periodic crystalline silicon nanodome arrays on nanoimprinted glass exhibiting photonic band structure effects. *Nanotechnology* **23,** 135302 (2012).

2. Jin, H. & Liu, G. L. Fabrication and optical characterization of light trapping silicon nanopore and nanoscrew devices. *Nanotechnology* **23,** 125202 (2012).

3. Zhang, K., Seo, J.-H., Zhou, W. & Ma, Z. Fast flexible electronics using transferrable silicon nanomembranes. *J. Phys. -Appl. Phys.* **45,** 143001 (2012).

4. Spinelli, P., Verschuuren, M. A. & Polman, A. Broadband omnidirectional antireflection coating based on subwavelength surface Mie resonators. *Nat. Commun.* **3,** 692 (2012).

5. Dubey, R. S. & Gautam, D. K. Synthesis and characterization of porous silicon layers for 1D photonic crystal application. *Optik* **122,** 494–497 (2011).

6. Abidi, D., Romdhane, S., Brunet-Bruneau, A. & Fave, J.-L. Microstructural characterization of porous silicon for use in optoelectronic devices. *Eur. Phys. J.-Appl. Phys.* **45,** 10601 (2009).

7. Ramizy, A., Hassan, Z., Omar, K., Al-Douri, Y. & Mahdi, M. A. New optical features to enhance solar cell performance based on porous silicon surfaces. *Appl. Surf. Sci.* **257,** 6112–6117 (2011).

8. Uhlir, A. Electrolytic Shaping of Germanium and Silicon. *Bell Syst. Tech. J.* **35,** 333–347 (1956).

9. Lehmann, V. & Gosele, U. Porous Silicon Formation - a Quantum Wire Effect. *Appl. Phys. Lett.* **58,** 856–858 (1991).

10. Canham, L. T. Silicon quantum wire array fabrication by electrochemical and chemical dissolution of wafers. *Appl. Phys. Lett.* **57,** 1046–1048 (1990).

11. Halimaoui, A. *et al.* Electroluminescence in the Visible Range During Anodic-Oxidation of Porous Silicon Films. *Appl. Phys. Lett.* **59,** 304–306 (1991).

12. Koshida, N. & Koyama, H. Visible Electroluminescence from Porous Silicon. *Appl. Phys. Lett.* **60,** 347–349 (1992).

13. Korotcenkov, G. & Cho, B. K. Silicon Porosification: State of the Art. *Crit. Rev. Solid State Mater. Sci.* **35,** 153–260 (2010).

14. Solanki, C. S., Bilyalov, R. R., Poortmans, J., Nijs, J. & Mertens, R. Porous silicon layer transfer processes for solar cells. *Sol. Energy Mater. Sol. Cells* **83,** 101–113 (2004).

15. Godinho, V., Rojas, T. C. & Fernandez, A. Magnetron sputtered a-SiOxNy thin films: A closed porous nanostructure with controlled optical and mechanical properties. *Microporous Mesoporous Mater.* **149,** 142–146 (2012).

16. Godinho, V. *et al.* SiOxNy thin films with variable refraction index: Microstructural, chemical and mechanical properties. *Appl. Surf. Sci.* **256,** 4548–4553 (2010).

17. Godinho, V. Synthesis and characterization of magnetron sputtered thin films of the Ti-Al-Si-N(O) system. (2011). at <University of Seville>

18. Lucas, A. Helium in Metals. *Phys. B C* **127,** 225–239 (1984).

19. *Handbook of Optics*. **4,** (McGraw-Hill, 2009).

20. Nieuwenhuizen, JM. & Haanstra, H. Microfractography of Thin Films. *Philips Tech. Rev.* **27,** 87–& (1966).

21. Mattox, D. M. *Handbook of Physical Vapor Deposition (PVD) Processing*. (William Andrew, 2010).

22. Novotny, M. *et al.* RF magnetron sputtering of silver thin film in Ne, Ar and Kr discharges-plasma characterisation and surface morphology. *Surf. Coat. Technol.* **228,** S466–S469 (2013).

23. Pokorny, P. *et al.* Mass Spectrometric Characterizations of Ions Generated in RF Magnetron Discharges during Sputtering of Silver in Ne, Ar, Kr an.d Xe Gases. *Plasma Process. Polym.* **10,** 593–602 (2013).

24. Petrov, I., Ivanov, I., Orlinov, V. & Kourtev, J. Comparison of Some Basic Plasma Parameters and Discharge Characteristics. *Contrib. Plasma Phys.* **30,** 223–231 (1990).

25. Somogyvari, Z., Langer, G. A., Erdelyi, G. & Balazs, L. Sputtering yields for low-energy Ar+- and Ne+-ion bombardment. *Vacuum* **86,** 1979–1982 (2012).

26. Shin, H., Zhu, W., Economou, D. J. & Donnelly, V. M. Ion energy distributions, electron temperatures, and electron densities in Ar, Kr, and Xe pulsed discharges. *J. Vac. Sci. Technol. A* **30,** 031304 (2012).

27. Song, P. K., Irie, Y., Sato, Y. & Shigesato, Y. Crystal structure and photocatalytic activity of TiO2 films deposited by reactive sputtering using Ne, Ar, Kr, or Xe gases. *Jpn. J. Appl. Phys. Part 2-Lett. Express Lett.* **43,** L358–L361 (2004).

28. Garcia-Martin, J. M., Alvarez, R., Romero-Gomez, P., Cebollada, A. & Palmero, A. Tilt angle control of nanocolumns grown by glancing angle sputtering at variable argon pressures. *Appl. Phys. Lett.* **97,** 173103 (2010).

29. Schierholz, R. *et al.* STEM-EELS analysis reveals stable highdensity He in nanopores of amorphous silicon coatings deposited by magnetron sputtering. *Nanotechnology* **26,** 075703 (2015).

30. Materials Science of Thin Films, 2nd Edition | Milton Ohring | ISBN 9780125249751. at <http://store.elsevier.com/Materials-Science-of-Thin-Films/Milton-Ohring/isbn-9780125249751/>

31. Greene, J. E. in *Handbook of Deposition Technologies for Films and Coatings (Third Edition)* (ed. Martin, P. M.) 554–620 (William Andrew Publishing, 2010). at <http://www.sciencedirect.com/science/article/pii/B9780815520313000120>

32. Nozawa, R., Takeda, H., Ito, M., Hori, M. & Goto, T. Substrate bias effects on low temperature polycrystalline silicon formation using electron cyclotron resonance SiH4/H-2 plasma. *J. Appl. Phys.* **81,** 8035–8039 (1997).

33. Jia, H., Saha, J. K., Ohse, N. & Shirai, H. Effect of substrate bias on high-rate synthesis of microcrystalline silicon films using a high-density microwave SiH4/H-2 plasma. *J. Phys. -Appl. Phys.* **39,** 3844–3848 (2006).

34. Jun, S.-I., Rack, P. D., McKnight, T. E., Melechko, A. V. & Simpson, M. L. Low-temperature solid-phase crystallization of amorphous silicon thin films deposited by rf magnetron sputtering with substrate bias. *Appl. Phys. Lett.* **89,** 022104 (2006).

35. Thornton, J. High-Rate Thick-Film Growth. *Annu. Rev. Mater. Sci.* **7,** 239–260 (1977).

36. Evans, J., Vanveen, A. & Griffioen, C. The Annealing of Helium-Induced Cavities in Silicon and the Inhibiting Role of Oxygen. *Nucl. Instrum. Methods Phys. Res. Sect. B-Beam Interact. Mater. At.* **28,** 360–363 (1987).

37. Evans, J. H. Mechanisms of void coarsening in helium implanted silicon. *Nucl. Instrum. Methods Phys. Res. Sect. B-Beam Interact. Mater. At.* **196,** 125–134 (2002).

38. Chao, D. S. & Liang, J. H. Annealing temperature dependence of photoluminescent characteristics of silicon nanocrystals embedded in silicon-rich silicon nitride films grown by PECVD. *Nucl. Instrum. Methods Phys. Res. Sect. B-Beam Interact. Mater. At.* **307,** 344–348 (2013).

39. Lucas, S. & Moskovkin, P. Simulation at high temperature of atomic deposition, islands coalescence, Ostwald and inverse Ostwald ripening with a general simple kinetic Monte Carlo code. *Thin Solid Films* **518,** 5355–5361 (2010).

40. NASCAM (NAnoSCAle Modeling) User's manual— Université de Namur. at <http://www.unamur.be/sciences/physique/pmr/telechargement/logiciels/nascam>

41. Ziegler, J. F., Ziegler, M. D. & Biersack, J. P. SRIM - The stopping and range of ions in matter (2010). *Nucl. Instrum. Methods Phys. Res. Sect. B-Beam Interact. Mater. At.* **268,** 1818–1823 (2010).

42. Aeken K V. DRAFT - Design, Research And Feasibility of Thin Films at Ghent University/UGent. at <http://www.draft.ugent.be/>

43. PoreSTAT » nanoSCOPS. at <http://nanoscops.icmse.csic.es/software/porestat/>

44. Godinho, V. *et al.* A new bottom-up methodology to produce silicon layers with a closed porosity nanostructure and reduced refractive index. *Nanotechnology* **24,** 275604 (2013).

45. Jia, J., Shi, L., Lai, X. & Wang, Q. Preparation of Al thin films charged with helium by DC magnetron sputtering. *Nucl. Instrum. Methods Phys. Res. Sect. B Beam Interact. Mater. At.* **263,** 446–450 (2007).

46. Shi, L. Q., Liu, C. Z., Xu, S. L. & Zhou, Z. Y. Helium-charged titanium films deposited by direct current magnetron sputtering. *Thin Solid Films* **479,** 52–58 (2005).

47. Zheng, H. *et al.* Introduction of helium into metals by magnetron sputtering deposition method. *Mater. Lett.* **59,** 1071–1075 (2005).

48. Wilson, W., Bisson, C. & Baskes, M. Self-Trapping of Helium in Metals. *Phys. Rev. B* **24,** 5616–5624 (1981).

49. Morishita, K. Nucleation path of helium bubbles in metals during irradiation. *Philos. Mag.* **87,** 1139–1158 (2007).

50. Guo, D.-L., Fan, L.-X., Wang, F.-H., Huang, S.-Y. & Zou, X.-W. Porous Anodic Aluminum Oxide Bragg Stacks as Chemical Sensors. *J. Phys. Chem. C* **112,** 17952–17956 (2008).

51. Rabaste, S. *et al.* Sol-gel fabrication of thick multilayers applied to Bragg reflectors and microcavities. *Thin Solid Films* **416,** 242–247 (2002).

52. Colodrero, S., Ocana, M. & Miguez, H. Nanoparticle-based one-dimensional photonic crystals. *Langmuir* **24,** 4430–4434 (2008).

53. Wu, Z., Lee, D., Rubner, M. F. & Cohen, R. E. Structural color in porous, superhydrophilic, and self-cleaning SiO2/TiO2 Bragg stacks. *Small* **3,** 1445–1451 (2007).

54. Reece, P. J., Lerondel, G., Zheng, W. H. & Gal, M. Optical nicrocavities with subnanometer linewidths based on porous silicon. *Appl. Phys. Lett.* **81,** 4895–4897 (2002).

55. Weiss, S. M., Zhang, J., Fauchet, P. M., Seregin, V. V. & Coffer, J. L. Tunable silicon-based light sources using erbium doped liquid crystals. *Appl. Phys. Lett.* **90,** 031112 (2007).

56. Reece, P. J., Lerondel, G., Mulders, J., Zheng, W. H. & Gal, M. Fabrication and tuning of high quality porous silicon microcavities. *Phys. Status Solidi -Appl. Res.* **197,** 321–325 (2003).

57. Venturello, A. *et al.* Controlled light emission from dye-impregnated porous silicon microcavities. *J. Non-Cryst. Solids* **352,** 1230–1233 (2006).